Sonic Crystal Noise Barriers

Thesis

The Open University

Sonic Crystal Noise Barriers

by
Yung Boon Chong, BEng

A doctoral thesis submitted in partial fulfilment for the degree of
Doctor of Philosophy

in the
Department of Design, Development,
Environment and Materials
Faculty of Mathematics, Computing and Technology
The Open University
Milton Keynes
United Kingdom

November 2012

The Open University

Faculty of Mathematics, Computing and Technology
Department of Design, Development, Environment and Materials
The Open University
Walton Hall
Milton Keynes
MK7 6AA
United Kingdom
Tel +44 (0) 1908 653686
Fax +44 (0) 1908 652192
www.open.ac.uk

Certificate of Originality

This is to certify that I am responsible for the work submitted in this thesis, that the original work is my own except as specified in acknowledgements, in text or in bibliography, and that neither the thesis nor the original work contained therein has been submitted to this or any other institution for a degree.

_____ (Signature)

(Y.B. Chong)

_____ (Date)

Acknowledgements

This dissertation would not have been possible without the guidance and the help of several individuals who in one way or another contributed and extended their valuable assistance in the preparation and completion of this study.

First of all, I would like to express my deepest gratitude to my supervisors Prof. Keith Attenborough and Dr. Shahram Taherzadeh for their unfailing guidance, support and patience during the years I worked on this research and dissertation at The Open University, United Kingdom. Also, through their meticulous reviews and keen observations, the quality of my research is enhanced. Working with them has not only opened my eyes to the multiple facets of acoustics, but also they played a shaping role in my personal development. It has been great pleasure and inspiration to work with them. Thanks are also due to Dr. David Brian Sharp who has shared his valuable and helpful comments.

This research has been undertaken with the support of Engineering and Physical Science Research Council, United Kingdom (Grant number EP/E062806/1) which is gratefully acknowledged. I should also mention with gratitude that my graduate studies were supported by the University as part of the employee subsidy scheme. I could not fulfil my dream to pursue this higher degree without these sponsors. Sincere appreciations are given to our project collaborators Dr. Olga Umnova and Dr. Anton Krynkin from the University of Salford for providing their expertise and the many productive and challenging discussions. I also wish to acknowledge the help from Dr. Anton Krynkin for providing and guiding the use of the MST algorithms. Special thanks are due to Dr. Juan V. Sanchez-Perez and Dr. Vincent Romero Garcia from the Polytechnic University of Valencia for collaboration in several aspects of the work related to this Thesis, notably in respect of the influence of ground effect on sonic crystal performance.

The assistance given by the staff and fellow research student in the Acoustic Research Group throughout the research periods are acknowledged and appreciated. I am indebted to Dr. Roland Kruse, Dr. Toby Hill, Dr. Ho-chul Shin and Dr. Adrien Mamou-mani for their constructive advice on my research. Special thanks to Peter Seabrook (Project Officer) who contributed much time and effort to source and fabricated specimens to be used for the sonic crystal both in laboratory and outdoor measurements. I should mention with gratitude to Roger Frith and Mikki Thomas (Project Officers) for their help rendered during the laboratory measurements. Credit also goes to Stan Hiller (Project Officer) from the Material's Department for his expertise in performing tensile strength testing for the latex specimen used in our design. I would also like to thank Imran Bashir (PhD student) for his insightful suggestions, discussions and help rendered.

Last, but not least, I am truly grateful to my family whose care and support have been the important factors which let me seek this higher degree without worries. This dissertation is dedicated to them.

Preface

This PhD Thesis entitled “Sonic Crystal Noise Barriers” contains the results of research undertaken at the Department of Design, Development, Environment and Materials of the Open University, United Kingdom. The Supervisors involved in this research are Prof. Keith Attenborough, Dr. Shahram Taherzadeh and Dr. David Brian Sharp who are all members of academic staff at the Open University. This research was funded by the Engineering and Physical Science Research Council (EPSRC), United Kingdom (Grant number EP/E062806/1). Under an EPSRC joint research scheme, this research closely collaborated with the School of Computing Science and Engineering, University of Salford, United Kingdom (Grant number EP/E063136/1). During the course of research, there was a close collaboration with Dr. Olga Umnova and Dr. Anton Krynkin from University of Salford. Their works on the development of the Multiple Scattering Theory (MST) and computational model (rigid, elastic shell, composite scatterers and sonic crystal above a ground surface) have been used extensively in this Thesis (Chapter 3, 6, 7 and 8). An alternative modelling using Finite Element Method (FEM) and experimental works are developed and performed at the Open University and Diglis Weir, Worcester. The sonic crystals work on Diglis Weir arose from an opportunity due to the “Organ of Corti” project, (see details in Section 5.6). Based on the outcome of the research findings, there has been a total of 3 peer reviewed journal papers and 7 conference proceedings published. The list of publications is provided on the next page.

List of Publications

International journals

1) A. Kyrnkin, O. Umnova, J.V. Sanchez-Perez, A.Y.B. Chong, S. Taherzadeh, K. Attenborough, “Acoustic insertion loss due to two dimensional periodic arrays of circular cylinders parallel to a nearby surface”, J. Acoust. Soc. Am., **130**, (6) (2011).
2) A. Kyrnkin, O. Umnova, A.Y.B. Chong, S. Taherzadeh, K. Attenborough, “Scattering by coupled resonating elements in air”, J. Phys. D: Applied Physics, **44**, (12), 125501 (2011).
3) A. Kyrnkin, O. Umnova, Y.B. Chong, S. Taherzadeh, K. Attenborough, “Predictions and measurements of sound transmission through a periodic array of elastic shells in air”, J. Acoust. Soc. Am., **128**, (6) (2010).

Conference proceedings

1) Y.B. Chong, S. Taherzadeh, K. Attenborough, “Numerical and experimental studies of sonic crystal noise barriers”, Universities Transport Studies Group conference 2011, Milton Keynes, United Kingdom.
2) J.V. Sanchez-Perez, V. Romero-Garcia, K. Attenborough, S. Taherzadeh, Y.B. Chong, “The influence of the ground on the attenuation properties of sonic crystal barriers”, 2nd Pan-American/Iberian Meeting on Acoustics 2010, Cancun, Mexico.
3) K. Attenborough, Y.B. Chong, S. Taherzadeh, “Resonant elements for sonic crystal barriers”, 2nd Pan-American/Iberian Meeting on Acoustics 2010, Cancun, Mexico.
4) A. Kyrnkin, O. Umnova, Y.B. Chong, S. Taherzadeh, K. Attenborough, “Sonic crystal noise barriers made of resonant elements”, International Congress of Acoustic 2010, Sydney, Australia.
5) Y.B. Chong, S. Taherzadeh, K. Attenborough, “The performance of vertical and horizontal sonic crystal noise barriers above a ground plane”, InterNoise 2010 conference, Lisbon, Portugal.
6) Y.B. Chong, S. Taherzadeh, K. Attenborough, “laboratory studies on sonic crystal noise barrier”, EuroNoise 2009 conference, Edinburgh, United Kingdom.
7) Y.B. Chong, S. Taherzadeh, K. Attenborough, “laboratory studies on sonic crystal noise barrier”, InterNoise 2009 conference, Ottawa, Canada.

Contents

List of Figures

List of Tables

List of Symbols

Symbol	Descriptions
f	Frequency (Hz)
λ	Wavelength (m)
c and c_0	Speed of sound In air (m/s)
c_L and c_1	Speed of sound, longitudinal wave (m/s)
c_s and c_2	Speed of sound, transverse wave (m/s)
c_o and c_i	Speed of sound describing acoustic environment of outside and inside of each elastic shell respectively
ρ	Density of the medium (kgm-3)
ρ_o and ρ_i	Density describing acoustic environment of outside and inside of each elastic shell respectively
ν	Poisson's ratio for the material
ω	Angular frequency
k or k_0	Wave number in air
E	Young's Modulus (Pa)
E_j	Dynamic Young's Modulus (N/m^2)
κ	Compressibility of air
t	Time (s)
$e^{-i\omega t}$	Negative time harmonic dependence
π	pi (3.1416)
i	$\sqrt{-1}$

p	Pressure (Pa)
IL	Insertion Loss (dB)
IL_{DC}	Insertion Loss (dB) with source distance correction
p_{direct}	Pressure (direct field, Pa)
$p_{total\_transmitted}$	Pressure (total transmitted field, Pa)
$(\vec{r})$	Vector for space r
A_{uc}	Area of the unit cell
A_{cyl}	Area of the considered cylinder
$\vec{G}$	Reciprocal lattice of periodic structure
$F(\vec{G})$	Structure factor
J_1	Bessel function of the first kind
$\rho_{\vec{k}}\left(\vec{G'}\right)$ and λ_{eigen}	Eigenvector
$\omega(\vec{\mathrm{K}})$ and f_{eigen}	Eigenfrequencies
$\omega.(\vec{k})$	Band structures
ff	Filling fraction
f_{Bragg}	Lowest Bragg band gap central frequency (square lattice array)
f_{Bragg_Hex}	Lowest Bragg band gap central frequency (Hexagonal lattice array)
L	Lattice constant
p_{inc}	Incident wave (pressure, Pa)
p_{sc}^{j}	Scattered wave by the j-th scatterer (superscript to change for other scatterer eg. k)

(x, y, z)	Cartesian coordinates
(r_j, θ_j)	Polar coordinates centred at the j-th cylinder
a_j	Radius of cylindrical j-th scatterer
$\nabla^2 = \frac{\partial^2}{\partial x_1^2} + \frac{\partial^2}{\partial x_2^2}$	Laplacian
B_e	Unbounded exterior
ψ_n	Incident wavefunction (outgoing cylindrical wavefunction of n-order)
$\mathrm{H}_n^{(1)}$	Hankel function of n-order of the first kind
$\hat{\psi}_n$	Regular cylindrical wavefunctions of the first kind (outgoing wave radiating from each cylinder)
J_n	Bessel function of n-order of the first kind
Y_n	Bessel function of n-order of the second kind
$p(x, y)$	Pressure at position defined by Cartesian coordinates
$p_{(r_q, \theta_q)}$ and $p_o(r, \theta)$	Pressure at position defined by polar coordinates
Z_n^j and Z_n^m	Impedance factor of j-th and m-th scatterer respectively
Z_c	Relative characteristic impedance
A_n^m	Unknown coefficient to be solved in Multiple Scattering Theory model
I_j	Phase factor associated with the j-th cylinder
M	Truncation number for Multiple Scattering Theory model
p_{in_p}	Plane wave source (pressure, Pa)
p_{in_c}	Cylindrical wave source (pressure, Pa)

L_{MLS}	Samples number in one period of an m order MLS signal
L_{sc}	Depth of the SC array (m)
ϑ	Acoustically-deduced temperature in ($°C$)
Ref pt	Reference microphone locations during measurements at Diglis weir
Pt 1, Pt 2 and Pt	Receiver microphone locations during measurements at Diglis weir
$\hat{\Phi}(\mathbf{r})$	Particle velocity potential with respect to vector r (space)
ε	Relative impedance
R	Mid-surface radius of elastic shell
η	Half Wall Thickness (WT)
$f(t)$	Relaxation function of elastic shell
S	Cross section area of the neck in a Helmholtz resonator
L_n	Effective neck length of a Helmholtz resonator
V	Volume of a Helmholtz resonator
γ	Ratio of specific heats (1.4 for air)
h	Rigid cylindrical shell thickness
d_n	Widths of slits for rigid cylindrical shell
β	Incident angle of incident sound wave.
EA	Excess Attenuation (dB)
k_c	Sound wave propagation constant
σ	Flow resistivity (Pa s m-2)
C_m	Position of each scatterer in the sonic crystal array

$p_{0,d}(\mathbf{r})$	Pressure from the direct point source with respect of vector r (space)
$p_{0,r}(\mathbf{r})$	Pressure from the image point source with respect of vector r (space)
d_1	Sound source distance to sonic crystal array for sonic crystal with ground measurement
h_{r1}, h_{r2} and h_{r3}	Height of the receiver microphone to sonic crystal array for sonic crystal with ground measurement

Abstract

An alternative road traffic noise barrier using an array of periodically arranged vertical cylinders known as a Sonic Crystal (SC) is investigated. As a result of multiple (Bragg) scattering, SCs exhibit a selective sound attenuation in frequency bands called band gaps or stop bands related to the spacing and size of the cylinders. Theoretical studies using Plane Wave Expansion (PWE), Multiple Scattering Theory (MST) and Finite Element Method (FEM) have enabled study of the performance of SC barriers. Strategies for improving the band gaps by employing the intrinsic acoustic properties of the scatterer are considered. The use of the tube cavity (Helmholtz type) resonances in Split Ring Resonator (SRR) or the breathing mode resonances observed in thin elastic shells is shown to increase Insertion loss (IL) in the low-frequency range below the first Bragg stop band. Subsequently, a novel design of composite scatterer uses these 2 types of cylindrical scatterer in a concentric configuration with multiple symmetrical slits on the outer rigid shell. An array of composite scatterers forms a system of coupled resonators and gives rise to multiple low-frequency resonances. Measurements have been made in an anechoic chamber and also on a full-scale prototypes outdoors under various meteorological conditions. The experimental results are found to confirm the existence of the Bragg band gaps for SC barriers and the predicted significant improvements when locally resonant scatterers are used. The resonant arrays are found to give rise to relatively angle-independent stop bands in a useful range of frequencies. Good agreement between computational modelling and experimental work is obtained. Studies have been made also of the acoustical performances of regular arrays of cylindrical elements, with their axes aligned and parallel to a ground plane including predictions and laboratory experiment

Chapter 1

Introduction

1.1) Fundamentals of acoustics

Sound is produced by movement of particles from a vibrating body in a given medium. Sound can be described as the variations in pressure, particle displacement or particle velocity that propagate through any medium. The frequency of mechanical vibration associated with the sound wave can be expressed by,

$$f = \frac{c}{\lambda}, \tag{1.1}$$

where,

f = frequency, reciprocal of a time period (Hz),

c = speed of sound in the medium (m/s),

λ = wavelength in which the distance of sound travels to complete one cycle (m).

There are various types of wave motions studied in the science of acoustics and the first mode pertaining to the propagation of wave in a compressible fluid (i.e. air) will be introduced. Such acoustic waves produce the aural sensation of sound we encounter in our everyday life. There are also ultrasonic and infrasonic waves whose frequencies are beyond the audible

limits of human which span from 20 Hz to 20 kHz. The molecules in the undisturbed air can be assumed to be located at their equilibrium positions (figure 1.1(a)). Acoustic waves propagating in air are described as longitudinal (also known as compressional) waves, where the motion of the air molecules transmitting the wave is parallel to the direction of propagation of the wave creating a series of compressions and rarefactions as shown in figure 1.1(b). At any instance, some of the particles move closer together and some are further apart from their equilibrium positions. This type of wave mode can travel through solid, liquid and gases. Another type of wave mode to consider is the transverse (also known as shear) wave which is observed in solid material. Without any disturbance, the atoms in a homogeneous solid material are periodically arranged in space and for simplicity the atoms of the solid material at equilibrium can be shown similarly as in figure 1.1(a). Contrary to longitudinal wave, for transverse wave the particle move perpendicular to the direction of propagation of the wave (see figure 1.1(c)).

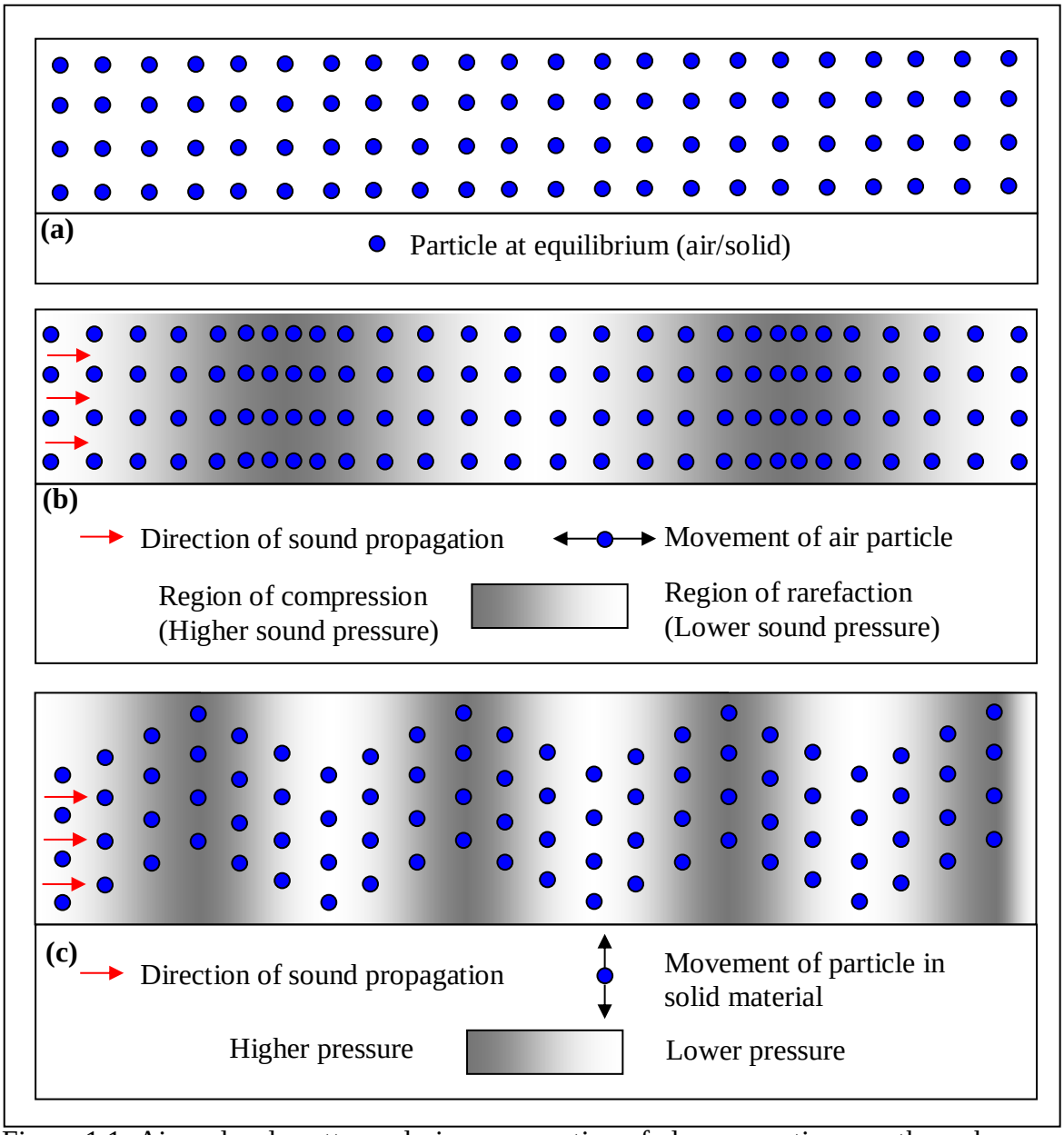

Figure 1.1: Air molecule patterns during propagation of plane acoustic wave through infinite space: (a) the arrangement of air molecules at equilibrium positions without any external force excitation, (b) during plane acoustic waves propagating through the air medium and (c) during transverse wave propagation through a homogeneous solid material.

Using the equation of motion for elastic wave as described by Ewing [1], the speed of sound for the longitudinal signal, c_L, can be determined from the elastic constants of the underlying solid material by,

$$c_L = \sqrt{\frac{E(1-\nu)}{\rho(1+\nu)(1-2\nu)}}, \tag{1.2}$$

where,

$E =$ Young's Modulus,

$\rho =$ density of the medium,

$\nu =$ Poisson's Ratio for the material.

whereas the speed of sound for the transverse wave can be calculated by,

$$c_s = \sqrt{\frac{E}{\rho(1+\nu^2)}}, \tag{1.3}$$

In general, sound waves have non-planar waveforms and propagate in a complex three dimensional manner. Consequently their motion can be difficult to model. However, there are conditions under which a simplified model is sufficient to describe acoustic wave propagation. This is the plane wave model, in which sound waves are assumed to have the same direction of propagation everywhere in space and their wavefronts are in planes perpendicular to that direction of propagation.

For one-dimensional acoustic wave propagation (in air) in the x-direction, the wave equation in terms of the pressure can be expressed as [2],

$$\frac{\partial^2 p}{\partial x^2} = \frac{1}{c^2}\frac{\partial^2 p}{\partial t^2}, \tag{1.4}$$

where c is the acoustic wave and t is the time. Note that $\frac{1}{c^2} = \rho\kappa$ where ρ and κ are the equilibrium density and the compressibility of air respectively. It

is worth to note that equation 1.4 is restricted to homogeneous, isotropic fluid and that small wave amplitude is assumed. For this reason, equation 1.4 is often referred to as the linear, lossless wave equation.

Also Equation 1.4 can be modified with the assumption of time-harmonic waves to give, the Helmholtz equation [3].

$$\nabla^2 p + k_0^2 p = 0, \tag{1.5}$$

where p is the complex valued function and $k = \frac{2\pi f}{c}$ is the wave number in air.

A solution of the equation 1.4 has the following form

$$p(x,t) = F(x - ct) + G(x + ct), \tag{1.6}$$

where F and G can be any function.

The first part of equation 1.6 refers to wave travelling in the $+x$ direction and the second part of the equation refers to wave travelling in the $-x$ direction respectively.

1.2) Complex number notation

It is convenient to use complex number notation when working with the wave equation and its solution (see equation 1.5) due to the frequent interest in simple harmonic waves. If the wave is not simple harmonic, the waveform may be expanded by means of a Fourier series, which involves a series of sinusoidal terms. In addition, a complex notation provides information for both magnitude of a quantity and its phase angle. A complex number may be written in Cartesian form,

$$p = x + iy = \mathbf{Re}\,(p) + i\mathbf{Im}\,(p), \qquad \textbf{(1.7)}$$

Where $x = \mathbf{Re}\,(p)$ = real and $y = \mathbf{Im}\,(p)$ = imaginary part of the complex quantity. The complex quantity may also be written in polar form as,

$$p = |p|e^{i\phi}, \qquad \textbf{(1.8)}$$

And $|p|$ is the magnitude and ϕ is the phase.

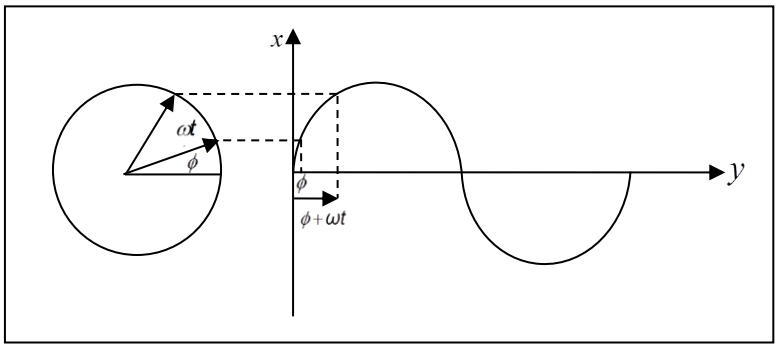

Figure 1.2: Simple harmonic waves illustrated in polar form.

1.3) The conventional road traffic noise barrier

Noise, defined as 'unwanted sound', is perceived as an environmental stressor and nuisance. Road traffic noise is a prolific source of environmental noise especially during the night time in urban areas and has been identified as a major source of sleep disorder. Considering the continuing growth of vehicular traffic and the large number of people exposed to it, disturbance of sleep by road traffic noise has become an increasing important cause of concern. Many studies have shown that exposure to road traffic noise may induce further adverse health effects, including cardiovascular effects [4, 5 and 6]. Road traffic noise control can be achieved through better engineering design of vehicles for example through quieter power plants, improvement of road or tyre surfaces and controlling the flow of the vehicles in a particular area. When these at-source strategies are insufficient to reduce noise, the implementation of noise barriers is often necessary to further reduce noise level at the receiver. Usually these noise barriers are airtight and sufficiently dense to shield the noise from the source to the receiver. Most of the sound energy reaches the receiver only as a result of diffraction around the barrier edges [7]. In the UK, £5 million are spent annually on highway noise barrier schemes with the intention to provide between 5 and 10 decibels (dB) reduction within the protected areas [8]. The drawbacks of using such barrier are the aesthetic impact such as restriction of view and natural lighting caused by the barrier. One consequences of the adverse visual impact of opaque barriers has been the design of transparent (Perspex) barriers. Anecdotally, there are cases where an architect wishes to incorporate acoustic barriers within a new construction but is unable to do so because of planning

constraints. The presence of barriers alters the wind profile and turbulence in their vicinity and this can act to reduce the barrier effect in outdoors. Fluctuations of ±2 m/s in the wind velocity can result in between 5 and 7 dB degradation in the spectral values of insertion loss for frequencies above 800 – 1000 Hz [9].

The performance of barrier used along highways is affected by temporal effects from moving traffic and by vehicle composition and speed. According to the British Standards (see figure 1.3), the normalised traffic noise spectrum expressed in A-weighted decibel (dBA) lies between 100 Hz to 5 KHz, with the main noise energy centred at 1 kHz [10]. It should be noted that this normalised traffic noise spectrum does not take accounts into the temporal effects. Although a more comprehensive traffic noise model (European Commision project "Harmonoise") [134] is available but for simplicity the British Standards is used. Usually the effectiveness of a road traffic noise barrier is measured by the Insertion Loss (IL) expressed in Decibel (dB) shown in equation 1.9. p_{direct} and $p_{total\_transmitted}$ denote the pressure obtain without and with the barrier respectively.

$$IL = 20\log_{10}\left|\frac{p_{direct}}{p_{total\_transmitted}}\right|, \qquad \textbf{(1.9)}$$

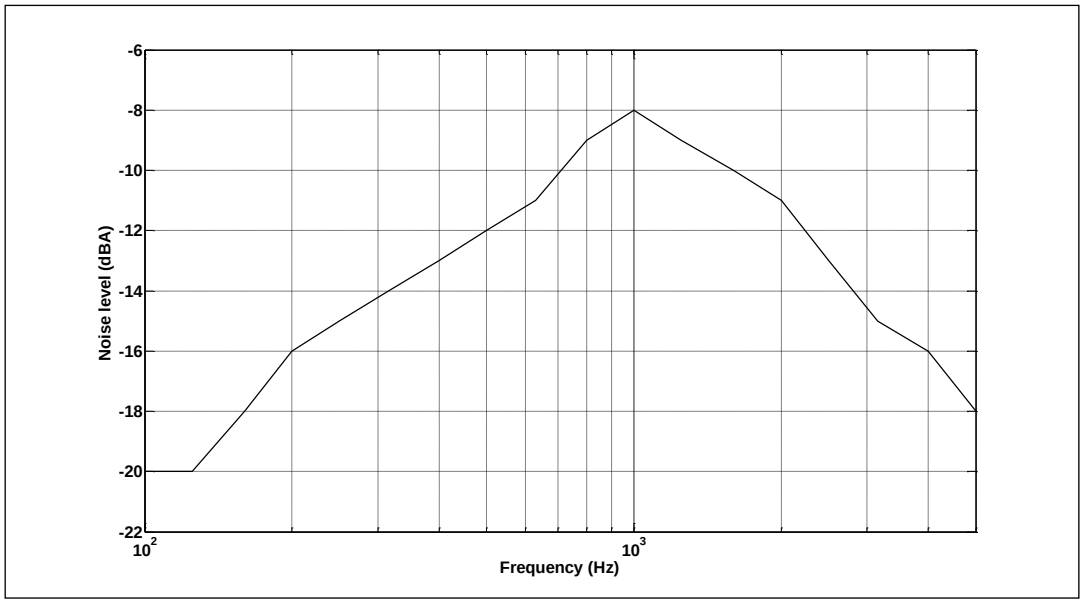

Figure 1.3: Normalised A-weighted traffic noise spectrum [10].

1.4) Sonic crystals

1.4.1) History

The first comprehensive book about wave in periodic structure was written by Brillouin 1946 [11]. The book covers the mathematical background to a broad variety of problems. These problems ranged from solid-state physics to propagation along electric lines, X-rays, optical reflections, electrical engineering and wave mechanics of the spinning electron. Subsequently, the work on the transmission properties of the electromagnetic wave inside periodic systems [12] in the late 80s generated much research on periodic systems. It is known that infinite periodic structures do not support wave propagation in certain frequency ranges known as Bandgaps relating to the spacing between the scattering elements (Lattice constant).The ability to manipulate the propagation properties of electromagnetic radiation have produced a number of practical application such as manipulating the group

velocity of light [13], superlensing effect [14], designing highly efficient nanoscale lasers [15], sharp bend radius waveguides [16], microwave cloaking devices [17], optical computer chips [18] and enhancing surface mounted microwave antennas [19].

The pioneering experimental work on the sound attenuation by periodic structure - in the form of an outdoor modern art sculpture - was made in 1995 [20]. The minimalistic sculpture by Eusebio Sempere, exhibited at the Juan March Foundation, Madrid, consists of a periodic square symmetry arrangement of hollow stainless steel cylinder with a diameter of 0.029 m and a lattice constant (distance between 2 cylinders next to each other) of 0.10 m was used in their experiment (figure 1.4). In such case of the acoustic audible sound, these periodic distributions of cylinders (also called scatterers) are known as Sonic Crystal (SC). The cylinders were fixed on a circular platform which can be rotated around the vertical axis. Sound attenuation was measured at various angles in outdoor conditions for sound-wave vectors perpendicular to the cylinders' vertical axes. Having a small filling fraction of 0.066 the experiment results showed several maxima (sound attenuation) and minima (sound reinforcement) in the frequency spectrum. The first (lowest) gap in the band structure which has a centre frequency at 1.7 kHz could be attributed to the geometry of the structure as shown in figure 1.4. Ever since this publication, research on the application of periodic arrays of cylinders for noise control has increased [21, 22 and 23].

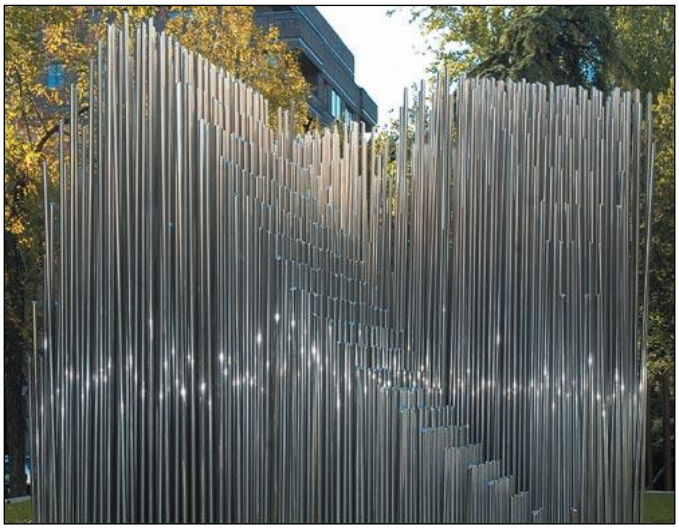

Figure 1.4: Minimalistic sculpture by Eusebio Sempere.

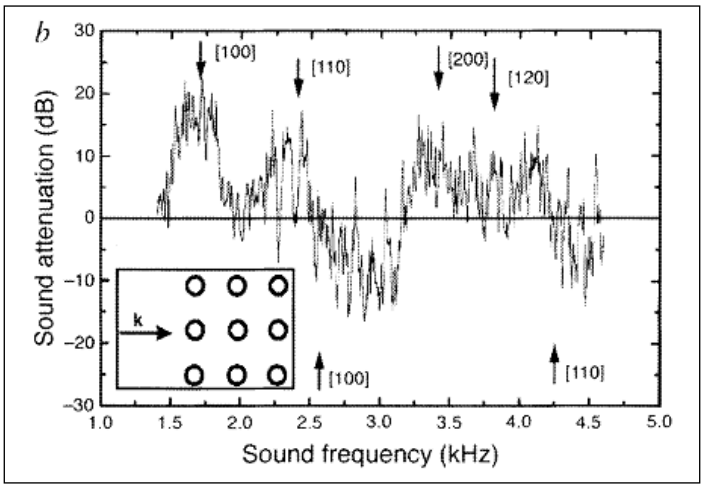

Figure 1.5: Sound attenuation as a function of frequency, also known as Insertion Loss.

Investigations of sound attenuation effects of regularly-planted vegetation have been conducted also. It was found that there are two mechanisms of attenuation that were highly frequency dependent [24]. At the lower end of the frequency spectrum of interest, defined as below 1 kHz, “ground effect” is the most important mechanism; at frequencies that are greater than 2 kHz, noise was attenuated by foliage sound absorption. In both cases, it was necessary to employ a thick vegetation belt to obtain a little extra attenuation. Rosa Martines-Sala *et al* went on to investigate belts of

trees arranged in periodic array in bid to achieve attenuation at low frequencies. Peaks of attenuation at low frequencies (f<500 Hz) were obtained which can be considered to be results of destructive interferences of scattered wave, not results of “ground effect”. Furthermore, using periodic arrangements of trees belts, greater attenuation effect was observed using less width, making them more effective noise screen than typically more randomly spaced tree belts. More recent work on sonic crystal noise barriers exploits the use of localised sound absorption properties (i.e. rigid perforated cylindrical shells filled with recycled rubber crumb material). Both numerical and experimental studies have been made of the reflectance and transmittance spectra of such a sonic crystal [25]. Such design offers the additional mechanism of absorption, apart from the multiple scattering phenomenon in periodic structure, to further attenuate noise (as did Umnova et al [59]). It is also shown in this work that having three rows of scatterers are sufficient to achieve well defined bandgaps which would be an important factor with respect to economics and land take. The subject of wind generated noise affecting SC performance is considered also. It is concluded that there should not be such adverse influence up to wind speeds of 30 m/s.

Another type of optimisation of SC noise barrier which has been studied numerically is the use of concentrically placed Helmholtz resonators (i.e. in a Matryoshka configuration) [26]. It was found that the intrinsic resonance properties of the six shell Matryoshka SC give rise to multiple independent resonance bandgaps below the first Bragg bandgap (i.e. due to the periodicity of the SC) between 400 and 1600 Hz which is important for traffic noise

reduction. Essentially this design is based on the use of concentric split ring resonators (SRR). The basis for split ring resonator designs is investigated in Chapter 7.

1.4.2) Crystallography

The basic unit of an ideal crystal structure can be defined as an identical group of atoms (in term of composition, arrangement and orientation) in space [27]. When this basic unit is repeated infinitely and joined up in space by specific lattice points (used to define the structure), the result is the crystal structure (see figure 1.6).

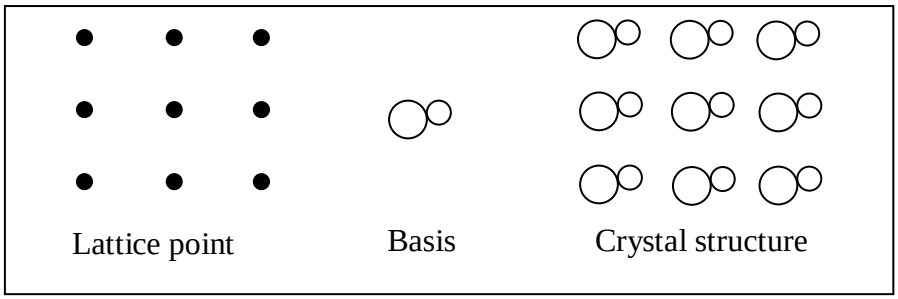

Figure 1.6: An ideal crystal structure.

In two dimensions, a primitive lattice can be defined by two translational vectors a_1 and a_2 such that the arrangement of atoms in the crystal structure looks the same when viewed from the point r as when viewed from every point r' translated by an integral multiple of the translation vectors, T, such that,

$$r' = r + T, \tag{1.10}$$

where $T = u_1 a_1 + u_2 a_2$ and u_i are integer between $-\infty \leq u_i \leq \infty$.

Thus it can be said that the crystal structure is invariant under translations and, sometimes, under rotations. The crystal structures are classified into three categories, that is, one-dimension (1D), two-dimensions (2D), and three-dimensions (3D) crystal by means of the group theory (see figure 1.7). A primitive cell is a minimum cell corresponding to a single lattice point of a structure with translational symmetry in the given dimensions. A lattice can be characterized by the geometry of its primitive cell.

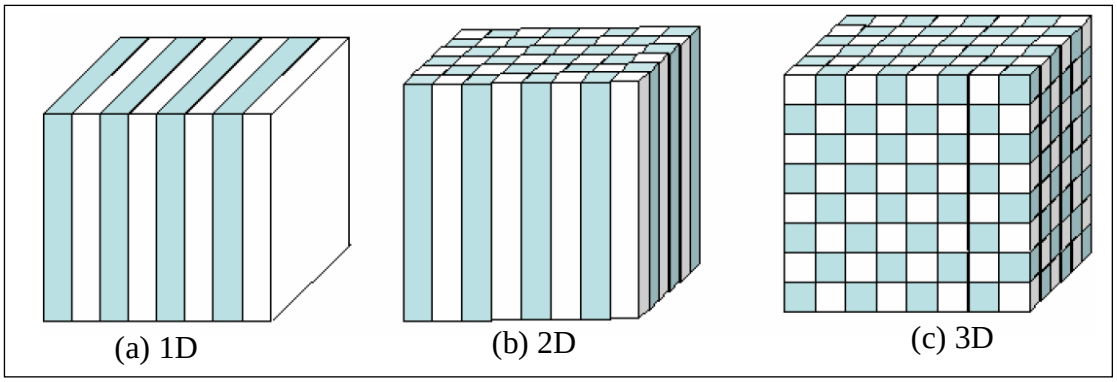

Figure 1.7: Schematic illustrations of crystal structure (a) one-dimensional, (b) two-dimensional and (c) three-dimensional.

By means of the use of group theory, it has been proved that there are only one unique 1D periodic system, five 2D and fourteen 3D different lattices. The majority of this work considers the sonic crystal as 2D arrangement, for which the five distinct Bravais lattices with their principle lattice vectors and angles are shown in figure 1.8.

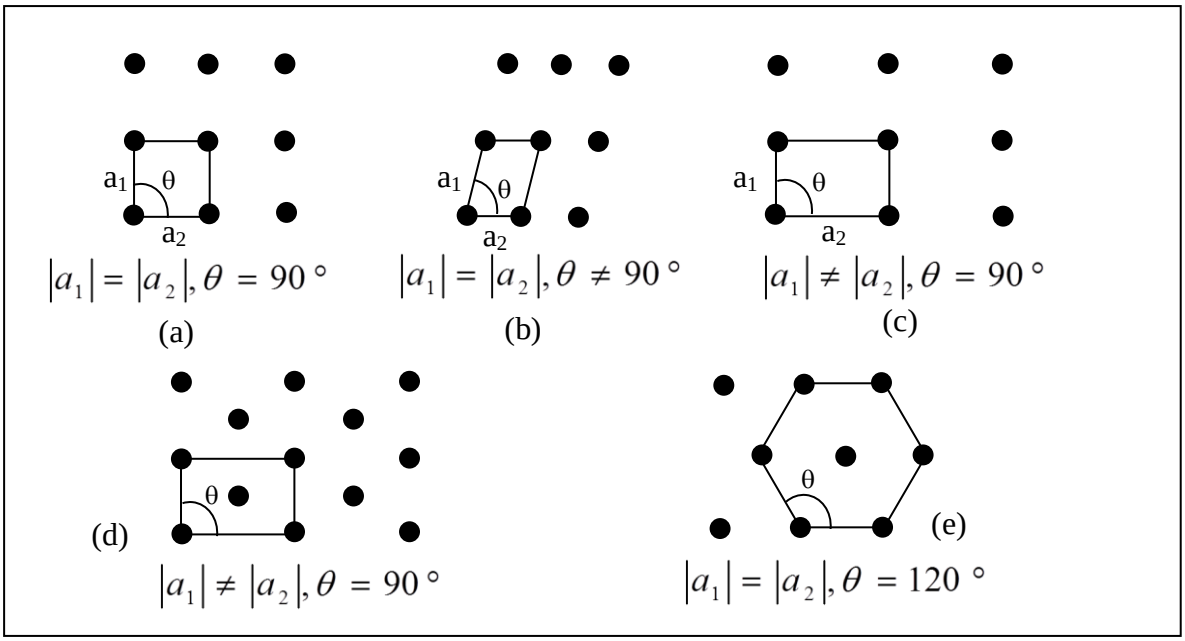

Figure 1.8: The five fundamental 2-Dimensionals Bravais lattices (a) square, (b) oblique, (c) rectangular, (d) centered rectangular and (e) hexagonal.

The parallelepiped defined by the vectors $\vec{a}_i$ forms the well known primitive cell which defines the smallest possible area of a cell that can be used as a basis for the crystal structure. The translation of the unit cell following the vectors $\vec{a}_i$ in space produces the lattice of the periodic system. As the periodic replication is done in the direct space, such lattice is defined as the direct space, or direct lattice. Another important feature associated with the direct lattice is the reciprocal lattice. The reciprocal lattice may be used for better understanding of the physical properties of these systems since the particle momentum is occurring in this reciprocal space (see figure 1.9). The vectors of the 2D primitive cell in the reciprocal lattice are defined from the vectors of the direct lattice via the following expression,

$$b_1 = 2\pi \frac{\vec{a}_2}{\vec{a}_1 \times \vec{a}_2}, \tag{1.11}$$

$$b_2 = 2\pi \frac{\vec{a}_1}{\vec{a}_1 \times \vec{a}_2}, \tag{1.12}$$

Where both the vectors of the direct ($\vec{a}_1$ and $\vec{a}_2$) and the reciprocal ($\vec{b}_1$ and $\vec{b}_2$) arrays satisfy an orthogonality relationship which can be expressed as,

$$b_j \bullet a_i = 2\pi\delta_{ij}, \tag{1.13}$$

where $\delta_{ij} = 1$ if $i = j$ and $\delta_{ij} = 0$ if $i \neq j$.

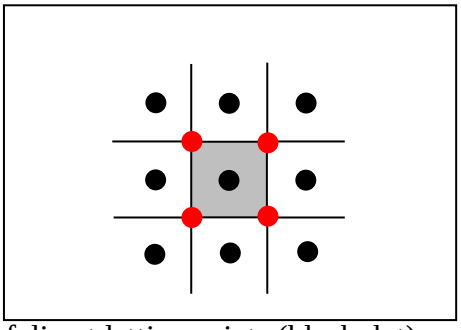

Figure 1.9: Illustration of direct lattice points (black dot), reciprocal lattice points (red dots) and a shade region indicate the reciprocal space.

Another physical property of the periodic system is known as the filling fraction, ff, and can be determined once the lattice constant and the size of the scatterers are known. The filling fraction is defined as the ratio between the volume occupied by the scatterers and the total volume occupied by the unit cell. If we consider cylindrical scatterers with radius, r_0, the ff for both the square and hexagonal lattices can be expressed as,

$$ff_{square} = \frac{\pi r_0^2}{a^2}, \tag{1.14}$$

$$ff_{hexagonal} = \frac{2\pi r_0^2}{\sqrt{3}a^2}, \tag{1.15}$$

It should be noted that the concept of a periodic system is a mathematical abstraction that implies the existence of an infinite structure. In practice such an infinite system may not be attainable but under certain assumptions a finite structure may mimic an infinite periodic system. For example, crystalline structures can be studied as periodic media using periodic boundary conditions if the size of the crystal is much smaller than the wavelength of the wave used to examine the crystal.

The performance of sonic crystals can be interpreted in a similar way to that used for the analysis of semiconductor bandgap materials. In a semiconductor, electrons are confined in certain energy bands and forbidden from others. The energy span between the valence band and the conduction band is called an energy bandgap. The properties of this energy bandgap are determined by the size, periodicity and arrangement of atoms in the crystal lattice of the semiconductor which cause the diffraction of electrons based on Bloch's Theorem [28]. The same concept of wave reflection in Bragg's Law which refers mainly to light diffraction can be analogously used for sound waves. It was found that artificial crystals can produce strong peaks over a range of frequencies that depends on the lattice constant of the array as given by Bragg's Law (see equation 1.16). When a wave passes through a crystal, part of it will be reflected by the first layer while the rest of it will continue to

move to the second layer, some portion of it will again be reflected and the remaining part will be reflected once more, hence the process continues.

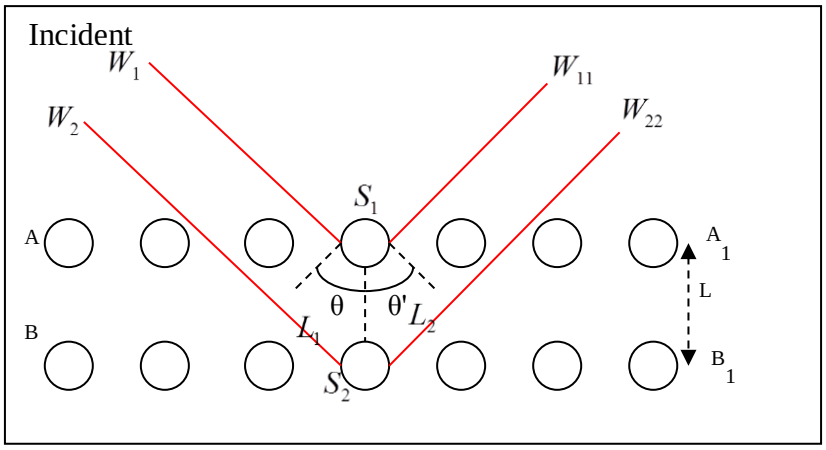

Figure 1.10: Bragg diffraction.

Consider two parallel planes of cylinders A-A1 and B-B1 (figure 1.10) having an inter-planar spacing, L. Now assume that a plane wave of wavelength, λ , is incident on the two planes at an angle, θ. Two waves labelled W_1 and W_2 are scattered by cylinders S_1 and S_2. Constructive interference of scattered sound waves W_{11} and W_{22} occurs at an angle, θ and θ' to the planes if the path difference between $W_1 \rightarrow S_1 \rightarrow W_{11}$ and $W_2 \rightarrow S_2 \rightarrow W_{22}$, i.e. $L_1 + L_2$ is equal to the whole number n, of wavelengths. Therefore condition for diffraction is $n\lambda = L_1 + L_2$. The interference is constructive when the phase shift is a multiple of 2π .

Bragg's law is given by:

$$2L\sin\theta = n\lambda, \qquad \textbf{(1.16)}$$

where, L is the spacing between planes (lattice constant), λ is the wavelength, θ is the angle between incident ray and scattering planes

n is an integer.

In a similar way, an SC can be described as a finite-size periodic array composed of scatterers embedded in a homogeneous host (sometime called the matrix) material. The geometry of the SC takes the form of a single unit cell made of Bravais Lattice (basic geometries in solid-state) as illustrated in figure 1.8. In these periodic structures (when we consider having rigid scatterers), coherence interference phenomena such as aforementioned Bragg diffraction (this term and the equivalent term Bragg resonance are used interchangeably in this Thesis) based scattering are responsible for a total reflection regime in certain frequency ranges creating full or complete band gaps. At these frequencies, the amplitude of the transmitted wave decreases as it passes through the crystal. Sound waves are therefore forbidden to pass through in such band gaps which physically can be well described by the classical wave theory for the multiple scattering of waves within the periodic structure. The 2D schematic diagram (figure 1.11) illustrates a square lattice of cylindrical scatterers with acoustic impedance, Z_s, and acoustic velocity, V_s, arranged in a homogeneous host material with acoustic impedance, Z_m, and acoustic velocity, V_m. The distinct ΓX and ΓM directions of acoustic wave propagation are also depicted in the figure. This denotes the first irreducible Brillouin Zone (BZ). For example ΓX refers to the [100] direction and ΓM refers to the [110] direction, while XM refers to the wave vector varying from [100] and [110] on the side of the first BZ. The geometrical

parameters, L, which is the lattice constant of the scatterers, and r_0, which is the radius of each cylindrical scatterer, together define the ff of the square lattice array in the matrix (see equation 1.14). The Bragg resonance conditions are essential for opening a wide spectral bandgap utilizing a sonic crystal. The fundamental Bragg resonance frequencies are found where the lattice constants in the ΓX and ΓM directions, L and $\sqrt{2}L$, are equal to half of the acoustic wavelength in which L equal to Lx and Ly. In a square lattice sonic crystal, the fundamental Bragg resonance frequencies in the ΓM and ΓX directions are, therefore, separated by a factor of $\sqrt{2}$,

$$f_{Bragg\_\Gamma X} = \frac{c}{2L}, \tag{1.17}$$

$$f_{Bragg\_\Gamma M} = \frac{c}{\sqrt{2}(2L)}, \tag{1.18}$$

where c is the speed of sound in the host medium (i.e. 344 m/s for sound speed in air at room temperature 20ºC).

If the two Bragg resonances are wide enough in frequency to overlap, then a complete bandgap can be realised based solely on the Bragg resonance condition. The width and depth of each Bragg resonance are dependent on the acoustic impedance mismatch between the matrix and scatterer as well as the filling fraction (function of lattice constant). The filling fraction must be large enough to restrict transmission through the matrix material around the scatterers. On the other hand, if the filling fraction

becomes too high, constructive wave interference between the scatterers leads to acoustic transmission. Opening a sonic bandgap requires the careful selection of materials with both the mass densities and modulus to yield the desired acoustic impedance and velocity mismatch between the matrix and scatterer.

The acoustic impedance of a material, Z, is

$$Z = \rho V = \sqrt{E\rho}\,, \tag{1.19}$$

where ρ and K are the density and bulk modulus of the material and the velocity V, is given by

$$V = \sqrt{\frac{K}{\rho}}\,, \tag{1.20}$$

In a hexagonal lattice the Bragg resonances are separated by $\sqrt{3}$ which may result in a wider bandgap but requires higher acoustic impedance mismatch between the matrix and the scatterer [29 and 130].

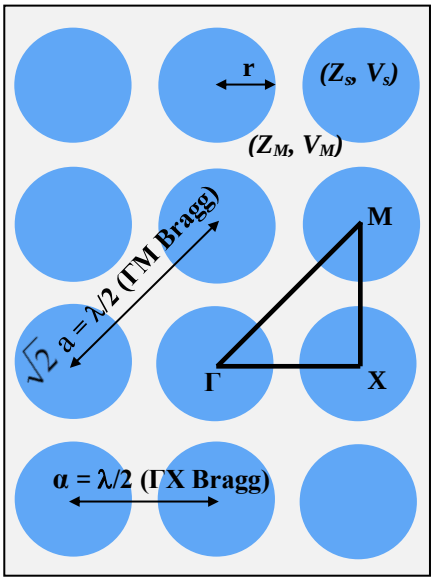

Figure 1.11: 2D schematic of square lattice array showing the Brillouin zone (triangle depicted by points Γ, X and M). (Z_M, V_m) and (Z_s, V_s) denote the acoustic impedance and velocity for the medium and scatterer respectively.

Such bandgap phenomena require a large contrast in physical properties such as density and speed of sound between the scatterer and the matrix material. Sonic crystals seem therefore very attractive as acoustic passband filters. The nature of the host materials can be used to differentiate between sonic and phononic crystals. If the host material (matrix material) is solid then the term 'Phononic Crystal' is used for the artificial crystal. In a phononic crystal, both longitudinal and transverse shear waves (elastic waves) may exist and couple with one another which will add to the complexity of the nature of eigenmodes. In contrast, sonic crystals are considered to be independent of the transverse waves. The scatterers are typically made of solid materials and the host matrix is air/fluid to give high acoustic impedance contrast between them.

1.5) Aims and thesis organisation

This Thesis offers a study of the interaction of sound with periodic structures. The objective and scopes of the study are as follows:

(i) To review the various numerical techniques for modelling an SC.

(ii) To find ways of improving the size and magnitude of the band gaps in an SC through both computational modelling and experiment.

(iii) To develop a multi-channel measurement system suitable for performing measurements at outdoors.

(iv) Test and evaluate a full scale SC traffic noise barrier (*in-situ*).

(v) To gain an understanding on the influence on the effects of wind and ground in the vicinity of an SC noise barrier.

Among these studies, the most important contributions in this thesis are:

- novel designs of SC noise barriers based on multiple resonances to enhance the noise shielding performance at frequencies below the first Bragg band gap.
- pioneering investigations of the influence of ground effects on SC noise barriers.

The introduction presented in the previous sections of this first chapter indicated that accurate predictions of the interactions of acoustic waves with periodic structures can be applied in various ways. It has served also to describe the general context of road traffic noise control. The basic theories

on acoustic wave propagation and concepts of crystallography were reviewed to facilitate the derivations of the formulations in the subsequent work. A brief summary of the aim and content of the other chapters is as follows.

Chapter 2 reviews the Plane Wave Expansion (PWE) prediction method and is intended to serve as a starting point for the creation of acoustic band gaps in 2D infinite periodic structures.

Chapter 3 describes an alternative prediction model viz. Multiple Scattering Theory (MST) on which the subsequent research work has been largely based. Contrary to the PWE described in Chapter 2, MST allows computation for 2D finite sonic crystals and the results obtained can be directly compared with experimental data.

Chapter 4 provides another means of predicting the performance of 2D finite sonic crystal using the Finite Element Method (FEM). Such a numerical modelling technique is suitable for considering different shapes of scatterer in sonic crystal design. It is used also for analysis of elastic shells and concentric cylinders in chapters 6 and 7 respectively. Preliminary attempts at transient analysis for SC using FEM are also made.

Chapter 5 is devoted to the development and implementation of the acoustic measuring systems (single and multiple channels) as well as the fabrication of the different types of scatterers. Some issues arising from experimental methods and signal are broadly discussed.

Chapter 6 studies numerically and experimentally the feasibility of replacing the conventional rigid scatterer with thin elastic shell whereby a local resonance (i.e. breathing mode) effect is exploited to enhance the band gap frequency below the first Bragg band gap. It provides an understanding of how some parameters could be optimised in a sonic crystal noise barrier design.

Chapter 7 first re-visits of the widely known Split Ring Resonator (SRR) based on Helmholtz resonance to enhance the Band gap in sonic crystal. Both numerical and experimental attempts to improve the latex shell design (chapter 6) are made. A novel design combines the elastic shell with an outer protective rigid shell (with symmetrical slits).

Chapter 8 presents a study of the effects of ground in the vicinity of a sonic crystal. A method is described of characterising the ground by fitting measured Excess Attenuation (EA) spectra with a widely known ground impedance deduction model (Delany and Bazley). Comparison of the performance of the sonic crystal with and without acoustically “hard” or “soft” grounds are made.

Chapter 9 states conclusions for each chapter and offers some ideas for future work.

Chapter 2

The Plane Wave Expansion (PWE) Method

2.1) Introduction

The periodicity of any system structure plays a crucial role in understanding the physical properties of both micro and macro crystalline structures. To design sonic crystals and determine how sound will propagate through a particular crystal structure it is possible to use numerical techniques. The pioneering work on band theory describing electromagnetic wave transmission inside a periodic system was introduced by Yablonovitch [12], and the study of wave dispersion bands for electronic waves in solids [30, 31, 32 and 33] provides the basis of understanding the properties of conductors, semiconductors and insulators. Following the principles of Bloch waves, the concepts of dispersion relations and Brillouin Zones (BZ) can be extended to all kinds of periodic structures. One special characteristic is the prospect of achieving a complete band gap; this is defined to be the stop band in which, sound waves are prohibited for all values of the wave-vector (or Bloch vector). There has been considerable subsequent research into the analogous phononic or sonic crystal band gaps [34, 35 and 36]. There are several techniques, but one of the most studied method is the Plane Wave Expansion (PWE) method [37 and 38] as it can be applied to an infinite arrays of any scatterer shape. It was used in some of the earliest studies of photonic crystals and can be readily applied in acoustics. The PWE method uses the periodicity of the given structure and the Bloch theorem to solve the wave

equation. This allows the computation of the allowable frequencies also known as eigenfrequencies for sound propagation in all directions of the crystal and can be used also to determine the field distributions in the crystal over a broad range of frequencies. The accuracy in calculating the eigenfrequencies from this method depends on the computational time. This section presents the theory of acoustic band structures for periodic composite structures.

2.1.1) Two-dimensional periodicity

Consider a sonic crystal array composed of circular cylinders made of an isotropic solid *A*, embedded periodically using a square lattice in an air background *B*. Such a system is assumed to have a translational symmetry in one direction (i.e. the z axis). This means that the material parameters of mass density and velocity of sound in this case depend on the coordinates x and y. The propagation of the incidental wave is also limited to the xy plane (2D) – an assumption which is used in other studies, both theoretical and experimental, on the photonic band structure of dielectric cylinders. Thus, the field parameter, pressure (p) is also independent of the z coordinate.

The wave equation describing the propagation of sound is

$$\nabla.\left(-\frac{1}{\rho(\vec{r})}\nabla p(\vec{r})\right)-\frac{\omega^2 p(\vec{r})}{\rho(\vec{r})c_l^2(\vec{r})}=0\,, \qquad \textbf{(2.1)}$$

At every point r the medium is characterized by two material parameters as follows:

$\rho(\vec{r})$ = mass density

$c_l(\vec{r})$ = velocity of sound

This inhomogeneous medium exhibits spatial periodicity and by using this periodicity, it is possible to expand the material properties of the medium by means of reciprocal lattice, both $\rho(\vec{r})^{-1}$ and $c_l(\vec{r})^{-1}$ in the wave equation using Fourier series:

$$\sigma = \frac{1}{\rho(\vec{r})} = \sum_{\vec{G}} \sigma_{\vec{K}}(\vec{G})\, e^{i\vec{G}\cdot\vec{r}}\,, \qquad \textbf{(2.2a)}$$

$$\eta = \frac{1}{\rho(\vec{r})\, c_l^2(\vec{r})} = \sum_{\vec{G}} \eta_{\vec{K}}(\vec{G})\, e^{i\vec{G}\cdot\vec{r}}\,, \qquad \textbf{(2.2b)}$$

where $(\vec{G})$ is the 2D reciprocal-lattice vector (see section 1.4.2) and $(\vec{r})$ is the direct lattice vectors. Since $\rho(\vec{r})$ and $c_l(\vec{r})$ are both known parameters, the terms $\sigma_{\vec{K}}$ and $\eta_{\vec{K}}$ can be determined from an inverse Fourier transform as shown in Kushwaha *et al* [39, equation 7(a) and 7(b)]. The summation in equations 2.2 is made for all possible reciprocal lattices that correspond to the Bravais lattice of the system. The solution of the sound pressure field p can be obtained by applying the Bloch theorem and negative time harmonic dependence ($e^{-i\omega t}$) is used throughout the Thesis:

$$p(\vec{r},t) = e^{i(\vec{K}\cdot\vec{r}-\omega t)} \sum_{\vec{G}} p_{\vec{K}}(\vec{G})\, e^{i\vec{G}\cdot\vec{r}}\,, \qquad \textbf{(2.3)}$$

where K is called the 2D Bloch wave vector and $\omega = 2\pi f$ is the angular frequency of the wave.

For a 2D sonic crystal system with square lattice geometry we have to define some variable in the PWE method. For such a system the cylinder material has density ρ_a and it occupies the filling fraction ff of the background material with density ρ_b. It can be shown that:

$$\Lambda(\vec{G}) = \begin{cases} \sigma_a \eta_a^2 f + \sigma_b \eta_b^2 (1-f), & \vec{G} = 0 \\ (\sigma_a \eta_a^2 - \sigma_b \eta_b^2) F(\vec{G}), & \vec{G} \neq 0 \end{cases}, \qquad \textbf{(2.4)}$$

where $F(\vec{G})$ is the structure factor, subscripts a and b denotes the host and scatterer media respectively. Since the system has circular scatterers, the structure factor will be defined in the PWE method as:

$$F(\vec{G}) = \frac{1}{A_{uc}} \int_{A_{cyl}} \overrightarrow{d^2 r} e^{-i\vec{G}\cdot\vec{r}} = 2 f J_1\left(\vec{G} r_0\right) / \left(\vec{G} r_0\right), \qquad \textbf{(2.5)}$$

such that A_{uc} is defined as the area of the unit cell, A_{cyl} is the area of the considered cylinder and J_1 is the Bessel function of the first kind of order 1.

After substituting the expanded wave equations (2.2) and the Bloch form equation (2.3) into the initial wave equation we obtain:

$$\sum_{\vec{G}'} \left(\left(\vec{\mathrm{K}} + \vec{G}\right) \sigma_k \left(\vec{G} - \vec{G}'\right) \left(\vec{\mathrm{K}} + \vec{G}'\right) - \omega^2 \eta \left(\vec{G} - \vec{G}'\right) \right) \rho_{\vec{k}} \left(\vec{G}'\right) = 0 . \qquad \textbf{(2.6)}$$

Equation 2.6 is based on a simple modification which excludes the transverse term in reference [39, equation 9]. For $\vec{G}$ taking all the possible values, equation (2.6) constitutes an infinite set of linear, homogeneous equations for the eigenvector $\rho_{\vec{k}}\left(\vec{G}'\right)$ and the eigenfrequencies $\omega(\vec{\mathrm{K}})$. The $(')$ is introduced to differentiate summation over spatial position relative to the acoustic field from those relative to the static distributions of material properties [40].

In numerical computations, truncation of the Fourier series has to include a number of spatial harmonics large enough to ensure convergence. Assuming N terms in the Fourier expansion, an appropriate $N \times N$ matrix equation can be solved for equation 2.6. The following vector notations are considered for the generalised displacement fields [40],

$$p = \begin{bmatrix} p(G_1) \\ \vdots \\ p(G_{N\times N}) \end{bmatrix}. \qquad \textbf{(2.7)}$$

The same explicit matrix formulation can be applied to matrices H and Ω (generalised displacement fields) as follows:

$$\mathrm{H} = \begin{bmatrix} \sigma(G_1 + G_1) & \cdots & \sigma(G_1 + G_{N\times N}) \\ \vdots & \ddots & \vdots \\ \sigma(G_{N\times N} + G_1) & \cdots & \sigma(G_{N\times N} + G_{N\times N}) \end{bmatrix}, \qquad \textbf{(2.8)}$$

$$\Omega = \begin{bmatrix} \eta(G_1 + G_1) & \cdots & \eta(G_1 + G_{N\times N}) \\ \vdots & \ddots & \vdots \\ \eta(G_{N\times N} + G_1) & \cdots & \eta(G_{N\times N} + G_{N\times N}) \end{bmatrix}. \qquad \textbf{(2.9)}$$

Having Γ_i as the diagonal matrix whose terms are generated by first-order spatial derivatives:

$$\Gamma_i = \begin{bmatrix} \mathrm{K}_i + G_i & 0 & \cdots & 0 \\ 0 & \mathrm{K}_i + G_i & \cdots & 0 \\ \vdots & \vdots & \ddots & \vdots \\ 0 & \cdots & \cdots & \mathrm{K}_i + G_i \end{bmatrix}, \qquad \textbf{(2.10)}$$

where i is equal to 1, 2, 3.

Thus, equation 2.6 can be expressed by a compact formulation:

$$\sum_{i=1}^{3} \Gamma_i \mathrm{H} \Gamma_i \, p = \omega^2 \Omega p \, . \qquad \textbf{(2.11)}$$

The specific Bravais lattice to be considered is the square lattice. Its reciprocal lattice is also square, with the reciprocal-lattice vectors given by

$$\vec{G} = (2\pi / a)\left(N_x + N_y\right). \qquad \textbf{(2.12)}$$

Where a is defined as the lattice constant, N_x and N_y assume all the integer values. With the substitutions of equations (2.5) and (2.12) into equation (2.6) and then by solving the system equation given in (2.11) for each Bloch vectors in the irreducible area of the first BZ for $\left(-N,\ldots,N\right)$, ω^2, are obtained and they can be used to represent the band structures, $\omega.(\vec{k})$.

2.2) Plane Wave Expansion Results

2.2.1) Band structure of Sonic Crystal

We consider a solid-fluid composite structure. The sonic crystal system studied consists of solid circular cylinders embedded in air. A square lattice array with lattice constant L of 0.069 m and scatterer diameter of 0.055 m is used for the initial case. This geometry gives a filling fraction (ff) of 50%. These parameters will describe the contrast parameter and shape function for the composite structure in the PWE method. Table 2.1 shows the material parameters based on hollow PVC cylinders used in the PWE calculations. We compute the band structure in the three principal symmetry directions, letting k scan the periphery of the irreducible triangle of the first BZ. The dispersion relation is obtained by plotting frequency against the Bloch wave vector in the first BZ related to the incident direction of the wave. This is also known as the reduced wave vector as it is the vector confined to only the first BZ. The PWE method tends to have a large convergence problem due to the large number of plane waves needed to calculate the band structure [41]. For reasonable accuracy (less than 5% discrepancy) and computational time, we allow the integer N_x and N_y to take values in the interval defined by $-10 \le N_x, N_y \le +10$, thus giving $(2N+1)^2 =$ 441 planes waves. This results in very good convergence in our numerical results. Figure 2.1 show the first 10 bands for PVC cylinders in an air background predicted using the PWE method in MATLAB® (see Appendix A) This indicates any regions where the band gaps exist (see figure 2.1).

Material	Density kgm^{-3}	Speed of sound ms^{-1}
Air	1.2	344
PVC	1380	2400

Table 2.1: Material parameters for sonic crystal system comprising of PVC cylinders embedded in air.

Assuming linear dispersion, the lowest Bragg band gap central frequency is approximately given by

$$f_{Bragg} = \frac{c_l}{2L}. \qquad \textbf{(2.13)}$$

As a test case, the band structure has been computed for a homogeneous material. The PWE method solved for the first ten bands with material parameters equal to that of air, $\rho_a = \rho_b$ = 1.2 kg/m^3 and $c_{la} = c_{lb}$ = 344 m/s (see figure 2.1).

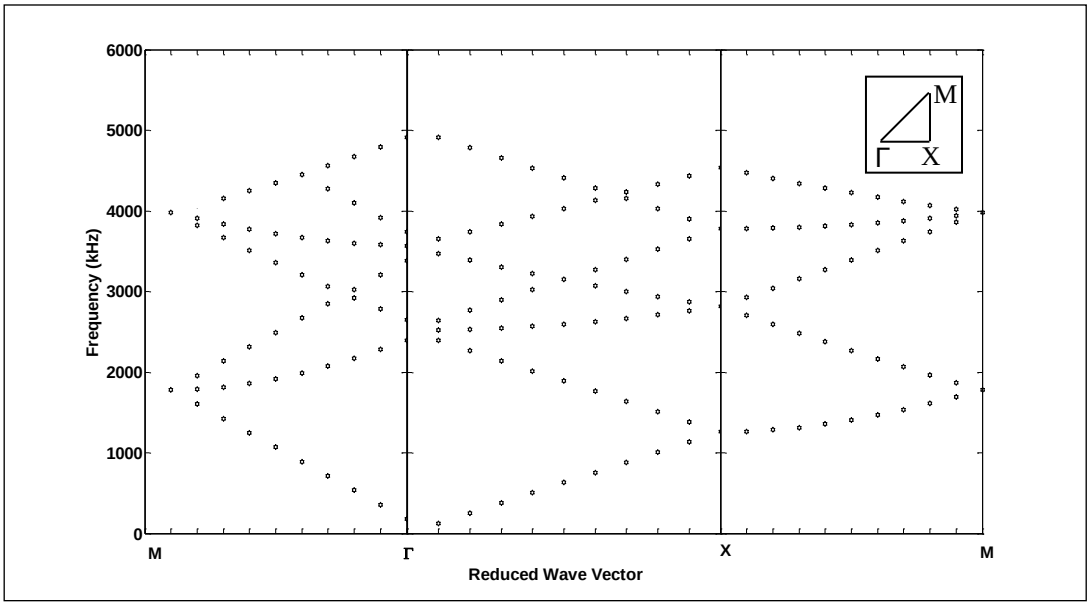

Figure 2.1: Plane wave expansion computed band structure for a homogeneous medium with equivalent material properties of air. Inset: Brillouin zone. ΓX refers to [1,0] direction, ΓM refers to [1,1] direction and XM refers to the wave vector varying from [1,0] to [1,1] on the extreme side of the Brillouin zone.

Clearly in figure 2.1, it is evident that such a homogeneous system has a dispersion relation with an almost linear trend with phase velocity and group velocity being equal. Such structure does not exhibit any band gap properties.

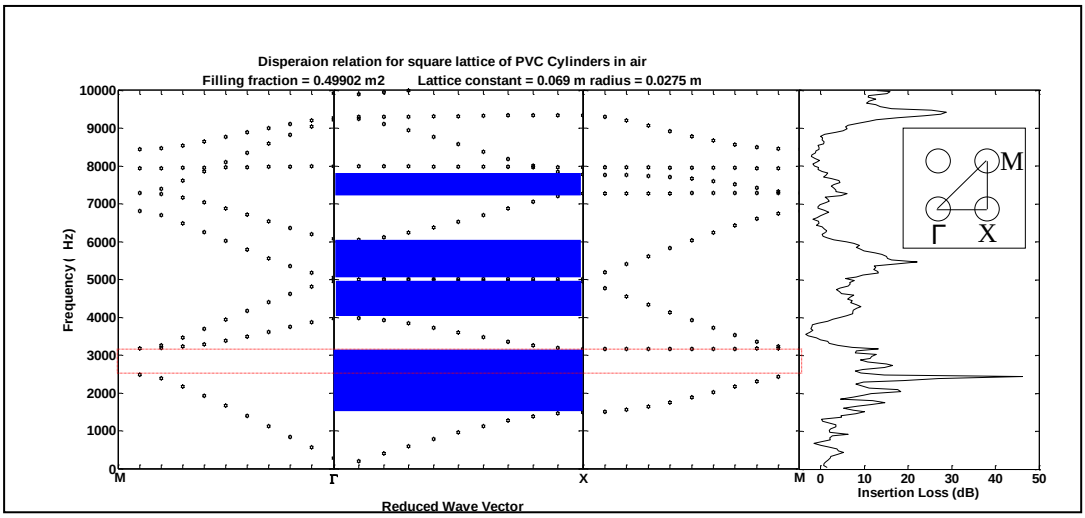

Figure 2.2: The left hand panel shows the plane wave expansion computed band structure for a SC consisting of cylindrical PVC scatterers embedded in air in a square array with lattice constant L of 0.069 m and filling fraction of 50%. The right hand panel shows the laboratory measured IL spectrum for 7x3 array for ΓX the [1, 0] direction. Inset: schematic of a Brillouin zone. ΓX refers to [1,0] direction, ΓM refers to [1,1] direction and XM refers to the wave vector varying from [1,0] to [1,1]. The (red) dotted box indicates a full bandgap and the (blue) shaded regions indicate partial bandgaps.

The left hand panel in figure 2.2 shows the band structure due to a SC consisting of acoustically rigid PVC cylinders embedded in air. The blue shading indicates the location of the first band gap (ΓX direction) which spans from 1.6 kHz to 3.2 kHz with centre frequency at 2.4 kHz. The lowest Bragg band gap central frequency, calculated using equation 2.13 is 2.5 kHz. This calculated central frequency falls well within the PWE method computation for the mid frequency in the first band observed in the band structure diagram albeit with a 4% discrepancy. We note the good agreement between both PWE method and measured IL (see Chapter 5 for measurement) of a finite size SC for the case of the pseudogaps (partial

bandgaps) in the ΓX direction. It is also worth noting that a complete band gap can be achieved for such SC configuration marked by the red dotted box.

2.2.2) Predicted influence of the lattice constant

A study of how the lattice parameter influences the location of the band gap has been performed. The diameter of the scatterer has kept constant at 0.055 m whilst the lattice parameter was varied.

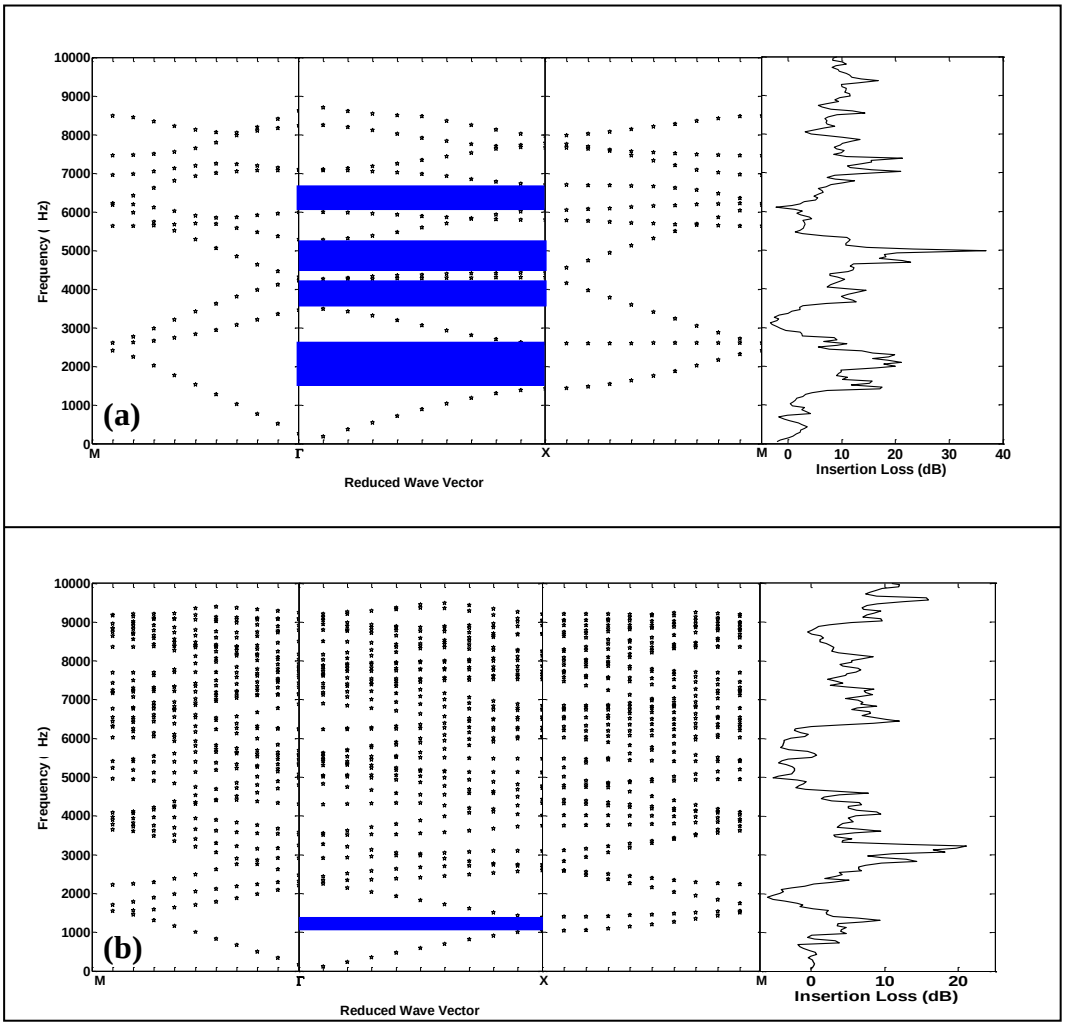

Figure 2.3: Plane wave expansion predictions of the effect of varying the lattice constant in a SC comprising of 0.055 m diameter PVC cylinders embedded in air. Lattice constant L of (a) 0.08 m and (b) 0.135 m. Left hand panels show the band structure of the corresponding SC and right hand panels show the measured IL for the different lattice parameters.

For a lattice constant of 0.08 m, the plane wave expansion method is solved for the first 10 bands whereas the first 40 bands would be required to extend the range of frequencies to 9 kHz. Focusing on the lowest band gap at ΓX direction for SC with lattice constant of 0.08 m (see figure 2.3a – area marked blue), the band gap lies between 1.4 kHz to 2.6 kHz, centred at 2 kHz. These band gaps are shifted to lower frequency as compared with the original lattice constant of 0.069 m (see figure 2.2). We observed a further shift of the first Bragg band gap to an even lower frequency when the lattice constant is further increased to 0.135 m (see figure 2.3b). The first band gap (ΓX direction) predicted by PWE method spans from 1 kHz to 1.4 kHz, and is centred at 1.2 kHz (area marked blue). The lowest Bragg band gap central frequencies calculated using equation 2.13 are found to be exactly matched with the PWE method for lattice constants of 0.08 and 0.135 m. The corresponding measured IL spectral for both lattice constant are also found to agree well on the first Bragg band gap. From this investigation it is clear that lower frequencies are attenuated as the lattice parameter is increased. On the other hand, for the same number of array elements this increasing the lattice constant increases the size of the sonic crystal.

2.2.3) Predicted influence of filling fraction

Plane Wave Expansion predictions of the influence of the filling fraction have been studied. It should be noted that in the previous section 2.2.2, the filling fraction is inherently changed by varying the lattice constant. In the current study the lattice constant is kept constant but the scatterer size is varied as shown in table 2.2.

Cylinder diameter (m)	Filling fraction (%)
0.055	13
0.09	35
0.11	52
0.13	73

Table 2.2: Cylinder diameter and corresponding filling fraction for a lattice constant of 0.135 m.

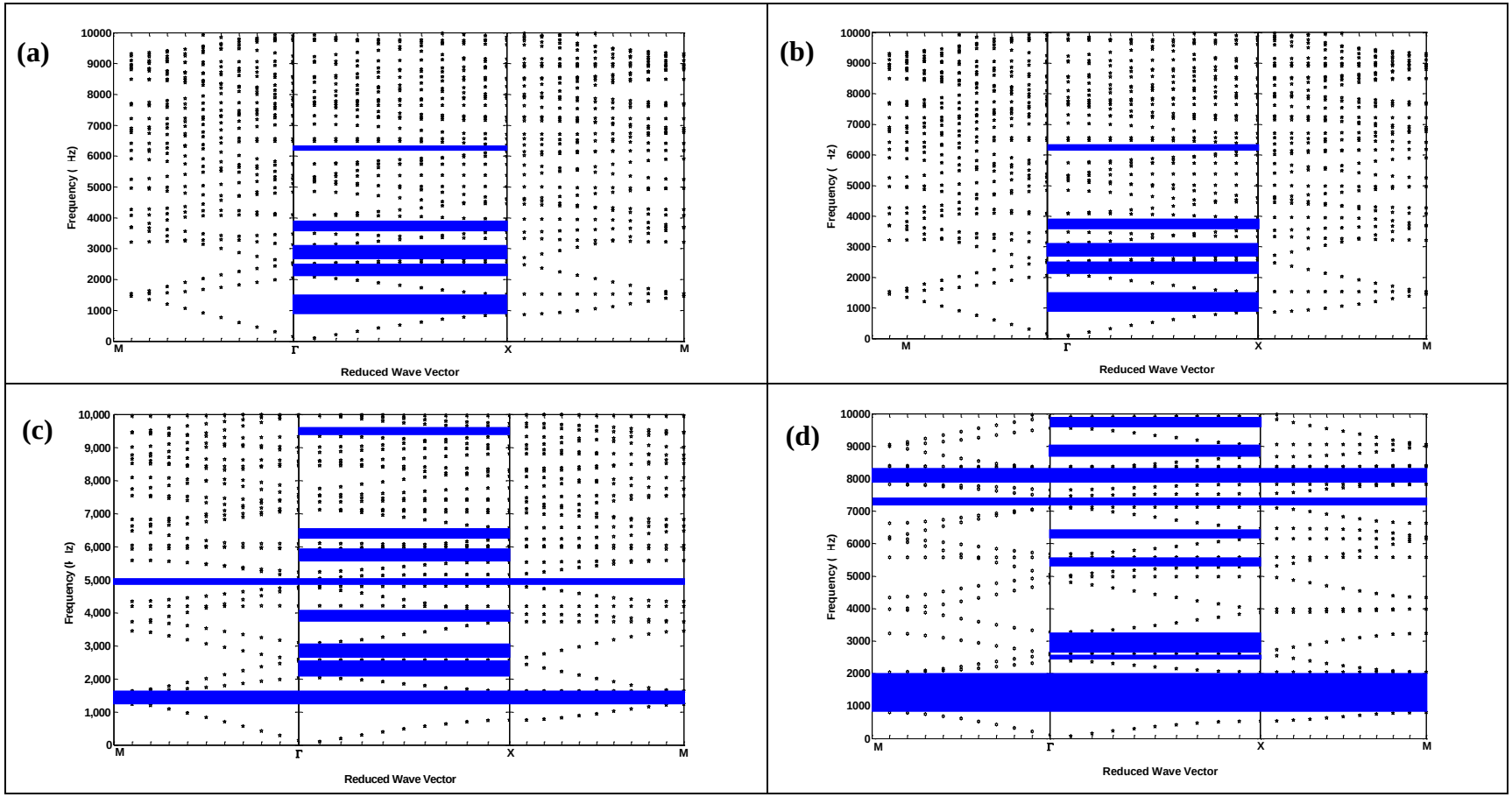

Figure 2.4: Plane Wave Expansion predictions of the band structure with Lattice constant fixed at 0.135 m and varying scatterer diameters (a) 0.055, (b) 0.09, (c) 0.11 and (d) 0.13 m.

According to the PWE predictions, the wave propagation in different directions is inhibited within different frequency regimes for different filling fractions. An indication of the complete band gap can be observed when the filling fraction exceeds certain value. For systems with low filling fractions of 13% and 35%, narrow pseudogaps are observed for the ΓX direction in the band structure (see figure 2.4a and 2.4b). Although there have the same number of band gaps predicted for these two filling fractions at similar frequencies, careful examination reveals that they are not identical. The lowest band gap extends from 1030 to 1390 Hz for the case of 13% filling fraction whereas the lowest band gap for 35% filling fraction extends from 850 to 1530 Hz. Also the mid frequency for the first band in both filling fractions occurs at about 1.2 kHz. It is evident that as the filling fraction increases further to 52% and 73%, the band gaps are widened and additional band gaps are formed. Complete acoustic band gaps are allowed to form for such filling fraction as the frequency bands in different directions of periodicity overlapped. Two complete band gaps are observed for the range of frequencies calculated. Clearly, for a given lattice constant, increasing the filling fraction results in enlargement of Bragg band gaps and the enhancement of the IL performance of the SC in the ΓX direction.

2.2.4) Predicted influence of material parameters

This section looks at how changes to the density and speed of sound in the scatterer material and the embedding medium will influence the band gap structure of a SC. Different materials and their corresponding density and speed of sound are listed in table 2.3 [42]. The lattice constant and diameter of scatterers are fixed at 0.069 m and 0.055 m respectively. First 5 different materials are used to model the properties of cylindrical scatterers embedded in air and the results are shown in figure 2.4. Secondly, water is used to substitute air as the embedding medium with PVC scatterers.

Material	Density (kgm^{-3})	Speed of sound (ms^{-1})
PVC	1380	2400
Silicon rubber	1300	948
Steel	7780	5985
Poly(methyl methacrylate), PMMA	1180	2680
Wood (Lignum vitae)	1300	3450
Water	1000	2400

Table 2.3: Material properties.

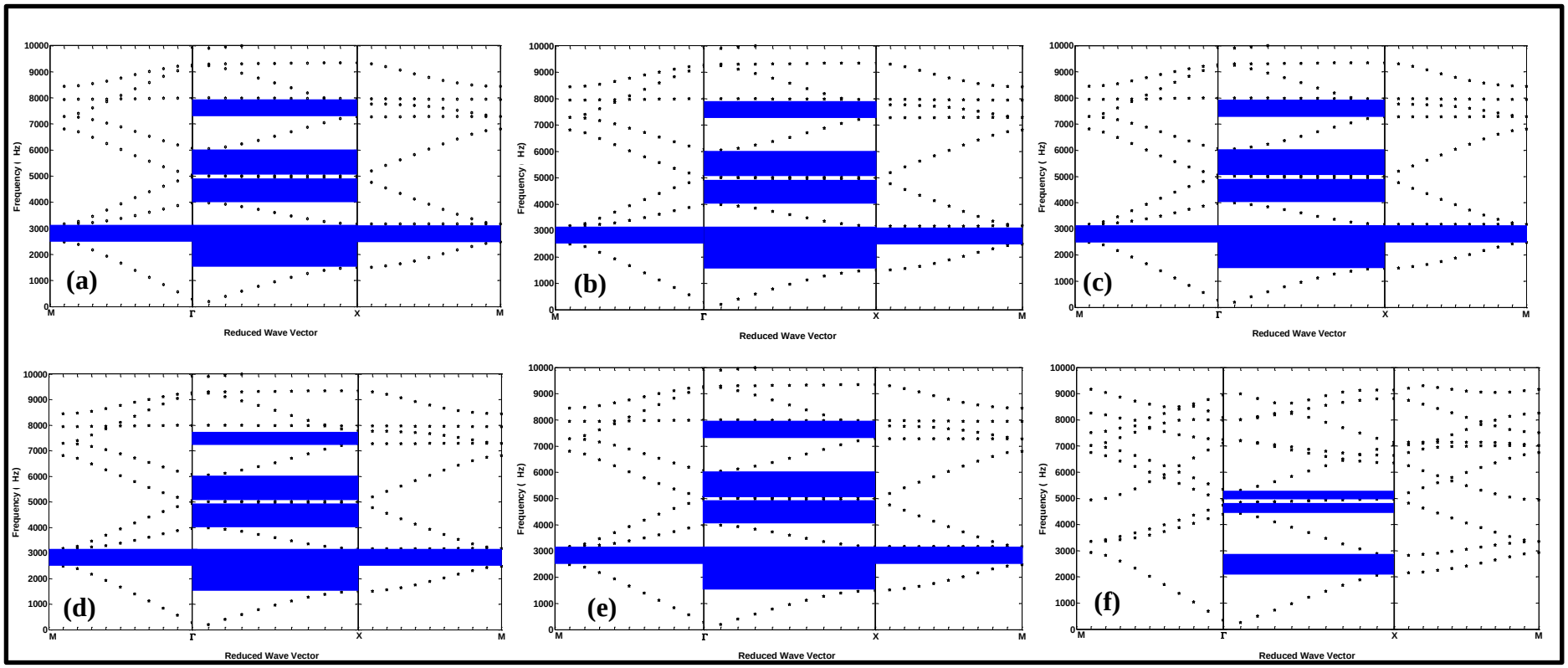

Figure 2.5: Plane Wave Expansion predictions of the influence of material parameters on the band structure. The lattice constant is fixed at 0.069 m and scatterers are made from different materials (a) PVC, (b) silicone rubber, (c) steel (d) PMMA, (e) wood and (f) PVC scatterers embedded in water

Figures 2.5(a), (b), (c), (d) and (e) show the predicted band structures for scatterers made from PVC, silicon rubber, steel, PMMA and wood respectively. The width of the first Bragg band gaps are identical for all of these scatterers and the first Bragg band gaps lie between 1490 to 3170 Hz. This demonstrates that so long as the scatterers are acoustically hard they have no effect on the band structure of the SC. On the other hand, when PVC scatterers are embedded in water, a different band structure is observed (see 2.5(f)). In such system, fewer band gaps are predicted for the ΓX direction since the impedance contrast between PVC and water is smaller than that between PVC and air.

Chapter 3

Multiple Scattering Theory (MST)

3.1) Introduction

When waves travelling in a homogeneous medium such as air encounter an obstacle (sometimes called a scatterer), parts of the waves remain undisturbed while others are scattered and spread out from the scatterer in all directions distorting and interfering with the incident wave. If the scatterer is large in comparison to the wavelength some of an incident wave spreads uniformly in all directions from the scatterer and the rest is more or less concentrated behind the scatterer such that it interferes destructively with the unchanged incident wave. On the other hand, if the scatterer is small compared to the wavelength (which is often the case with sound wave) then, the entire scattered wave is propagated in all directions and there is no interference behind the scatterer [2]. For a single obstacle, calculation of the total field includes the sum of the scattered field and the incident field. This assumption is valid only if the scatterer placed far enough from other scatterers and the incident wavelength is small compared to the distance between the scatterers. Some authors have suggested that the centre to centre distance of two identical wavelength-sized spheres has to be four times the radius of the scatterer for independent scattering to be valid [44]. Clearly a single scattering approximation will not be valid if multiple scatterers are placed within close proximity to each other: a situation often encountered in many areas of physics. Research on multiple scattering of

waves dates back to 1913 [45] when a method for predicting scattering of acoustic waves by two dimensional finite arrays was described. Ever since, there has been a growing interest in wave propagation in periodic or randomly arranged composites. The underlying theory is also applicable to other types of waves. A few examples of various fields in which relevant research is known to have taken place are electromagnetic waves [46 and 47], condensed matter physics [48], water waves [49], optics [50 and 51] and acoustics [52].

In general multiple scattering can be defined as the interaction of the fields due to two or more scatterers [53]. As explained previously for single scattering where an incident field impinges on the individual scatterer, the total scattered field is just the sum of the incident field and the field scattered by that individual scatterer. However, multiple scattering (due to several scatterers within close proximity) takes account of the field scattered from one scatterer which will induce further scattered fields from all the other scatterers, which will again induce further scattered fields from all the other obstacles and so on until the energy in the field has decayed. In multiple scattering, it is possible to have constructive or destructive interference between waves. Multiple Scattering Theory can be classified as a self-consistent method which is valid for both periodically and randomly placed scatterers. In this section, we follow a previously published multiple scattering approach first published by Lord Rayleigh in 1892 when he worked on the potential flow through a periodic rectangular array of identical cylinders [54]. Subsequently, investigations on multiple scattering have been made for a variety of 2D or 3D

problems e.g. Mal and Bose [55] in 1974 and Linton and Evans in 1990 [49]. Martin's book [53] explains each technique developed during these periods of time in great detail. In this section, periodically arranged rigid cylinders will be considered.

Suppose we have *N* disjoint scatterers and an incident wave impinging on them, the problem is to calculate the scattered waves [53],

$$p_{inc} + \sum_{j=1}^{N} p_{sc}^{j} \,, \tag{3.1}$$

where p_{inc} is the incident wave and p_{sc}^{j} is the wave field scattered by the *j*-th scatterer.

Then the effective field over the *k*-th scatterer which is the radiation incident on the *k*-th scatterer in the presence of all other scatterers (*N*-1) can be defined as,

$$p_k = p_{inc} + \sum_{\substack{j=1 \\ j \neq k}}^{N} p_{sc}^{j} \,. \tag{3.2}$$

Since this is a linear problem, it is possible to write,

$$p_{sc}^{j} = \mathrm{T}_j \, p_{inc}^{j} \,, \tag{3.3}$$

where T_j is an operator relating the field incident on the *j*-th scatterer, p_{inc}^{j}, to the field scattered by the *j*-th scatterer, p_{sc}^{j}. Thus substituting equation 3.3 into equation 3.2 gives,

$$p_k = p_{inc} + \sum_{\substack{j=1 \\ j \neq k}}^{N} \mathrm{T}_j \, p_{inc}^{j} \,, \tag{3.4}$$

or equivalently,

$$p_{sc}^{k} = \mathrm{T}_k \left(p_{inc} + \sum_{\substack{j=1 \\ j \neq k}}^{N} p_{sc}^{j} \right), \tag{3.5}$$

by solving equation 3.4 for p_k or equation 3.5 for p_{sc}^{k} where k = 1, 2…, *N*, the total field would then be given by,

$$p = p_{inc} + \sum_{j=1}^{N} \mathrm{T}_j \, p_j \,, \tag{3.6}$$

This over simplified equation hides the complexity through the operator T_j which has not been clearly defined at this stage and also where equation 3.5 and 3.6 is required to hold in space. The next section will show how the separations of variables is done for the acoustic scattering problem involving two or more cylindrical scatterers. For system made up of circular or spherical scatterers, a self-consistent method can be easily realised using the multipoles method.

3.2) Multipole method for circular scatterers in 2-dimensional system

There are several methods for defining T_j in equation 3.6 such as T-matrix [56], iterative technique [57] and the multipole methods [45]. The multipole method is preferred for treating simple geometries, such as circular and spherical scatterers. This method was developed by Zaviska, 1913 for two-dimensional scattering by circular scatterers. This method combines separated solutions of the Helmholtz equation using an important concept of addition theorem for expanding multipoles centred at one origin in terms of similar multipoles centred on a different origin. Such a scattering problem can be conveniently formulated using polar coordinates. This chapter will consider the multipole method using both plane and cylindrical incident waves developed by our collaborators in University of Salford.

Assuming the sonic crystal is formed from *N* infinitely long cylinders of radius a_j, with *j* = 1, 2,…, *N* in either a regular lattice or a random array. The various parameters relating to the relative positions and sizes of the *N* = 2 cylinders are shown in figure 3.1. The acoustic source transmitting monochromatic waves is positioned at the origin $(0,0)$ of the Cartesian coordinate system, some distance away from the array. We will introduce *N*+1 coordinate systems in the x-y plane normal to the cylinder axes (r,θ) centred at the origin and (r_j,θ_j) centred at the *j*-th cylinder. The vertical circular cylinders are fixed along the z-axis and it is assumed that waves propagate in the plane perpendicular to the main axis of the cylinders. Since the boundary

conditions and the geometry do not change with z, the problem can be reduced to a two-dimensional one where the scatterers are taken as its cross section. R_{jq} is defined as the centre-to-centre spacing (often called the lattice constant) between the *j*-th and *q*-th scatterers. The distance of the centre of the *j*-th scatterer from the origin is denoted by R_j.

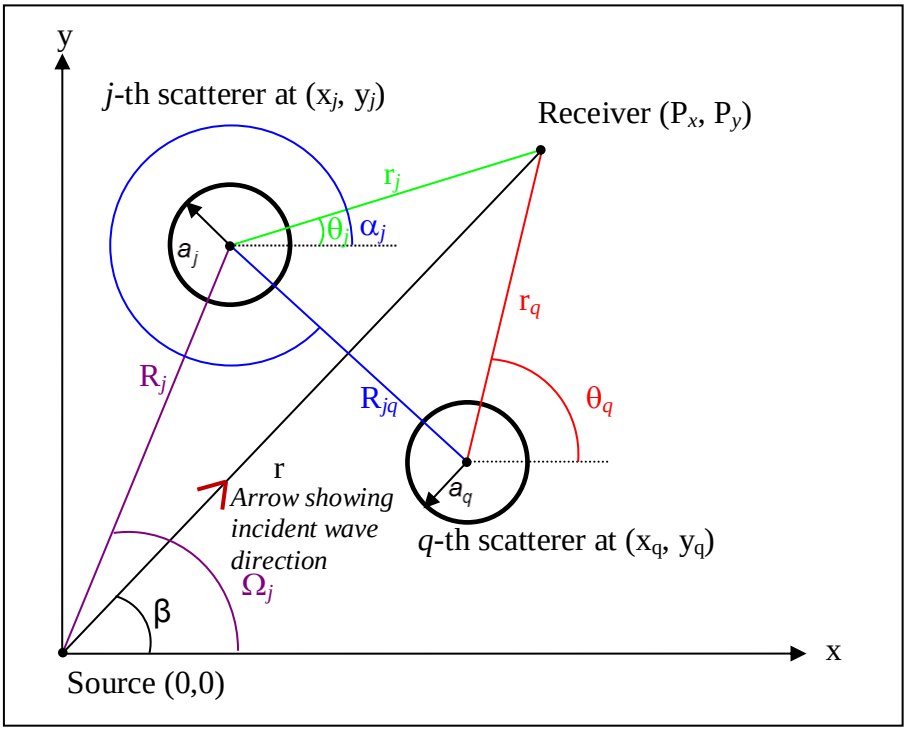

Figure 3.1: Plan view of two identical cylinders and corresponding cartesian and polar coordinates [49, figure 1].

The equation for cylindrically-spreading acoustic waves in a homogeneous, compressible fluid is,

$$\nabla^2 p = \frac{1}{c^2}\frac{\partial^2 p}{\partial t^2}, \qquad \textbf{(3.7)}$$

where $\nabla^2 = \frac{\partial^2}{\partial x_1^2} + \frac{\partial^2}{\partial x_2^2}$ is the Laplacian, c is the constant speed of sound t is time and p is the pressure (see equation 1.4).

Assuming that an external wave p_{inc} with temporal dependence $e^{-i\omega t}$ impinges the array of scatterers where ω is the angular frequency $(2\pi f)$, we can write,

$$p_{inc} = \mathbf{Re}\left\{p\, e^{-i\omega t}\right\}. \tag{3.8}$$

Hence, the complex-valued function p satisfies the well known Helmholtz equation as shown,

$$\nabla^2 p + k_0^2 p = 0 \text{ in } B_e, \tag{3.9}$$

Where $k_0 = \dfrac{2\pi f}{c_0}$, is the wave number in air and B_e is the unbounded exterior to the cylinders region occupied by the air medium. Thus, solution can be obtained by solving for equation 3.9 satisfying some boundary conditions on the exterior of the scatterers and a radiation condition at infinity.

Each individual cylinder scatters the waves which are incident upon it and the total field around the *j*-th cylinder is a superposition of the external field and the radiation scattered by the rest of cylinders. Solutions of the Helmholtz equation are called wavefunctions and two essential wavefunctions [53] which can be expressed in term for the scattering of waves by cylindrical scatterers will be discussed. Firstly, the incident wavefunction ψ_n is represented by an outgoing cylindrical wavefunction of *n*-order and this ensures that the Sommerfeld radiation condition (in two dimensions) at infinity

is satisfied. Such a condition implies that there are no incoming scattered waves at infinity (i.e. no reflection from the boundaries).

$$\psi_n(\vec{r}) = \mathrm{H}_n^{(1)}(kr)e^{in\beta},\ n = 0, \pm 1, \pm 2, \ldots \quad \textbf{(3.10)}$$

Assuming plane polar coordinates, r the radius vector is equal to $(r\cos\beta, r\sin\beta)$.

Secondly, a regular cylindrical wavefunctions of the first kind represent a general outgoing wave radiating from each cylinder is given by,

$$\hat{\psi}_n(\vec{r}) = J_n(kr)e^{in\beta},\ n = 0, \pm 1, \pm 2, \ldots \quad \textbf{(3.11)}$$

The general solution for solving the total wave field at any point exterior to the cylinders (position that is within the host medium which is air in this case) will be introduced here for later convenience,

$$p(x, y) = p_{inc} + \sum_{j=1}^{N} \sum_{n=-\infty}^{+\infty} A_n^j Z_n^j H_n^{(1)}(k_0 r_j) e^{in\theta_j}\ , \quad \textbf{(3.12)}$$

where p_{inc} is the incidence wave over a two dimensions system of scatterers in the form of either a plane wave from infinity or a cylindrical wave from a point. It is also worth noting that p_{inc} can also be modelled with a spherical wave which will extends the problem to three dimensions but will necessarily require higher computing resource. We restrict further consideration to two dimensional systems so plane and cylindrical incident waves. The formulation of this equation will be discussed further in the next section where incident wave (p_{inc}), coefficient (A_n^j), and impedance factor (Z_n^j) will be defined. We

will assume in our model that all motion is time harmonic with angular frequency which uses positive time dependence $e^{i\vec{k}\vec{x}}$ where the wave is propagating from the negative values of x axis. $\vec{k}$ and $\vec{r}$ are defined as the wave vector (with $k = 2\pi f$ as the angular frequency) and location respectively.

3.3) Plane wave scattering model

As previously explained, the scattering problem of *N* scatterers can be conveniently formulated using polar coordinates. Suppose an incident plane wave with angle β propagating to the *j*-th cylinder as shown in figure 3.1 (brown arrow), such plane wave can be written as an expansion of Bessel functions of the first kind centred at the origin of coordinates [49],

$$p_{inc} = e^{ik(x\cos\beta + y\sin\beta)}. \qquad \textbf{(3.13)}$$

Cartesian x and y coordinates can then be easily defined,

$$x = r\cos\theta \text{ and } y = r\sin\theta. \qquad \textbf{(3.14)}$$

Substitute equation 3.14 into equation 3.13 gives,

$$\begin{aligned} p_{inc} &= e^{ik(r\cos\theta\cos\beta + r\sin\theta\sin\beta)} \\ &= e^{ikr(\cos\theta\cos\beta + \sin\theta\sin\beta)}. \end{aligned} \qquad \textbf{(3.15)}$$

Using rules of trigonometric transforms (compound angle formulae), equation 3.15 can be written as,

$$p_{inc} = e^{ikr(\cos(\theta-\beta))} \quad \textbf{(3.16)}$$

The plane wave impinging the *j*-th scatterer is then scattered to other positions (e.g. the receiver position) thus, the scalar product $(r_j)k$ is now replaced with $(R_j + r_j)k$. Following a similar approach in equation 3.14 gives,

$$\begin{aligned} \mathbf{p}_x &= R_j \cos\Omega_j + r_j \cos\theta_j \text{ and} \\ \mathbf{p}_y &= R_j \sin\Omega_j + r_j \sin\theta_j, \end{aligned} \quad \textbf{(3.17)}$$

where,

$$x_j = R_j \cos\alpha_j \text{ and } y_j = R_j \sin\alpha_j. \quad \textbf{(3.18)}$$

Therefore,

$$p_{inc} = I_j e^{ikr_j(\cos(\theta_j-\beta))}, \quad \textbf{(3.19)}$$

where $I_j = e^{ik(x_j\cos\beta + y_j\sin\beta)}$ is a phase factor associated with the *j*-th cylinder. As $e^{ik(x_j\cos\beta+y_j\sin\beta)}$ can be written as series of Bessel function [58], equation 3.19 can be written as,

$$p_{inc} = \sum_{n=-\infty}^{n=+\infty} i^n J_n(kR_j) e^{in\Omega_j}, \quad \textbf{(3.20)}$$

where $k = \frac{2\pi f}{c}$, and J_n is the Bessel function of *n*-th order of the first kind. Thus, equation 3.20 becomes [49],

$$p_{inc} = I_j \sum_{n=-\infty}^{n=+\infty} J_n\left(kr_j\right) e^{in\left(\pi/2-\theta_j+\beta\right)}, \qquad \textbf{(3.21)}$$

The effect of a given scatterer on the incident wave will be to produce a scattered wave which will in turn be scattered by a neighbouring scatterer and so on as this process is repeated. A general form for such a radiating wave emanating from the *j*-th cylinder can be expressed with respect to the origin of coordinates of the *j*-th cylinder using *n*-th order Hankel functions of the first kind,

$$p_{sc}^{j} = \sum_{n=-\infty}^{n=+\infty} A_n^j H_n^{(1)}\left(kr_j\right) e^{in\theta_j}, \qquad \textbf{(3.22)}$$

where

$$r_j = \sqrt{\left(x-x_j\right)^2 + \left(y-y_j\right)^2}, \qquad \textbf{(3.23)}$$

and

$$\theta_j = \sin^{-1}\left(\frac{y-y_j}{r_j}\right), \qquad \textbf{(3.24)}$$

We note that A_n^j incorporate the complex amplitude function I_j (equation 3.21) that includes a phase factor associated with the corresponding *j*-th scatterer.

Substituting equation 3.21 and 3.22 into equation 3.2, we are able to solve for the total wave over the *j*-th cylinder. However, in order to perform the computation, all the terms must be expressed in terms of the same origin

coordinates (r_q, θ_q). This can be done using Graf's addition theorem (See Appendix B). When using the addition theorem for Bessel functions it is important to note that in order to write functions of (r_j, θ_j) in terms of the coordinates (r_q, θ_q), we have to ensure that $r_q < R_{jq}$ for all $j \neq q$. This geometry restriction implies that the expression obtained is only valid if the point (r_q, θ_q) is closer to the centre of cylinder *q* rather than to the centre of any other cylinders or the source and thus we can write the expression obtained for (r_q, θ_q) as,

$$p_{(r_q,\theta_q)} = \sum_{n=-\infty}^{n=+\infty} \left[I_q J_n(k_0 r_q) e^{in(\pi/2-\theta_q+\beta_p)} + A_n^k Z_n^k H_n^{(1)}(k_0 r_q) e^{in\theta_q} \right] + \sum_{\substack{j=1 \\ j\neq q}}^{N} \sum_{n=-\infty}^{n=+\infty} A_n^j Z_n^j \times \sum_{m=-\infty}^{m=+\infty} J_m(k_0 r_q) H_{n+m}^{(1)}(k_0 R_{jq}) e^{im(\pi-\theta_q)} e^{i(n+m)(\alpha_j)} , \quad \textbf{(3.25)}$$

for some set of unknown complex numbers A_n^j. Both A_n^j and Z_n^j are related by the boundary conditions of the scatterers surface. Definition of the term Z_n^j which is the impedance factor [49] of the scatterers will follow.

We apply boundary conditions of continuity of both pressure and particle velocity between the scatterer and the surrounding air medium. Thus, for the case of the *q*-th scatterer, the boundary condition can be expressed by,

$$\rho_{ext}\Big|_{r_q=a_q} = \rho_{\text{int}}\Big|_{r_q=a_q} , \quad \textbf{(3.26)}$$

Leading to,

$$\frac{1}{\rho}\frac{\partial \rho_{ext}}{\partial r_q}\Big|_{r_q=a_q} = \frac{1}{\rho_q}\frac{\partial \rho_{\text{int}}}{\partial r_q}\Big|_{r_q=a_q}, \qquad \textbf{(3.27)}$$

where ρ is the density of the surrounding medium (air) and ρ_q is the density of the *q*-th scatterer. If the scatterers are acoustically-rigid, the condition of zero velocity is applied. This is widely known as the Neumann boundary condition which specifies the values that the derivative of a solution is to take on the boundary of the domain,

$$\frac{\partial \rho_{ext}}{\partial r_{qp}}\Big|_{r_q=a_q} = \frac{\partial\left(p_{inc}^{q} + p_{sc}^{j}\right)}{\partial r_q}\Big|_{r_q=a_q} = 0, \qquad \textbf{(3.28)}$$

where p_{inc} the total incident pressure over the *q*-th scatterer (refer to equation 3.21 and p_{sc}^{j} is the scattered wave by the *j*-th scatterer (refer to equation 3.22).

This boundary condition leads to the definition of impedance for the rigid scatterers as follow,

$$Z_n^j = \frac{J_n^{'}\left(k_0 a_q\right)}{H_n^{(1)'}\left(k_0 a_q\right)}, \qquad \textbf{(3.29)}$$

Applying this boundary conditions for pressure and velocity on the outer surface of *q*-th scatterer and after using the orthogonality of the functions $e^{im\theta q}$ taking $m = 0, \pm 1, \pm 2,...,$ make it possible to derive an infinite system of equations which can lead to solve for coefficients A_m^q.

$$A_m^q + \sum_{\substack{j=1 \\ j\neq q}}^{N} \sum_{M=-\infty}^{M=+\infty} A_n^j Z_n^j e^{i(n-m)(2\pi-\alpha_j)} H_{n-M}^{(1)}\left(k_0 R_{jq}\right) = -I_q e^{im(\pi/2-\beta)}. \qquad \textbf{(3.30)}$$

The obtained algebraic system can then be truncated to the finite number $N(2M+1)$ of equations. Where $n = 0, \pm 1, \pm 2, ... \pm M$ and $q = 1, 2, 3, .., N$. In [49], it was found that taking M = 6 gave results accurate to four significant figures, except when the scatterers were positioned very close together.

3.4) Cylindrical wave scattering model

The previous scattering model was for incident plane waves. The source may not be placed sufficiently far enough from the scatterers for such approximation to be valid so it is necessary to consider cylindrical wave incidence. For simplicity without compromising generality, we approximate the acoustic source as a line source located at origin $\vec{r} = 0$. The wave in free field is governed by the following equation,

$$\left(\overrightarrow{\nabla^2} + k_0^2\right) p\left(\vec{r}\right) = -4\pi\delta^2\left(\vec{r}\right) \text{ in } B_e, \qquad \textbf{(3.31)}$$

where $k_0 = \frac{2\pi f}{c}$, δ^2 is the 2-dimension delta-function and B_e is the unbounded exterior to the cylinders region occupied by the air medium. In cylindrical polar coordinates, the solution can be expressed as,

$$p_{inc} = H_0^{(1)}(k_0 r), \qquad \textbf{(3.32)}$$

where $H_0^{(1)}$ is the zero-th order of Hankel function and of the first kind.

Following similar procedure in equation 3.21 where we considered the scattering in the presence of *N* cylinders (repeated for convenience). The radiating wave emanating from the *j*-th cylinder can be expressed with respect to the origin of coordinates of the *j*-th cylinder using *n*-th order Hankel functions of the first kind,

$$p_{sc}^{j} = \sum_{n=-\infty}^{n=+\infty} A_n^j H_n^{(1)}\left(kr_j\right) e^{in\theta_j} \,. \tag{3.33}$$

Similarly by applying Graf's addition theorems to solve for the total wave

$$\begin{aligned} p_{(r_q,\theta_q)} = & \sum_{n=-\infty}^{n=+\infty}\left[I_q J_n\left(k_0 r_q\right) e^{in\left(\pi/2-\theta_q+\theta_p\right)} + A_n^k Z_n^k H_n^{(1)}\left(k_0 r_q\right) e^{in\theta_q}\right] \\ & + \sum_{\substack{j=1 \\ \neq q}}^{N} \sum_{n=-\infty}^{n=+\infty} A_n^j Z_n^j \times \sum_{m=-\infty}^{m=+\infty} J_m\left(k_0 r_q\right) H_{n+m}^{(1)}\left(k_0 R_{jq}\right) e^{im\left(\pi-\theta_q\right)} e^{i(n+m)\left(2\pi-\partial_j\right)} \,. \end{aligned} \tag{3.34}$$

Applying the boundary condition for acoustically-rigid cylinders as shown in equation 3.25 and 3.29 leads to the definition of impedance as follow,

$$Z_n^j = \frac{J_n^{'}\left(k_0 a_q\right)}{H_n^{(1)'}\left(k_0 a_q\right)}, \tag{3.35}$$

Using the same approach as for equation 3.30, i.e. applying boundary conditions for pressure and velocity on the outer surface on the *q*-th scatterer and using the orthogonality of the functions $e^{im\theta q}$ taking $m = 0, \pm 1, \pm 2, \ldots$, it is possible to derive an infinite system of equations which can be solved for coefficients A_m^q with cylindrical incident waves [59]. The obtained algebraic

system can then be truncated to the finite number $N(2M+1)$ of equations. Where $n=0,\pm1,\pm2,...\pm M$ and $q=1,2,3,..,N$. This gives,

$$A_m^q+\sum_{\substack{j=1\\ j\neq q}}^{N}\sum_{n=-\infty}^{n=+\infty}A_n^j Z_n^j e^{i(n-m)(2\pi-\alpha_j)}H_{n-M}^{(1)}\left(k_0R_{jq}\right)=-H_m^{(1)}\left(k_0R_q\right)e^{-im(\pi+\xi_p)}. \qquad \textbf{(3.36)}$$

3.5) Simulation and results

Assuming we have *N* = 21 identical rigid cylindrical scatterers arranging in a 7x3 square lattice array. The radius of the scatterers is 0.0275 m. Three lattice constants (*L*) of 0.069, 0.08 and 0.135 m were used and thus give filling fractions of 50, 37 and 13% respectively. The source is located at 1.5 m away from the front face of the array and the receiver is placed 0.05 m from the nearest face of the array but on the opposite side of the source. Such configuration is equivalent to the measurement of the ΓX direction in the Brillouin Zones defined in chapter 1 such that the source-receiver axis is normal to the array orientation (see figure 3.2). The results are computed in terms of Insertion Loss (IL) which has been defined in equation 1.9. However without loss of generality and for clarity in term of the notation used in this Chapter the IL is defined as,

$$IL=20\log_{10}\left|\frac{p_{inc}}{p(r)}\right|, \qquad \textbf{(3.37)}$$

where p_{inc} can be modelled either in plane (equation 3.16) or cylindrical incident wave (equation 3.31) and the total field $p(r)$ defined in equation 3.12. Solution of both incident waves are shown in our results.

The calculated results using MST are validated with the laboratory results of similar sonic crystal configuration. The detailed descriptions of the laboratory measurements are explained in chapter 5. Investigation of the numerical solution of the MST is also done since there is an infinite linear system to be solved by truncation. This is done by incrementing *M* in the system of equations.

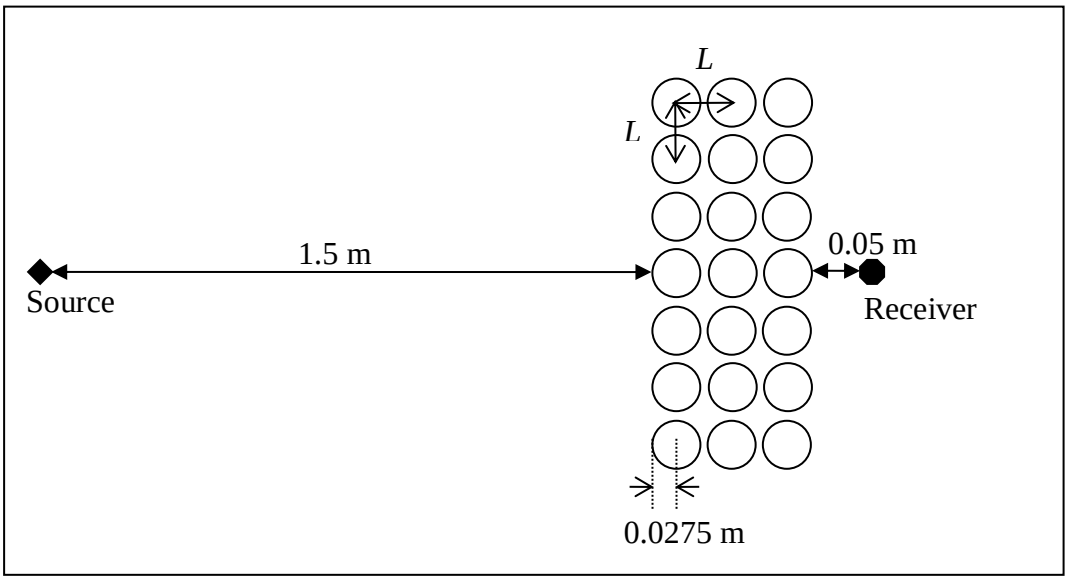

Figure 3.2: Example scenario including an array of rigid circular scatterers.

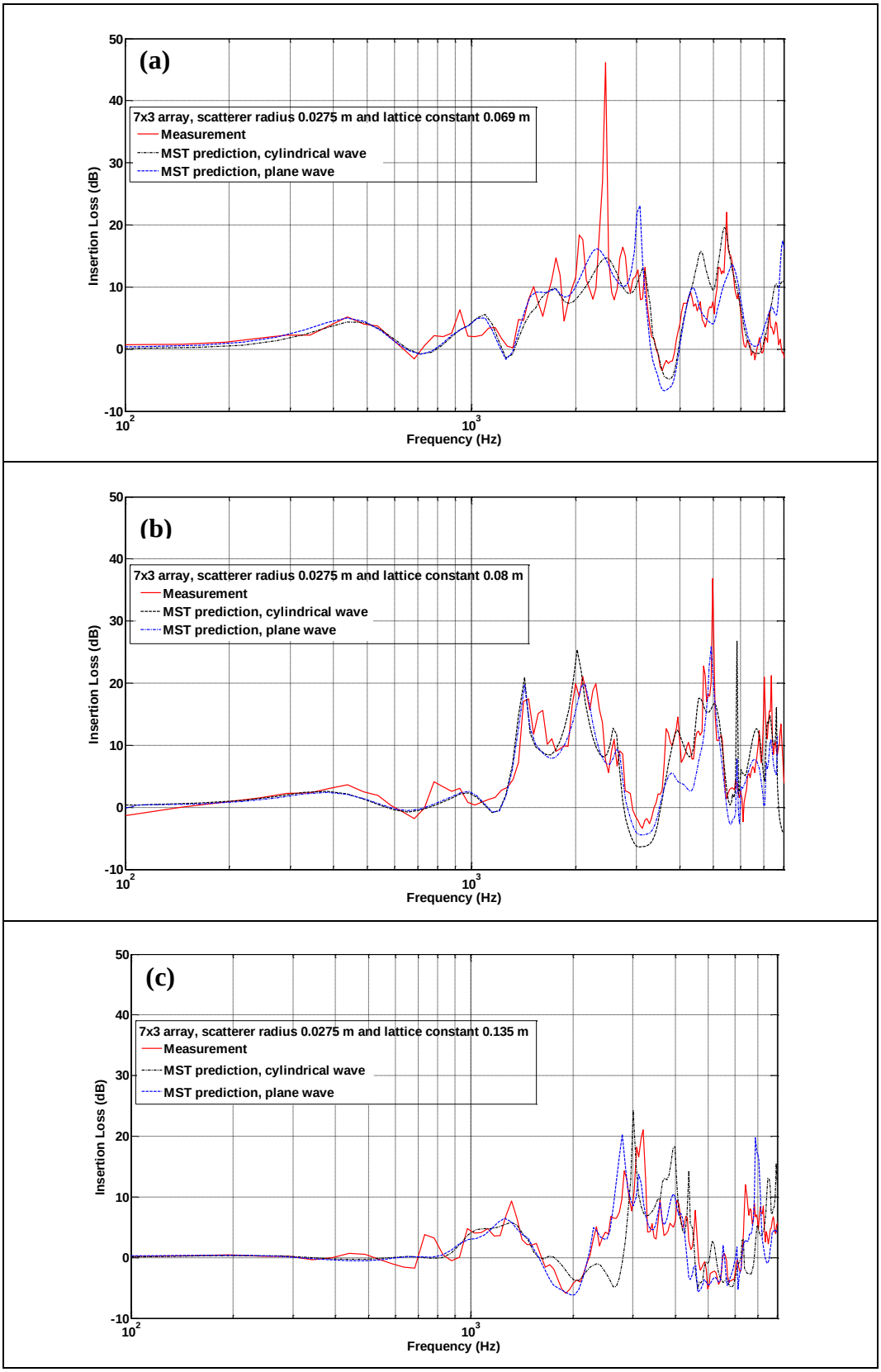

Figure 3.3: MST predictions and measured Insertion Loss spectra for square lattice arrays of rigid circular scatterers of 0.055 m diameter with lattice constants of (a) 0.069, (b) 0.08 and (c) 0.135 m respectively. Both plane and cylindrical waves are compared for all three cases.

According to figure 3.3, the theoretical (MST) predictions for both plane and cylindrical incident waves show relatively good agreement with the laboratory measurement data for 7x3 square lattice array of rigid circular scatterers. The shifting of the band gaps due to the effect of changing the periodicity by varying the lattice constant for the structure can be observed. The first Bragg diffraction frequency can be predicted by using the formulation given in equation 2.13.

Measurements and predictions demonstrate that the first Bragg diffraction frequency can be controlled by altering the lattice constant in a finite sonic crystal array. The peaks near 2.5, 2 and 1.3 kHz for 50, 37 and 13 % filling fractions respectively correspond to the first Bragg frequencies for the corresponding lattice constants of 0.069, 0.08 and 0.135 m respectively. The relatively minor peaks occurring before the first Bragg frequencies can be attributed to the finite length and depth of the array.

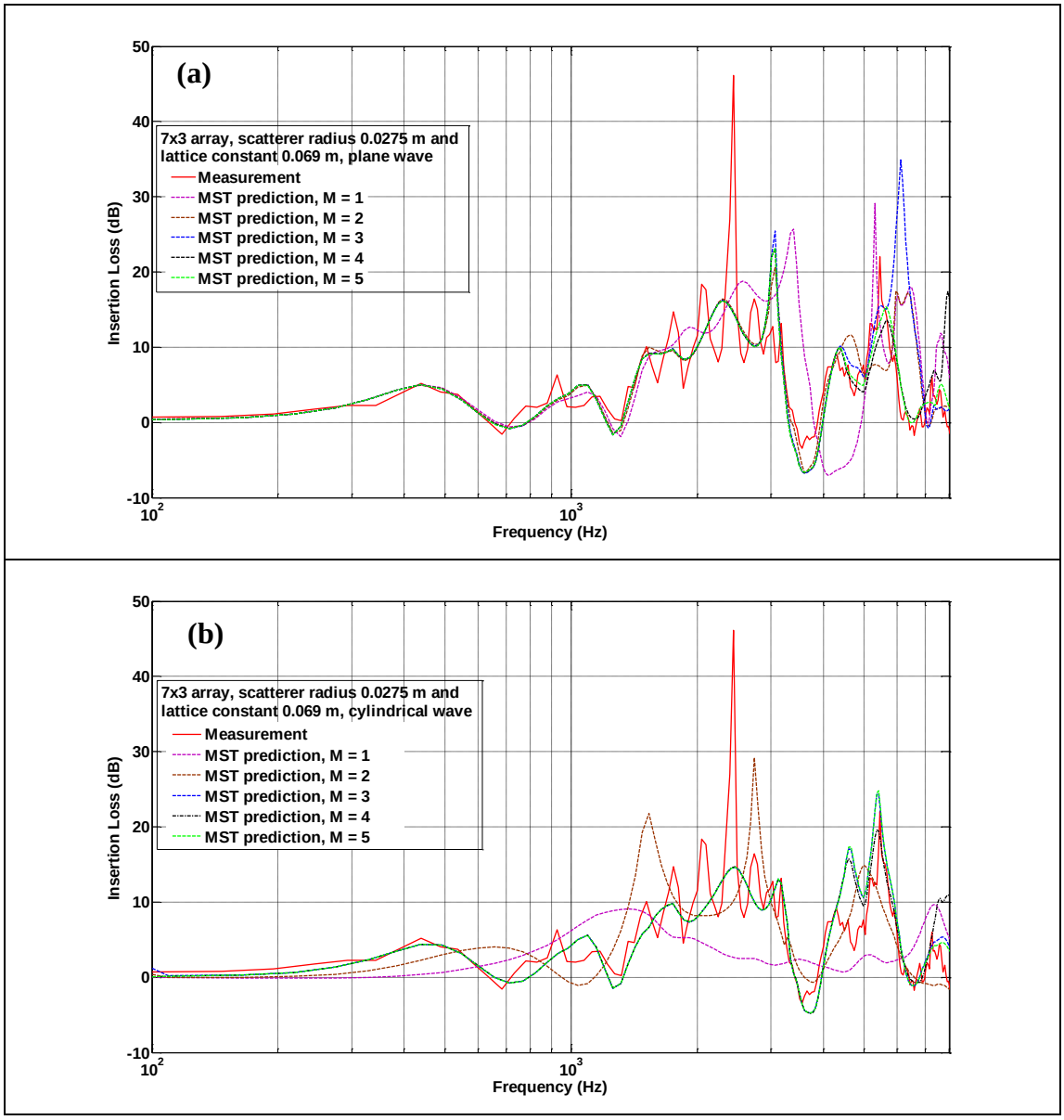

Figure 3.4: MST predictions and measured Insertion Loss spectra for square lattice arrays of rigid circular scatterers of 0.055 m diameter with lattice constants of 0.069. Different truncation number of $M = 1, 2, \ldots, 5$ is used for the MST predictions for (a) plane wave and (b) cylindrical wave.

Figure 3.4 shows IL spectra with different number of truncation number *M*, for both plane and cylindrical incident waves. This test is to determine the accuracy of the numerical MST solution. We assume a lattice constant of 0.069 m for both types of incident wave and increment *M* from 1 to 5. It can be observed that for our geometry, the accuracy of the numerical results converge as long as $M \geq 4$ for the case of plane waves and $M \geq 3$ in the case

of cylindrical waves. Using $M = 4$ and $M = 3$ for plane and cylindrical incident wave respectively requires less than 3 minutes computation time on a standard office PC (Intel core 2 Dual CPU 2.4 GHz, 2GB RAM with 32 bit Operating System).

Chapter 4

Numerical method using Finite Element Method (FEM)

4.1) Introduction

It is not always feasible to solve for scatterers with non-geometrical shapes or resonant constructions by means of an exact analytical solution. The Finite Element Method (FEM), also known as Finite Element Analysis (FEA), based on numerical solutions of Partial Differential Equations (PDEs) offers a method for finding approximate numerical solutions of the scattered and total fields in a wide range of physical and engineering problems. The solution approach involves either eliminating the differential equations completely (steady state problems) or rendering the PDEs into an approximating system of ordinary differential equations, which are then solved numerically by integration using standard techniques such as Euler's method. The history of FEM dates back to 1943 when Courant determined the torsional rigidity of a hollow shaft by dividing the cross section into triangles and interpolating values of the stress function at each intersecting point [60]. Subsequently, the first publication using FEM for determining the frequencies and mode shapes of acoustic cavities was published by Gladwell [61]. Beside of having the capability to solve for a structure with an irregular shape, the common advantages of using FEM include a reduction of development time due to elimination or reduction of the need for testing, optimising product performance, cost saving and improved information for making engineering

decisions. In the early 70's, the use of FEM was limited to the expensive mainframe computers available in the defence, automobile and aeronautical industries. With the increased availability of powerful computers, this technique has become much more widely available. Driven by research and industry demands, FEM codes have developed rapidly and become increasingly popular. The advent of FEM commercial software such as COMSOL® or ANSYS® has greatly helped to promote the wide acceptance of FEM. Its impact on the advancement of modern technology is well demonstrated by its implementation in various fields such as acoustics [62 and 63], optics [64 and 65], biomechanics [66], thermodynamics [67], materials [68] and telecommunications [69]. By 1995, it is estimated that about 3800 papers on FEM were being published annually and that the cumulative total of FEM publications amounted to some 380 books, 400 conference proceedings and 56000 papers [70].

Given an acoustic space with specified conditions on the boundaries generally yields five standard problems. Firstly, the radiation problem where we have a source (i.e. speaker) radiating sound into the surrounding space. For such a problem, a far-field boundary condition is necessary to model an unbounded domain. Secondly, the scattering problem where the incident wave impinges on an acoustically hard structure which in turn creates a scattered wave. Thirdly, the transmission problem where the incident sound wave propagates into a structure which can have different acoustical properties (i.e. absorbing). Fourthly, the sound field in an enclosed space such as a room (bounded domain). Lastly, the coupled fluid-elastic structure

interactions (also known as structural acoustics) where the scattering structure consists of an elastic material in which the interaction between the structure and the surrounding fluid must be considered. Such modelling is done in chapter 6 and 7 for cases where an elastic scatterer is used as an element in sonic crystal design.

Finite element method computations for sonic crystals have been reported using different finite element method software packages such as COMSOL® Multiphysics [71] and the Local Interaction Simulation Approach (LISA) [72]. In this chapter, COMSOL® Multiphysics (version 3.5a) has been used to simulate the scattering of acoustic waves in two-dimensional sonic crystals. This software is relatively easy to use due to its user friendly graphical user interface simulation environment for all of the steps of the modelling process: definition of geometry, specification of physics, meshing, solving and post-processing of results. In addition, the user is able to customise PDEs to allow complex analyses such as acoustic and structural interactions (see chapter 6 and 7).

4.2) Acoustic modelling in COMSOL® Multiphysics

The fundamental concept of the finite element method is that a complicated domain can be divided into a series of small interconnected subregions in which the PDEs are approximately solved. Each subregion of the domain is referred to as an element and the process of subdividing a domain into a finite number of elements is referred to as discretization (see figure 4.1). The particular arrangement of elements is called a mesh. The set

of equations for each element can be assembled to compute the behaviour of the system over the entire domain. These elements are connected at specific points, called nodes, and the assembly process requires that the solution be continuous along common boundaries of neighbouring elements.

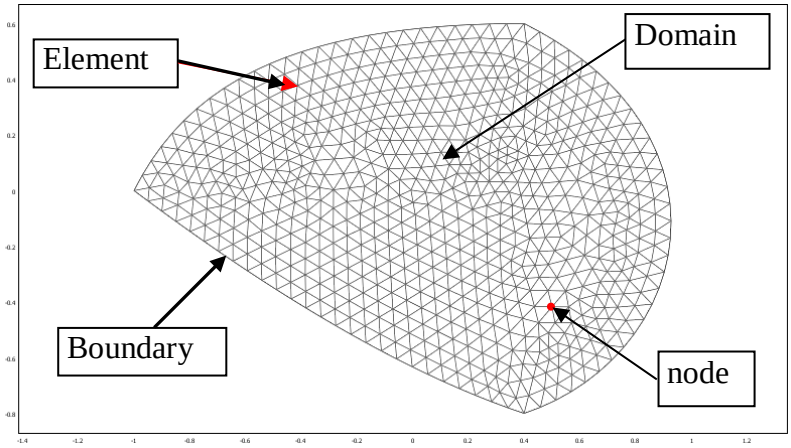

Figure 4.1: Definition of domain discretized using triangular shape finite elements.

The equation for cylindrically-spreading acoustic waves in a lossless fluid medium previously shown as chapter 3, equation 3.9 is repeated here for convenience,

$$\nabla^2 p + k_0^2 p = 0\,, \qquad \textbf{(4.1)}$$

where $\nabla^2 = \frac{\partial^2}{\partial x_1^2} + \frac{\partial^2}{\partial x_2^2}$ is the Laplacian, $k_0 = \frac{2\pi f}{c_0}$ is the wave number in air, and the complex-valued function p satisfies the well known Helmholtz equation in unbounded exterior occupied by the air medium.

The expressions for the pressure emitted by:

either a plane wave source or a cylindrical source are

$$p_{in\_p} = e^{ik_0 x}, \tag{4.2}$$

$$p_{in\_c} = \frac{i}{4}\left(J_0(k_0 r_c) - iY_0(k_0 r_c)\right), \tag{4.3}$$

respectively, where $r_c = \sqrt{x_c^2 + y_c^2}$ is the distance defined by the source location to the travelling wave position. There have been more advanced studies allowing for oblique incidence of the waves [73] but, in our model, we consider that the direction of waves is normal to the symmetry axis of the scatterer.

We define an acoustically-hard boundary condition (widely known as the Neumann boundary condition) to model the rigid surface of the scatterers whereby the normal acceleration of particle velocity is equal to zero,

$$\vec{n}.\left(\frac{1}{\rho_0}\nabla p\right) = 0, \tag{4.4}$$

where ρ_0 represents the density of the scatterer.

To compute two dimensional scattering problems in an unbounded domain involves a domain decomposition by introducing an artificial boundary around the obstacles. The radiation boundary conditions are applied to the surrounding boundaries of the modelling domain (see figure 4.2). For the

outward travelling wave, this boundary condition ensures minimal or no reflections from the model boundary. The radiation boundary conditions can be expressed as [74],

$$-\vec{n}\left(-\frac{1}{\rho_0}\nabla p\right)+\left(ik_0+\kappa(r)\frac{p}{\rho_0}\right)=\left(ik_0+\kappa(r)-i\left(\vec{\mathrm{K}}\cdot\vec{n}\right)\right)\frac{p_0}{\rho_0}e^{-i\left(\vec{\mathrm{K}}\cdot r\right)}, \qquad \textbf{(4.5)}$$

where $\kappa(r)$ is a function whose form depends on the type of wave as described in the following,

plane wave: $\kappa(r)=0$, or

cylindrical wave: $\kappa(r)=\frac{1}{2r}$,

in which r is define as the shortest distance from the point on the boundary to the source.

The term on the right hand side represents an incoming pressure wave with amplitude, p_0 and direction of propagation given by wave vector, $\vec{\mathrm{K}}$ and normal vector, $\vec{n}$.

A triangular mesh is used and the number of elements per wavelength is at least 6 to obtain the desired accuracy. The accuracy of FEM will be discussed in section 4.4. Equation 4.1 can now be solved using a parametric solver to obtain the pressure field for the rectangular domain modelled as air. This is done by performing a frequency sweep over 100 Hz to 8 kHz with frequency step of 100 Hz to produce a frequency spectrum for both direct field and total

transmitted field (without and with sonic crystal respectively). The Insertion Loss (IL) for the sonic crystal noise barrier can then be obtained using chapter 1 equation 1.9 (repeated here for convenience),

$$IL = 20\log_{10}\left|\frac{p_{direct}}{p_{total\_transmitted}}\right|, \qquad \textbf{(4.6)}$$

The hardware configuration used to run the simulations was a 64-bit windows platform with 3.07 GHz Intel core i7 processor and 6 GB of RAM. This gives a maximum solution time of 12 minutes for the case with the highest mesh density which is reasonable.

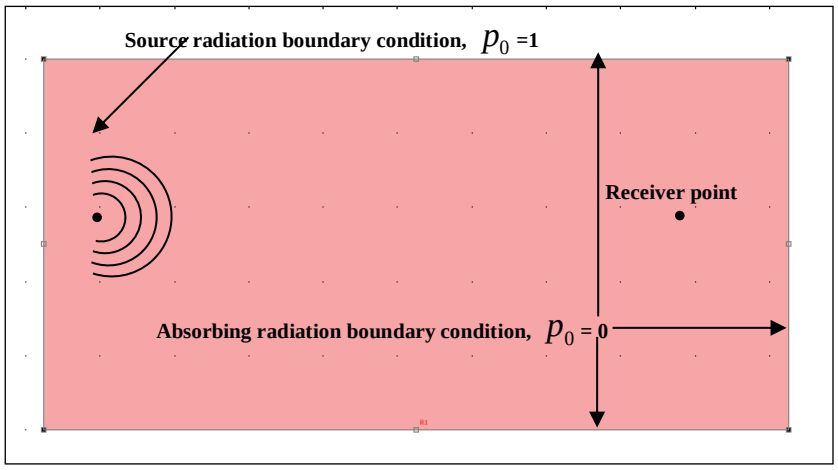

Figure 4.2: Definition of geometry for a rectangular domain modelled as air and an incoming cylindrical wave source.

4.3) FEM computed results

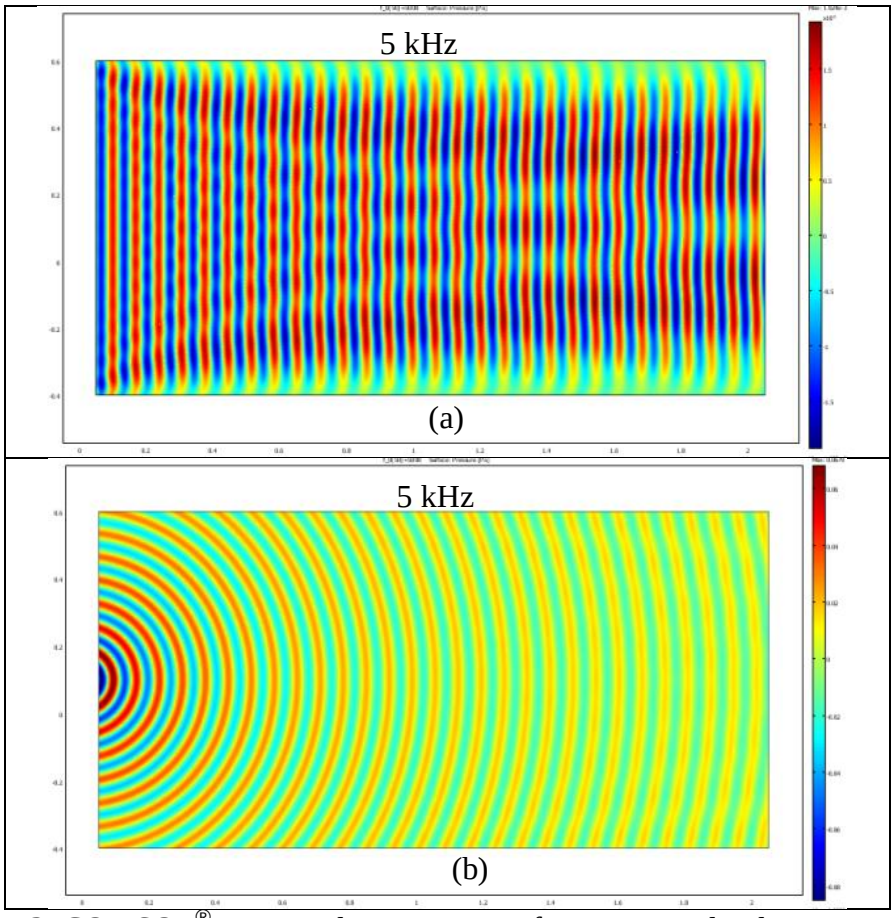

Figure 4.3: COMSOL® computed pressure map for a rectangular domain modelled as air and an incoming plane (a) or cylindrical wave (b) source.

In figure 4.3, the FEM-predicted pressure maps are shown for incident 300 Hz 1.2 kHz 5 kHz (a) plane and (b) cylindrical waves for direct field computed in a rectangular domain modelled as air. The incoming waves are propagated from the left boundary to the right and the radiation boundary conditions are applied to both simulations. Clearly, in the case for plane wave, the boundaries cause some unwanted reflections which suggests that the radiation boundary conditions applied may not be ideal for such geometry. On the other hand, this radiation boundary conditions work very well for cylindrical waves as little or no reflection effects can be observed.

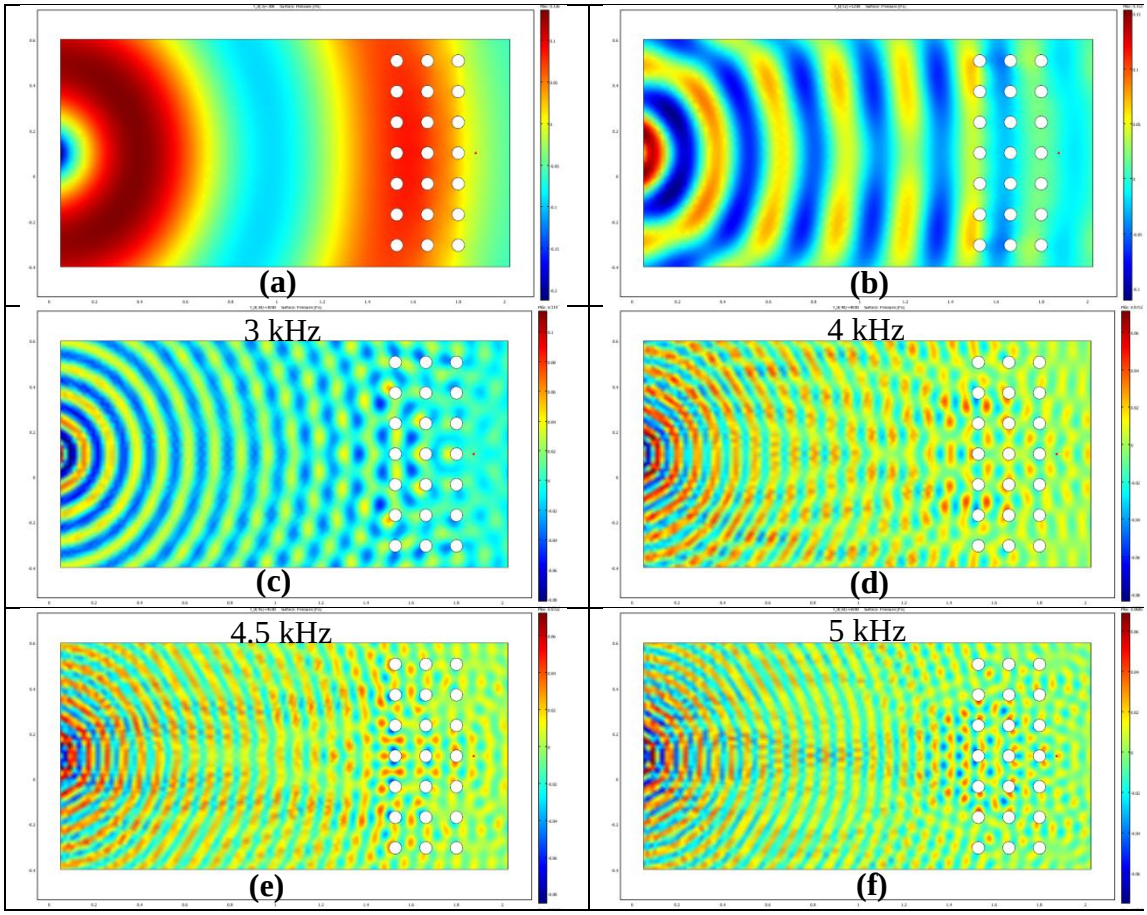

Figure 4.4: COMSOL computed pressure maps for 7x3 array of sonic crystal (acoustically hard scatterer) modelled in rectangular air domain. Cylindrical waves is performed and pressure maps at 200 Hz, 1.2, 3, 4, 4.5 and 5 kHz are shown for figure (a), (b), (c), (d) and (e) respectively.

Figure 4.4 shows the FEM-predicted pressure maps for a square lattice array of 7x3 rigid circular scatterers with lattice constant of 0.135 m modelled with similar boundary conditions to those used for the direct field computations shown in figure 4.3. The radius of the scatterers is 0.0275 m. The cylindrical wave source is located at 1.5 m away from the front face of the array and the receiver is positioned 0.05 m from the nearest face of the array but on the opposite side of the source. The number of triangular elements for this model is 157392. The pressure maps are shown for various frequencies ranging from 300 Hz to 5 kHz. Clearly, these results support the introductory section on scattering (MST chapter 3, section 3.1), whereby incident waves

pass through relatively unaffected when the wavelengths are large compared to the scatterers (see figure 4.4(a)) but as the incident wavelengths decrease, scattering patterns appear (see figure 4.4(b) to (f)).

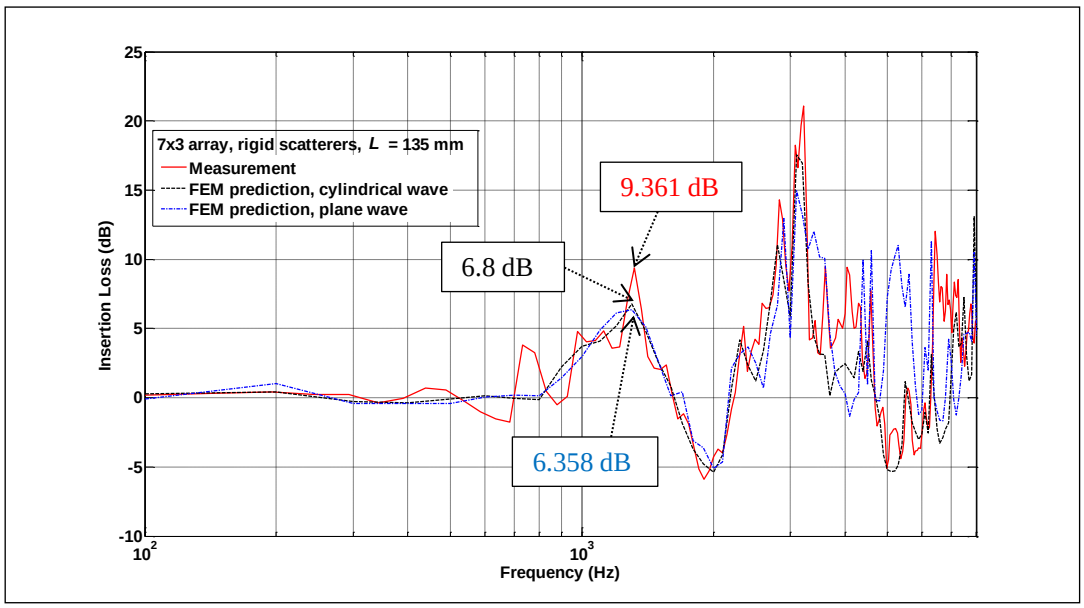

Figure 4.5: FEM predictions and laboratory measured Insertion Loss spectra for 7x3 square lattice arrays of rigid scatterers of radius 0.0275 m with lattice constant 0.135 m. FEM predictions are performed with plane and cylindrical wave sources for a rectangular domain modelled as air.

Figure 4.5 shows the Insertion loss (IL) spectra comparing laboratory measurements and FEM predictions using plane and cylindrical wave source with the boundary conditions similar to figure 4.4. The details of laboratory measurement are discussed in chapter 5. The IL is calculated using equation 4.6 and the calculated Bragg frequency (refer to PWE chapter, equation 2.13) for this particular set up is 1.3 kHz. Results show that FEM predictions agree fairly well with the laboratory measurements up to 5 kHz using plane waves and up to 6 kHz in the case of cylindrical waves. The IL values at 1.3 kHz for all the 3 spectra are shown in the figure. The discrepency between the prediction and measurement at the Bragg frequcny is about 3 dB. The Bragg frequency is also well predicted by the FEM simulation. Higher frequency

agreement could be improved using higher mesh densities which inevitably require a higher computational resource (explained in next section) or by improvement of the boundary conditions to further minimise reflection as in the case for plane wave. Peaks occurring in the measurements before the first Bragg frequencies could be due to the finite height of the array (finite length of the cylinders).

4.4) Investigation of accuracy of FEM

FEM is renowned for its versatility, being applicable to a wide range of problems with complex geometries. But also the method lends itself easily to a rigorous error analysis. Acoustics is a wave phenomenon in which the waves are characterized by its wavelength λ in space, whose value depends on the frequency f and the speed of sound in the medium c relating to equation 1.1. To solve wave problems governed by the Helmholtz equation using FEM, the mesh must offer sufficient resolution. Generally for FEM, this requires mesh grids with around ten nodal points per wavelength [75]. The Mesh elements have to be increased even more when curvature or sharp edges are present in the geometry. This section will discuss how frequency convergence can be used to establish a high level of accuracy based on the quality of mesh. In this study, an identical rectangular domain (direct field) to that described in section 4.2 is modelled with cylindrical waves. Similar radiation boundary conditions are applied to the edges of the rectangular domain. The FEM computation is solved for the different mesh densities listed in table 4.1 using a parametric solver (frequency sweep over 100 Hz to 8 kHz

with frequency step of 100 Hz) to obtain the pressure field. The computation time taken to completely solve the 80 iterations for each mesh density is also shown in the table. Notably, the computation time increases with each increment of mesh density.

Maximum Element size (m)	Number of Elements	Number of Degrees of Freedom	Computation Time (s)
0.5	26	65	2.361
0.2	128	287	3.141
0.1	476	1011	5.161
0.04	1651	6451	16.811
0.007	121856	244641	637.255

Table 4.1: Mesh qualities and computational results.

The accuracy of an FEM simulation can be determined in two ways. First, the different set of mesh densities will be solved and the pressure maps at similar frequency will be compared. Although this method presents stimulating graphics for the eyes but it can be tedious to analyse for all frequencies. Another alternative is to analyse the computed frequency spectrum for a fixed point in all the sets. The Sound Pressure Level, SPL (Decibels) for all calculated frequencies can be easily extracted at a given point expressed by,

$$SPL = 20\log_{10}\left|\frac{p}{p_0}\right|, \qquad \textbf{(4.7)}$$

where p is the pressure at a given point and p_0 is the reference sound pressure $\left(2\times10^{-5}\ \text{Pa}\right)$. Note that the SPL is measured in root mean square (rms) of the pressure wave and is representing the energy level of the sound wave (i.e. 0.707 x peak pressure level).

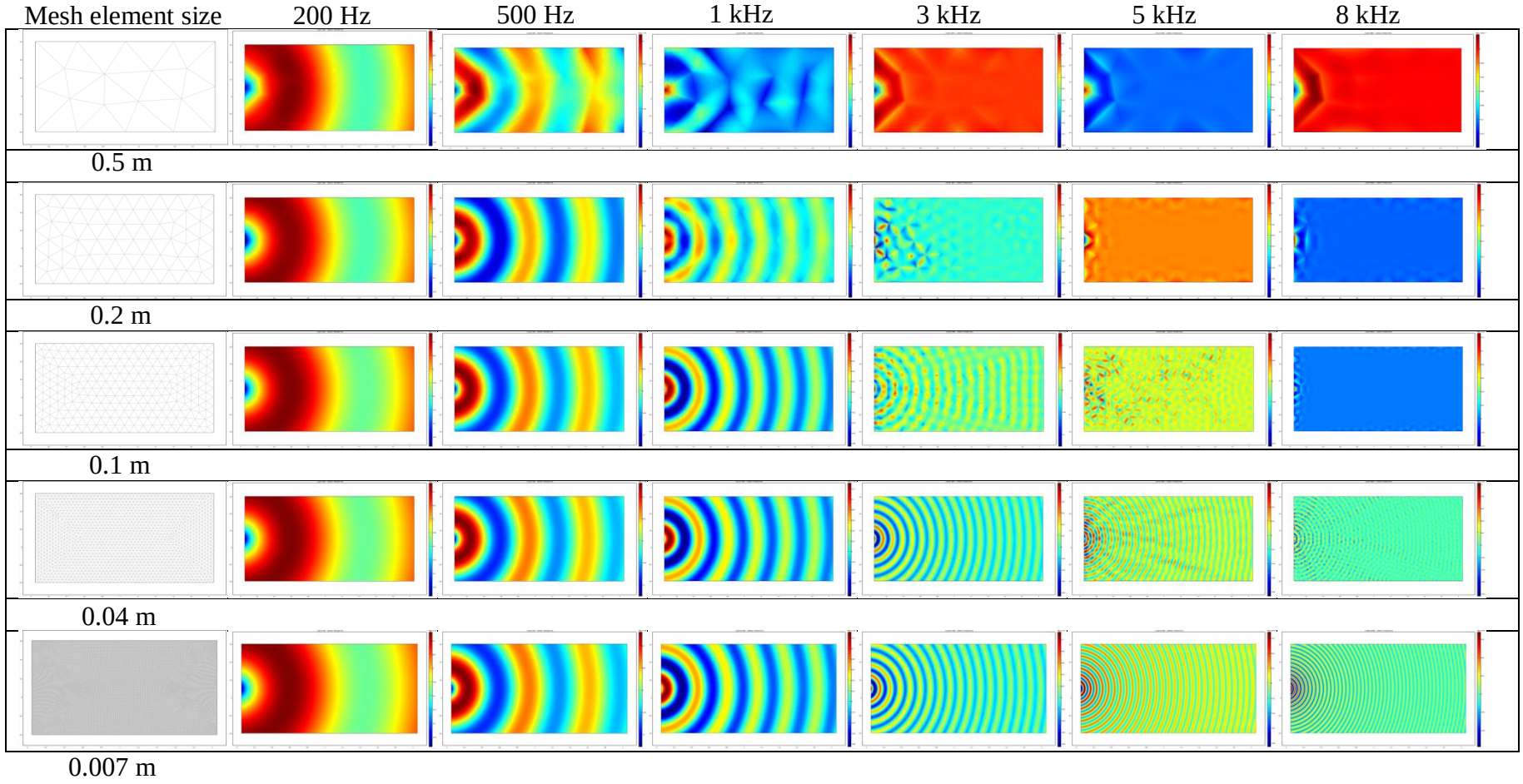

Figure 4.6: FEM predicted pressure plots for cylindrical waves with different mesh element sizes.

Inaccuracy of the results will arise when there are an insufficient number of elements. This is due to the inability to capture high-frequency (short wavelength) solutions when using a mesh with large element size which leads to the non-convergence of the solution and so the pressure map will have poor resolution at these high frequencies. This is clearly demonstrated in the FEM computed pressure maps (figure 4.6), which illustrate that solutions are unresolved at high frequencies ranges for low mesh density and that the resolution of the computed pressure map at higher frequencies improves as the mesh density increases.

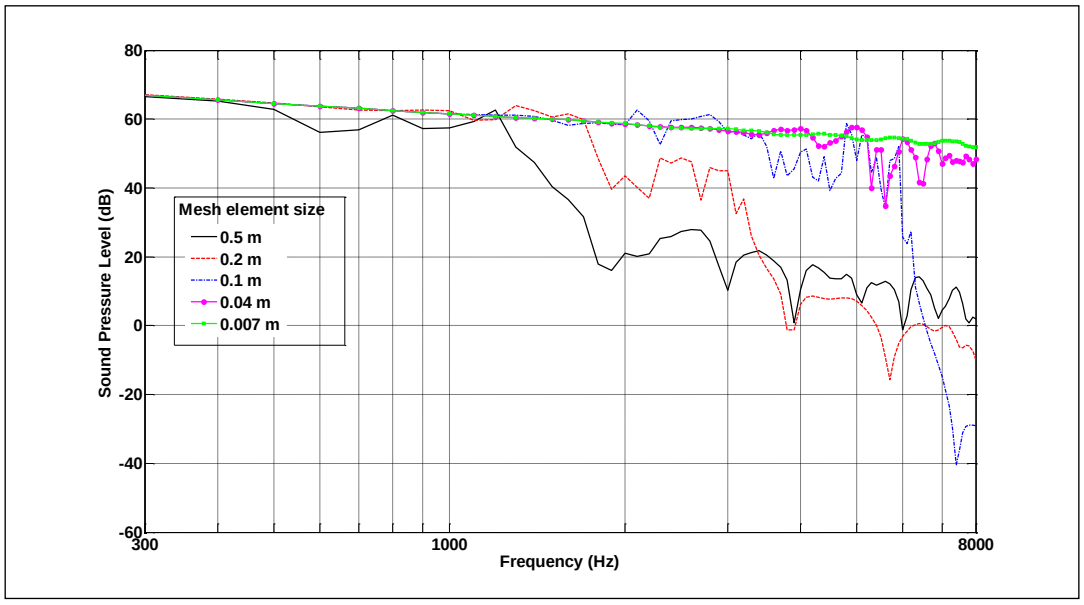

Figure 4.7: Sound pressure level spectra at single point position for FEM computations of the field due to a cylindrical wave computed using different mesh element sizes.

Figure 4.7 shows the SPL in dB for the range of frequencies. Evidently convergence problems can be observed in the high frequency range for an insufficient mesh density (i.e. Roll off from the nominal SPL value of near 60 dB. The frequency spectrum for the highest mesh density demonstrates that the cylindrical wave source has a flat frequency content.

Bearing this convergence study in mind, the maximum element size of 0.007 m will be chosen for all subsequent computational modelling in FEM. This set the convergence criterion to about 3%. This allows good convergence up to 8 kHz which is sufficient for the study of barriers subject to a traffic noise spectrum. For FEM simulations at higher frequencies, the maximum element size must be at least 6 times smaller than the shortest wavelength.

4.5) Investigation of sonic crystal performance using scatterers with different shapes

The relative ease of modelling different shapes in FEM allows the study of sonic crystals in two-dimension with different geometrical shapes of the scatterers and different lattice configurations. The first part of this section looks at predictions of the insertion loss spectra due to 7x3 arrays with a filling fraction of about 13% containing different (rigid) scatterer shapes including triangular, square and elliptical shapes, and compares them with predictions for cylindrical scatterers in an array of similar size. These studies are also performed with the similar source and receiver distances mentioned in section 4.3. A source of cylindrical waves propagating parallel to the scatterer axis and radiation boundary conditions are assumed in the FE models.

4.5.1) Triangular scatterers

Each triangular scatterer has a surface area of 0.0024 m^2 (base 0.074 m and height 0.064 m) that is similar to the surface area of a cylindrical scatterer considered previously. The array size and lattice constant are

identical with the reference sonic crystal with cylindrical scatterers. Three different orientations are studied and the pressure maps at 1.3 and 2.3 kHz are compared (see figure 4.8). Comparisons are made also with an equivalent cylindrical scatterer design (see figure 4.9).

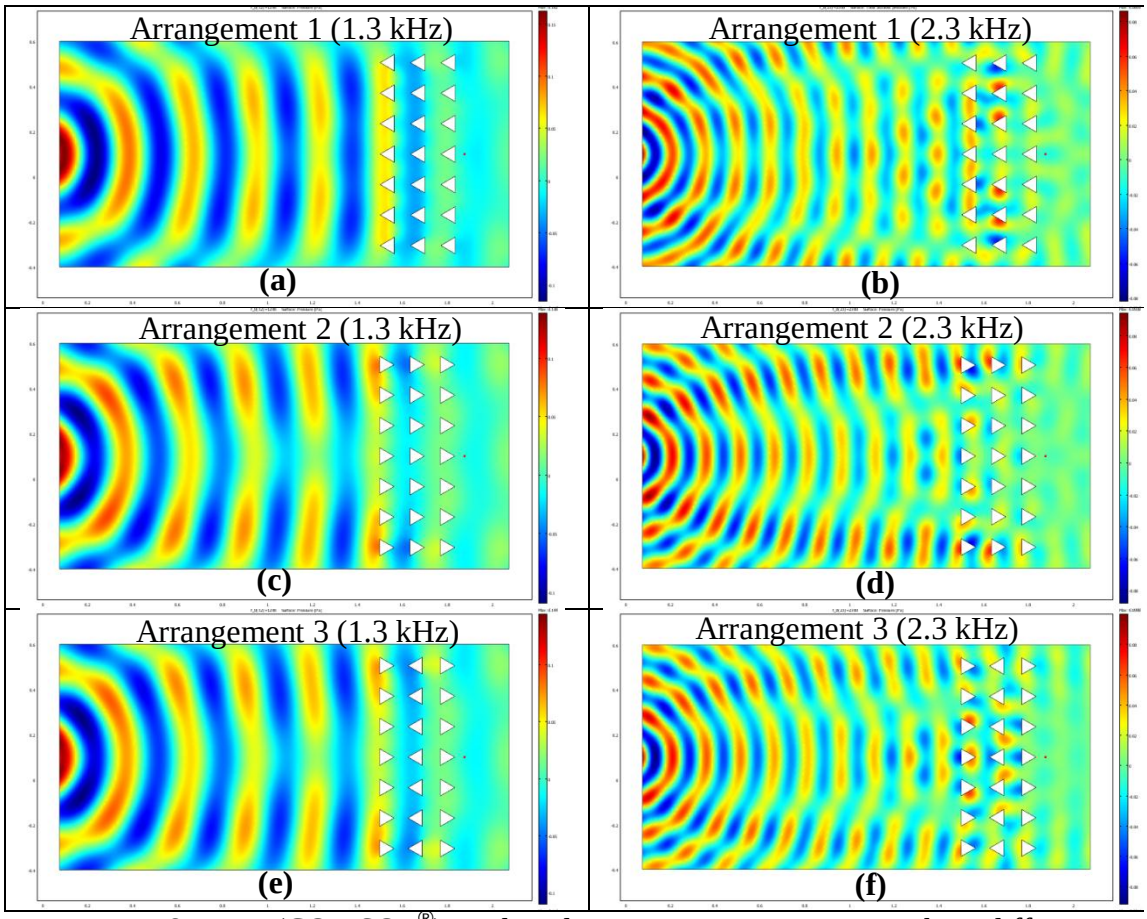

Figure 4.8: FEM (COMSOL®) predicted pressure maps comparing three different arrangements (top to bottom) and 2 frequencies pressure maps for each arrangement (left 1.3 kHz and right 2.3 kHz) of 7x3 triangular rigid scatterer arrays (square lattice) with lattice constant of 0.135 m.

Figure 4.8 shows the FEM computed pressure maps for the 3 different arrangements of 7x3 triangular shape arrays in a square lattice configuration. For all the 3 arrangements, similar scattering patterns are observed at 1.3 kHz which is the first (Bragg) band gap frequency due to the periodicity. At the higher frequency of 2.3 kHz, the scattering patterns vary from one

arrangement to the other. Notably at this frequency, higher sound energy is trapped in the middle of the array for arrangement 3.

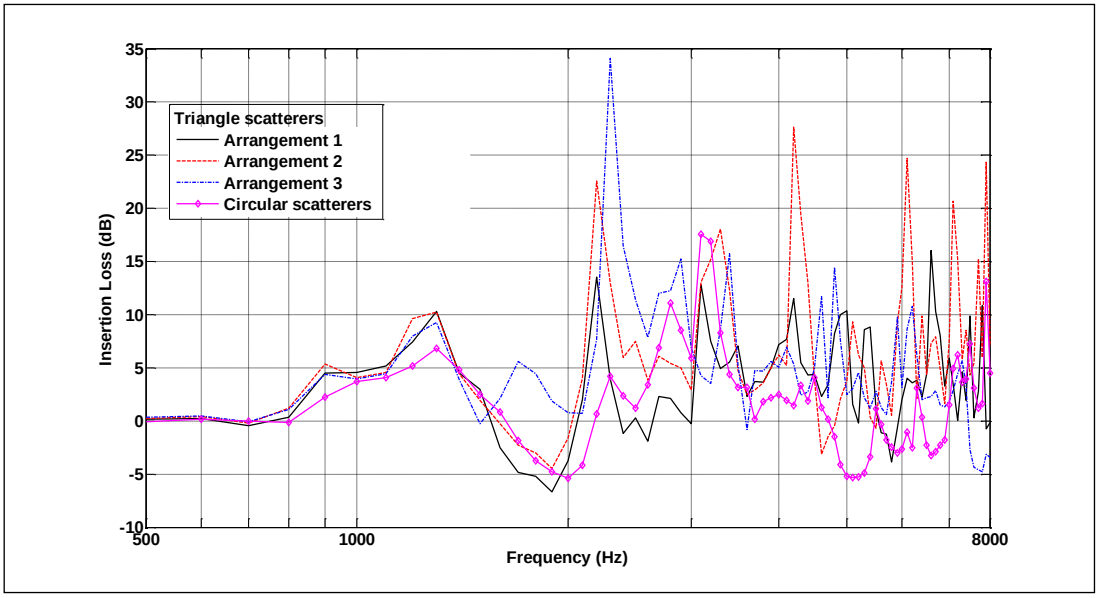

Figure 4.9: FEM predictions of Insertion Loss spectra for 7x3 square lattice arrays of triangular rigid scatterers with lattice constant 0.135 m. A cylindrical wave source is assumed and a rectangular domain is modelled as air.

Figure 4.9 shows the FEM predictions for all three triangular scatterer array compared to those for a cylindrical scatterer array of comparable size. For all triangular scatterer arrangements, the Bragg band gaps near 1.3 kHz are observed to result in nearly 3 dB higher IL than that for the cylindrical element design. Clearly, arrangement 3 gives the best overall performance as an additional band gap is observed around 1.8 kHz and the third band gap (2.3 kHz) is also higher in amplitude than those for the other designs. In addition, the amount of negative IL is also reduced especially at higher frequencies for this configuration.

4.5.2) Square scatterers

The predicted performance of arrays containing square scatterers is also studied in a similar fashion to that used for the triangular scatterer arrays. The length of the square sides is modelled as 0.049 m to obtain the same filling fraction as used for the reference cylindrical scatterer array.

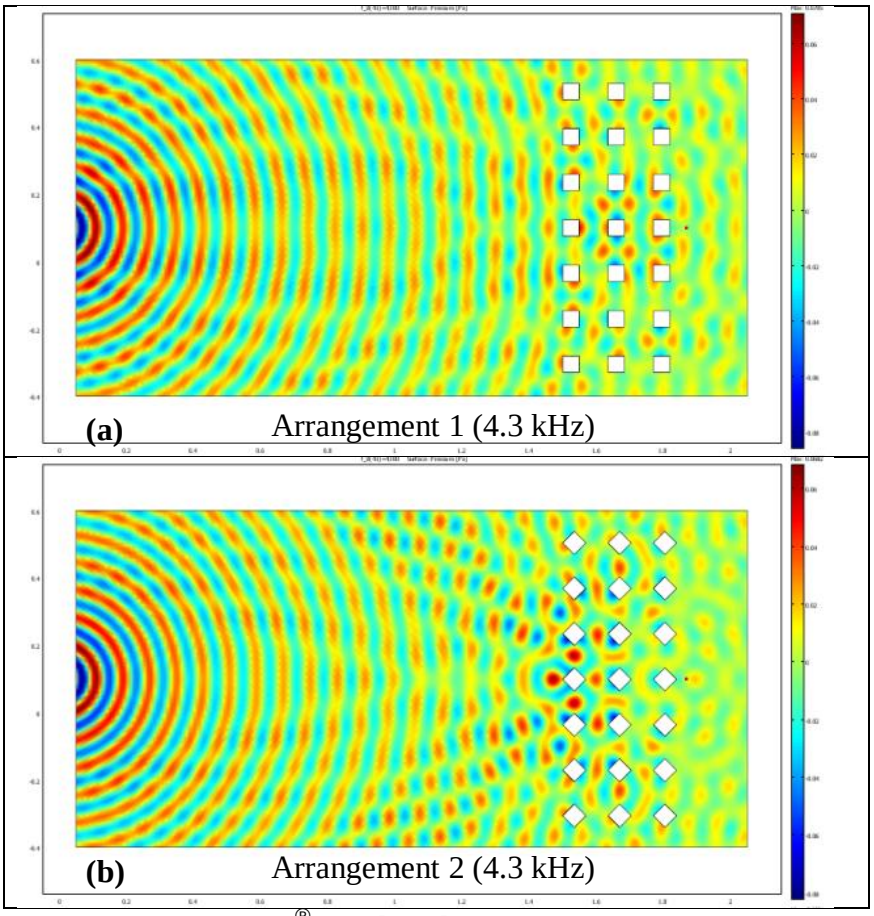

Figure 4.10: FEM (COMSOL®) predicted pressure maps comparing two 7x3 square scatterer arrangements (square lattice with lattice constant of 0.135 m) at 4.3 kHz.

Figure 4.10 shows FEM predicted pressure maps for 2 arrangements of square scatterer arrays. Cleary the scattering patterns at 4.3 kHz are predicted to be different. Higher sound energies are observed to be trapped in arrangement 2 at this frequency.

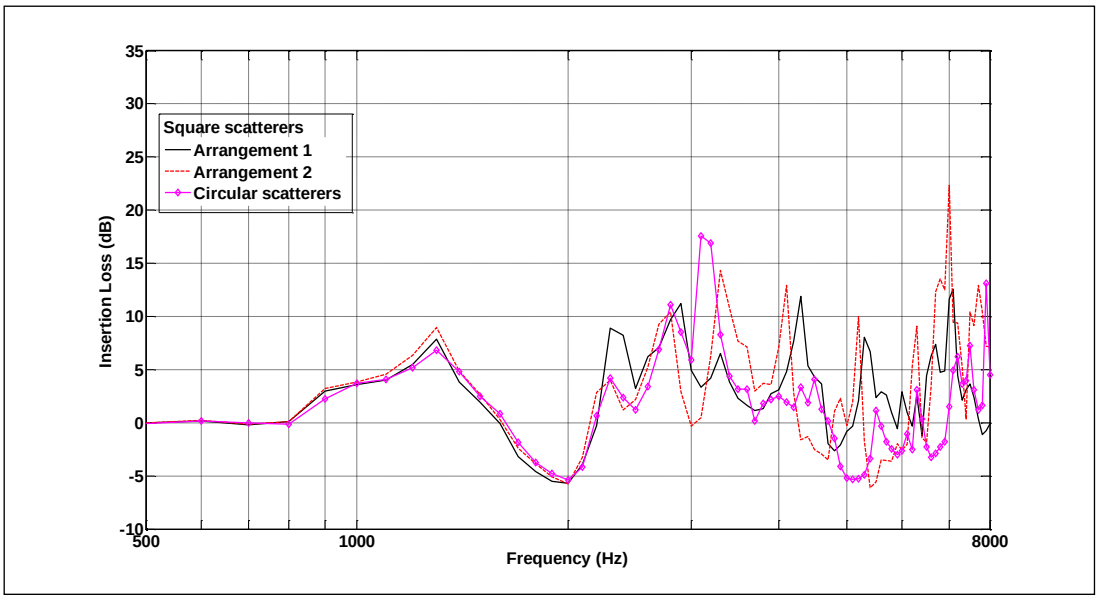

Figure 4.11: FEM predictions of Insertion Loss spectra for two arrangements of 7x3 square lattice arrays of square rigid scatterers and a reference array of cylindrical rigid scatterers with lattice constant 0.135 m. A cylindrical wave source is assumed and a rectangular domain is modelled as air.

Figure 4.11 shows the FEM predicted IL spectra for the 2 square scatterer arrangements and the reference cylindrical scatterer array. The Bragg band gaps (1.3 kHz) are predicted to be of similar size and amplitude for all the designs. The results show no significant advantage in using square scatterers.

4.5.3) Elliptical shape scatterer

Previous research on sonic crystals with elliptical shape scatterers has reported that certain configurations can vary the direction of propagation due to the geometry anisotropy of the elliptical scatterer [76]. In our model, the elliptical scatterers have a semi-major axis of 0.035 m and semi-minor axis of 0.0218 m. This geometry provides the same filling fraction as that assumed

for different scatterer shapes previously. The elliptical scatterer arrays are modelled with 3 different arrangements (see figure 4.12).

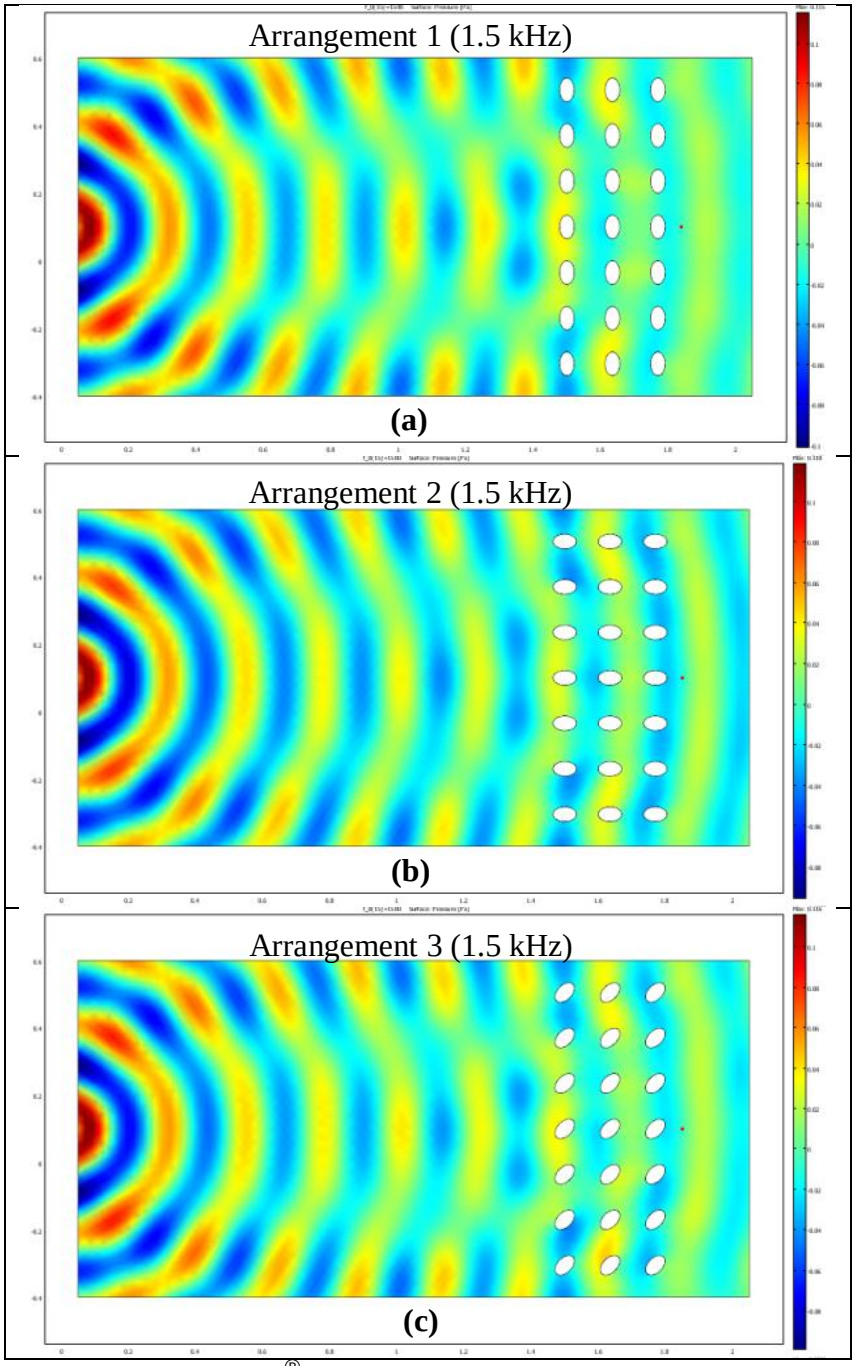

Figure 4.12: FEM (COMSOL®) predicted pressure maps for three 7x3 arrangements of elliptical rigid scatterers (square lattice) with lattice constant of 0.135 m at 1.5 kHz

Figure 4.12 shows FEM predicted pressure maps for 3 arrangements of elliptical scatterer arrays. The scattering patterns for all arrangements are predicted to be different at 1.5 kHz.

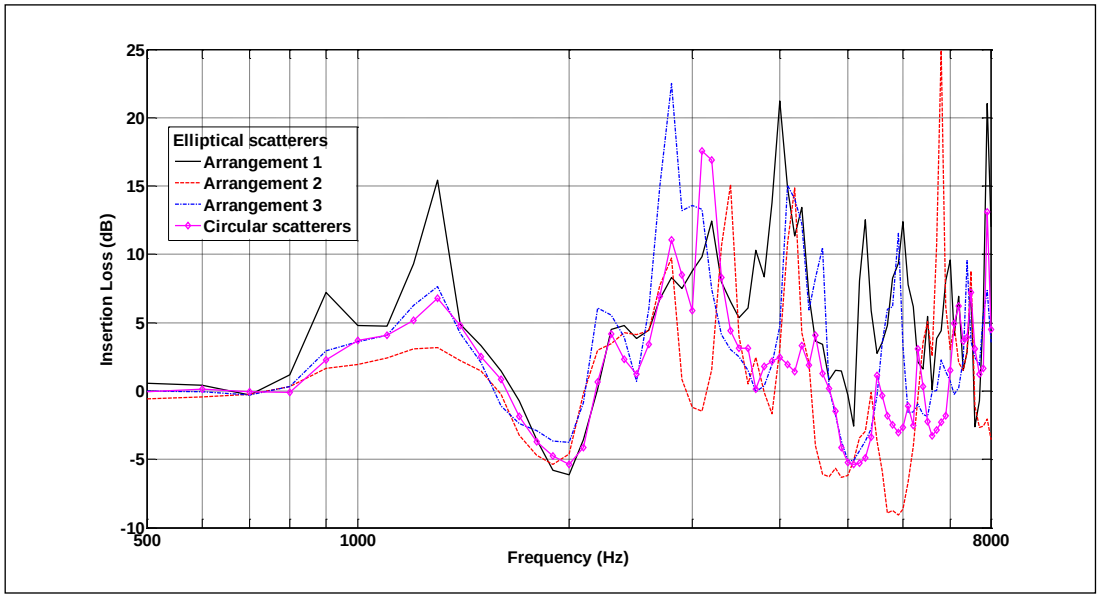

Figure 4.13: FEM predicted Insertion Loss spectra for 7x3 square lattice arrays of elliptical rigid scatterers with lattice constant 0.135 m compared with that predicted for an equivalent cylindrical scatterer array. For the FEM predictions a cylindrical wave source is assumed and the rectangular domain is modelled as air.

In figure 4.13, IL spectra for the elliptical scatterer arrays at a similar receiver position are compared with that measured for the equivalent cylindrical scatterer array. Arrangement 1 which the elliptical scatterer has its semi-major axis perpendicular to the direction of wave propagation is predicted to produce the highest amplitude Bragg band gap at 1.3 kHz. This suggests that much of the incoming wave front is blocked by the larger surface of the scatterer. Also the Bragg band gap is predicted to contain two peaks instead of one for this particular arrangement. The lowest amplitude Bragg band gap is predicted for arrangement 2 where the semi-minor axis is parallel to the incoming wave. Thus, allowing the largest transmission of

incident waves. Arrangement 3 with scatterers having 45° orientation is predicted to give comparable IL to the equivalent cylindrical array near the Bragg band gap but is predicted to offer better performance at higher frequencies.

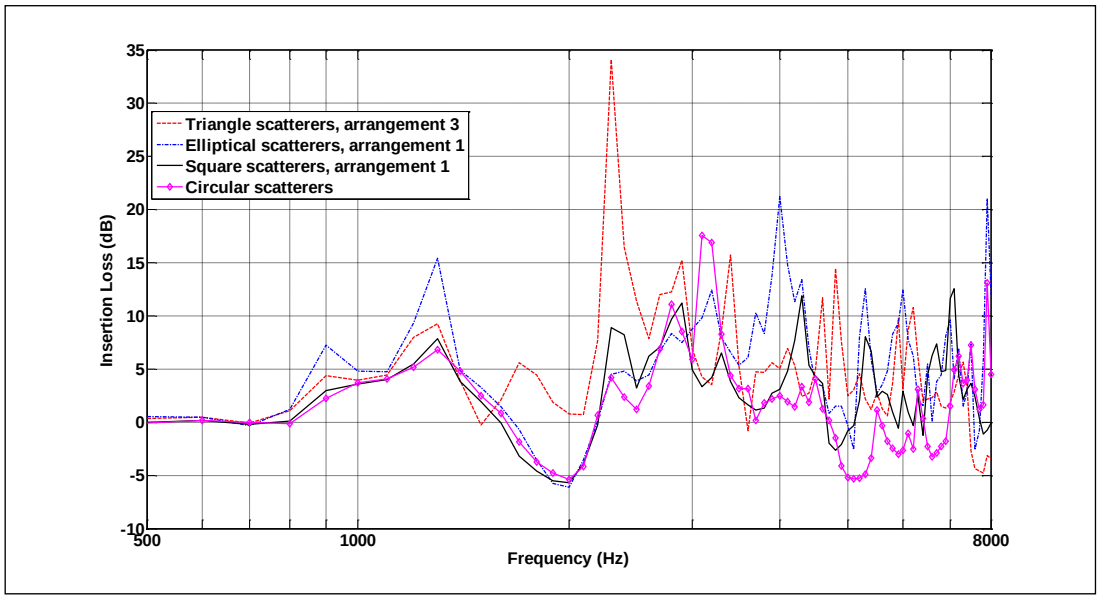

Figure 4.14: FEM predictions of Insertion Loss spectra for 7x3 square lattice arrays of the best performing triangular, square and elliptical rigid scatterer arrays compared to that predicted for the reference cylindrical scatterer array.

Figure 4.14 compares the predicted IL spectra for the best performing scatterer shape examples (circular, triangular, square and elliptical) discussed in this section. The array with triangular scatterers in arrangement 3 is predicted to reduce the focusing effect (negative IL) and that with elliptical scatterers in arrangement 1 offers the highest amplitude first Bragg band gap. Although predicted to give significant advantages in comparison with equivalent cylindrical arrays, the manufacturing cost for elliptical shapes will be much higher. For example, it costs more than £1000 for 21 3 m long elliptical scatterers made of stainless steel.

4.6) Investigation of arrays with different lattice arrangements

This section will look at using a hexagonal lattice instead of the square lattice that has been used hitherto.

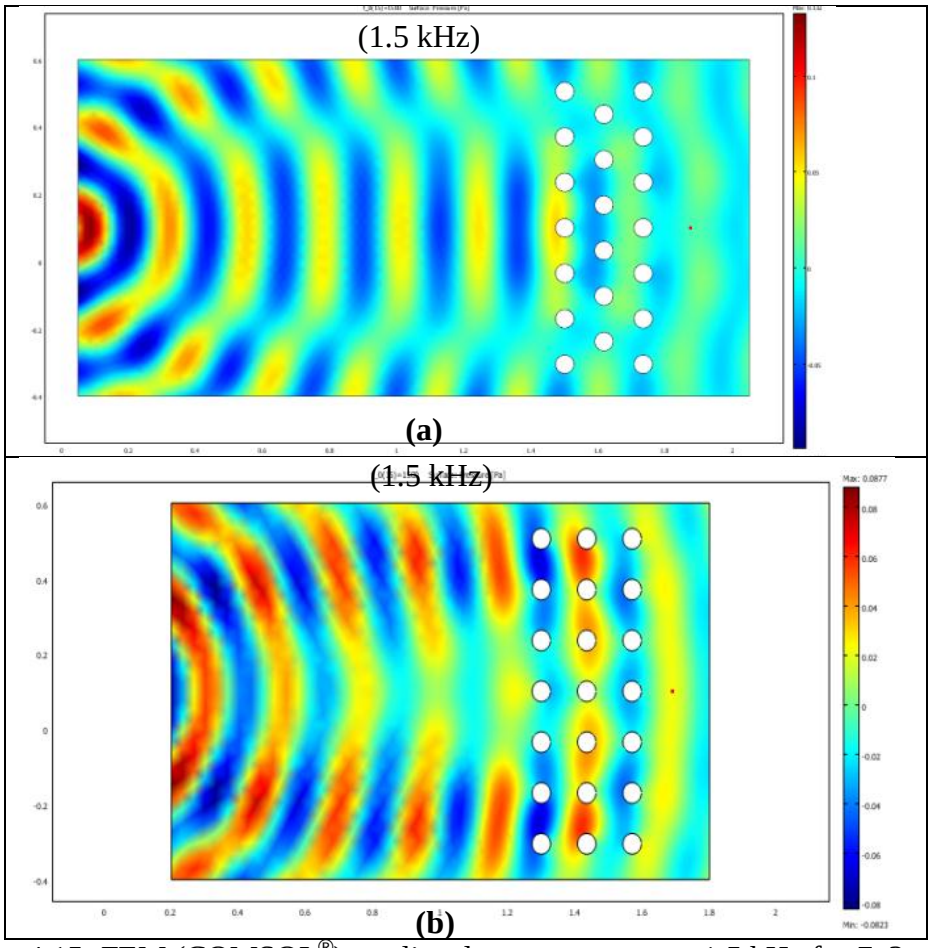

Figure 4.15: FEM (COMSOL®) predicted pressure maps at 1.5 kHz for 7x3 arrays of cylindrical rigid scatterers with lattice constant of 0.135 m (a) hexagonal lattice and (b) square lattice.

At 1.5 kHz the hexagonal lattice SC design is predicted to produce a very different pressure map compared to the square lattice shape design as shown in figures 4.15(a) and (b) respectively. This suggests that the hexagonal lattice offers an alternative method for altering the propagation of sound near the receiver point.

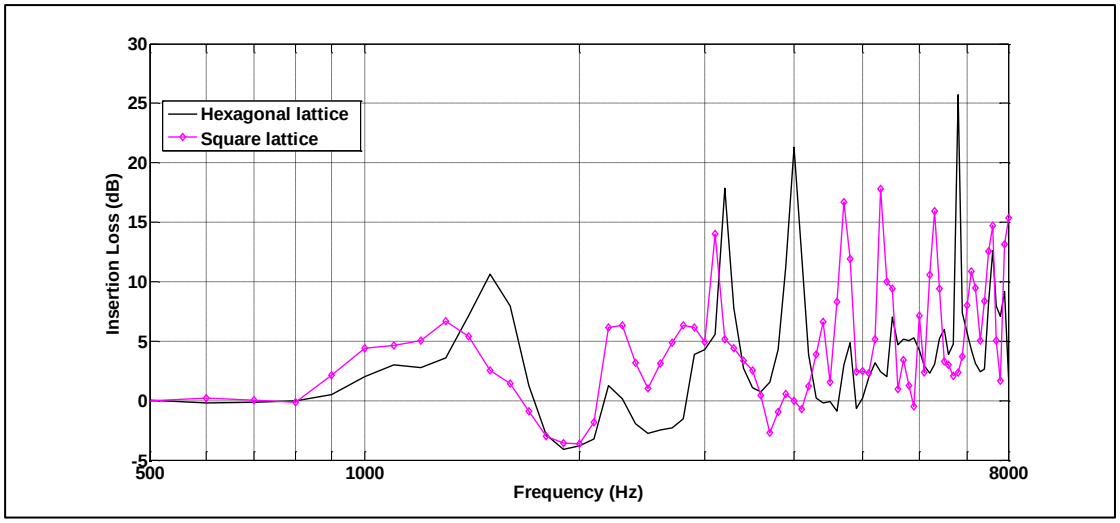

Figure 4.16: FEM predictions of Insertion Loss spectra for 7x3 hexagonal and square arrays of cylindrical rigid scatterers with lattice constant 0.135 m. FEM prediction are performed with cylindrical wave source and a rectangular domain modelled as air. The cylindrical wave source is located at 1.5 m away from the front face of the array and the receiver is positioned 0.05 m from the nearest face of the array but on the opposite side of the source.

In figure 4.16, the predicted IL spectra of 7x3 hexagonal and square lattice SC designs (lattice constant 0.135 m) are compared. For the hexagonal lattice array, the first Bragg band gap is shifted up to a higher frequency (near 1.5 kHz) compared to that for the square lattice array. For a hexagonal lattice array, the first Bragg band gap formula should be modified from that for a square lattice array (PWE chapter, equation 2.13) i.e.

$$f_{Bragg\_Hex} = \frac{c_l}{\sqrt{3}L}, \qquad \textbf{(4.8)}$$

where c_l is the speed of sound in air and L is the lattice constant.

For these configurations taking account of the scatterer size and lattice constant distance, a hexagonal lattice design offers a better IL between 3.5

and 7 kHz (based on a single receiver position). However as a traffic noise barrier the square lattice design could possibly be better.

4.7) Perfectly Matched Layers (PML)

The capability of emulating the Sommerfeld radiation condition, which requires that outgoing wave propagate out towards infinity and therefore the absence of reflection from the boundaries (i.e. creating an unbounded modelling enviroment), is critical for any numerical code concerned with the solution of wave problems. Normally, in FEM computations, the outer boundaries of the computational region are subjected to a radiation boundary condition and this has been used to treat these boundaries in the earlier sections. An alternative method is to implement Perfectly Matched Layers (PML) at these boundaries. This approach was first introduced by Bérenger [146] in 1994 for electromagnetic waves. It is commonly used for simulating wave problems with open boundaries. A PML is an artificial (non-physical) absorbing layer in which the wave equation has been modified with an anisotropic damping, which increases with distance in the direction perpendicular to the interface with the physical domain (see figure 4.17). The result is that waves entering the PML are absorbed only in the outgoing direction, while the wave components tangential to the interface between the PML and physical domain remain unaffected. The key property of a PML that distinguishes it from an ordinary absorbing material is that it is designed so that waves incident upon the PML from a non-PML medium do not reflect at the interface. The main advantages of the PML over radiation boundary

conditions are the relative ease of implementation using a complex coordinates scaling [77]. Thus making it possible to minimise the size of the computational domain and this in turn reduces the computational demands.

The implementation of a PML for computing the pressure field due to a 7x3 array of circular scatterers with similar setup to that investigated in section 5.3 has been studied. The incident waves are modelled as plane waves due to the reduced size of the domain.

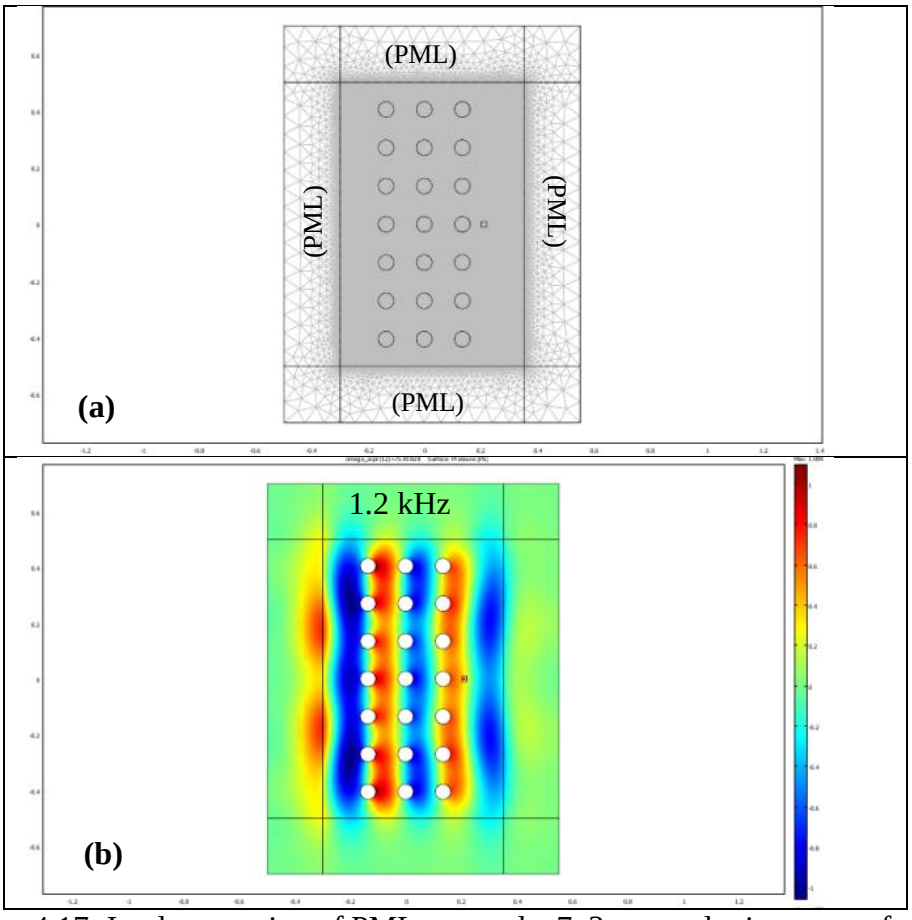

Figure 4.17: Implementation of PMLs around a 7x3 square lattice array of circular scatterers (a) location of PMLs and (b) FEM-computed pressure map at 1.2 kHz.

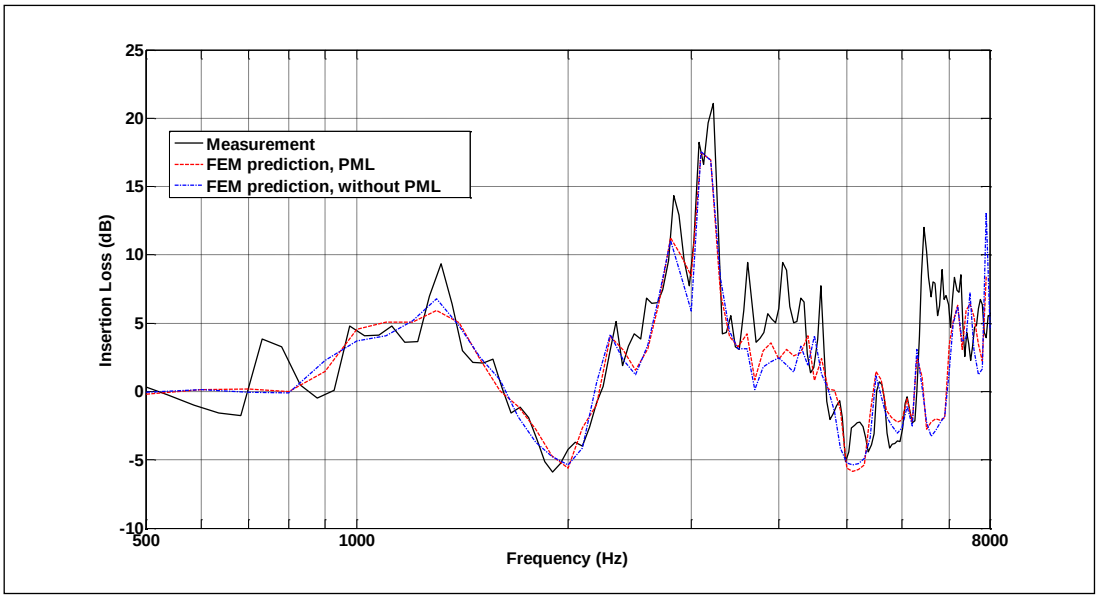

Figure 4.18: FEM predictions (with and without PML) compared to laboratory measurements of Insertion Loss spectra for a 7x3 square lattice array of circular rigid scatterers with a lattice constant 0.135 m.

As shown in figure 4.18, the FEM predicted IL spectra with and without PML implementation are in fair agreement with the laboratory data. The time taken to solve the problem using PML is 402.41 s which is 0.37 times faster than that taken when using radiation boundary conditions with the maximum element size (see table 4.1).

Chapter 5

Measurement Techniques

5.1) Introduction

It is important to validate any hypothesis and/or prediction by performing a relevant experiment. The first experimental evidence of the acoustical properties of a sonic crystal in air was performed in 1995 by Martinez-Sala *et al* [20]. The authors measured the transmission properties of a finite periodic minimalist sculpture in outdoor by Eusebio Sempere in Spain (see figure 1.4). It was observed that such periodic structures have similar acoustical characteristics to electromagnetic properties of solid crystalline structures. Subsequently, research has resulted in the development of improved experimental methods for checking theoretical results. The experiments reported in this Chapter were carried out either in an anechoic laboratory or outdoors at the Open University's noise barrier test site and at Diglis weir near Worcester.

To measure or analyse an acoustic waveform which consists of a variation in pressure as time passes, it is usual to generate an electrical analogue of the pressure variation by means of an input transducer (i.e. microphone). Likewise to generate a sound, we also start with an electrical waveform and use an output transducer (i.e. loudspeaker) to convert it into a pressure change. Under the assumption of source and receiver immobility, the acoustic space in which they are placed can be considered as linear and

time invariant and characterised by a system response $h(t)$ [83]. A common method to measure the system response is to generate an input signal $\bar{x}(t)$ using a PC (see figure 5.1). This is converted to a continuous-time signal $\bar{x}(n)$ by a Digital to Analogue Converter (DAC) and fed to the system under test with the unknown impulse response $\bar{h}(t)$. The resulting output $\bar{y}(t)$ is sampled to obtain $y(n)$ through an Analogue to Digital Converter (ADC) which is used together with the known signal to determine the sampled impulse response $h(t)$. It is well known that the Signal-to-Noise Ratio (SNR) can be improved by taking multiple averages of the measured output signal before the start of impulse response deconvolution process. In this chapter, two different experimental acquisition systems for both laboratory and outdoor measurements will be described.

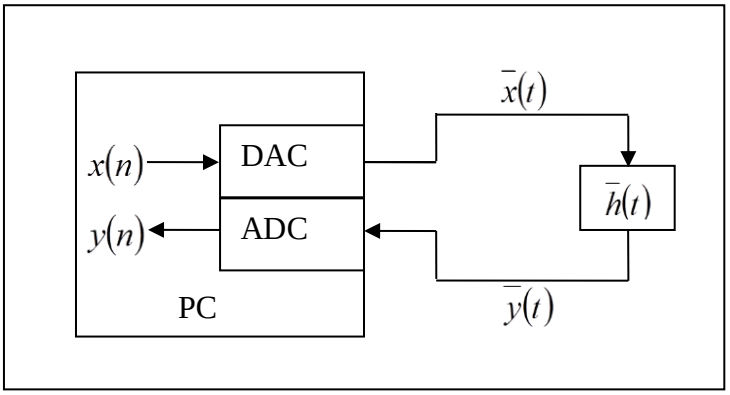

Figure 5.1: Flow diagram for a typical impulse response measurement.

5.2) Laboratory measurments using Maximum-Length Sequence System Analyzer (MLSSA).

5.2.1) Introduction to MLSSA

Acoustical impulse response measurements using the Maximum-Length Sequence (MLS) technique were first proposed by Schroeder in 1973 [84]. MLSSA can measure and analyze many types of linear systems and is widely used for audio and acoustics measurements [85, 86 and 87]. A MLS signal is a type of pseudorandom binary sequence which, unlike white noise, is deterministic and periodic yet still retains most of the desirable characteristics of white noise (i.e. broadband and flat response). MLS may be generated computationally by employing linear feedback shift registers as illustrated in figure 5.2. In contrast with a conventional dual channel analyzer, MLSSA is single channel but, given the periodic nature of the MLS, a single time domain circular cross-correlation calculation can recover the complete system impulse response. Thus, effectively it can do the work of a dual channel analyzer with the advantage of doubling the useful bandwidth and significant reduction in cost [88].

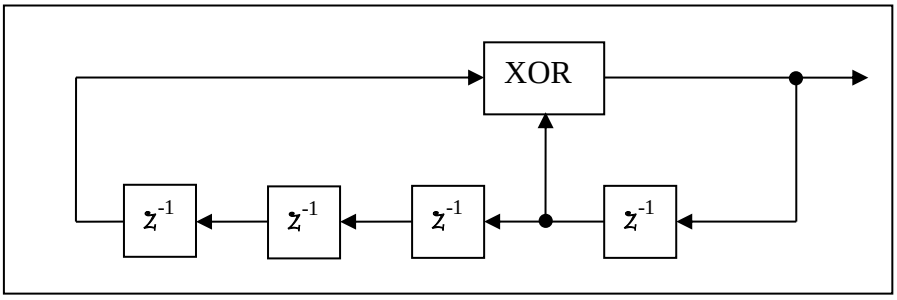

Figure 5.2: Linear feedback shift register for generation of a MLS (of length 2^4 - 1= 15) signal.

The number of samples of one period of an m order MLS signal is $L_{MLS} = 2^m - 1$. A 16-th order MLS corresponding to 65535 samples is used in our measurement. A system loopback test is performed to determine the response of the MLS signal by connecting the analogue output to the analogue input using an audio patch cable as shown in figure 5.3. A single measurement sequence is taken whereby MLSSA acquires 65535 samples and computes the first 16384 points of the impulse response. The time signal which is a result of the impulse response of MLSSA's anti-aliasing filter (Chebyshev) is shown in figure 5.4. This displays the unprocessed data in a similar manner to an oscilloscope. Subsequently, the filter's transfer function is obtained by a Fast Fourier Transform (FFT) computation on the measured impulse response. A FFT with 1024-points is performed to obtain the magnitude of the Chebyshev filter's transfer function. The magnitude is reasonably flat up to about 25 kHz and then sharply rolls-off (see figure 5.5).

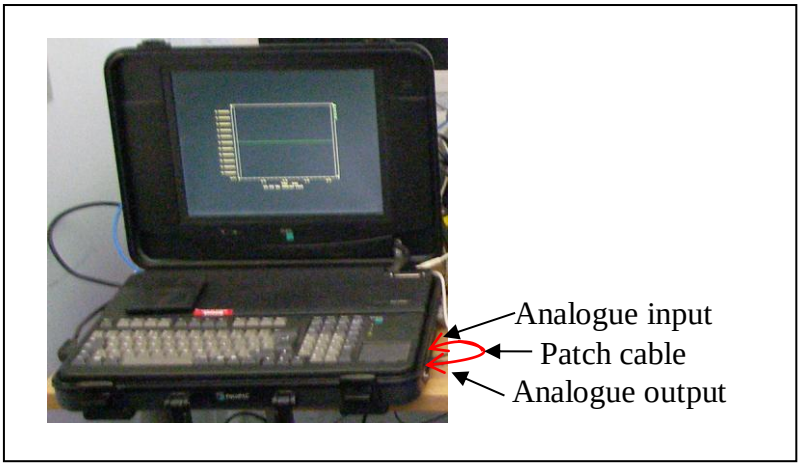

Figure 5.3: MLSSA system with audio patch cable connecting analogue output to input.

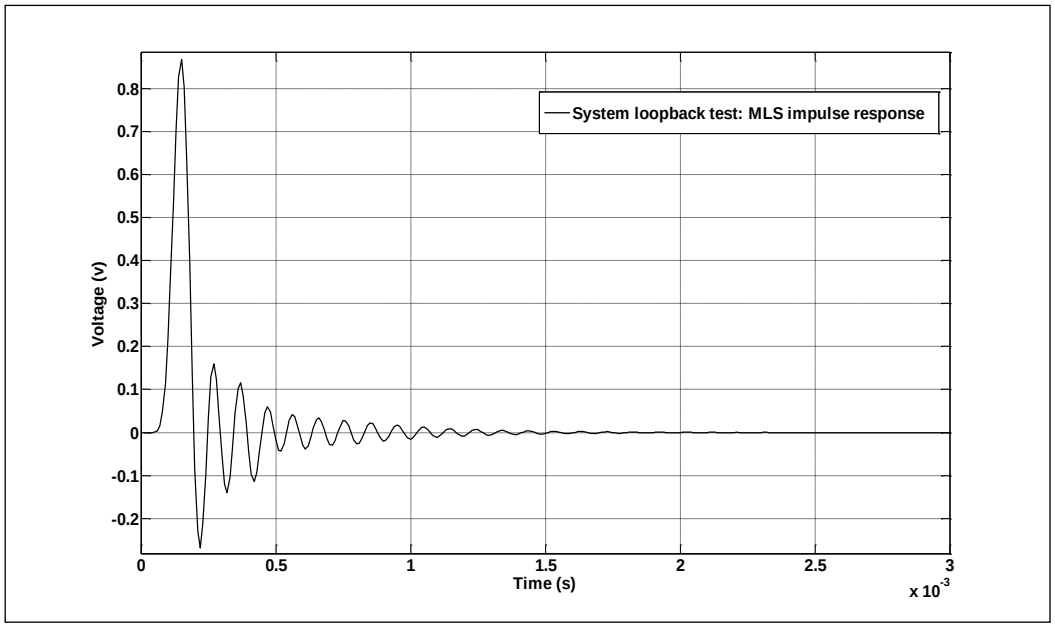

Figure 5.4: System loopback test - MLS time signal.

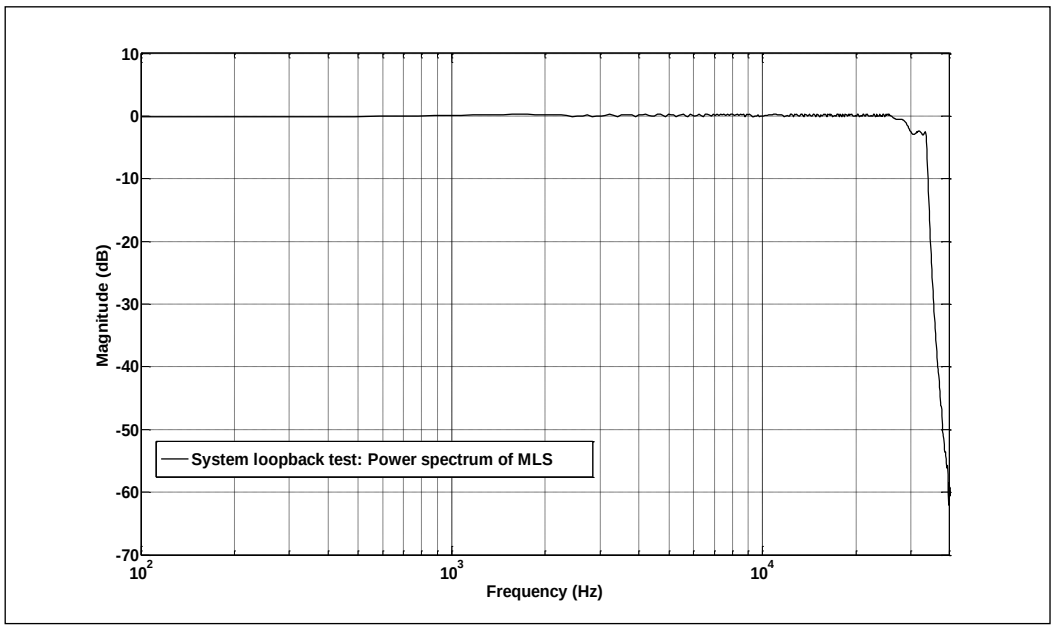

Figure 5.5: Transfer function for system loopback test - MLS power spectrum.

Some ripples occur in the power spectrum (see figure 5.5) which indicates that the Chebyshev filter transfer function is not perfectly flat. Considering the small amplitudes of the ripple (about ±0.3 dB), such deviation from flatness is normally due to the electronic production tolerance. This system loopback test serves as a functional check on the MLSSA system before performing the real measurement

5.2.2) MLSSA setup, data acquisition and analysis in laboratory

For acoustical measurements, specially constructed rooms called anechoic chambers can be designed with perfectly absorbing walls (in principle) and thereby prevent reflections of sound waves [83]. They are also insulated from external sources of noise which could influence the laboratory results. Thus, the combination of these two factors can simulate a quiet open space of infinite dimensions. The capability of the anechoic chamber depends largely on its size, the frequency of the signal used and also the size of the object being tested. Scaled models are sometimes used to represent large objects and corresponding tests use higher frequencies. The laboratory results shown in this work have been carried out in an anechoic chamber and far away from any reflecting surfaces. The size of the anechoic chamber used to conduct the experiments is approximately $3 \times 3 \times 3$ m. To prevent unwanted reflection from the human body or large measuring equipments, a small hole is drilled on one side of the wall to allow cables to be routed through from the exterior of the chamber. This allows the data acquisition to be performed remotely outside the chamber. Rock wool and polyurethane foam are used to seal up the hole after laying the cable in order not to jeopardise the anechoic conditions (see figure. 6.17(a)).

Having tested the MLSSA system electronically using the loopback test performed in section 5.2.1. The acoustic measuring system is completed by connecting up with the acoustic transducers and the associated amplifiers to perform the actual measurement (see figure 5.6). The system analogue

output of the MLSSA is connected to a Cambridge Audio stereo A1 amplifier (power output of 25 Watts) to drive the Brüel & Kjær (B&K) type 4295 point source loud speaker. Such sound source is known to be omnidirectional. The size of the orifice and the shape of the loud speaker have been carefully engineered to radiate sound evenly in all directions. A B&K type 4189-B-001 - ½ inch free-field microphone with type 2669-B preamplifier is then connected to a battery operated B&K type 5935 dual channel microphone power supply (which also has amplifying function) for the measured signal to feedback to the MLSSA system through the analogue input. Normally the microphone can only extract tiny amounts of energy (typically microampere of current) from a sound wave and therefore to increase the signal to a useable level, a high-impedance amplifier must be used. It is best to avoid reflections or, more precisely, to make sure they're very low in comparison with the wanted signal. A loudspeaker tripod, microphone holder and clamps are necessary to hold the loud speaker and microphone in place inside the chamber. Strictly speaking, it is crucial that any reflecting object should be placed as far from the set-up as possible. Care was taken to avoid unwanted reflection from these objects interfering with the result of the experiment by placing or orientating them far away from the acoustic test space or by covering them with sound absorbing material (see figure 6.17(a)). Although the anechoic chamber was potentially fully anechoic (having a mesh floor grille over absorbent material) these were found to interfere with the measurements. The influence of the metal mesh floor grille is discussed in section 5.2.5. The geometries used with specific scatterers (i.e. rigid, elastic shell, Split Ring Resonator (SRR) and composite cylinder) in the laboratory measurements are

stated in the associated chapters. Supports for the 2 m long rigid and SRR cylinder arrays were provided by holed wooden boards at the top and base of the array. Figure 5.7(a) shows the bottom plate. A similar plate was used as the top support. For the elastic shells, a bolt and nut securing systems was used to mount the cylinders in place (see figure 5.7(b)). The 2 m long latex sheets have been formed into cylinders with various outer diameters and wall thicknesses as specified in chapters 6 (elastic shell) and 7 (composite). The elastic shells were created by overlapping the edges of the latex sheets by a few millimetres and gluing them together. To maintain their shape and vertical orientation, the latex cylinders were slightly inflated above atmospheric pressure through a common pipe connecting to a small pump.

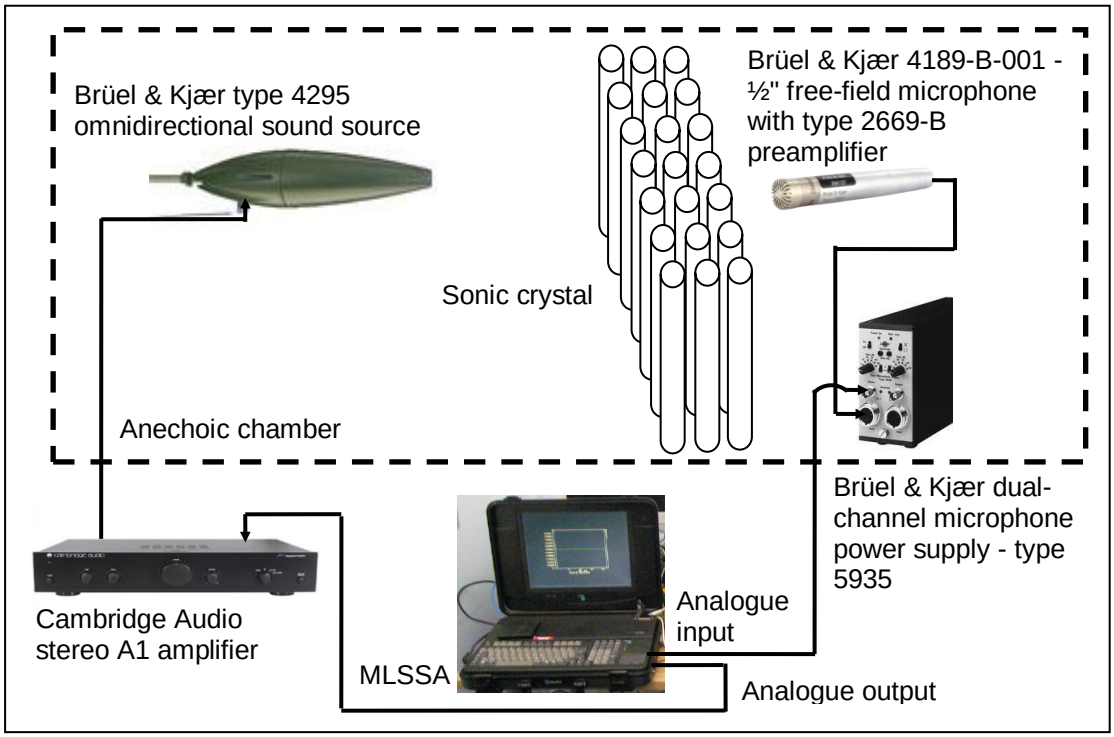

Figure 5.6: Laboratory measuring system incorporating MLSSA.

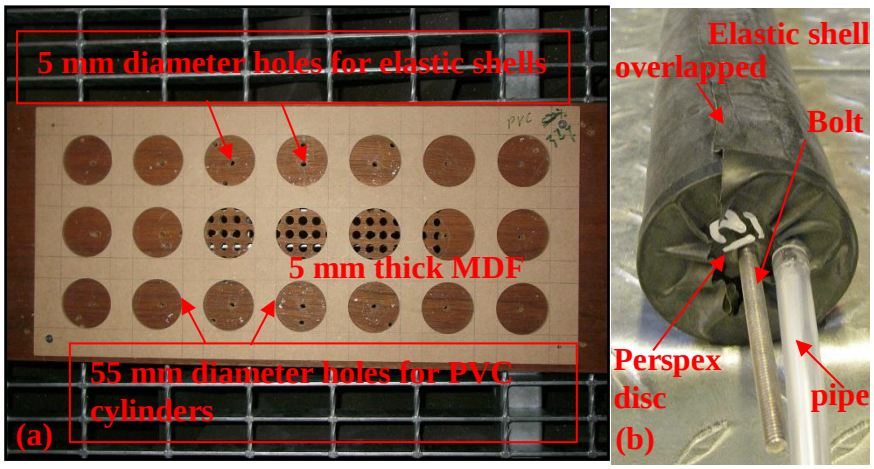

Figure 5.7: (a) Supporting base plate for 7x3 arrays of PVC or elastic cylinders. 55 mm diameter holes for PVC cylinders. 5 mm diameter holes for elastic shell using bolt and nut securing system. (b) Lower end of an elastic shell showing plastic pipe for air inlet and mounting bolt.

The direct sound field measurement method that has been used is closely related with that described in BS EN 1793-6 [89]. During the array measurements, the receiver microphone was positioned 50 mm from the nearest face of the array but on the opposite side of the source. Both source and receiver were 1.2 m above the floor of the chamber. The loud speaker was placed between 1.5 m and 1.63 m away from the array, such that the source-receiver axis was normal to the array orientation (see figure 5.8).

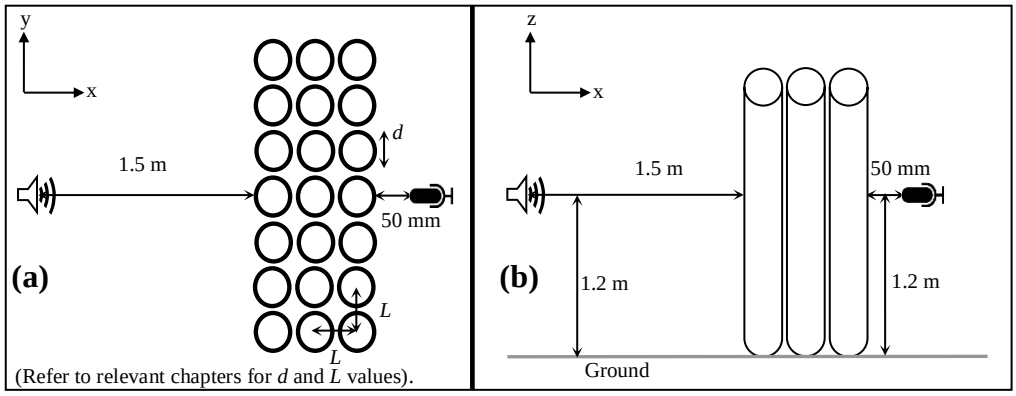

Figure 5.8: (a) Plan view of the source, receiver and array in the laboratory measurements at normal incidence (b) the corresponding side view. Refer to chapters 2, 3, 4, 6 and 7 for the outer diameters and lattice constants used.

The input signals are first passed through the fixed analogue Chebyshev filter implanted in MLSSA system to remove any signals with frequency component beyond the selected range which is 10 kHz in our case. The sampling rate was chosen to be greater than twice the maximum frequency contained in the signal to be measured. This Nyquist frequency is crucial to accurately reconstruct the measured signal. To improve the SNR using the MLSSA system, 16 time averages were carried out for each measurement. The time required for each measurement was very short, only a few seconds were necessary to obtain the impulse response for the acoustic test space (see figure 5.8). Example plots of the time signals corresponding to the direct field and total transmitted field through a sonic crystal are shown in figure 5.9. In contrast with figure 5.4, the direct field signal looks different to that in figure 5.4 since the complete system response is influenced by factors such as the physical setup, responses of loudspeaker and microphone. For the post-processing operation, a half Blackman Harris filter was used to frame the time signal and window out the unwanted reflections. An FFT was applied to decompose the time domain signal to yield

its complex frequency components for frequency analysis with a frequency resolution of 48 Hz. The frequency resolution could be improved by using a higher number of FFT points. In our case, we are interested in the magnitude of the measured signal (see figure 5.10). Insertion loss spectra have been calculated by subtracting signals received with (total transmitted field) and without (direct field) the cylinder array present as depicted in figure 5.11. The measurement procedure here described is based on ratios of the power spectra of signals extracted from impulse responses sampled with the same equipment in the same place under the same conditions. Therefore, calibration of the measurement chain with regard to the sound pressure level was not required.

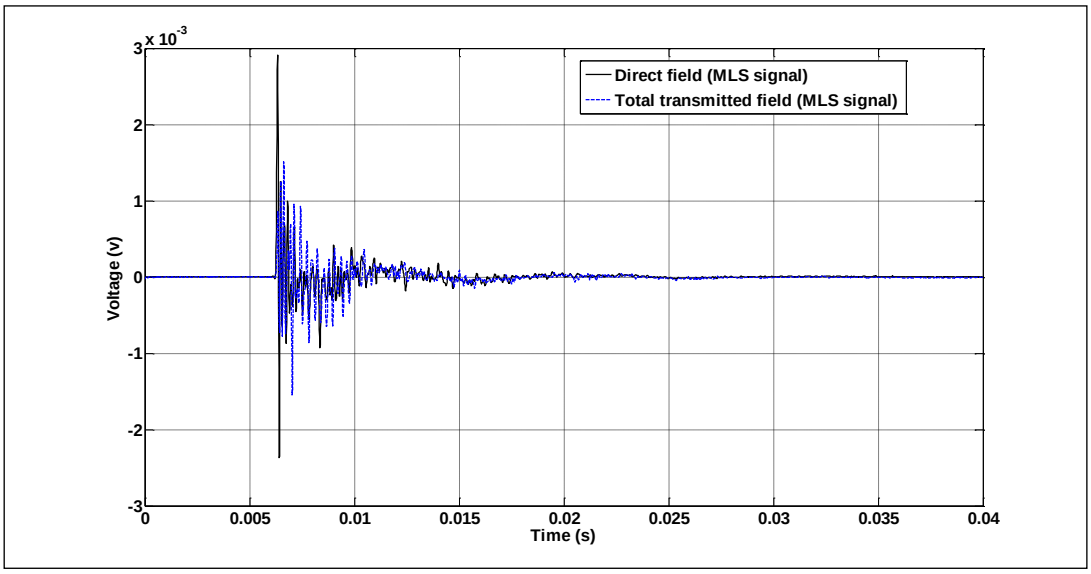

Figure 5.9: MLSSA time signals for direct and total transmitted fields.

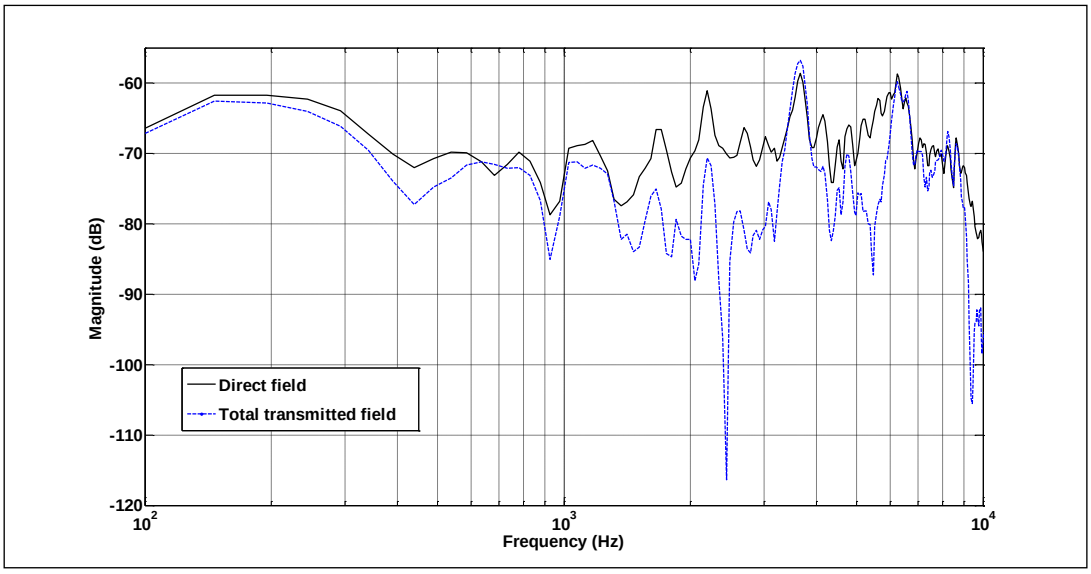

Figure 5.10: MLSSA Frequency spectra for direct and total transmitted fields.

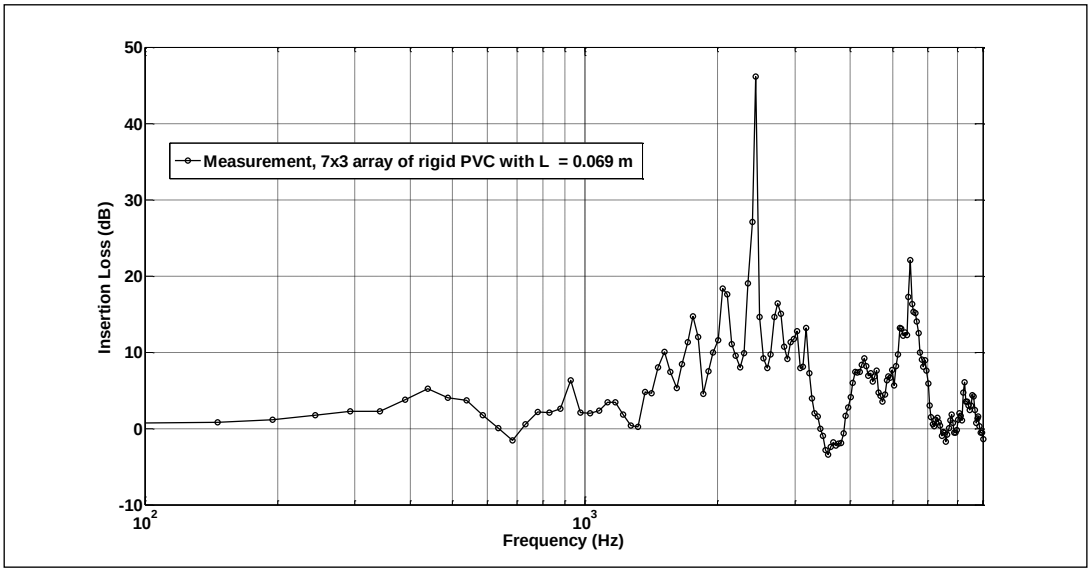

Figure 5.11: Insertion Loss (IL) spectrum using MLSSA of 7x3 square lattice arrays of rigid PVC scatterers of outer diameter 0.055 m and lattice constant 0.069 m. Frequency resolution at 48 Hz.

5.2.3) Influence on the difference of windowing size for signal post processing.

As discussed in section 5.2.2, a finite length of the input signal was chosen during the post-processing. A test was carried out to determine how truncation of the time domain signal by the size of the window could affect the power spectrum. The time domain signal of the total transmitted signal (see

figure 5.9) was used for this test. The starting of the signal is fixed at 6.2 ms and the end signal was varied from 10, 15, 20 and 30 ms corresponding to window sizes of 3.8, 8.8, 13.8, and 23.8 ms respectively. The resulting power spectra look different for each signal (see figure 5.12) in the low frequency region, this is especially so for the smallest window size in which a dip appears at 1.7 kHz. Such a phenomenon could be due to spectral leakage resulting from sampling discontinuities (i.e. integer number of periods are not sampled by the FFT. This causes the energy contained in the signal to 'leak' from the signal frequency points into adjacent frequency points [90] (see figure 5.12). This indicates that spectral leakage can occur if the length is not properly chosen. Also worth noting is that the true frequency resolution or lowest accurate frequency of a measurement is at best equal to 1/T where T is the duration of the measured signal used in the FFT calculation. This gives lowest accurate frequencies of 263, 113, 72 and 42 Hz respectively for the window sizes of 3.8, 8.8, 13.8 and 23.8 ms. For the laboratory measurements reported in this thesis, window sizes of at least 20 ms have been used.

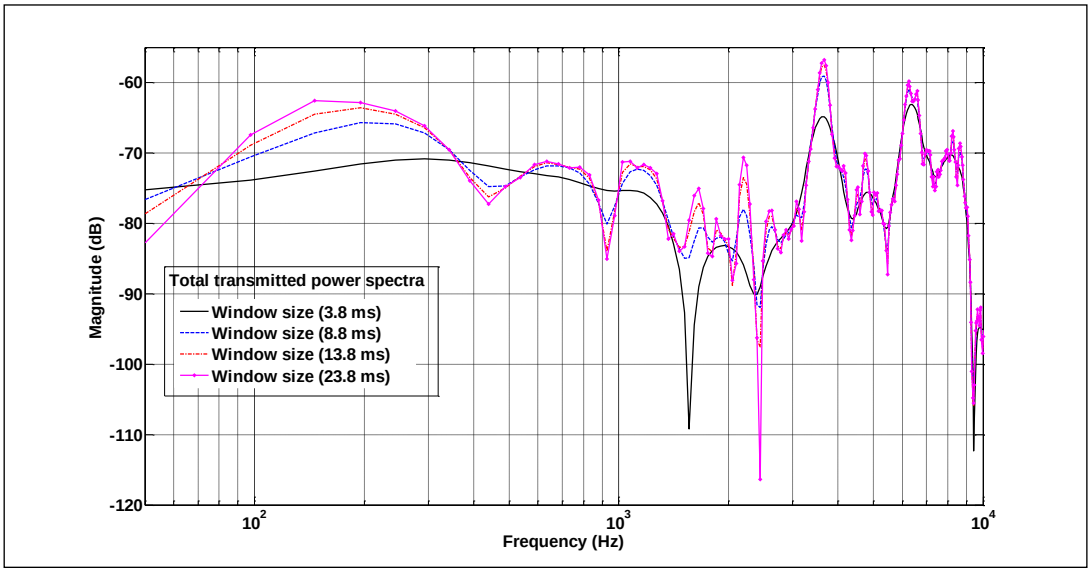

Figure 5.12: Power spectra for different window size taken in calculating the FFT for total transmitted fields.

5.2.4) Influence on the effect of different window functions for signal post processing.

The FFT computes the frequency spectrum from a block of sample of the input to which is an integral extending over time. The implicit assumption is made that the measured signal contained in the sampled block is repeated throughout time without any discontinuity. This is difficult to achieve in practice and window function is commonly implemented to reduce the effects of spectral leakage due to such discontinuity. The basis of a window function is to assign a weighting coefficient to each of the input signal and thus reducing those samples that cause spectral leakage. In this section, two types of window functions, namely the rectangular and half Blackman Harris were tested. Half Blackman Harris is known to exhibit less spectral leakage than rectangle window function [88]. A 4 term half Blackman Harris give excellent side band rejection [83]. The comparison is made with both the windows having the same size of 20 ms. In figure 5.13, the IL spectra shown are calculated from the same direct field and total transmitted field signal (see figure 5.9) for the two different window functions. The IL spectra for both windows function does not differ much except for the spike at 2.5 kHz for the windowing method with half Blackman Harris. This peak coincides with the Bragg centre frequency for such lattice constant and since the spectrum does not differ much for other frequency components, half Blackman Harris window function is chosen for all the data processing in MLSSA.

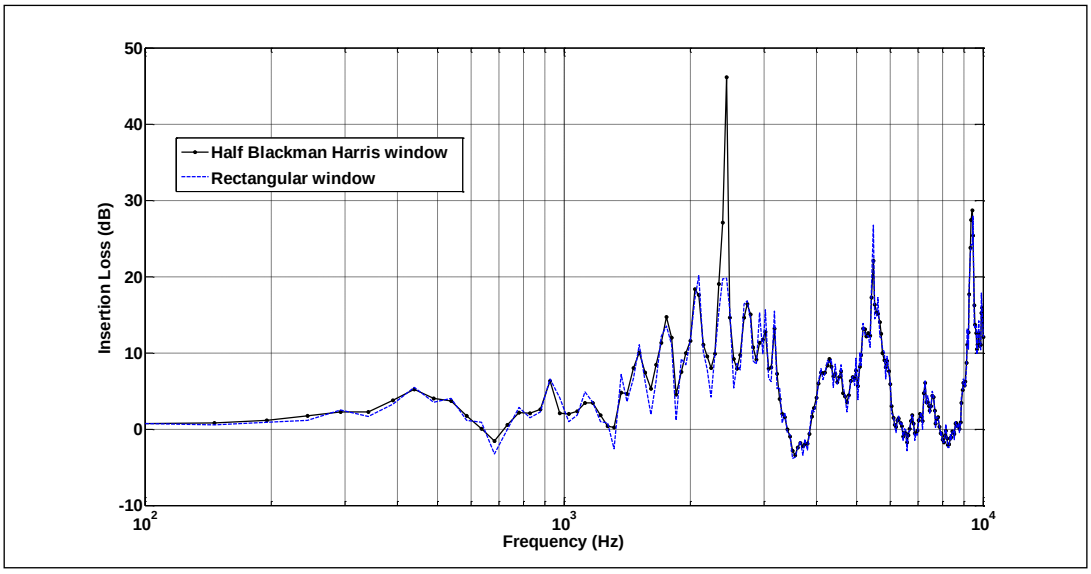

Figure 5.13: Insertion loss spectra for 7x3 array of PVC scatterers of outer diameter 0.055 m and lattice constant of 0.069 m using different FFT filters.

5.2.5) Influence of the floor grille in the anechoic chamber.

As explained in section 5.2.2, the presence of the floor grille made from steel in the anechoic chamber could affect the laboratory measurements. The insertion loss of a single latex scatterer of diameter 0.055 m and wall thickness of 0.25 mm has been measured with and without sections of the floor grille. During the measurement with the floor sections removed, the remaining grille edges and the steel beam (a permanent fixture to support the mesh floor grille) were covered with sound absorbing materials as shown in figure 6.17(a). The measured insertion loss spectra for the single latex scatterer are shown in figure 5.14. Clearly the presence of the grille floor sections interfere with the measurements.

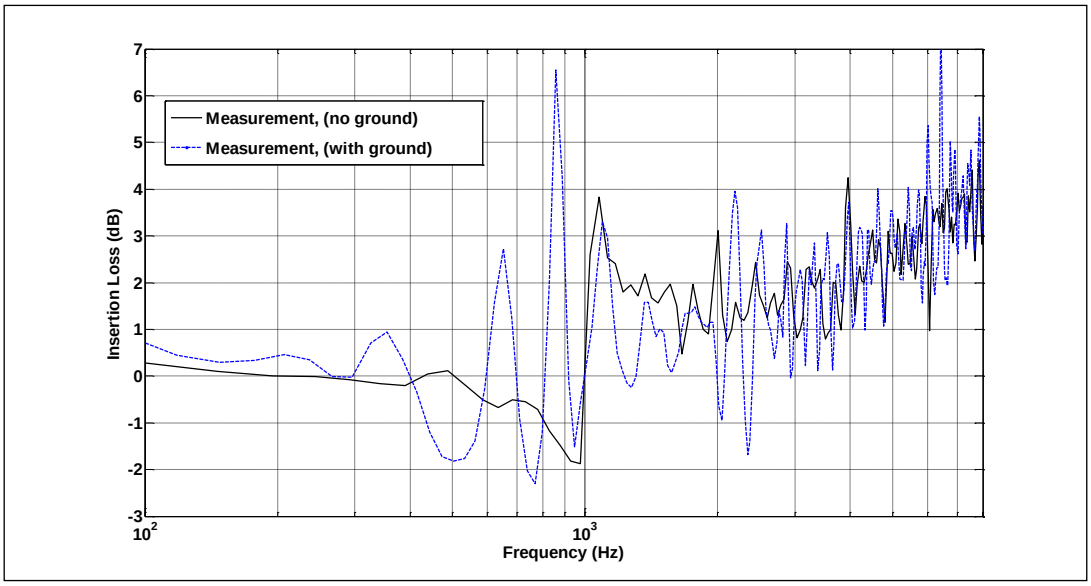

Figure 5.14: Insertion loss spectra for single latex scatterer.

5.2.6) Influence of microphone size.

The microphone is probably the most important element in the measurement chain. The influence of microphone size is briefly discussed in this section. Results of measurements made with a quarter-inch B&K free field microphone type 4190 are compared with those obtained previously with the half-inch microphone. In principle the smaller diaphragm gives a better high frequency response. Comparative measurements have been made on a single rigid (PVC) scatterer of outer diameter 0.11 m and wall thickness of 0.003 m with 4 symmetrical slits of size 0.012 m and the results are shown in figure 5.15 According to these data the influence of the microphone size is negligible.

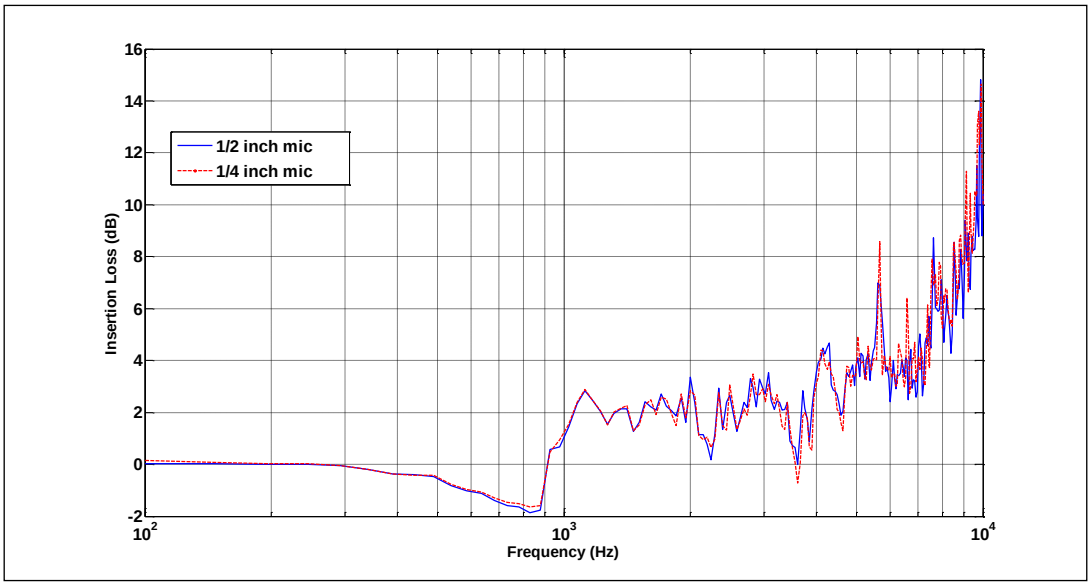

Figure 5.15: Insertion loss spectra for single PVC scatterer of outer diameter 0.11 m, wall thickness of 0.003 m with 4 symmetrical slits size of 0.012 m.

5.3) Excess Attenuation (EA) measurements in the laboratory

The acoustic instruments, data acquisition system (MLSSA) and post processing for Excess Attenuation (EA) spectra are basically the same as for IL spectra except that the EA is the reciprocal of Insertion Loss (see equation 8.1). As explained in chapter 8, a good direct field measurement is necessary for such measurement and therefore the ground plane to be measured is elevated by using a table instead of using on the floor grille in the anechoic chamber (see figure 5.16). In this way, the direct field measurement can be easily taken by removing both the ground plane and table altogether without changing the source and receiver locations. The measured EA spectra are not influenced as much by the mesh floor ground (see section 5.2.5) since the source to receiver distance for such measurement is shorter than the distance used for the insertion loss measurements.

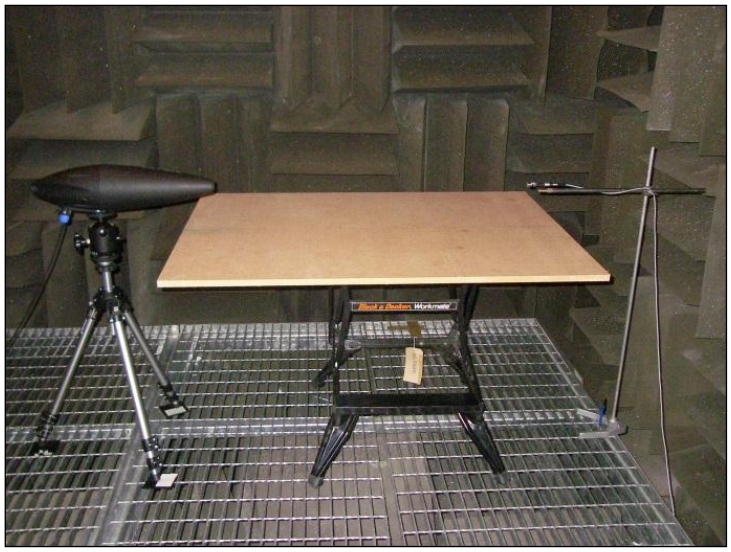

Figure 5.16: Arrangement for measuring Excess attenuation spectra above a Medium Density Fibreboard (MDF) in the laboratory.

5.4) Outdoor Measurements (Open University barrier test site)

Outdoor measurements have been made at the noise barrier test site situated at the Open University Milton Keynes campus. This section will give detailed descriptions of how the measurements (*in situ*) were performed using a multi-channel (2 outputs and 8 inputs) data acquisition system. Some of the outdoor measurements were on an array consisting of 3 rows of 54 3 m long composite scatterers (SRR4) as specified in table 7.2. The bottom ends of the PVC pipes were capped and bolted to a metal panel which was flush with the ground surface (see figure 5.17). The latex scatterers were inserted into the PVC pipes from the other end and bolted to the top cover. Perspex clips for each individual pipe were attached to the adjacent pipes at a height of around 2 m (see figures 5.18(a) and (b)). This reinforcement acted to maintain the uniformity of the periodicity and structural integrity of the array. Pieces of Medium-density fibreboard (MDF) were used to prevent the sound from passing underneath the barrier. Conventional road side noise barriers panels

(sometime referred to as fences) of comparable length (9 m) were erected on both sides of the SC. The measurement method used is closely related to the indirect prediction method described in ANSI S12.8 [91]. Insertion loss measurements were made simultaneously on the SC and neighbouring conventional barrier panel using different sources and receivers (see figure. 5.19). Both the speakers and receiving microphones were placed 5 m away from each face of the respective barriers (see figure 5.19) at a height of 1.6 m above the ground. Another pair of microphones was used for reference sound level measurements and they were placed at 1 m away from each source. The speakers were located above non-porous asphalt (a car park) and the receivers were located over grass.

MLSSA is based on the assumption of perfect linearity and time-invariance. Although this works well in laboratory (see section 5.2), the assumptions do not apply for outdoors as a result of variation in temperature, wind speed and humidity [92]. Consequently a more robust modified white noise measurement technique was used for the outdoor measurements. This applies a traffic filter (represented by the road traffic noise spectrum specific in EN 1793-3 [10]) to a white noise spectrum. For simplicity, this is termed as a Traffic Noise (TN) signal. The measurements were controlled remotely (approximately 10 m away from the test site) from the noise barrier to reduce any unwanted reflections due to equipment or people. A TN signal of 50 Hz to 10 kHz for duration of 7 seconds was produced by the DAC of a National Instruments NI USB-6259 board controlled by a PC built in with MATLAB® data acquisition toolbox. The TN signal was fed into a high powered Mordaunt

Short (Avant 902i) speaker and 48 repetitions were averaged for each measurement to improve the SNR. Matching pairs of microphones was used during the measurement: one pair were B&K microphones and the other pair were manufactured by ACO™. Pairs of identical microphones (i.e. of the same manufacture) were used for SC or fence type barrier measurements (see figure 5.19). As a result of using a higher sampling period (20 μs) in the data acquisition, a frequency resolution of 10 Hz was obtained for the outdoor data. A Graphic User Interface (GUI) has been implemented in MATLAB® for the ease of performing the measurements (see figure 5.20).

Figure 5.17: Drilled Metal panels used for securing the scatterers.

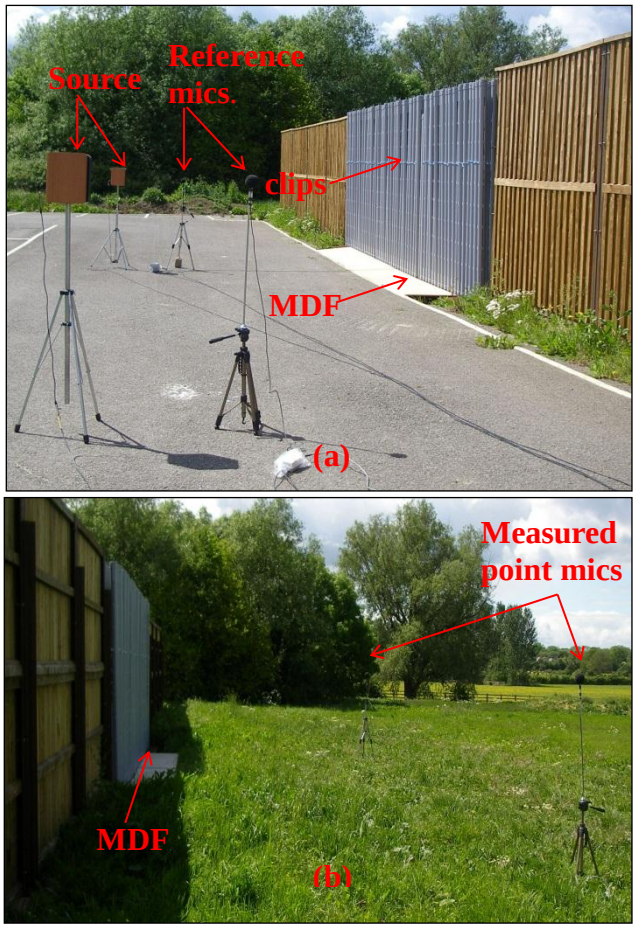

Figure 5.18: The outdoor noise barrier site, (a) source side of barrier showing SC and conventional noise barrier sections and (b) rear side of barrier.

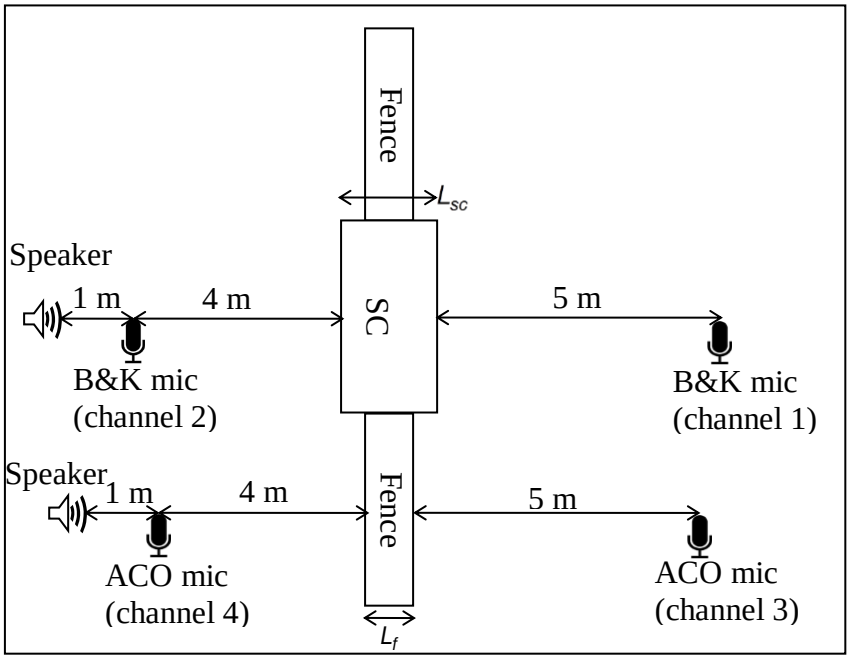

Figure 5.19: Plan view of the outdoor measurement arrangement using simultaneous multiple channels.

Often, outdoor measurements can be affected by wind [83]. If a microphone or any other obstacle is placed in a moving airstream, it will produce turbulence. Since turbulence generates a spurious signal superimposed on the sound being measured a sphere shape windshield made from foam material was used. This gives a low resistance to the airflow and reduces the turbulence.

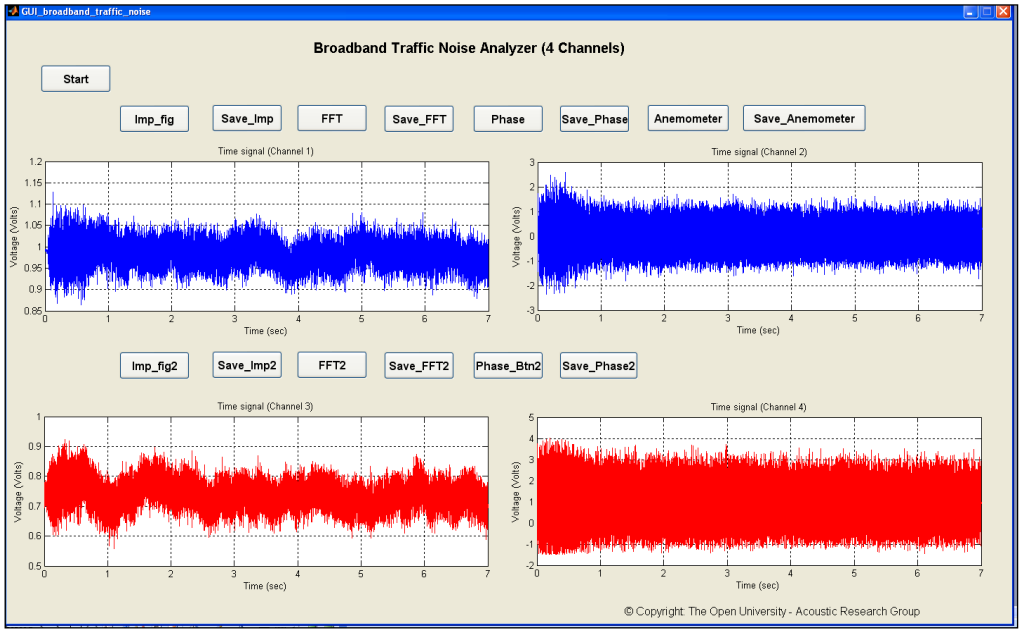

Figure 5.20: Graphical User Interface (GUI) Traffic Noise Analyzer implemented in Matlab®.

5.4.1) Data acquisition and data analysis for the outdoor measurements

Once the start button was pressed in the GUI, the measuring system performed 12 repetitions using the TN signal and displayed the averaged time spectrum for all of the 4 input channels. The buttons Imp_fig, Save_Imp, Imp_fig2, and Save_Imp2 were then activated to save the time domain figures and raw data from the input channels (see figure 5.21(a) and (b)). A DC off-set was observed in some of the time signals (see for example figure 5.21(b))

possibly as a result of insufficient grounding of the microphone cables. When FFT or FFT 2 button was pressed, transfer function estimates were performed to yield the corresponding frequency component for the time domain signal by comparing the measured signal with the input signal (see figure 5.22(a) and (b)). The data analysis was somewhat different from the laboratory measurements because of the indirect prediction method used. The measured free-field sound level, $p_{\mathrm{Re}\,ference\_field}$ (reference microphone) was adjusted to predict sound levels that would occur at the receiver positions in the absence of the barrier based only on distance corrections. For example the insertion loss with source distance correction IL_{DC} for the SC based on the measurement setup shown in figure 5.19 was calculated using,

$$IL_{DC} = 20\log\left(\frac{p_{Total\_field}}{p_{\mathrm{Re}\,ference\_field}}\right) - 20\log\left(\frac{5+L_{sc}+5}{1}\right), \qquad \textbf{(5.1)}$$

where L_{sc} is the depth of the array as shown in figure 5.19.

Due to the high levels of ambient noise (the test site location is near to a busy road), insertion loss results had to be corrected to take account of the noise. This was done by recording the ambient noise (muting the source) and performing the same procedure to obtain the power spectra of the ambient noise (see figure 5.23(a) and (b)). In fact, this noise level is an approximation as it did not represent the actual noise level during the barrier measurements. Although the ambient noise levels were high, according to [10], the measurement should have been immune to the noise as long as the signals were at least 10 dB higher than the background throughout the measurement

frequency range. Measurements were repeated at least 4 times and resulting IL were averaged to improve the SNR.

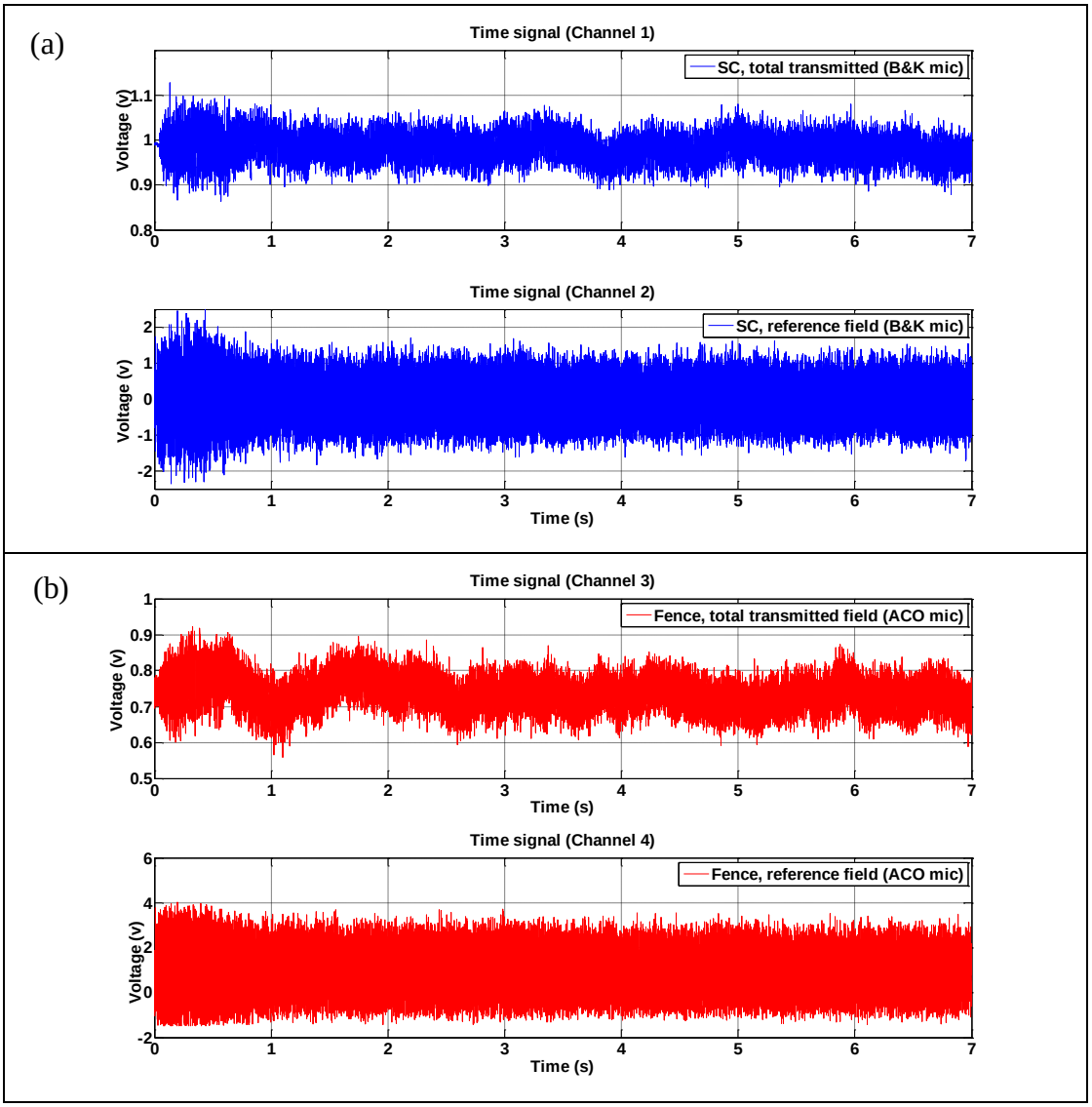

Figure 5.21: Example time domain signals measured outdoors (a) during SC barrier measurements using B&K microphones and (b) during fence measurements using ACO microphones.

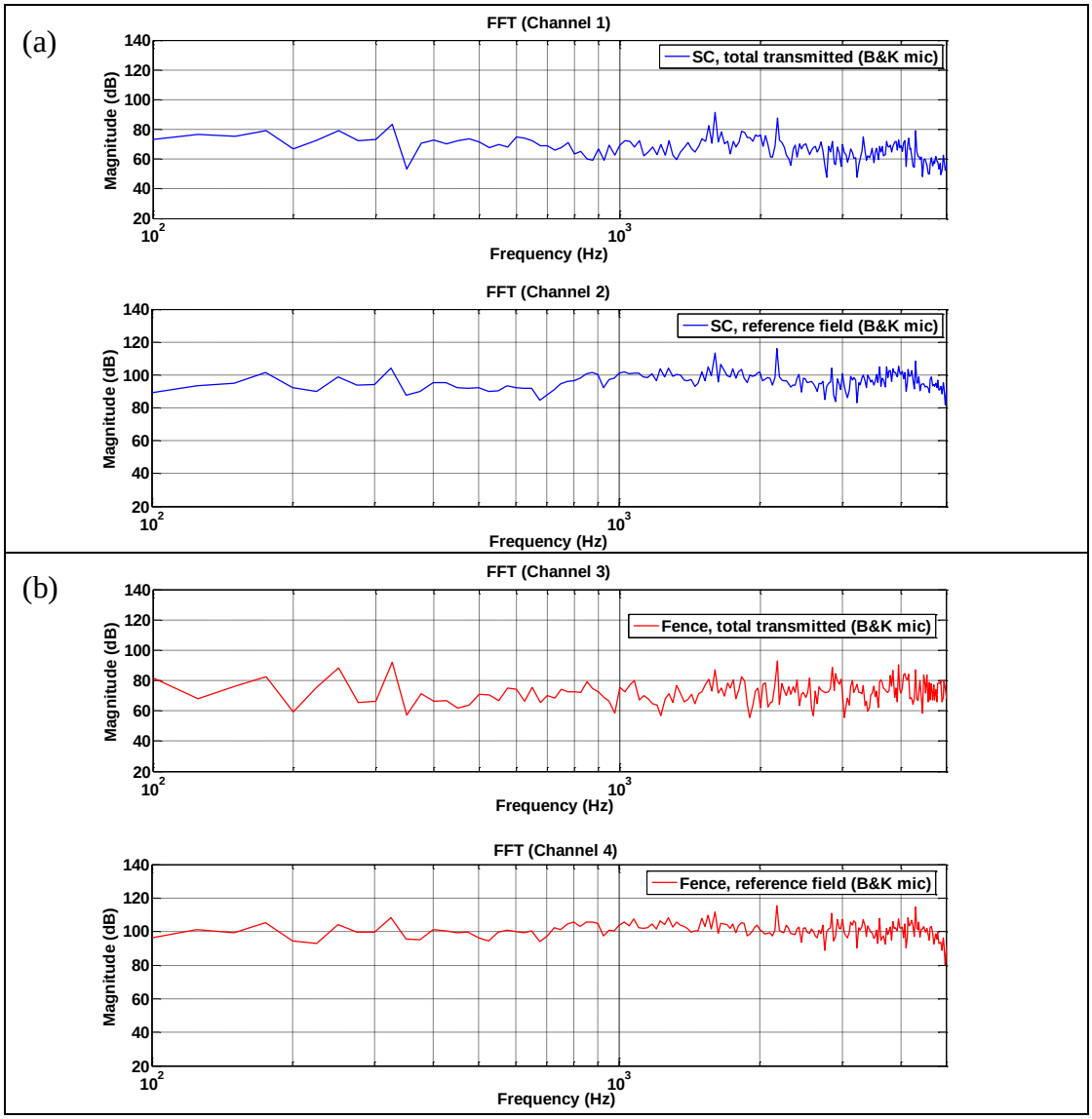

Figure 5.22 Example power spectra measured outdoors (a) during SC barrier measurements using B&K microphones and (b) during fence measurements using ACO microphones.

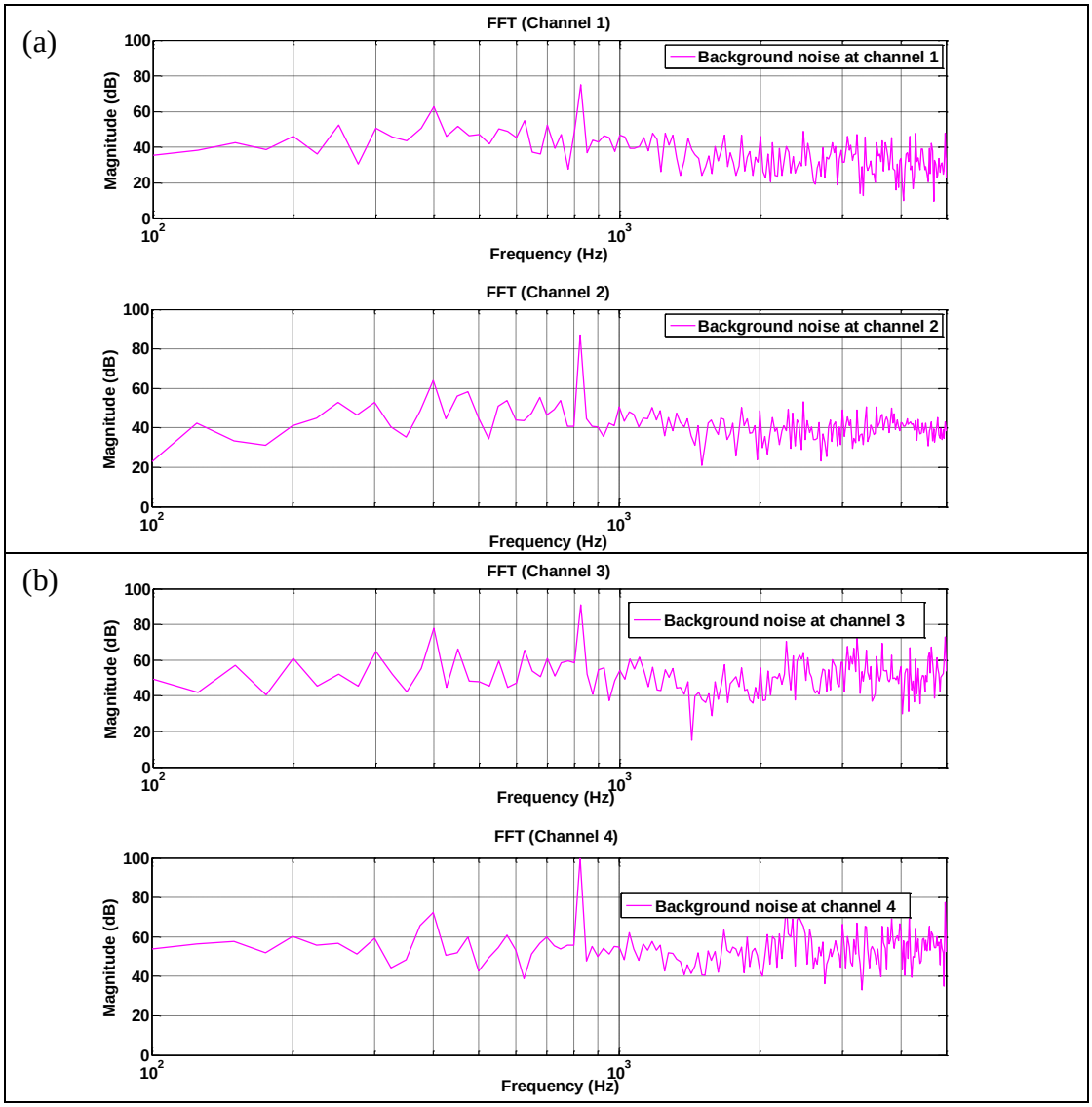

Figure 5.23: Example background noise power spectra measured at the barrier test site (a) during SC barrier measurements using B&K microphones and (b) during fence measurements using ACO microphones.

5.4.2) Microphone calibration

Given that the required precision is high and that outdoor conditions involve varying environmental temperature and humidity compared with laboratory conditions, the question of long term stability of the microphones arises. One approach that has been used for measuring ground impedance is to use more than two microphones. In that case, since more than one transfer function is measured it is possible that errors in the transfer function and

geometry partially average out. This procedure is similar to the phase gradient method [93].

The reliability of the indirect prediction method shown in section 5.4.1 relies on another important factor which is extent to which pair of microphones have identical responses. It is possible that by using a phase matched pair of microphones (an expensive method), the error in the measurement could be reduced. Another possibility is to determine the difference between two conventional microphones in the laboratory and use the results to subsequently correct the field data. This is a cheaper option but the question of long term stability arises (i.e. whether the laboratory data is still valid under outdoor conditions with different humidity and temperature). In this section, an example of how the calibration is done for the B&K microphones is briefly discussed. To perform the calibration, the source was isolated and replaced by a B&K sound calibrator type 4231 using the same NI acquisition system. The microphones (mic reference no. 306 and 307) were individually tested by inserting them into the calibrator as shown in figure 5.24. The calibrator emits a known sound pressure level at single frequency of 1 kHz with amplitude of 94 dB. Since the B&K dual-channel microphone power supply - type 5935 comes with selector switch to vary the gain, the calibration test was performed with the gain at zero and 30 dB to test for linearity.

Figure 5.24: Setup for B&K microphone calibration.

The calibration results for both B&K microphones at different amplifier gain levels are shown in figure 5.25. All the frequency spectra show the peak at 1 kHz and for the corresponding gains level, the amplitudes of the sound pressure are also within a reasonable range of the desired values of 94 dB and 124 dB. Undesirable features in these spectra are the spikes that occur at various frequencies. Since the spikes for both microphones occur at similar frequencies, the likely cause is electrical noise in the measuring system. However these spikes will cancel out after performing the correction procedure. From these calibration results and assuming linearity for all other frequencies, the differences between the microphones can be known and will be taken into account in our outdoor measurement. Hence the final calculated Insertion Loss (IL) spectra take account of the distance correction on reference microphone signal, the background noise and the system response.

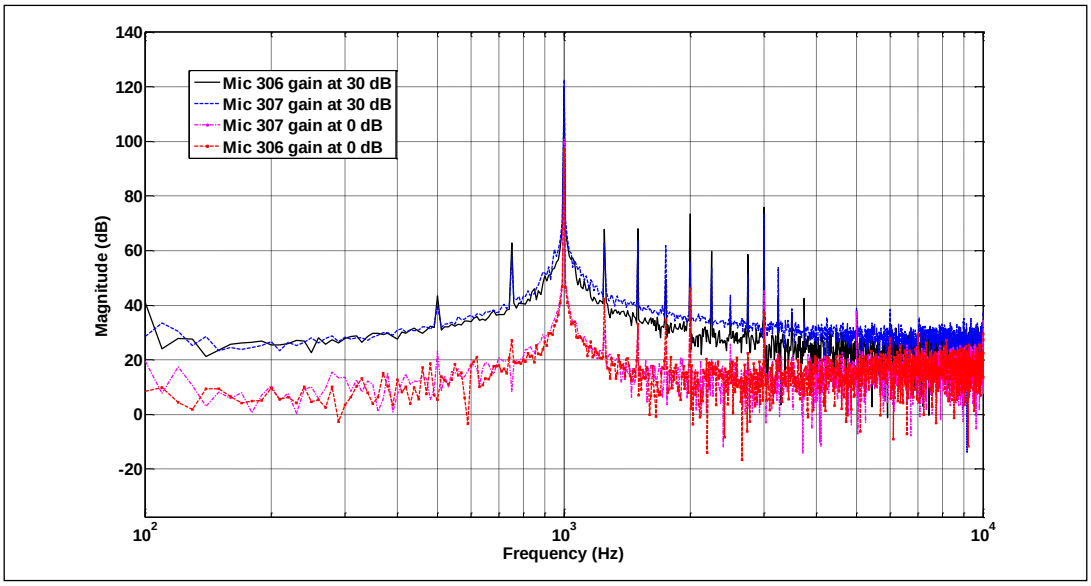

Figure 5.25: Calibration results for B&K microphones.

5.4.3) Measuring meteorological conditions using a sonic anemometer.

During the outdoor measurement, simultaneous measurements of wind and temperature profiles were made with a sonic anemometer (Gill Instruments type R3A-100) mounted about 2 m above the roof top of the instrumentation cabin (figure 5.26). It is important to note that the U-axis of the sonic anemometer is aligned to the North in order to determine the true wind direction. The sonic anemometer reads in 4 items of data (wind speed components along the three axes and the speed of sound (SOS)) which are fed through the analogue inputs of the NI Data acquisition box. Wind vectors were calculated from the U (x-axis) and V (y-axis) of the sonic anemometer. Values for the W (z-axis) representing the vertical components were typically negligible. Since the speed of sound is also obtained by the sonic anemometer it was possible to extract the corresponding temperature values from,

$$c_0 = 331.3 m.s^{-1}\left(\sqrt{1+\frac{\vartheta}{273.15°C}}\right), \qquad \textbf{(5.2)}$$

where c_0 = speed of sound in air and ϑ is the acoustically-deduced temperature in Degree Celsius.

When the anemometer button on the GUI was pressed (see figure 5.20), the reading from the sonic anemometer was displayed as in figure 5.27. These data were saved for further analysis.

Figure 5.26: Sonic anemometer mounted above the instrumentation cabin.

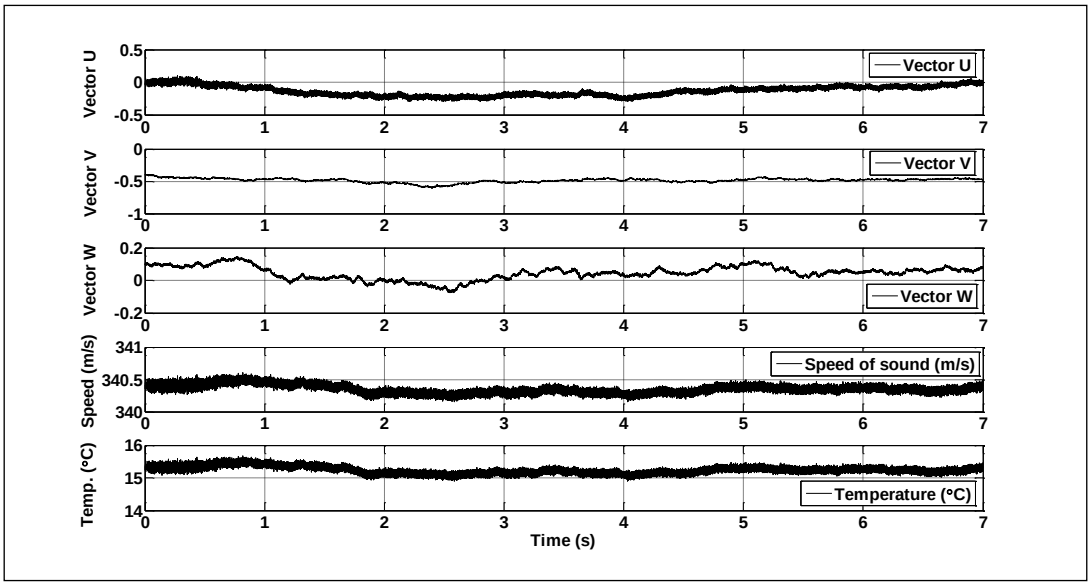

Figure 5.27: Data from sonic anemometer.

Figure 5.28 shows an example of the wind vector plot (north is at 0°), the black line indicates the barrier position and the red dotted line denotes the direction of sound propagation. Blue solid lines calculated from vector U and V show the wind speed according to this set of measurements which is about 0.8 m/s. The average speeds of sound and temperature for the entire 7 seconds (multiply by 4 repetitions) are also shown at the bottom of the wind vector diagram.

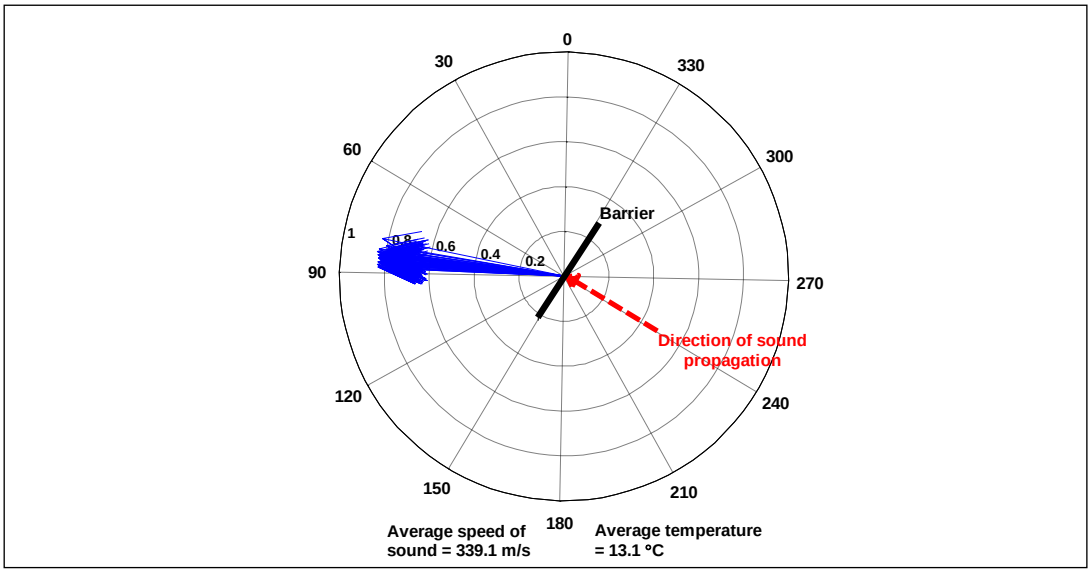

Figure 5.28: Example of a deduced wind vector diagram.

5.5) Swept sine signal

There are also various impulse response measurement techniques which depending on the circumstances may prove better than others [94]. We have considered another input source which uses the swept sine technique (also known as chirp) developed by Farina [92]. The swept sine method uses a sinusoidal signal with frequency increasing exponentially with time. This signal can be easily implemented in the multi-channel data acquisition system discussed in section 5.2. The MLS relies on the assumption of linear time invariant systems and can cause distortion artefacts to appear in the deconvolved impulse response when this condition is not met. It has been found that the swept sine can overcome this limitation. The sweep duration of 4 s, start and end frequency of 50 Hz and 10 kHz respectively were defined in our measuring system. It is common to add a segment of silence after each sweep sine signal to avoid time aliasing. The electrically generated swept sine signal is shown in figure 5.29.

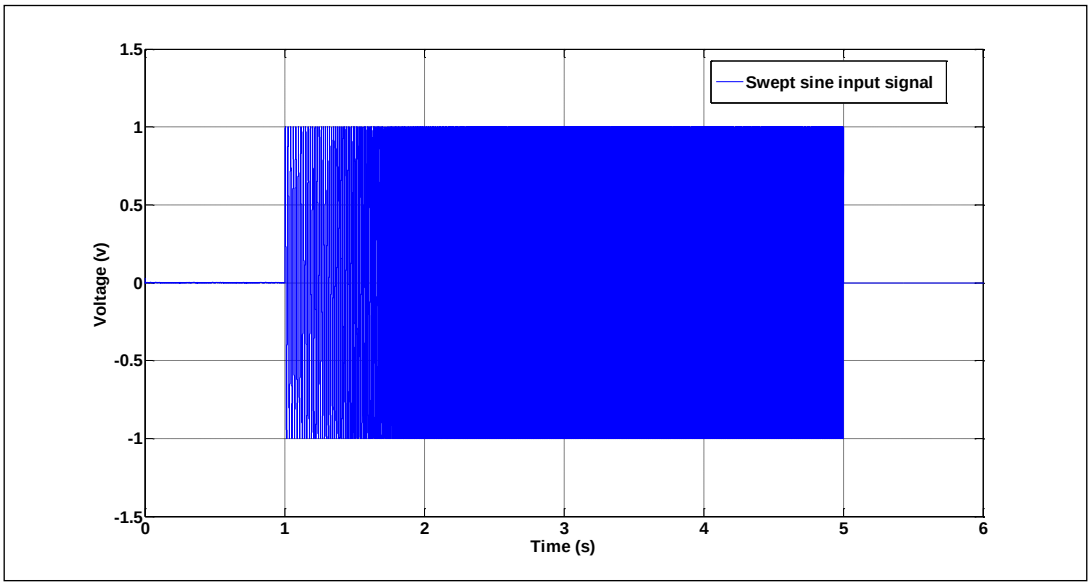

Figure 5.29: Swept sine signal generated electrically.

The swept sine signal was tested in the anechoic chamber using a loudspeaker and a single microphone. The direct sound field method described in section 5.2.2 was used to measure the IL spectrum due to a single PVC scatterer of outer diameter 0.11 m and wall thickness of 0.003 m with 4 symmetrical slits of 0.012 m. To make a fair comparison with MLSSA measurements, 16 repetitions were made for the direct field and total transmitted field measurements. The time domain signals for both measurements are shown in figure 5.30.

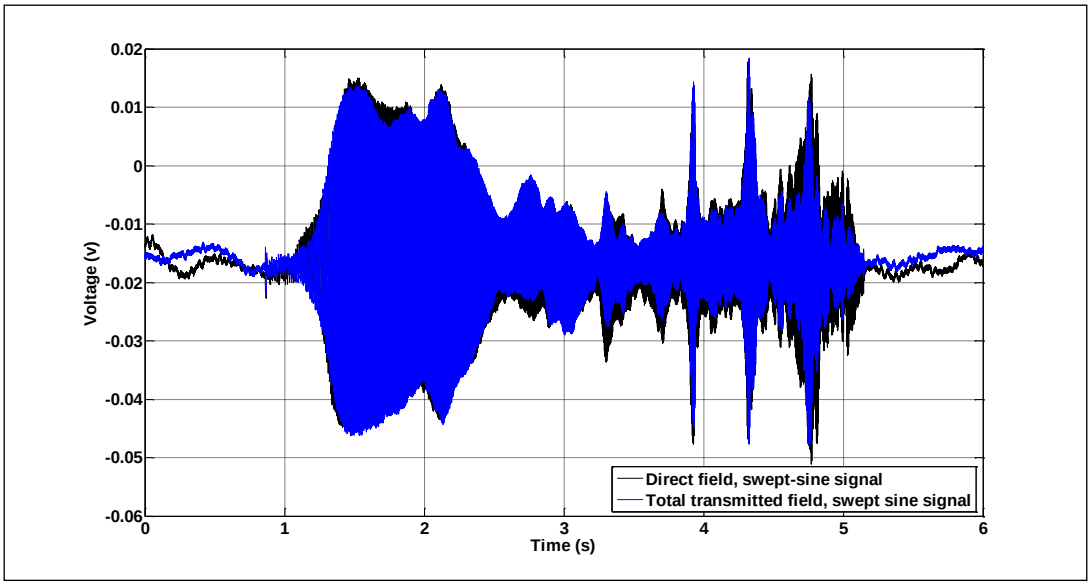

Figure 5.30: Direct and total transmitted fields measured using the swept sine method in the laboratory.

The transfer function estimate is used to deconvolve the time signal into its frequency component and the Insertion Loss (IL) is calculated. The IL spectra obtained using MLS and Swept sine methods are compared in figure 5.31 and show little difference. This swept sine method has also been implemented for the level difference measurements described in section 8.4.5.

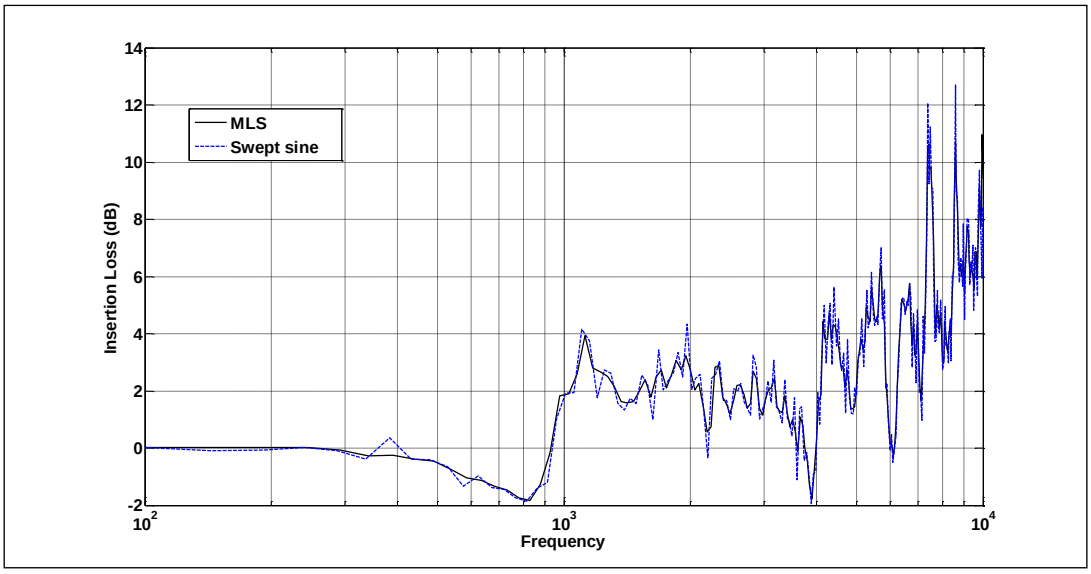

Figure 5.31: Comparison of IL spectra due to a single PVC scatterer of OD 0.11 m, WT 0.003 m with 4 symmetrical slits of 0.012 m measured using the MLS and swept sine methods.

5.6) Outdoor in situ measurement of a sonic crystal at Diglis Weir, Worcester.

During the course of research, the opportunity arose for investigating the creation of 'acoustical gimmicks' based on sonic crystals. This opportunity involved collaboration with Liminal – winners of PRS for Music Foundation's New Music Award 2010 [78]. The project entitled "Organ of Corti" involved creation of an experimental instrument that employs sonic crystal technology to accentuate and attenuate frequencies within the broad range of sounds present in road traffic or falling water.

The measurements on the "Organ of Corti" i.e. a sonic crystal composed of transparent acrylic cylinders mounted on a platform, which was used to accentuate and attenuate frequencies within the broad range of sounds present in road traffic and falling water (i.e. weir). This device was intended to draw attention to the sounds already present in the environment by re-harvesting them in a new way. One way of manipulating sound waves in

periodic arrays is to introduce defects (vacancies) in their structure [79, 80, 95, 96 and 97]. There has been increasing interest in application structures with a low number of defects with respect to the total number of scatterers in the structure, so that the periodicity is locally broken, to high precision wave filters [81] or waveguides [82].

The particular design studied in this section consists of eighty one 4 m long 0.22 m diameter vertical acrylic cylinders arranged in a hexagonal lattice with lattice constant, L = 0.3 m (see figure 5.32(a)). This structure was placed at Diglis Weir, river Severn, Worcester as part of the Worcester Music Festival in August 2011 (see figure 5.32(b)). The cylinders were arranged in a quasi-ordered lattice arrangement and some cylinders were intentionally removed to form a passageway. This allowed people to walk through the structure and listen to the different characteristics of sound at different locations within the structure as well as while walking around it. For an SC with regular hexagonal lattice arrangement of lattice constant 0.3 m, the calculated Bragg band gap (centre frequency) is:

$$f_{Bragg\_Hex} = \frac{344}{\sqrt{3}(L)} = \frac{344}{\sqrt{3}(0.3)} = 660\ Hz\ , \qquad \textbf{(5.3)}$$

This section will also provide some modelling results using Multiple Scattering Theory (MST) explained in chapter 3 to compare with our experimental data.

5.6.1) Measurement arrangement

During these measurements, the sound generated by the weir was acting as the source. Time signal was recorded for 7 seconds with data sampling rate of 20 μs for each set of measurement using the multi-channel data acquisition system discussed in section 5.2. Three sets of measurements were made and for each set of measurement there were 16 repetitions (thus a total of 48 measurements) to improve the SNR. Transfer function estimation was used to obtain the frequency spectrum from the recorded time signal. The positioning of the receivers and approximated source location are given in figure 5.32(a) and table 5.1. During the experiment, there were some errors made in the data acquisition system (due to crosstalk of signal) and thus, only 2 points (Ref pt and Pt 1) were correctly measured. This error resulted in an investigation of possible ways to prevent such mistakes from happening in future measurements. The insertion loss (IL) was deduced by using the indirect prediction method discussed in section 5.2 which takes accounts of the distance correction for the reference microphone, ambient noise and system response. The meteorological conditions were measured with handheld anemometer and thermometer. The meteorological conditions taken during the measurement were as follows:

i) Average temperature: 23°C.

ii) Average wind speed: 1m/s.

iii) Wind direction: West (cross wind).

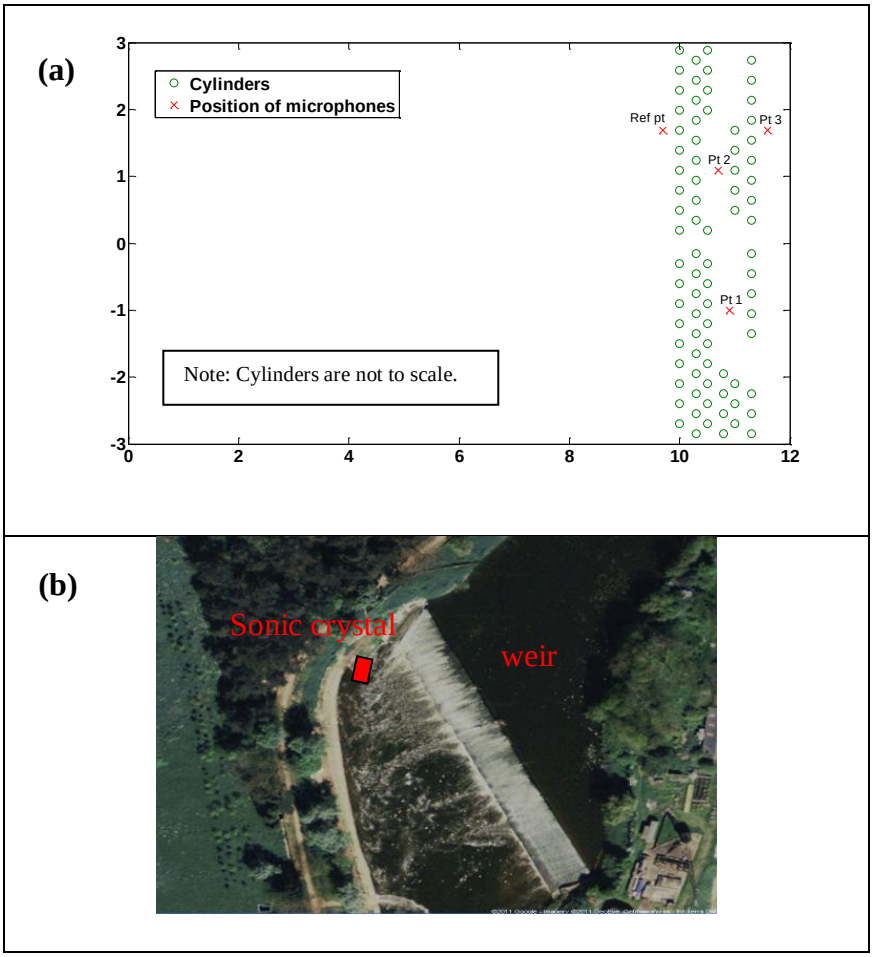

Figure 5.32: (a) Plan view schematic of the sonic crystal arrangement and microphone locations at Diglis weir Worcester. (b) Aerial map of the site showing where the sonic crystal was situated (picture taken from Google map).

Microphone locations (coordinates)	x	y
Reference point (Ref pt)	9.7	1.69
Point 1 (Pt 1)	10.9	-1
Point 2 (Pt 2)	10.7	1.09
Point 3 (Pt 3)	11.6	1.69

Table 5.1: Coordinates of source and receivers positions during 'Organ of Corti' measurements.

5.6.2) Measurement results

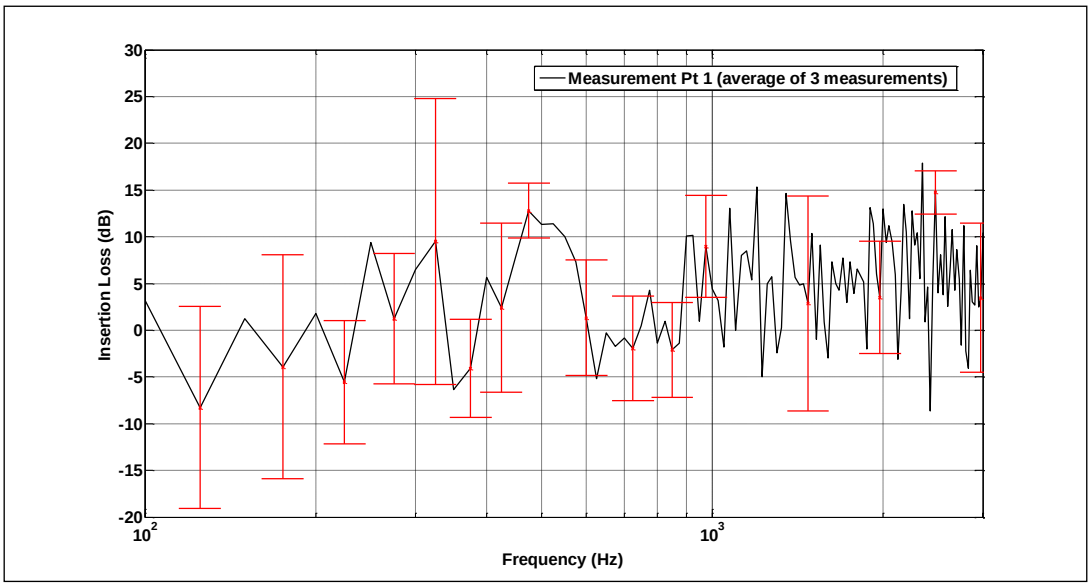

Figure 5.33: Mean IL spectrum (average of 3 measurements) with error bars for receiver position Pt 1.

The mean Insertion Loss (IL) spectrum averaged over 3 measurements (see figure 5.33) shows a "modified" Bragg band gap at a frequency of 480 Hz. One contributing factor to the shifting of Bragg band gap could be the effect of having a quasi ordered array rather than having a regular (full) lattice array structure. Further investigation of this effect is shown in a later section (5.6.5). The spectrum shows additional attenuation peaks around 250 and 320 Hz which possibly suggest evanescent (or localised) modes [98] in the vacancies (i.e. sound trapped in the vacancies). Negative IL (sound enhancement or focussing) is also present particularly at 150, 230, 350 and 650 Hz. In such an uncontrolled environment there are large differences between successive measurements (large error bars). The most likely cause is other noise sources present in the vicinity. Nevertheless, the variation at the peak of the "modified" Bragg band gap (480 Hz) is relatively small (< 6 dB).

5.6.3) Modelling with Multiple Scattering Theory (MST) assuming a single point source

Multiple Scattering Theory (MST) has been used to predict the IL spectrum at Pt 1 receiver position. Two predictions are made with the (assumed line) source located at coordinate (0, 0) and (0, 10), see figure 5.32(a). The receiver positions Pt 1 are averaged over 4 other positions (±0.05 m perturbation in both axes) from the original position (see figure 5.34). This is to give a more realistic prediction of the IL spectrum in the region of Pt 1.

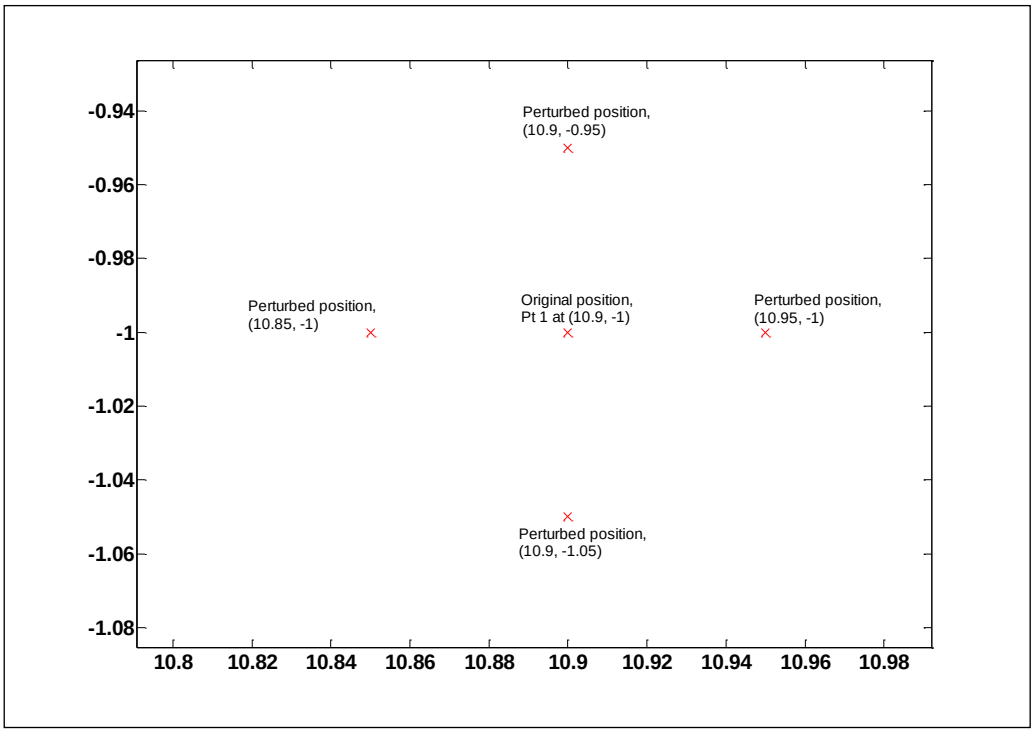

Figure 5.34: The original receiver position Pt 1 and 4 other perturbed positions made for MST modelling.

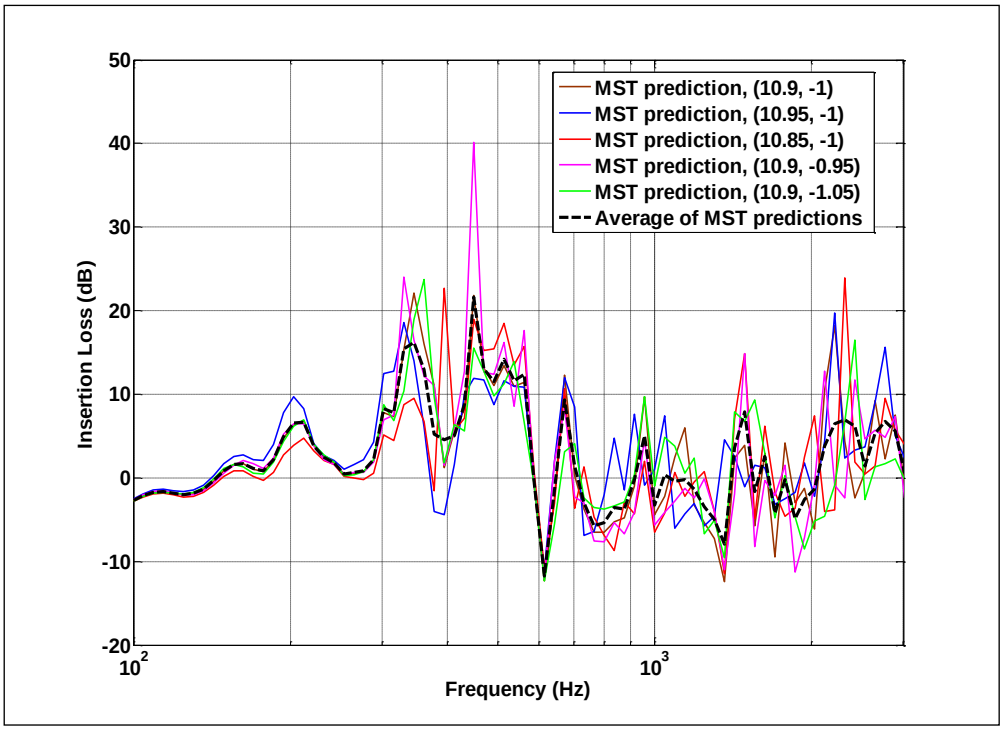

Figure 5.35: Predicted IL spectra of all the 5 individual positions (Pt 1 original and 4 perturbed positions) and the averaged IL spectrum. Source is located at coordinates (0, 0).

Figure 5.35 shows the predicted IL results for all the 5 positions (Pt 1 original and 4 perturbed positions) and the averaged IL spectrum. The source is modelled to be positioned at coordinates (0, 0). Some variations are noticeable when there is a slight change in the receiver position but the overall trend seems to be agreeing. An exception is at coordinates (10.9, -0.95) where almost 20 dB difference is observed near 450 Hz. This narrow band spike could be due to a numerical artefact as it occurs at only a single frequency point.

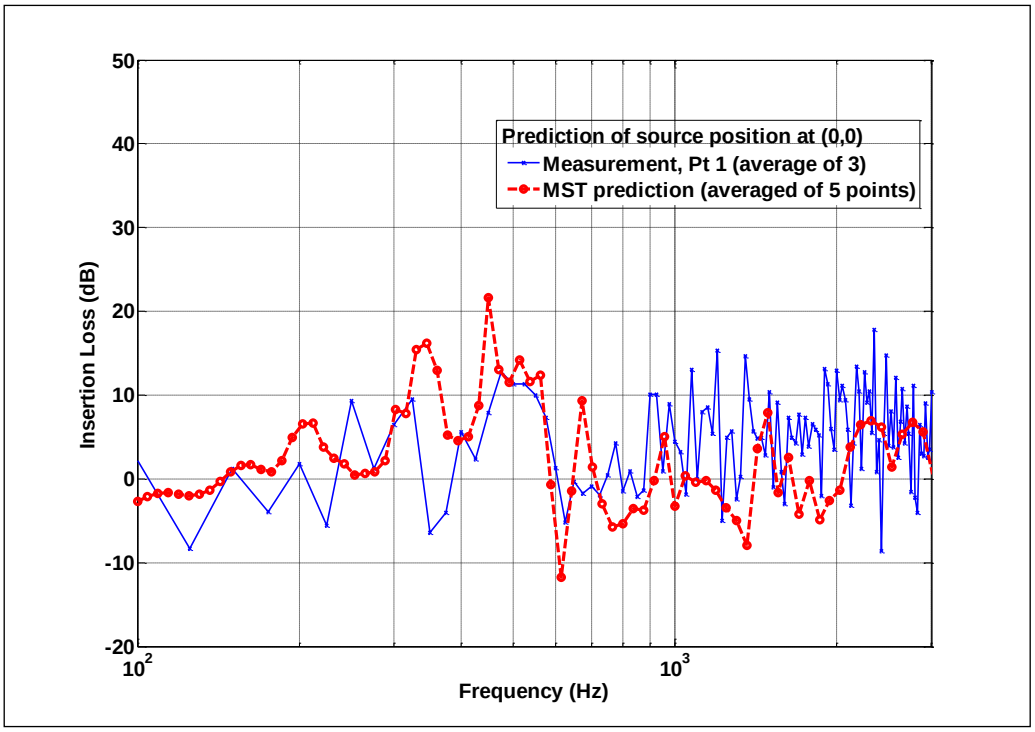

Figure 5.36: Measured (average of 3 measurements) and predicted (average of 5 receiver points) IL spectra for receiver position Pt 1 with source located at coordinates (0, 0).

Figure 5.36 compares the measured (average of 3 measurements) and MST predicted (average of 5 receiver points) IL spectra with the point source modelled at location (0, 0). The predictions agree fairly well with the measured data at low frequency. The first peak (200 Hz) in the predictions appears to be shifted in frequency. The second and thirds peaks are similar to those measured. The third peak corresponding to the 'modified' Bragg band gap is predicted well. One explanation for the negative IL shown in the measured data (low frequencies) could be the effect of the ground (see chapter 8).

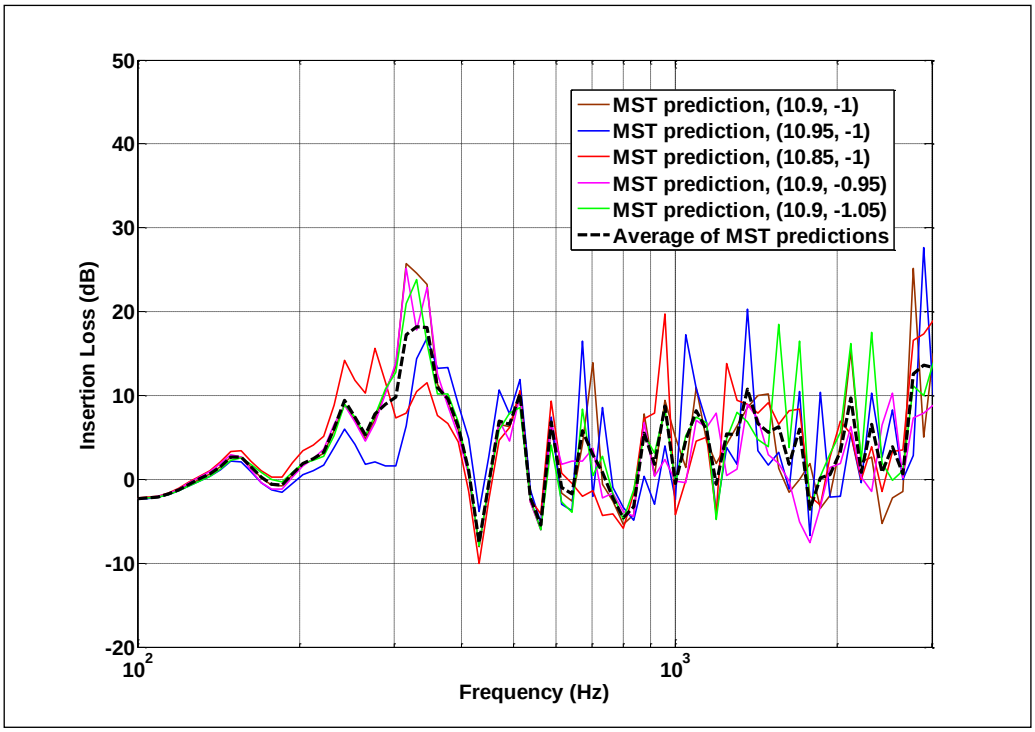

Figure 5.37: Predicted IL spectra at all the 5 individual positions (Pt 1 original and 4 perturbed positions) and the averaged predicted IL spectrum. The point source is assumed to be located at coordinates (0, 10).

Figure 5.37 shows the predicted IL results for all the 5 positions (Pt 1 original and 4 perturbed positions) and the averaged IL spectrum. The source is modelled to be positioned at coordinates (0, 10). Again, variations in the IL spectra are observed when there is a slight change in the receiver position as in figure 5.35.

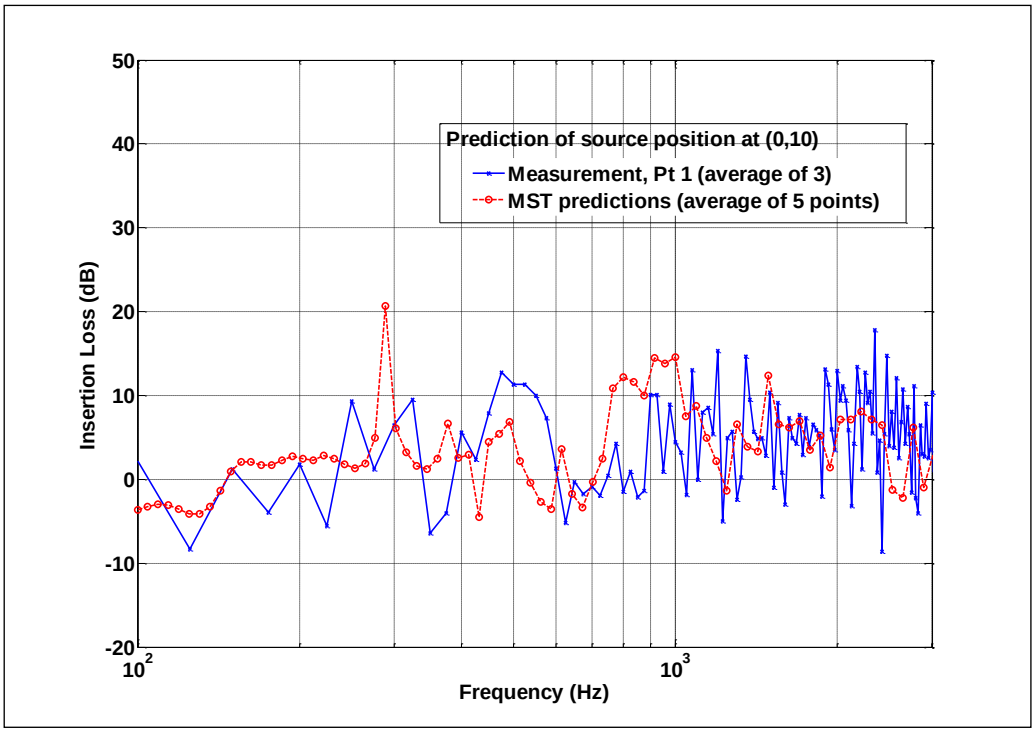

Figure 5.38: Measured (average of 3 measurements) and predicted (average of 5 points) IL spectra for receiver position Pt 1 with source located at coordinates (0, 10).

Figure 5.38 compares the measured (average of 3 measurements) and MST predicted (average of 5 points) IL spectra with the source modelled as a point at location (0, 10). The prediction agrees slightly better at high frequencies with the source modelled at an oblique angle rather than at coordinates (0, 0) see figure 5.32(a). Three peaks are again predicted at 290, 380 and 500 Hz. The Bragg band gap is well predicted in terms of the centre frequency (near 500 Hz) but with smaller amplitude.

5.6.4) Modelling with multiple point sources on a line

The fact that predictions using a single fixed point source at (0,0) are in better agreement with the measured data than those assuming a source at (0,10 suggests that using a line of point sources could improve the accuracy of the prediction. Consequently the weir was modelled by 10 point sources

spaced along the whole span of the weir (approximately 200 m). The positions of the sources are shown in figure 5.39 and the corresponding coordinates are shown in table 5.2. The MST prediction was run for each source location and receiver position, Pt 1 (see table 5.1). Similarly, averaging of all the 5 points (receiver Pt 1 and 4 perturbed positions) was carried out (see figure 5.34). It is reasonable to assume that all the point sources are coherent since the weir noise is caused by more or less the same flow and drop over the length of the weir. The direct pressure (without SC) in Decibel, $p_{Direct(dB)}$ was then summed over all sources at each frequency point, n,

$$p_{Direct\_total(dB)} = 10\log_{10}\sum_{0}^{n}\left(10^{\frac{p_{Direct(dB)}}{10}}\right). \qquad \textbf{(5.4)}$$

Likewise for the total transmitted pressure (with SC) in Decibel, $P_{total\_tranmitted(dB)}$ was summed over all sources at each frequency point, n,

$$p_{total\_tranmitted(dB)} = 10\log_{10}\sum_{0}^{n}\left(10^{\frac{P_{total\_tranmitted(dB)}}{10}}\right). \qquad \textbf{(5.5)}$$

The IL in dB could then be expressed by,

$$IL = p_{Direct\_total(dB)} - p_{Total\_transmitted\_total(dB)}. \qquad \textbf{(5.6)}$$

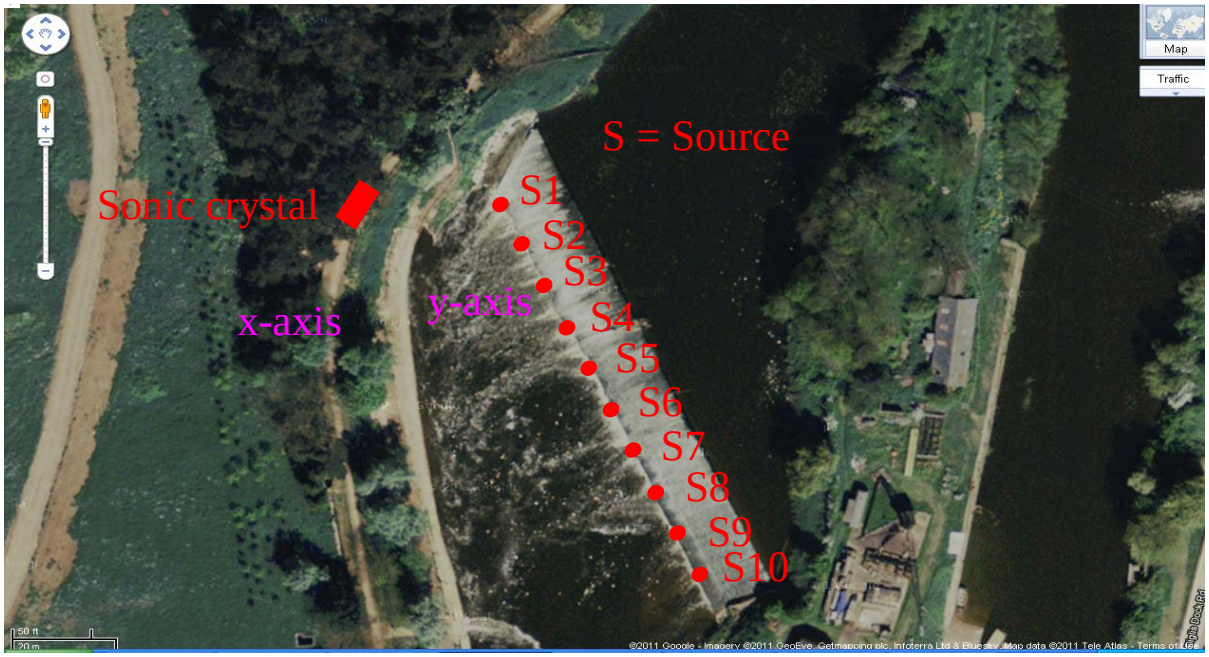

Figure 5.39: Picture illustration for the location of the 10 sources (S1 to S10) and the position of sonic crystal (photo taken from Google map).

Source no.	x	y
S1	-7.82	10.92
S2	-16.73	6.38
S3	-25.58	1.72
S4	-34.11	-3.55
S5	-42.83	-8.45
S6	-50.92	-14.47
S7	-58.93	-20.6
S8	-67.15	-26.35
S9	-75.63	-31.65
S10	-83.29	-38.29

Table 5.2: Coordinates of individual sources in a multiple point source model of the weir.

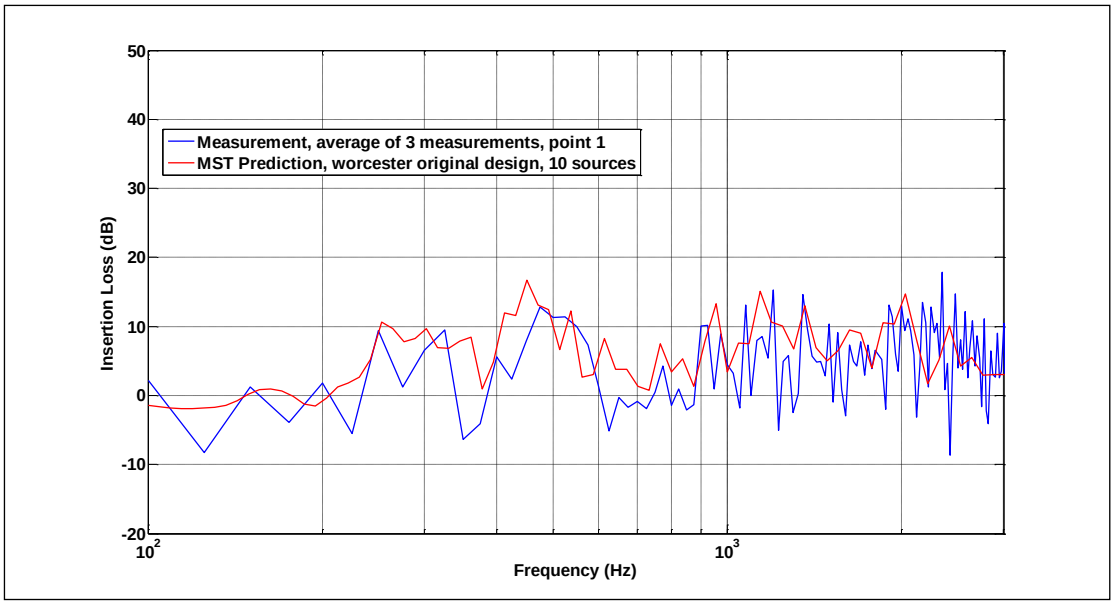

Figure 5.40: Measured (average of 3 measurements) and MST predicted with multiple point sources IL spectra for receiver position Pt 1 (averaged over 5 receiver points for each individual source).

Figure 5.40 shows the measured and MST predicted IL spectra at receiver position 1. The predictions resulting from the 10 source model of the weir show better agreement with measurements than those assuming a single point source at either location (0,0) or (0,10) (see figures 5.36 and figure 5.38). The first IL peak around 250 - 350 Hz is well predicted and this could be due to the evanescent mode suggested in figure 5.33. Also, the prediction for the modified Bragg band gap (possibly shifted due to the quasi periodic ordered array effect) near 450 Hz agrees fairly well with the measured data.

Chapter 6

Improving the performance of sonic crystal noise barriers by using resonant elastic shell elements

6.1) Introduction

A conventional technique for reducing low frequency noise transmission is to increase the thickness or the mass per unit area of the sound insulation material. A drawback of this technique is that usually it results in large size and mass of the insulator. On the other hand the stop and pass bands of a Sonic Crystal (SC) composed of solid rigid elements and their angle dependence makes an SC unsuitable for use as a barrier for broadband noise such as road traffic. To make a SC noise barrier appealing, methods must be found of reducing the angle-dependence of the stop bands and targeting the frequencies of interest without increasing the size. One possibility for achieving these objectives is to use resonant scatterers. There has been previous numerical and theoretical work in respect to periodic arrays of elastic scatterers in a gas involving hollow spheres and cylinders [99]. There have also been numerical studies of acoustical performance of a periodic array of resonant silicone rubber scatterers embedded in an epoxy resin matrix [100]. Previous experimental work in respect of periodic array of scatterers in air has investigated the use of pressurized gas-filled cylindrical balloons [101 and 102]. In Kushwaha *et al*, the authors examined (theoretically) a square lattice SC in 3 dimensions made up of hydrogen filled cylindrical balloons in air. In these systems, the authors analysed the band

gap creation for three different configurations relating to parameters such as the latex wall thickness, the filling fraction and the pressure inside the balloons. It's reported that the pressure inside the balloon is kept at 1.1 atm which is slightly above the ambient pressure and the latex wall thickness is made very thin to obtain high-velocity, low-density scatterer in a low-velocity and high-density host conditions thus giving high impedance mismatch in such matrix. It has been found that resonance attenuation peaks can be obtained at frequencies which do not depend on the periodicity of the SC but on the resonance frequency of the resonators. However it was found difficult to predict the measured effects due to the pre-stress condition i.e. to take account of any static external load and thereby model scattering by elastic materials under tension.

It is also known that for thin-walled elastic cylinder, the lowest resonance is corresponds to a radial or "breathing" mode of vibration which results in a significant change in volume of the cylinder on account of the variation of the radius through each cycle. Vibration analysis for the natural frequencies and mode shapes of an elastic shell is generally much more complex than that for a beam or plate because the generality of the shell equation permits a wide variety of mode shapes with vastly different characters. The modal shapes of the cylinder model are basically composed of two kinds of mode patterns: the breathing mode and the freely supported beam mode [103]. The combination of the two basic mode patterns support three modal shapes – axial, bending and torsional modes (see figure 6.1). It is possible to realise such a mode provided that the thickness of the cylinder

wall is less than 1/50th of the cylinder diameter and that the wall stiffness (Young's Modulus) is of the order of 1 MPa [104]. In this chapter, the theory of wave propagation through doubly periodic arrays of elastic shells based on the Multiple Scattering Theory (MST) covered in Chapter 3 will be discussed. It is a semi-analytical method and in this work the terms 'MST' and 'semi-analytical prediction' are used interchangeably. In addition, the breathing mode resonance is also verified by performing modal analysis with the Finite Element Method (FEM) using COMSOL® Multiphysics software. FEM is also used to predict the transmission problem for a single elastic shell. These predictions are compared with data from experiments using commercially available non-vulcanized rubber (latex) and data confirm the presence and identity of the resonances for the chosen material and geometry of the elastic shell. Some failed attempts to use different materials such as polyethylene and periodically stiffened latex are also reported in Appendix C.

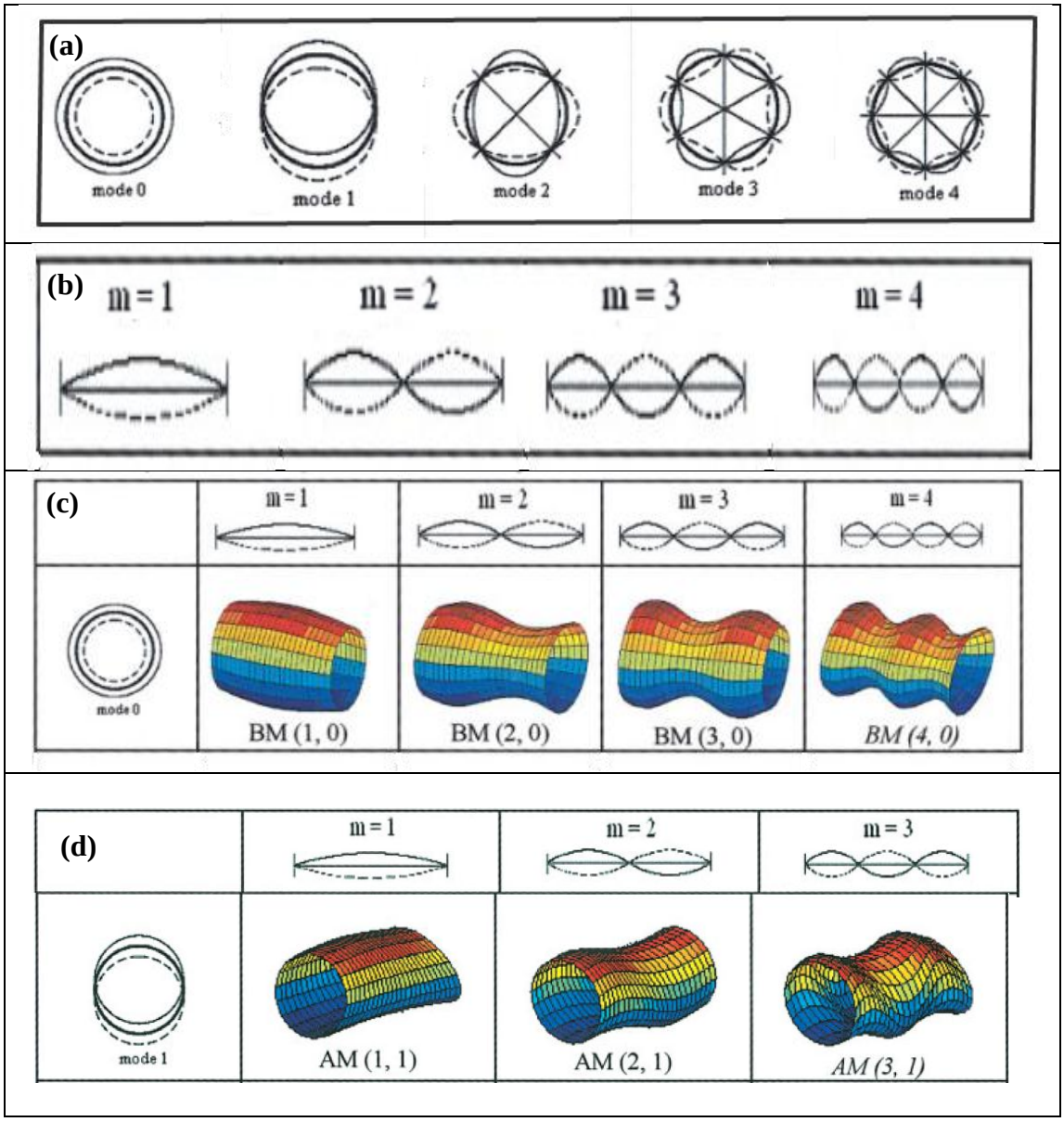

Figure 6.1: Example predictions of the two basic mode shapes of a freely supported cylinder – (a) radial (b) beam modes up to fourth order (c) the combination of the first radial mode (mode 0) and up to the fourth order of bending modes (d) the combination of the first radial mode (mode 1) and up to the third order of axial modes [103].

6.2) Acoustics of single elastic shells

In contrast to previous studies in earlier chapters where rigid cylinders were considered, the semi-analytical approximation technique developed here by our collaborators [111] will predict the results of the use of thin “soft” elastic

shells. For the elastic material to be classified as soft, $\frac{c_2}{c_1} < 1$, where c_1 and c_2 are the compressional and shear wave speeds of the elastic material respectively. The properties of this material allow several relatively low-frequency resonances that generate stop bands by multiple scattering in an array. These stop bands are independent from those related to the periodic arrangement of the rigid scatterers. Using the semi-analytical approximation results, the scattering problem is solved for a single scatterer in this section and for a finite array of scatterers in section 6.9.

The problem of acoustic wave propagation through a doubly periodic array of identical elastic shells is considered. The time-harmonic dependence is taken as $e^{(-i\omega t)}$ throughout the chapter. Assuming that waves propagate in the plane perpendicular to the normal axis of infinite cylindrical shells C_j, where *j* takes positive integer values, each shell can be replaced by its cross-section (i.e. an elastic ring), see figure 6.2. The acoustic environment outside/inside of each shell is described by density $\frac{\rho_o}{\rho_i}$ and sound speed $\frac{c_o}{c_i}$, whereas the elastic linear isotropic material of the shell is represented by density ρ, compressional velocity c_1 and shear velocity c_2.

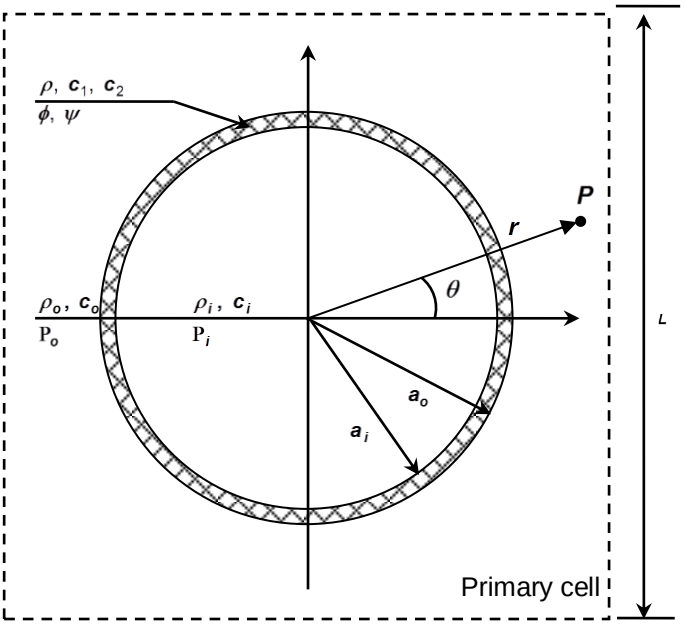

Figure 6.2: Cross-section of an elastic shell in the primary cell of doubly periodic array.

Without loss of generality, the origins of the Cartesian (x, y) and polar coordinates (r, θ) used in this section coincide with the centre of the scatterer C_0 in the primary cell of size *L*, also known as the lattice constant. Centre O_j of each scatterer in the infinite periodic array is defined by the position vector $R_j = n_1 a_1 + n_2 a_2$; where n_1 and n_2 take integer values and a_1 and a_2 are the fundamental translation vectors [105] (see chapter 1.4.2).

The equation for cylindrically-spreading acoustic waves in a lossless fluid medium previously shown in chapter 4, equation 4.1 is repeated here for convenience. The displacement potential $p(\mathbf{r})$ in the acoustic medium satisfies the two-dimensional Helmholtz equation,

$$\nabla^2 p + k_\alpha^2 p = 0\,, \qquad \textbf{(6.1)}$$

and the quasi-periodicity conditions which follow from Bloch theorem,

$$p\left(\mathrm{r}+\mathrm{R}_j\right)=e^{\left(i\beta^T \mathrm{R}_j\right)}p(\mathrm{r}). \tag{6.2}$$

Where $\nabla^2=\frac{\partial^2}{\partial x_1^2}+\frac{\partial^2}{\partial x_2^2}$ is the Laplacian, $k_\alpha=\frac{2\pi f}{c_\alpha}$ is the wave number in air defined as the ratio between angular frequency ω and sound speed of the outer acoustic environment c_α, is a given wave vector. Index α relates density to one of the acoustic media (i.e., it equals to either “o” or “i” for outside and inside environment respectively). $p(\mathbf{r})$ is related to the acoustic pressure $\Phi(\mathbf{r})$ and particle velocity potential $\hat{\Phi}(\mathbf{r})$ by:

$$\Phi=\rho_\alpha\omega^2 p\,, \tag{6.3}$$

$$\hat{\Phi}=-i\omega\, p\,, \tag{6.4}$$

The wave field in the elastic ring is represented by two displacement potentials describing the longitudinal wave $\phi(\mathbf{r})$ and the shear wave $\psi(\mathbf{r})$, which are solutions of the following equations [106]:

$$\nabla^2\phi+k_1^2\phi=0\,, \tag{6.5}$$

$$\nabla^2\psi+k_2^2\psi=0\,, \tag{6.6}$$

where $k_1=\frac{\omega}{c_1}$ and $k_2=\frac{\omega}{c_2}$.

The solutions to equation (6.1), (6.5) and (6.6) are subject to continuity conditions at the elastic–acoustic interface of scatterer C_j. This gives at $r = a_o$ and $r = a_i$:

$$\sigma_{rr} = -\rho_\alpha \omega^2 p\,, \tag{6.7}$$

$$\sigma_{r\theta} = 0\,, \text{ (no rotational)}, \tag{6.8}$$

$$\frac{\partial p}{\partial r} = \frac{\partial \phi}{\partial r} + \frac{1}{r}\frac{\partial \psi}{\partial \theta}\,. \tag{6.9}$$

Where stresses σ_{rr} and $\sigma_{r\theta}$ are defined by:

$$\sigma_{rr} = \frac{2\rho c_2^2}{r^2}\left[\frac{\partial}{\partial\theta}\left(r\frac{\partial\psi}{\partial r} - \psi\right) - \left(r\frac{\partial\phi}{\partial r} + \frac{\partial^2\phi}{\partial\theta^2}\right)\right] - \rho\omega^2\phi\,, \tag{6.10}$$

$$\sigma_{r\theta} = \frac{2\rho c_2^2}{r^2}\left[\frac{\partial}{\partial\theta}\left(r\frac{\partial\phi}{\partial r} - \phi\right) + \left(r\frac{\partial\psi}{\partial r} + \frac{\partial^2\psi}{\partial\theta^2}\right)\right] + \rho\omega^2\psi\,, \tag{6.11}$$

The solutions to the problems in equations (6.1) – (6.9) can be described by orthogonal series of Bessel and trigonometric functions. In the outer and inner acoustic media the potentials take the following forms:

$$p_o(r,\theta) = \sum_{n=-\infty}^{+\infty}\left[A_n J_n(k_o r) + B_n Y_n(k_o r)\right]\times e^{(in\theta)}\,,\ r > a_o\,, \tag{6.12}$$

$$p_i(r,\theta) = \sum_{n=-\infty}^{+\infty} E_n J_n(k_i r)\times e^{(in\theta)}\,,\ r < a_i\,, \tag{6.13}$$

whereas the solutions of the elastic shell are expanded as:

$$\phi(r,\theta)=\sum_{n=-\infty}^{+\infty}\left[C_{1,n}J_n(k_1r)+C_{2,n}Y_n(k_1r)\right]\times e^{(in\theta)},\ a_i<r<a_o, \qquad \textbf{(6.14)}$$

$$\psi(r,\theta)=\sum_{n=-\infty}^{+\infty}\left[D_{1,n}J_n(k_2r)+D_{2,n}Y_n(k_2r)\right]\times e^{(in\theta)},\ a_i<r<a_o. \qquad \textbf{(6.15)}$$

The set of unknown coefficients $\{A_n, C_{1,n}, C_{2,n}, D_{1,n}, D_{2,n}, E_n\}$ can be identified in terms of coefficient B_n by using boundary conditions at the surface of the elastic shell. Thus, substituting solutions of equations (6.12) - (6.15) into equations (6.7) - (6.9) and taking inner product $\int_0^{2\pi}\langle\cdot\rangle\, e^{(im\theta)}d\theta$ will result in an algebraic system of equations:

$$A_n=\frac{\left[a_oJ_n'(k_oa_o),\ inJ_n(k_oa_o),\ a_oY_n'(k_oa_o),\ inY_n(k_oa_o)\right]\mathrm{X}_n}{a_oJ_n'(k_oa_o)}-\frac{Y_n'(k_oa_o)}{J_n'(k_oa_o)}B_n, \qquad \textbf{(6.16)}$$

$$C_n\mathrm{X}_n=\left[0,0,-\frac{2\kappa_o\varepsilon_ok_o^2}{a_o\pi J_n'(k_oa_o)},0\right]^TB_n, \qquad \textbf{(6.17)}$$

where $a_o=$ outer boundary of the shell, J_n' = Bessel function of n-th order of the first kind, Y_n' = Bessel function of n-th order of the second kind, $-\infty<n<\infty$, $k_o=\frac{2\pi f}{c}$ (the wave number in air), $\kappa_\alpha=\frac{c_\alpha}{c_2}$, $\varepsilon_\alpha=\frac{\rho_\alpha c_\alpha}{\rho c_2}$, $Z_n'(k_\alpha r)=\frac{dZ_n(k_\alpha r)}{dr}$ is the derivative of cylindrical function, X_n is the vector $(C_{1,n}, D_{1,n}, C_{2,n}, D_{2,n})^T$ of unknown coefficients, and C_n is the matrix of 4×4 elements in the following form,

$$C_n = \begin{pmatrix} f_{1,i,J} & f_{2,i,J} & f_{1,i,Y} & f_{2,i,Y} \\ g_{1,i,J} & g_{2,i,J} & g_{1,i,Y} & g_{2,i,Y} \\ f_{1,o,J} & f_{2,o,J} & f_{1,o,Y} & f_{2,o,Y} \\ g_{1,o,J} & g_{2,o,J} & g_{1,o,Y} & g_{2,o,Y} \end{pmatrix}, \quad \textbf{(6.18)}$$

where the coefficients are defined as:

$$f_{1,\alpha,Z} = \left[-\frac{2}{a_\alpha} + \frac{\varepsilon_\alpha \kappa_\alpha k_\alpha^2 Z_n(k_\alpha a_\alpha)}{Z_n^{'}(k_\alpha a_\alpha)} \right] Z_n^{'}(k_1 a_\alpha) + \frac{2n^2 - k_2^2 a_\alpha^2}{a_\alpha^2} Z_n(k_1 a_\alpha), \quad \textbf{(6.19)}$$

$$f_{2,\alpha,Z} = \frac{in}{a_\alpha} \left\{ 2Z_n^{'}(k_2 a_\alpha) + \left[-\frac{2}{a_\alpha} + \frac{\varepsilon_\alpha \kappa_\alpha k_\alpha^2 Z_n(k_\alpha a_\alpha)}{Z_n^{'}(k_\alpha a_\alpha)} \right] \times Z_n(k_2 a_\alpha) \right\}, \quad \textbf{(6.20)}$$

$$g_{1,\alpha,Z} = \frac{2in}{a_\alpha} \left[Z_n^{'}(k_1 a_\alpha) - \frac{Z_n(k_1 a_\alpha)}{a_\alpha} \right], \quad \textbf{(6.21)}$$

$$g_{2,\alpha,Z} = \frac{1}{a_\alpha} \left[2Z_n^{'}(k_2 a_\alpha) - \frac{2n^2 - k_2^2 a_\alpha^2}{a_\alpha} Z_n(k_2 a_\alpha) \right]. \quad \textbf{(6.22)}$$

In the case of the rigid scatterer equation 6.16 is reduced to the well-known relation between coefficients A_n and B_n by setting X_n to the zero vector and ε_o to the zero value (Neumann boundary condition).

The contrast between elastic material of the shell and air medium considered here is relatively large. This can be described in term of the relative impedance,

$$\varepsilon = \frac{\rho_o c_o}{\rho c_2} << 1. \quad \textbf{(6.23)}$$

If the thickness of the elastic shell is much smaller than its mid-surface radius $R = \frac{(a_o + a_i)}{2}$, then $\eta = \frac{h}{R} < 1$, where h is half Wall Thickness (WT) of the shell.

In order to have better interaction between elastic and acoustic media, the contrast has to be reduced. This can be achieved by assuming that the relative impedance is of the same order as the ratio between half-thickness and mid-surface radius of the elastic shell. This assumption can be written as $\varepsilon \approx \eta$.

Acoustic waves are generated by a cylindrical source, which is positioned in the outer region of the shell. For convenience, but without loss of generality, the origin of the Cartesian (x, y) and polar coordinates (r, θ) coincides with the source location. Potential $p_o(\mathbf{r})$ in the outer acoustic medium satisfies the Helmholtz equation (6.1) and Sommerfeld's radiation conditions (refer to chapter 3 equation 3.10),

$$\frac{\partial p_o}{\partial r} - ikp_o = 0\left(r^{-1/2}\right), \text{ as } r \to \infty, \qquad \textbf{(6.24)}$$

where $r = \sqrt{x^2 + y^2}$. The solution representing the scattered field is given by,

$$p_{o,s}(r, \theta) = \sum_{n=-\infty}^{+\infty} A_n Z_n H_n^{(1)}(k_o \hat{r}) e^{(in\hat{\theta})}, \ \hat{r} > a_o, \qquad \textbf{(6.25)}$$

so that the total field in the outer acoustic medium takes the following form,

$$p_o(r,\theta) = H_o^{(1)}(k_o r) + p_{o,s}(r,\theta), \qquad \textbf{(6.26)}$$

where $\hat{r} = (r,\theta)$ and $\hat{\theta} = (r,\theta)$ are the polar coordinates of receiver with origin placed at the centre of scatterer, A_n are unknown coefficients and factors Z_n are found from,

$$Z_n = \frac{J_n^{'}(k_o R)}{H_n^{(1)}(k_o R) + i\hat{U}_{1,n}}. \qquad \textbf{(6.27)}$$

Note that when $\hat{U}_{1,n} = 0$ factors Z_n transform to those for the case of a rigid cylinder.

Solution for the field in the inner acoustic medium can be described by the formulation in equation 6.7. The following will describe the formulation of the thin shell medium.

Using a technique described in detail by [107], a long-wave low-frequency approximation for the wave equations of the thin-walled elastic shell based on the previous assumption regarding the thickness and relative impedance can be formulated.

The problem stated by equation 5.5 and 5.6 and boundary conditions in equation 5.7 to 5.9 can be reduced to the asymptotic equations given by:

$$\frac{1}{R^2}\left(\frac{\partial u_2}{\partial \theta}+u_1\right)-k_3^2 u_1=-\frac{\varepsilon}{k_o}\frac{k_3^2\left[\rho_o(R,\theta)-\rho_i(R,\theta)\right]}{2h}, \qquad \textbf{(6.28)}$$

$$\frac{1}{R^2}\left(\frac{\partial^2 u_2}{\partial \theta^2}+\frac{\partial u_1}{\partial \theta}\right)+k_3^2 u_2=0, \qquad \textbf{(6.29)}$$

where $u_1(\theta)$ and $u_2(\theta)$ are the approximations of the in-plane displacement components in the elastic shell, $k_3=\frac{\omega}{c_3}$ and $k_o=\frac{c_o}{c_2}$. The p-wave speed c_3 for a thin elastic plate can be defined as,

$$c_3=\sqrt{\frac{E}{\rho\left(1-\nu^2\right)}}, \qquad \textbf{(6.30)}$$

The right-hand side of equation 6.28 describes the types of surface loading applied to the walls of the shell which in our case is a membrane compression type of loading.

Equation 6.28 and 6.29 are solved in conjunction with the conditions imposed on the displacements at the shell mid-surface that are:

$$\left.\frac{\partial p_o(r,\theta)}{\partial r}\right|_{r=R}=\left.\frac{\partial p_i(r,\theta)}{\partial r}\right|_{r=R}, \qquad \textbf{(6.31)}$$

$$\left.\frac{\partial p_o(r,\theta)}{\partial r}\right|_{r=R}=u_1(\theta). \qquad \textbf{(6.32)}$$

The displacements of the elastic shell can be expanded into the Fourier series:

$$u_1(\theta)=\sum_{-\infty}^{+\infty}u_{1,n}e^{(in\theta)}\,, \qquad \textbf{(6.33)}$$

$$u_2(\theta)=\sum_{-\infty}^{+\infty}u_{2,n}e^{(in\theta)}\,, \qquad \textbf{(6.34)}$$

To perform the computation, the cylindrical source function in equation 6.26 has to be expanded into series using Graf's additional theorem (Appendix B) so that all the terms can be expressed in terms of the same origin coordinates as explained in chapter 3. This gives,

$$p_o(\hat{r},\hat{\theta})=\sum_{n=-\infty}^{+\infty}\left\{J_n(k_o\hat{r})H_n^{(1)}(k_oQ)e^{-in(\pi+\alpha)}+A_nZ_nH_n^{(1)}(k_o\hat{r})\right\}e^{in\hat{\theta}},\ \ \hat{r}>a_0\,, \qquad \textbf{(6.35)}$$

within which vector $Q=Q(\cos\alpha,\sin\alpha)$ is the radius vector to the centre of the shell.

The unknown coefficients can be derived by using asymptotic equations 6.28 and 6.29, boundary conditions 6.31 and 6.32, and the modified solution 6.35. After solving the appropriate algebraic system, coefficients A_n are derived as,

$$A_n=-H_n^{(1)}(k_oQ)e^{-in(\pi+\alpha)},\ \ -\infty<n<\infty\,. \qquad \textbf{(6.36)}$$

The formulation outlined here describes wave scattering from a thin shell made of a perfectly elastic material. Relevant viscoelasticity has to be taken into account. For rubber-like solids, viscoelasticity can be described by a linear model. The dynamic Young's modulus is,

$$E(t)=\hat{E}(1-f(t))\,, \qquad \textbf{(6.37)}$$

within which we introduce dynamic Young's modulus $\hat{E}$ and relaxation function of the following well-known form,

$$f(t)=\sum_j \hat{E}_j\left[1-e^{-\frac{t}{\tau_j}}\right], \qquad \textbf{(6.38)}$$

where the sum of measured extensional moduli $\hat{E}_j$ is taking over the relaxation time τ_j.

Applying the Laplace transform $\int_0^{+\infty}\langle\bullet\rangle e^{-st}dt$, one can derived the Young's modulus in term of the transform parameter s as:

$$E(s)=\hat{E}(1-sF(s)), \qquad \textbf{(6.39)}$$

$$F(s)=\sum_j \frac{\hat{E}_j}{(s(1+s\tau_j))}. \qquad \textbf{(6.40)}$$

This can be represented in the frequency domain by using $s=-i\omega$, so that,

$$E(\omega)=\hat{E}\left[1-\frac{\hat{E}_j}{(1-i\omega\tau_j)}\right], \qquad \textbf{(6.41)}$$

Equation 6.41 may also be obtained from the general stress-strain relationship by taking the Fourier transform $\int_0^{+\infty}\langle\bullet\rangle e^{i\omega t}dt$.

We use viscoelasticity data measured for the material with properties similar to latex used in our experiment [108]. Instead of equation 6.41, this requires use of:

$$E(\omega) = E - \sum_{j=1}^{N} \frac{i\omega\tau_j E_j}{(1 - i\omega\tau_j)}, \qquad \textbf{(6.42)}$$

$$E = \hat{E} - \sum_{j=1}^{N} \hat{E}_j \quad \text{and} \quad E = \hat{E}\hat{E}_j . \qquad \textbf{(6.43)}$$

where the Young's modulus corresponds to the equilibrium state and values of and are taken for an elastomer with properties similar to latex [108] (see table 6.1).

Relaxation time τ_j (s)	Dynamic Young's Moduli, $E_j\left(N/m^2\right)$
0	1.745361577x106
0	2.13x106
4.32x10-9	9.00x106
5.84x10-8	4.20x106
3.51x10-7	2.94x106
2.28x10-6	2.41x106
1.68x10-5	1.87x106
2.82x10-4	1.31x106
7.96x10-3	7.02x105
9.50x10-3	4.45x105

Table 6.1: Relaxation time and dynamic Young's Modulus.

Since the surrounding acoustic environment is assumed to be always the same (ρ_o = ρ_i = 1.25 kg/m^3 and c_o = c_i = 344 m/s). Also the latex material properties used for prediction are kept constant (except in section 6.7) with ρ = 1100 kg/m^3, c_1 = 954m/s, c_2 = 23m/s, E = 1.75 MPa and ν = 0.4997. Tensile testing to yield the E of latex was performed with the kind assistance of the Materials Department. The test procedure and results are provided in Appendix D and data confirmed that the E value is consistent with the approximation used. Initially, the prediction is made for a latex cylinder

with an Outer Diameter (OD) = 0.055 m and Wall Thickness (WT) = 0.00025 m but in later sections, this semi-analytical method is applied to other cylinders as well. The results shown in figure 6.3 are computed in terms of insertion loss (IL) defined as,

$$IL = 20\log_{10}\left|\frac{H_o^{(1)}(k_o r)}{p_0}\right|. \qquad \textbf{(6.44)}$$

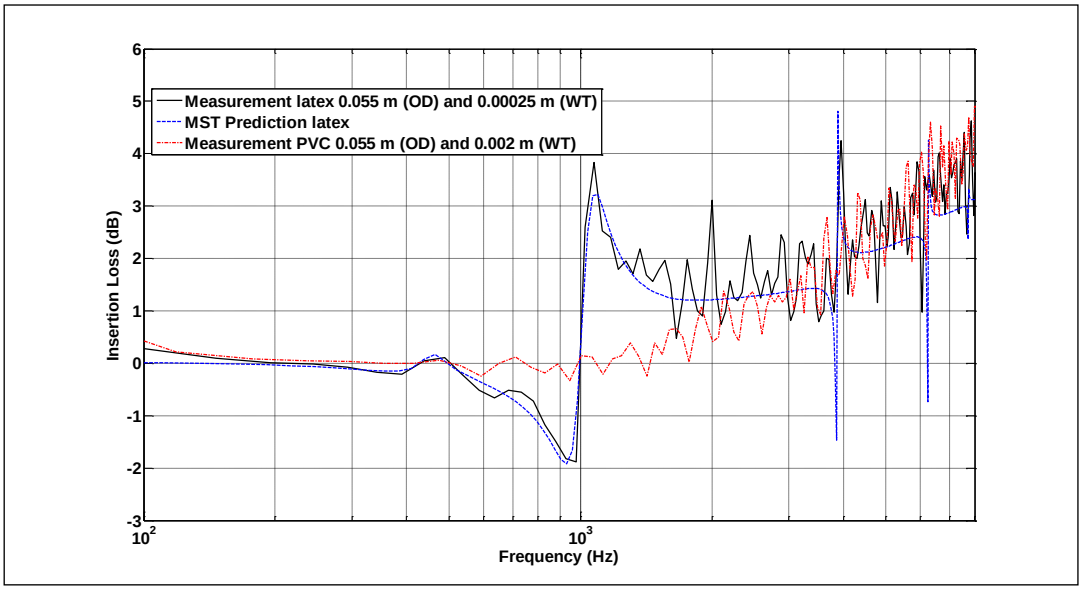

Figure 6.3: Measured (solid black line) and MST predicted (broken blue line) IL spectra for single latex scatterer of outer diameter (OD) 0.055 m, wall thickness (WT) 0.00025 m and length of 2 m. For comparison the IL spectrum measured for an acoustically "rigid" Poly Vinyl Chloride (PVC) pipe with similar diameter and length is shown also (broken red line).

In figure 6.3, the measured and MST predicted IL spectra for a single latex scatterer of Outer Diameter (OD) 0.055 m and Wall Thickness (WT) 0.00025 m are shown. A non-resonating reference spectrum (measured data) for a single Poly Vinyl Chloride (PVC) pipe of similar length (2 m), outer diameter (0.055 m) and WT (0.002 m) is shown for comparison with the latex scatterer. Clearly, the latex scatterer produces a resonance peak around 1.1 kHz which is not observed in the data for the PVC scatterer. The MST

prediction for latex agrees well with the measured latex data showing resonance peaks at around 1.1, 4 and 6.1 kHz. A negative IL peak between 500 Hz and 1 kHz is observed just below the latex resonance. The narrow band higher order resonance mode that appears in the predicted IL spectrum at around 6 kHz is not visible in the data. This might suggest that such narrow band resonance mode is difficult to excite in practice.

6.3) Proof of breathing mode concept using modal analysis through FEM - single elastic shell in vacuum (undamped)

To better understand the structural vibration problem and support the existence of a breathing mode in thin walled latex cylinder, the resonant frequencies of a structure need to be identified and quantified, this can be done using FEM. Eigenfrequencies and modes of deformation of a component can be determined using the structural mechanics module in COMSOL® Multiphysics. The modes are inherent properties of a structure and are determined by the material properties (i.e. mass, damping and stiffness) sometimes referred to as the free vibration of a structure. Firstly, eigenfrequency analysis is to find the undamped eigenfrequencies and mode shapes of an elastic shell. In COMSOL®, there is an option to choose between working with eigenfrequencies, f_{eigen} and working with eigenvalues, λ_{eigen}. The relationship for the eigenfrequencies in the structural mechanics field is related to the eigenvalue returned by the solver through,

$$f_{eigen} = \frac{\mathrm{Im}\left(\lambda_{eigen}\right)}{2\pi}. \qquad \textbf{(6.45)}$$

The eigenvalue solver extracts the Jacobian, the damping matrix and the mass matrix through Taylor expansion of the problem with respect to the eigenvalue variable around a specified eigenvalue linearlisation point. This involves finding the eigensolutions u with their associated eigenvalues, λ_{eigen}, in a Partial Differential Equation (PDE) problem of the following form,

$$\nabla.\left(-c\nabla u-\alpha u\right)+\beta.\nabla u+\alpha u=\lambda_{eigen}d_a u-\lambda_{eigen}^2 e_a u\,. \qquad \textbf{(6.46)}$$

The 2-dimensional simulation is first performed for an elastic shell with similar geometry and material properties stated in section 6.2 (figure 6.3). This is performed under vacuum for the inside and outside environments of the cylinder. Although not practical in our application the comparative study between vacuum and air environments (see section 6.4) serves as an underlying understanding of how the eigenfrequencies can be shifted due to damping. Eigenfrequency analysis istiffness chosen for this simulation and therefore solution is presented directly under the COMSOL® defined variable eigfreq_smps. Note 3-dimensional simulation for such modal analysis is not performed as it involves much higher computational resource.

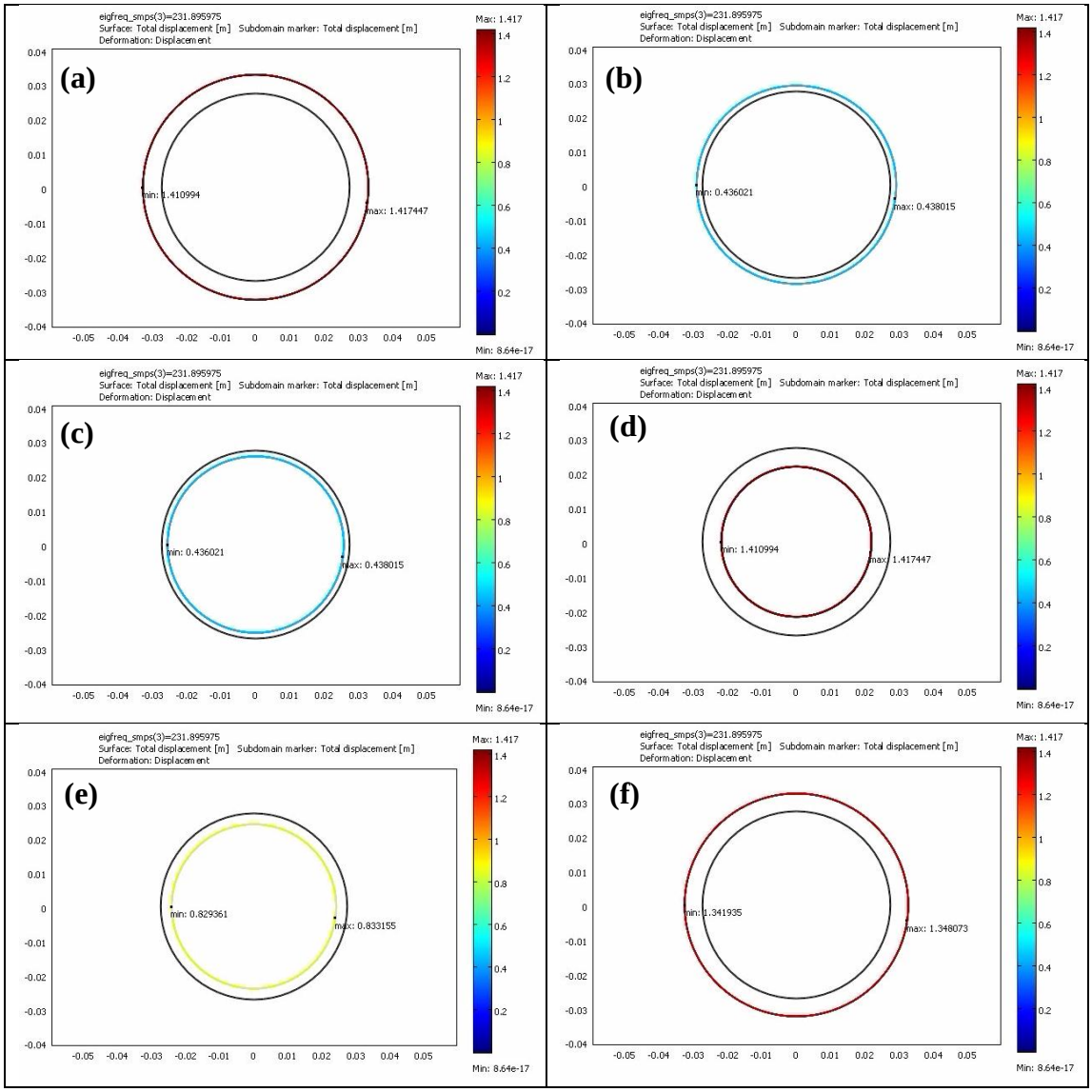

Figure 6.4: 2-Dimensional modal analysis showing static deformation plots in sequence (a-f) on the "Breathing mode" shape of elastic element in vacuum.

Figures 6.4 (a - f) shows the 2-dimensional static deformation plots in sequence of the latex breathing mode in vacuum predicted by modal analysis using FEM. Clearly, the characteristic of the mode shapes (mode of deformation) looks similar to mode 0 in figure 6.1 (a). The breathing mode (mode 0) frequency is predicted to be 232 Hz with displacement of +0.0075 m and –0.0025 m for the volumetric expansion and contraction respectively. This result differs from semi-analytical and measurement results (figure 6.3) as no damping is introduced in this simulation.

6.4) Proof of breathing mode concept using modal analysis through FEM - single elastic shell in air (damped)

The interaction between structure and air is called air-structural coupling and this must be taken into account. The important characteristic is the interaction between the two media, that is, the elastic structure will generate deformation or movement under loading by air. This in turn will influence the air flow resulting from changes in the distribution and the size of the air load. It is imperative that the solution of the single elastic shell takes account of the presence of air and thus the additional complexity of modelling air-structural coupling is necessary. The ability to couple various physics in a single modelling environment can be achieved in COMSOL® multiphysics. In this model, the boundary conditions are done in a more rigorous manner using Perfectly Matched Layers (PML) intended to absorb incident radiation without producing any reflection. In addition this formulation provides good performance for a wide range of incidence angles and is not particularly sensitive to the shape of the wave fronts. The PML formulation introduces a complex-valued coordinate transformation whereby the eigenvalue λ_{eigen} is used to perform the calculation instead of eigenfrequencies and thus equation 6.45 is required to determine the eigenfrequencies.

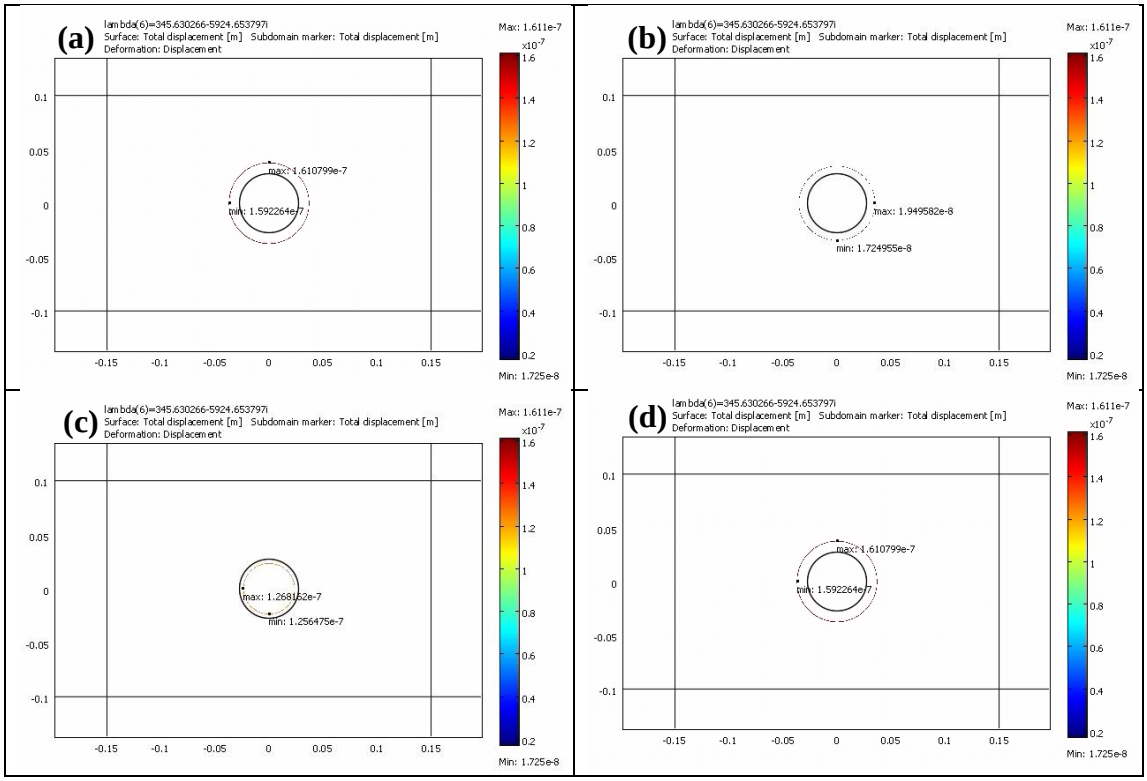

Figure 6.5: 2-Dimensional modal analysis showing static deformation plots in sequence (a-d) on the "Breathing mode" shape of elastic element coupled with air surrounded by a perfectly matched layers for the domain boundaries.

Figures 6.5 (a-d) show in sequence 2-dimensional static deformation plots of the latex breathing mode results after using perfectly matched layers for the domain boundaries. The eigenvalues have to be converted to eigenfrequencies using equation 6.45. For example $\left(\frac{5924}{2\pi}\right)$ gives an eigenfrequency of 942 Hz. Clearly with the introduction of air damping, the breathing mode (mode 0) frequency is predicted to shift to a much higher frequency with the volumetric expansion and contraction displacement of +0.0075 m and –0.0025 m respectively. The FEM predicted breathing mode resonance frequency also agrees fairly well with the semi-analytical and measurement results of about 1 kHz (figure 6.3). These modal analysis results show that the resonance is indeed a breathing mode type resonance and that there is a possibility of tuning the resonance frequency by using a

different damping ratio between the latex scatterer and surrounding environments (inside and outside).

6.5) Influence of shell diameter

In this section, the influence of the size of the elastic scatterer is studied both in laboratory and using MST. Three different types of diameter (0.0275, 0.043 and 0.055 m) with similar wall thickness of 0.00025 m are investigated.

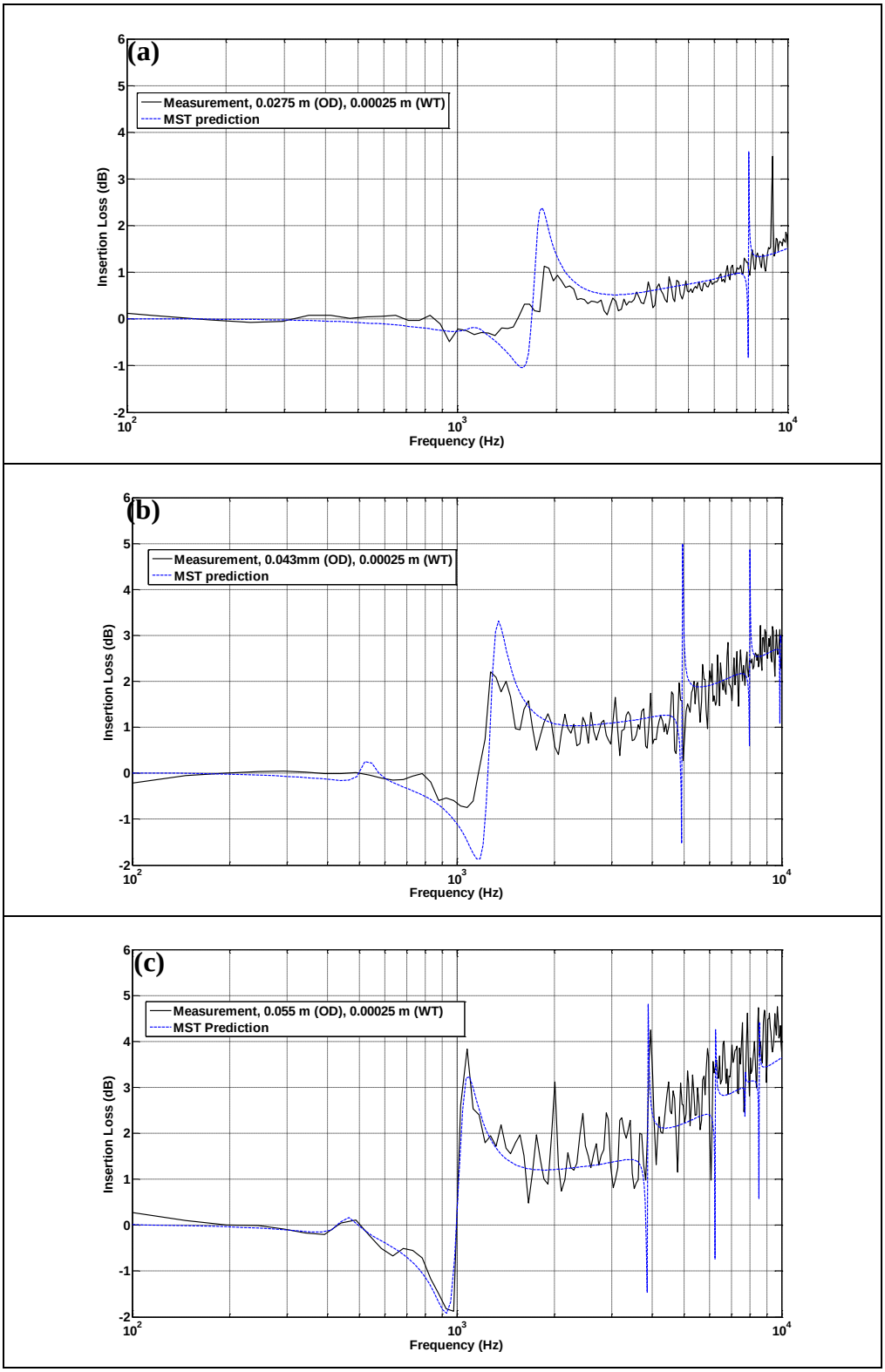

Figure 6.6: IL spectra of measurements and MST predictions for different outer diameter 0.0275, 0.043 and 0.055 m in figure (a), (b) and (c) respectively.

Figure 6.6 shows the measured and MST predicted IL spectra for single elastic shell scatterer of similar thickness of 0.00025 m but of different

diameter 0.0275, 0.043 and 0.055 m in figure (a), (b) and (c) respectively. The breathing mode resonance frequencies for diameters of 0.0275, 0.043 and 0.055 m are observed to be near 1.8, 1.5 and 1.1 kHz respectively. This clearly shows that the “breathing mode” resonance can be tuned to lower frequency by increasing the diameter of the elastic shell scatterer. For all three cases, the MST predictions agree well with the experimental results. It is also noted that the accuracy of the MST prediction for the IL amplitude improves as the diameter of the scatterer is increased. Again, the predicted narrow-band higher order modes are not observed in the data.

6.6) Influence of wall thickness

Another physical parameter of which we are keen to investigate is wall thickness of the elastic shell. Experiments and semi-analytical predictions using MST are performed for 2 different diameter sizes of elastic shell 0.043 and 0.055 m. For each of the different diameters, wall thicknesses of 0.00025 (figure 6.7(a) and (c)) and 0.0005 m (figure 6.7(b) and (d)) are used.

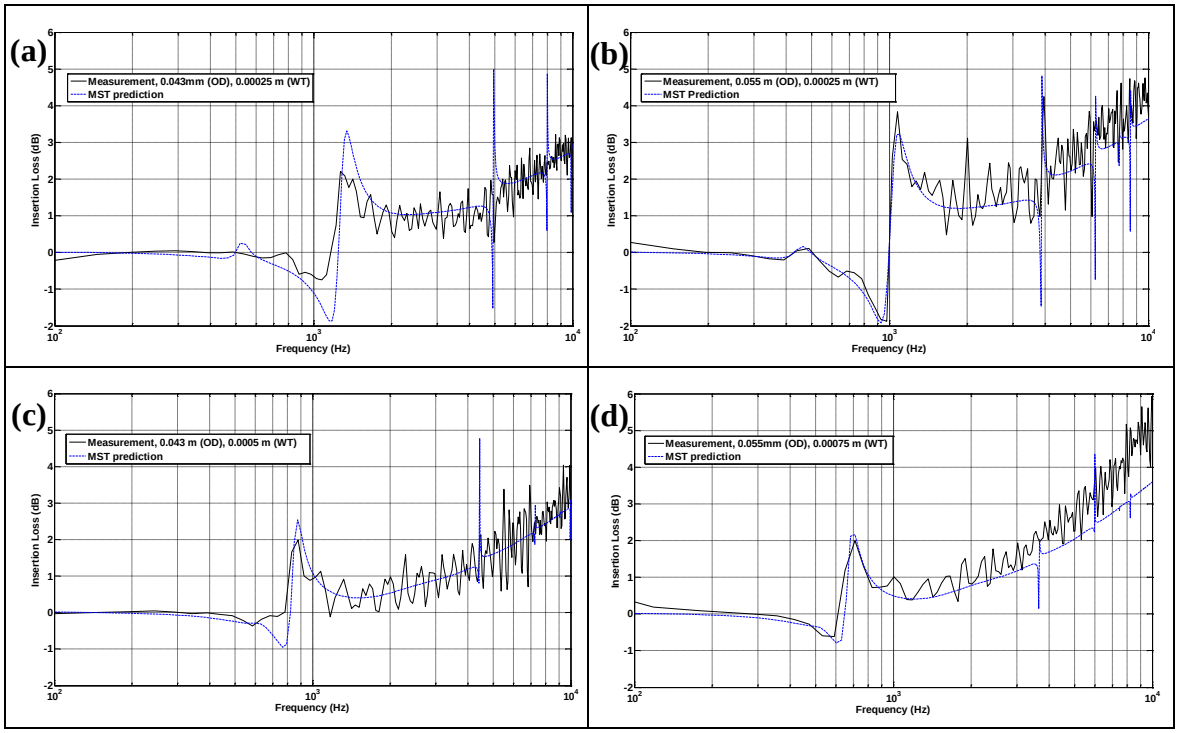

Figure 6.7: Measured and predicted IL spectra for outer diameter of 0.043 m (left panel) and 0.055 m (right panel) with two wall thicknesses of 0.00025 ((a) and (b)) and 0.0005 m ((c) and (d)) in each case.

Figure 6.7 shows the measured and MST-predicted IL spectra for single elastic shell scatterer for 2 different diameters of elastic shell 0.043 m (left panel) and 0.055 m (right panel). In the case of an elastic scatterer with outer diameter 0.043 m, the measured and predicted breathing mode resonance frequency for both experiment and MST prediction is shifted from near 1.5 kHz down to 900 Hz as the wall thickness is increase from 0.00025 m to 0.0005 m (figures 6.7(a) and 6.7(c)). A similar shift is measured and predicted with another elastic scatterer of different diameter 0.055 m (see figures 6.7(b) and 6.7(d)). The accuracy of the MST prediction is again observed to improve with increase in either the diameter or the wall thickness of the elastic shell.

6.7) Influence of material stiffness

The improved accuracy of MST predictions by associated with either increasing the diameter or the wall thickness of the elastic shell might be due to variation in the material stiffness. In this section, MST predictions are reported using the material parameters listed in table 6.2. The table specifies the longitudinal and transverse wave speed, density and Poisson's ratio for the elastic material. The upper, lower limit and the median for elastic shell are calculated.

	Longitudinal wave speed, c_1 (m/s)¤	Transverse wave speed, c_2 (m/s)	Density (kg/m^3)
Minimum	40[ж]	11	920[¥]
Median	95	22	1010
Maximum	150 [ж]	29	1100 [ж]

Table 6.2: Typical material properties of latex.

[¥] [109]
[ж] [110]

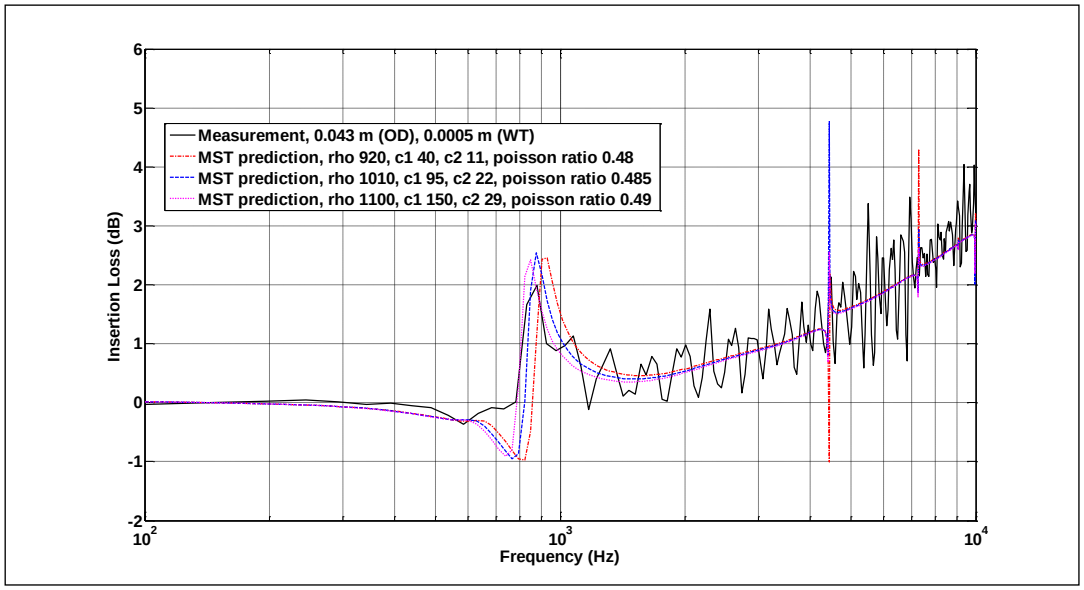

Figure 6.8: IL spectra of measurement and MST predictions of latex geometry of 0.043 m and wall thickness of 0.0005 m. MST predictions are made for the 3 different stiffness of latex (refer to table 6.2).

Figure 6.8 compares the MST predicted IL spectra using the latex material parameters provided in table 2 with measurement data for diameter 0.043 and wall thickness of 0.0005 m. The predicted resonance peak frequencies for minimum, median and maximum stiffness values for latex are near 930, 880 and 840 Hz respectively. Increasing the material density is predicted to shift the breathing mode resonance to lower frequency. This result indicates the robustness of the breathing mode resonance for such material where only a small deviation (about 100 Hz) of the resonance frequency results from the change in latex density between lowest and highest typical values.

6.8) Influence of tensioning

The complexity and computational resource that would be required for both semi-analytical and FEM calculations do not allow consideration of the influence of the 3 dimensional aspect of the latex cylinder (i.e. the finite height of the cylinder). The robustness of the breathing modes of latex cylinders to the method of end support has been investigated empirically by varying the tension at the ends of the latex cylinders between ‘loose’ and ‘tight’. To quantify the tension, the numbers of turns on the securing nuts are recorded. First, the single latex cylinder is mounted with ‘normal’ tension. Then a further 15 turns of the securing nuts (top and bottom of supporting plate) has been used to give ‘tight’ tensions and 15 less turns than required for ‘normal’ tension has been used as ‘loose’ tension.

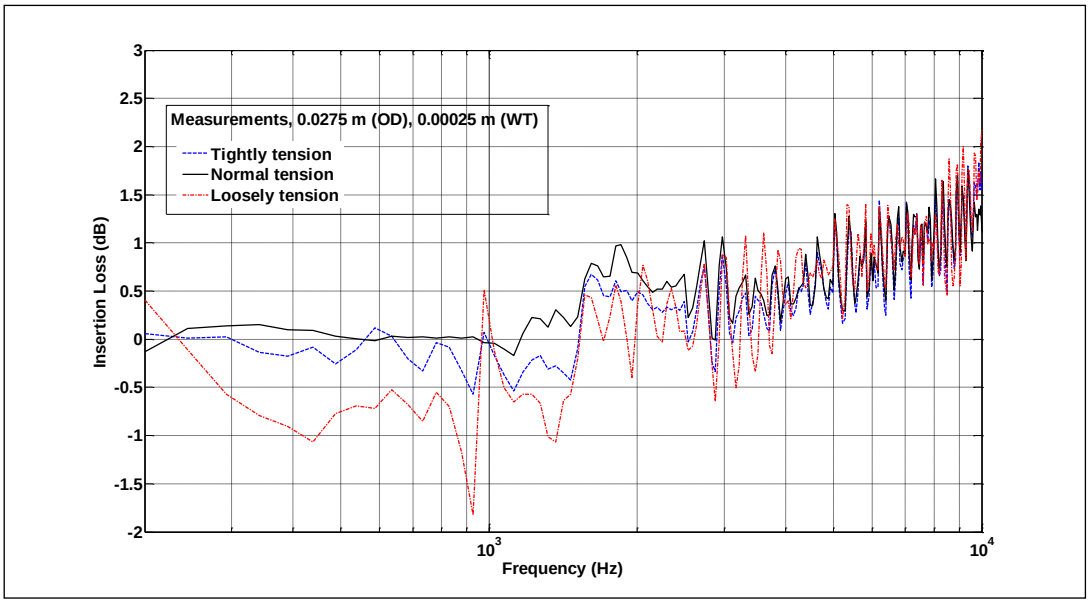

Figure 6.9: Measured IL spectra of single latex of OD 0.0275 m and WT 0.00025 m with different tensioning states (tightly, normal and loosely tension).

Figure 6.9 shows measured IL spectra obtained with a single latex cylinder of OD 0.0275 m and WT 0.00025 m with different tensioning states ('tight', 'normal' and 'loose'). The tension is controlled by the 2 mounting nuts at both top and bottom of the latex cylinder. The breathing mode resonance at around 1.7 kHz is clear for the 'tight' and 'normal' tensioning states. However for 'loose' the IL is reduced especially at low frequency.

6.9) Arrays of elastic shells

We next consider a finite array of thin elastic shells distributed in a lattice with square cells of size L (figure 6.2). Assuming that a cylindrical source generates sound waves and using a multiple scattering technique developed by our collaborators [111], the solution in the outer acoustic environment can be derived in the following form,

$$p_o(r,\theta) = H_o^{(1)}(k_o r) + \sum_{m=1}^{M}\sum_{n=-\infty}^{+\infty} A_n^m Z_n^m H_n^{(1)}(k_o \hat{r}_m) e^{(in\hat{\theta}_m)}, \qquad \textbf{(6.47)}$$

where M is the number of scatterers in the array, the first sum is taken over all numbers of shells in the array, the factors Z_n^m take the previously derived from equation 6.27 specified to the scatterer with index m, and variables $\hat{r}_m(r,\theta)$ and $\hat{\theta}_m(r,\theta)$ are the polar coordinates with origin in the center of shell of index m. Note that the solutions for the shells and the inner acoustic medium are identical to those in section 6.2.

To compute the unknown coefficients A_n^m in equation 6.47, we again need to express solution in equation 6.47 in terms of one set of polar coordinates $(\hat{r}_m, \hat{\theta}_m)$ using Graff's Additional theorem that results in,

$$p_o(\hat{r}_m, \hat{\theta}_m) = \sum_{n=-\infty}^{+\infty} \left\{ \begin{array}{l} J_n(k_o \hat{r}_m) H_n^{(1)}(k_o Q_m) e^{-in(\pi+\alpha_m)} + A_n^m Z_n^m H_n^{(1)}(k_o \hat{r}_m) \\ + \sum_{p=1, p\neq m}^{M} \sum_{q=-\infty}^{+\infty} A_q^p Z_q^p J_n \times (k_o \hat{r}_m) H_{q-n}^{(1)}(k_o Q_{mp}) e^{i(q-n)(\pi+\alpha_{mp})} \end{array} \right\} \times e^{in\hat{\theta}_m} \qquad \textbf{(6.48)}$$

$$, \; m = 1,...,M,$$

where vector $Q_m = Q_m(\cos\alpha_m, \sin\alpha_m)$is the radius vector to the centre of scatterer C_m and vector $Q_m = Q_{mp}(\cos\alpha_{mp}, \sin\alpha_{mp})$ defines the position of scatterer C_p with respect to scatterer C_m.

Use of the modified solution 6.48 in equations 6.28, 6.29, 6.31 and 6.32 together with the solutions of inner acoustic medium and elastic shell makes it

possible to derive the system of algebraic equations, which is similar to the equation 3.36 (chapter 3). This gives,

$$A_n^m + \sum_{p=1,\,p\neq m}^{M}\sum_{q=-N}^{+N} A_q^p Z_q^p H_{q-n}^{(1)}\left(k_o Q_{mp}\right) e^{i(q-n)(\pi+\alpha_{mp})} = -H_n^{(1)}\left(k_o Q_m\right) e^{-in(\pi+\alpha_m)}, \quad m = 1,\ldots,M, \tag{6.49}$$

The obtained algebraic system must be truncated to the finite number M(2N+1) of equations, and then can be used to obtain the coefficients A_n^m, $n = 1, \ldots, N$, $m = 1,\ldots, M$ numerically. Again the results are plotted in terms of Insertion Loss (IL) as in equation 6.27.

To compare the semi-analytical results with data for arrays, viscoelasticity defined by a Young's modulus of complex form (equation 6.42 and 6.43) is again introduced and this leads to redefining unknown coefficient in equation 6.48 by solving system equation 6.49 with modified elastic parameters.

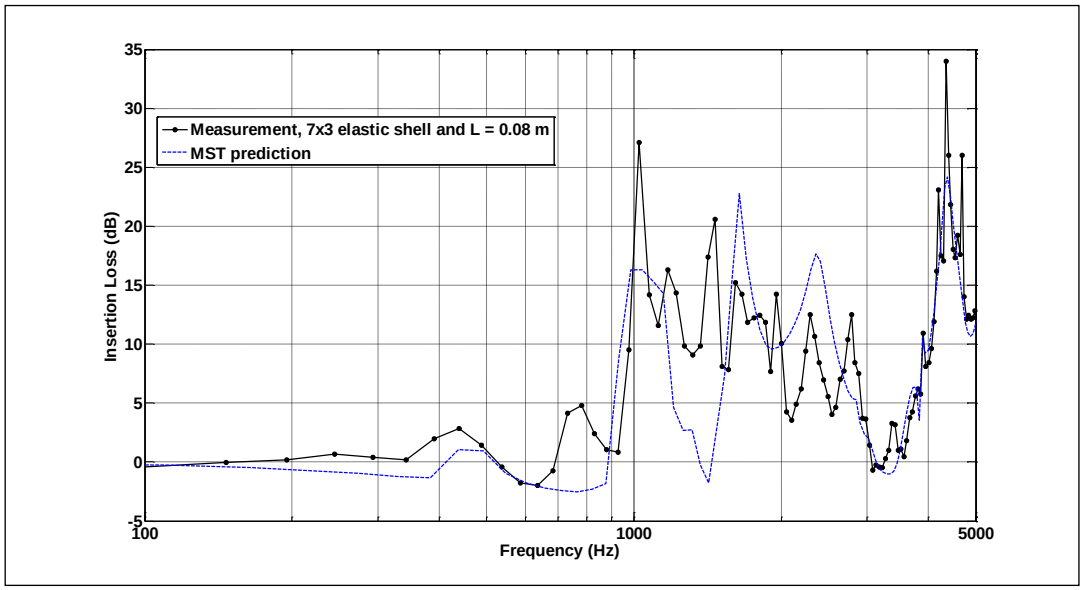

Figure 6.10: Measured and MST predicted IL spectra for an array of latex shell scatterers of outer diameter (OD) 0.055 m and wall thickness (WT) 0.00025 m with lattice constant 0.08 m.

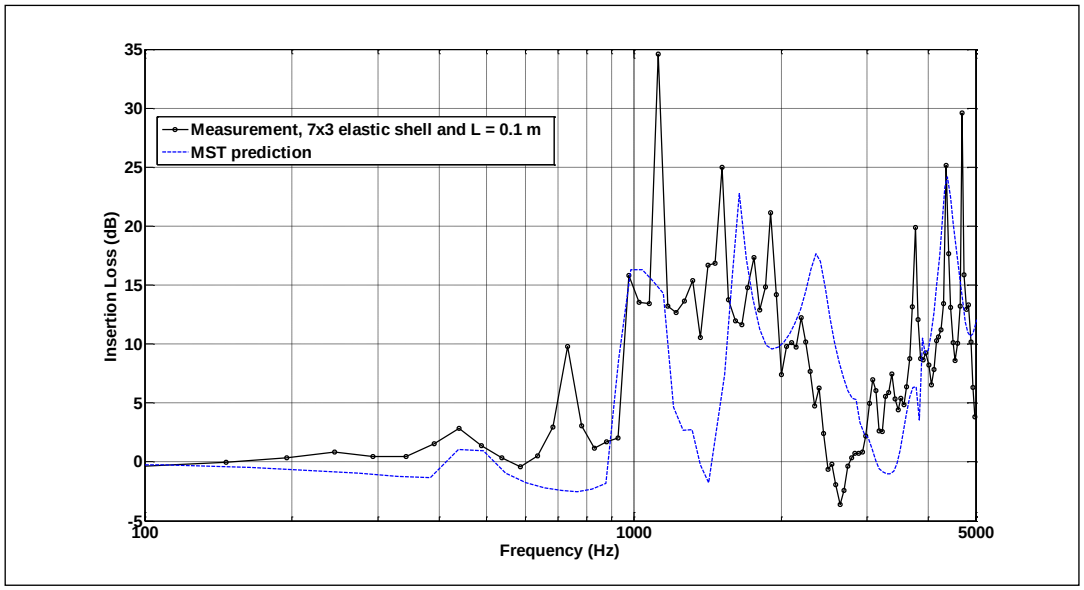

Figure 6.11: Measured and MST predicted IL spectra for an array with lattice constant 0.1 m of latex shell scatterers having outer diameter (OD) 0.055 m and wall thickness (WT) 0.00025 m.

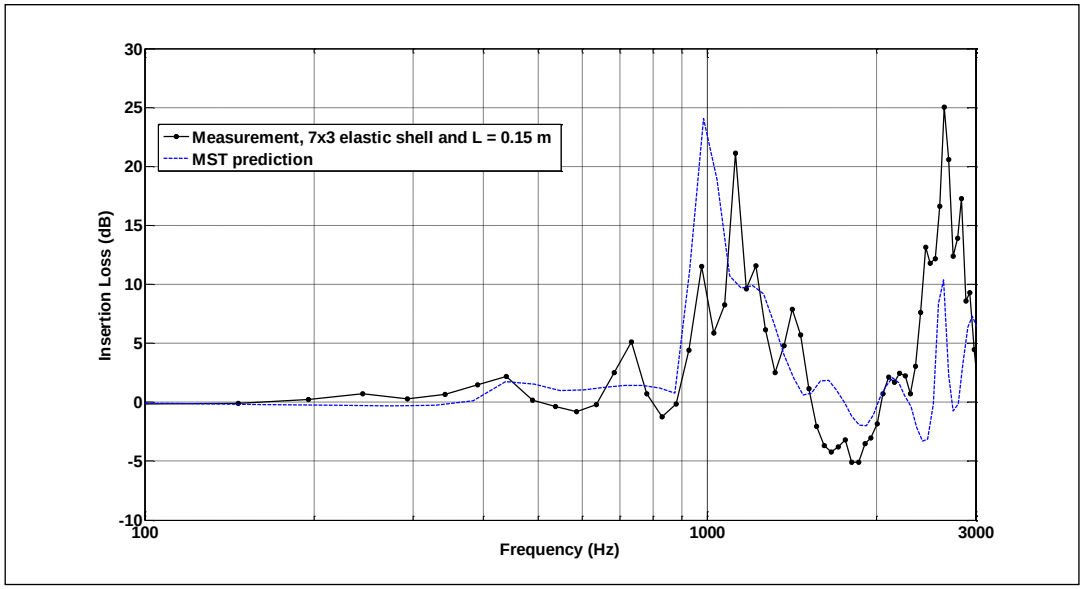

Figure 6.12: Measured and MST predicted IL spectra for an array with lattice constant 0.15 m of latex shell scatterers having outer diameter (OD) 0.055 m and wall thickness (WT) 0.00025 m.

In figure 6.10 – 6.12 show the measured and MST predicted IL spectra for a 7x3 square lattice array with lattice constants of 0.08 m, 0.1 m and 0.15 m respectively. Each latex shell used in all three array configurations has OD 0.055 m and WT 0.00025 m (similar to the single scatterer use in figure 6.3).

The calculated Bragg band gap central frequencies defined by equation 2.13 (chapter 2) for lattice constants of 0.08 m, 0.1 m and 0.15 m are 2.1 kHz, 1.7 kHz and 1.1 kHz respectively. The predictions show relatively good agreement with measured data. The peaks near 1 kHz in figures 6.10 and 6.11 can be identified as the result of the resonant behaviour of the elastic shells which is independent of the effect due to periodicity. The discrepancy in amplitude between theoretical and experiment results for the resonant peak may be explained by the differences between assumed and actual source and receiver positions during the experiments. Also in the low-frequency regime, the assumed values of the viscoelasticity parameters influence the agreement between data and predictions. The peak at about 750 Hz could be due to the finite height of the array as discussed in chapter 4.

6.10) Influence of angle between source-receiver and array axes

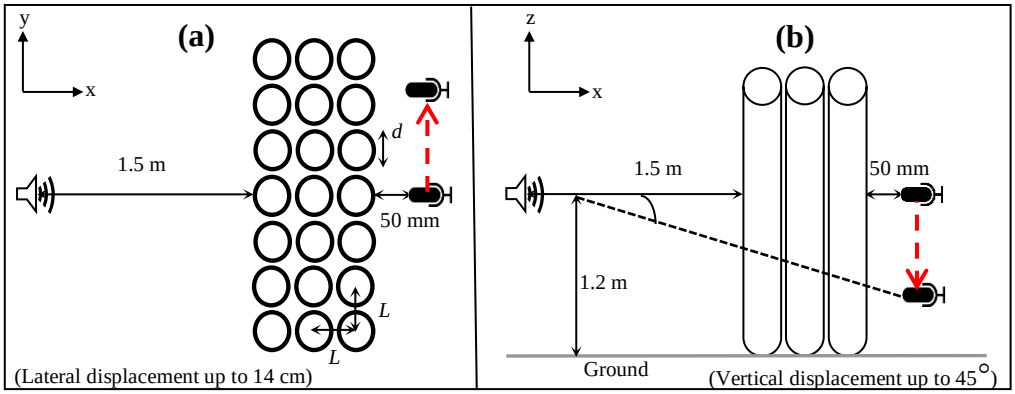

Figure 6.13: (a) Plan view of the source, receiver and array in the laboratory measurements at normal incidence and microphone laterally displace (see red arrow) up to 14 cm (b) the corresponding side view with microphone vertically displace (see red arrow) up to 45° from normal incidence.

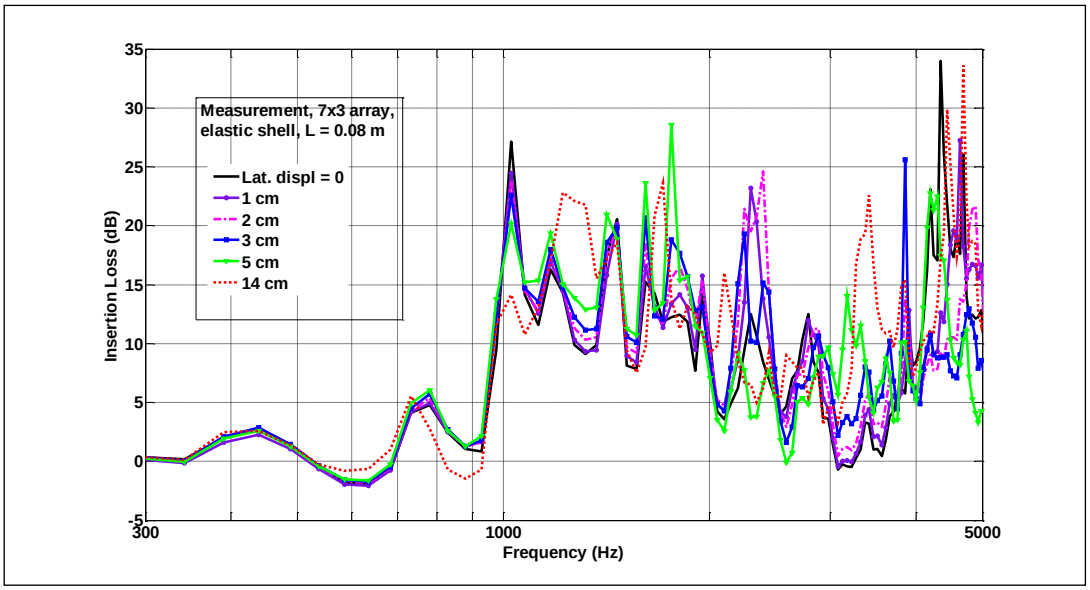

Figure 6.14: Lateral displacement, measurement IL spectra for array with lattice constant 0.08 m of latex scatterers having outer diameter (OD) 0.055 m and wall thickness (WT) 0.00025 m.

Figure 6.14 shows the IL spectra measured for 7x3 square lattice array of latex scatterer of OD 0.055 m and WT 0.00025 m with lattice constant of 0.08 m. The microphone position is laterally displaced up to 14 cm from the normal incidence position (corresponding to an angle of less than 10°), see figure 6.13(a). The constancy of the low frequency peaks around 1 kHz supports the contention that these IL peaks correspond to resonance of the latex cylinders and should therefore be relatively independent of the source-receiver angle. The Bragg band gap central frequency for this lattice configuration is around 2 kHz, similar to that for a rigid scatterer array with the same dimensions. It seems that the classical band gap is not angle dependent either. However further displacement of the receiving microphone was not possible without introducing diffraction from the array edges. The peak at around 700 Hz attributed to the finite height of the array (refer to FEM chapter 4) is fairly constant except for the largest displacement.

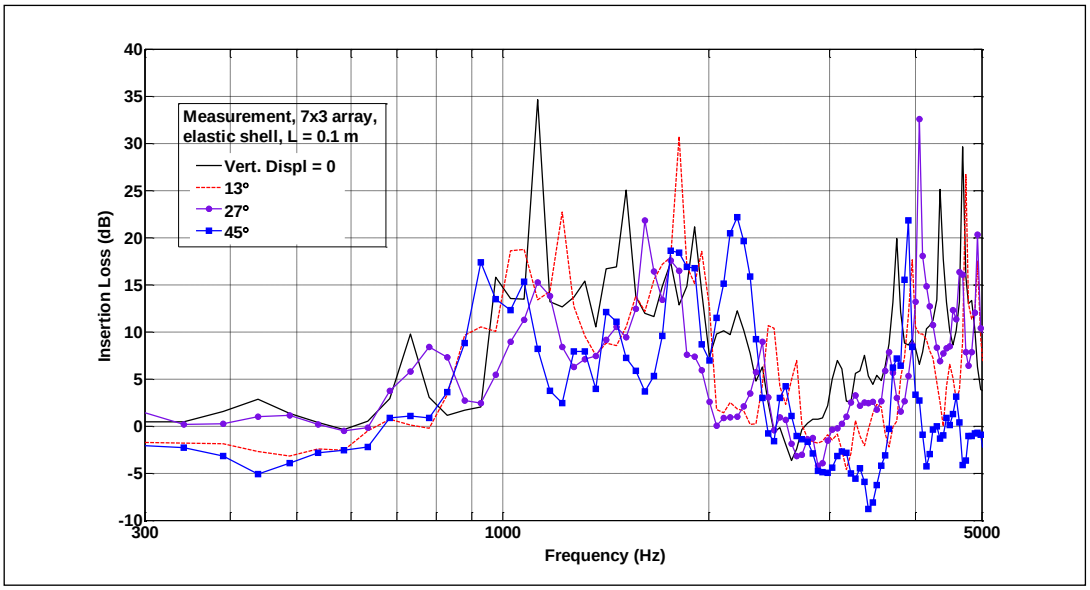

Figure 6.15: Lateral displacement, measurement IL spectra for array with lattice constant 0.15 m of latex scatterers having outer diameter (OD) 0.055 m and wall thickness (WT) 0.00025 m.

Figure 6.15 shows the measured IL spectra due to a 7x3 square lattice array with lattice constant of 0.1 m of latex scatterers having OD 0.055 m and WT 0.00025 m as the microphone position is vertically displaced up to 45° from the normal incidence source-receiver axis, see figure 6.13(b). On average there is a decrease of about 15 dB in the band gap magnitude between 1 and 2 kHz as the elevation angle is changed from 0 to 45°. One possible explanation is that the breathing mode for the latex shell is supported only by waves incident in the plane normal to the cylinders. A second possible reason could be the influence of reflections from the end plates of the supporting structure (see 6.17). Further displacement of the receiving microphone was not possible to avoid diffraction from the base of the supporting structure. These results also support the argument that the peak at around 700 Hz could be attributed to the finite height of the array.

6.11) Calculation of transmission for a single latex cylinder using FEM

An alternative proof of the breathing mode concept for latex shells results from the use of FEM. The transmission problem for a single latex scatterer can be solved using COMSOL® Multiphysics. An acoustic-structural interaction model for an elastic shell and air both inside and outside of the elastic shell is developed. The model combines 2 acoustic time harmonic analyses representing internal and external air which is separated geometrically by an axial-symmetric structural-mechanic analysis that represents the elastic shell (figure 6.16 (a)). The domain boundaries are implemented by using Perfectly Matched Layers (PML) which eliminates reflection from the edges. A cylindrical source is assumed which propagates parallel to the Ox axis of the elastic shell. The boundary condition at the interface between each model is summarised in table 6.3. A triangular mesh has been used and inside the domain the element size is at least 6 times smaller than the shortest wavelength to be computed. A parametric sweep solver is run as explained in section 4.2 (chapter 4). The predicted pressure plot is plotted at 1050 Hz for the exterior environment (figure 6.16 (b)). Clearly lower acoustic pressure is observed behind the elastic scatterer at this particular frequency.

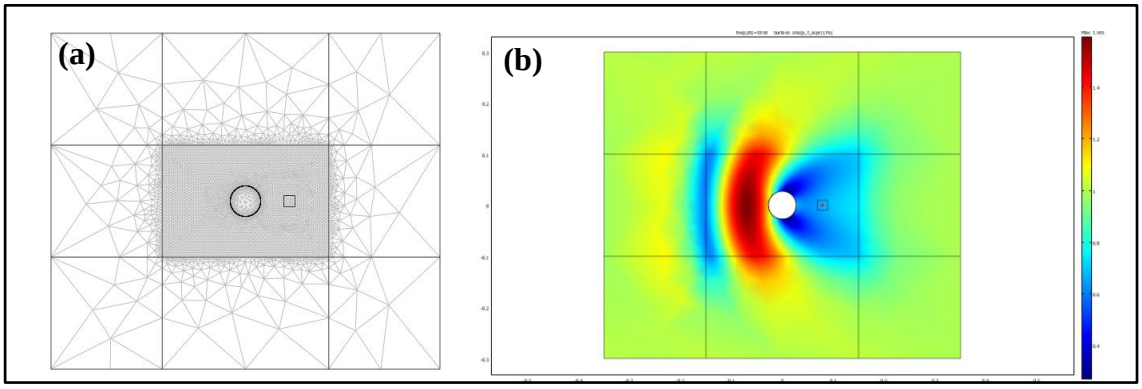

Figure 6.16: Meshing of single latex with OD 0.055 m and wall thickness (WT 0.00025 m (a). FEM predicted pressure plot at 1050 Hz for the exterior environment of the model (b).

	Air outside cylinder	Elastic cylinder	Air inside cylinder
Model suffix	Acpr (Acoustic)	smps (Structural Mech.)	acpr2 (Acoustic)
Inner wall	Continuity	Load (N/m^2) -p2*nx_smps (x-direction) -p2*ny_smps (y-direction)	Normal acceleration (m/s^2) u3_tt_smps*nx_smps+ v3_tt_smps*ny_smps
Outer wall	Normal acceleration (m/s^2) u3_tt_smps*nx_smps+ v3_tt_smps*ny_smps	Load (N/m^2) -(p+p_i_acpr)*nx_smps (x-direction) -(p+p_i_acpr)*ny_smps (y-direction)	Continuity

Table 6.3: Summary of boundary conditions used in the acoustic structural interaction model.

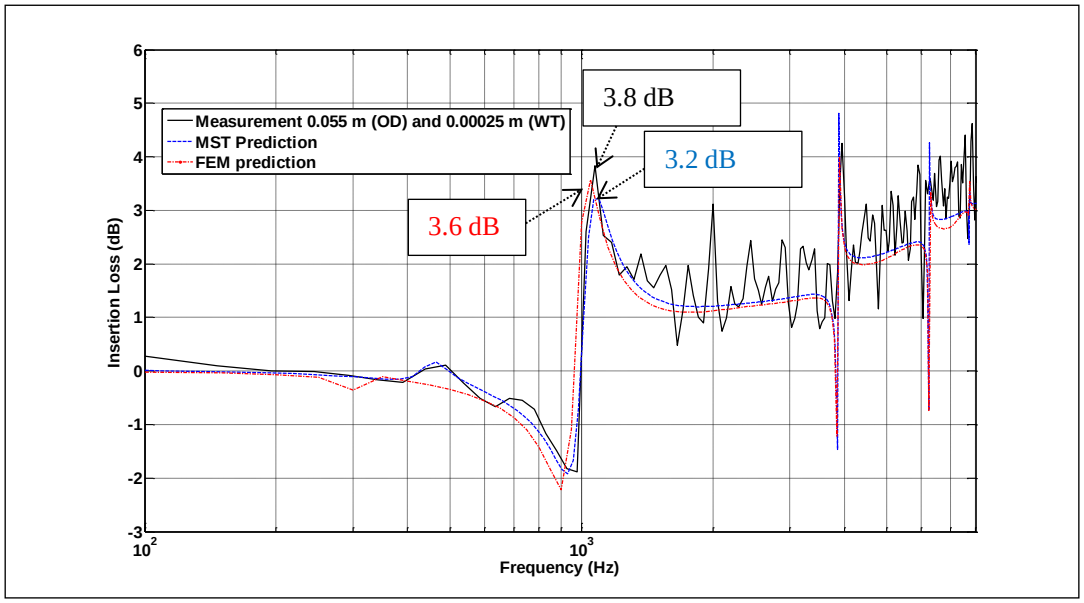

Figure 6.17: Measured and predicted (FEM and MST) IL spectra for a single latex scatterer having 0.055 m (OD) and wall thickness 0.00025 m (WT).

According to figure 6.17, the IL spectrum predicted by FEM agrees with both MST predictions and the measurement data for the single latex scatterer (0.055 m (OD) and wall thickness 0.00025 m (WT)). For all measurements and predictions, the receiver is positioned 0.05 m away from the scatterer. The IL values at 1 kHz (breathing mode resonance frequency) for all the 3 spectra are shown in the figure. The discrepency between the prediction and measurement at the Bragg frequency is about 0.6 dB. Higher order modes are observed by FEM as well as MST but due to the narrow band characteristics, these modes are not observed in the measurements.

6.12) Fabrication of specimen and effect of non-uniformity in latex scatterer

To make the 2 m long elastic shells, latex sheets (2 m long and 0.00025 m thick) have been formed into cylinders with outer diameter of 0.0275 and 0.055 m, respectively. This has been achieved by folding each latex sheet into a cylindrical shape, overlapping the edges by a few millimetres (< 0.01 m) and gluing them together using cyanoacrylate. Perspex circular end caps with metal bolts were made for both ends of the latex cylinder and used to attach them to holed wooden boards at the top and base of the cylinders. To maintain their shape and vertical orientation, the latex cylinders were slightly inflated above atmospheric pressure through a common pipe driven by a small pump. Nevertheless some deviations from the cylindrical shape could not be avoided.

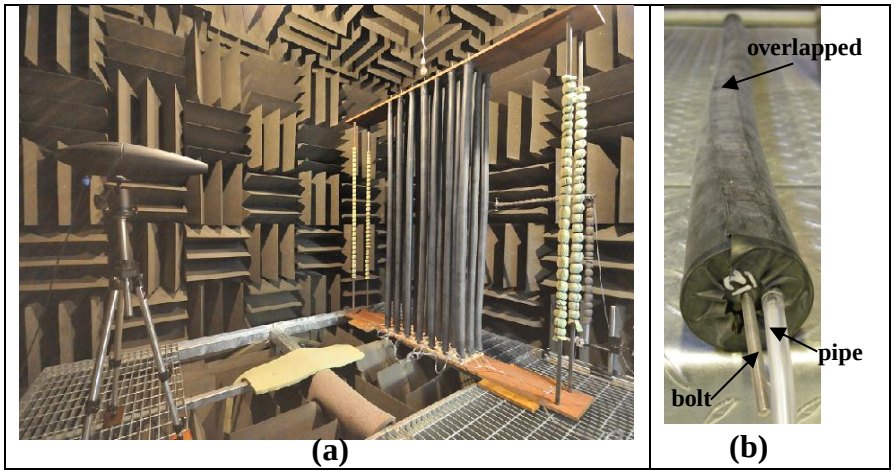

Figure 6.18: Measurement setup for array of cylinders of 7x3 arrays of latex (a) and a single latex showing the overlapping strip, mounting bolt and pipe for air inlet (b).

To quantify the variation in the shapes of the latex scatterers, 21 latex cylinders of OD 0.055 m, WT 0.00025 m and length of 2 m were tested individually. The diameters were measured at 3 positions with a calliper (see table 6.4). The resulting mean diameter and standard deviation are 0.05732 m and 0.00126 m respectively.

Scatterers no.	Diameter measured at 0.5 m of the scatterers (m)	Diameter measured at 1 m of the scatterers (m)	Diameter measured at 1.5 m of the scatterers (m)
1	0.0574	0.0573	0.0587
2	0.0575	0.0599	0.0577
3	0.058	0.0587	0.0588
4	0.0597	0.056	0.0557
5	0.0563	0.0572	0.0574
6	0.0585	0.0584	0.0587
7	0.0566	0.0568	0.0566
8	0.0564	0.0587	0.0572
9	0.0568	0.0584	0.055
10	0.0567	0.056	0.0574
11	0.0579	0.056	0.0579
12	0.0566	0.0583	0.0578
13	0.0582	0.0575	0.055
14	0.0569	0.0566	0.0577
15	0.0562	0.0587	0.056
16	0.0563	0.0592	0.0588
17	0.0585	0.06	0.0587
18	0.0564	0.0547	0.0577
19	0.0591	0.0563	0.056
20	0.0572	0.0564	0.055
21	0.057	0.0567	0.0556

Table 6.4: Diameters at three cross sections along 21 latex cylinders.

To check the extent to which the variation in shape influenced the acoustical performance, the IL has been measured for each individual scatterer. To carry out the IL measurements, the individual latex scatterers were marked and positioned at specific locations in the support structure corresponding to their positions in the arrays which were considered in section 6.11. This simultaneously tested the influence of the metal beams at the side of the supporting structure (see figure 6.18a). During the test the overlapping and glued section of each cylinder was positioned to face the microphone. For comparison, the mean latex diameter of 0.057 m (measured) is simulated using the MST prediction.

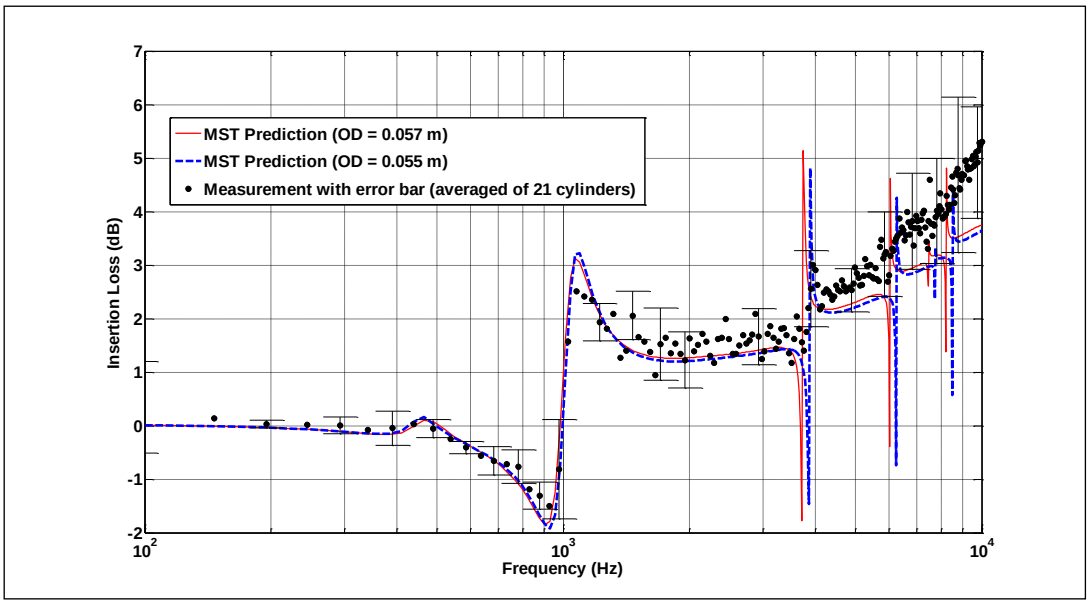

Figure 6.19: Averaged of 21 measurements of IL with error bars (indicating the range of data at each frequency) and MST predicted IL spectra for a single latex scatterer of (outer diameter (OD) 0.055 m and wall thickness (WT) 0.00025 m) (blue broken line) and (OD 0.057 m and WT 0.00025 m) (red solid line).

The averaged measured IL spectrum with error bars representing the range of data at each frequency for 21 individual scatterers and the comparison with the MST prediction are shown in figure 6.19. The agreement between the measured and predicted IL spectra indicates that the latex resonance was not greatly influenced by the variation in cylinder shapes. Given the small variation in the diameter (OD) of latex cylinder in the predictions, the effect is negligible.

6.13) Effect of gluing on the resonances of the shell

The elastic shell with glued section has a non-uniform cross section both in respect of thickness and stiffness which may have a significant effect on the performance of the SC composed of these shells. To study this effect the shell has been modelled, using COMSOL® Multiphysics 3.5, as an elastic

material containing a rigid strip. Figure 6.20 illustrates the geometry used in the 2D numerical simulation. A rigid inclusion of width 0.01 m has Neumann boundary conditions imposed at the acoustic interface and fixed faces (zero displacement) at the elastic interface. The source is a cylindrical wave propagating parallel to the Ox axis. In the formulation of the FE model, the outer environment is surrounded by perfectly matched layers (PML) which replaces the radiation condition and as such the domain size can be reduced. The 2-Dimensional Finite Elements (FE) simulation is defined by the triangular elements and the active domain is meshed by at least six elements per wavelength. The hardware configuration used to run the simulations was a 64-bits windows platform with 3.07 GHz Intel core i7 processor and 6 GB of RAM. The estimated computational time for solving the full problem in the frequency interval (0, 8000) Hz is 15 mins. Constrained by the computational resources, only a single latex scatterer is simulated. However a full array simulation has been performed by our collaborators [111]. Also note that in contrast with their simulation, the simulation done here is performed with a cylindrical wave rather than a plane wave. The results are found to have similar characteristics despite the differences in the source and number of scatterers,

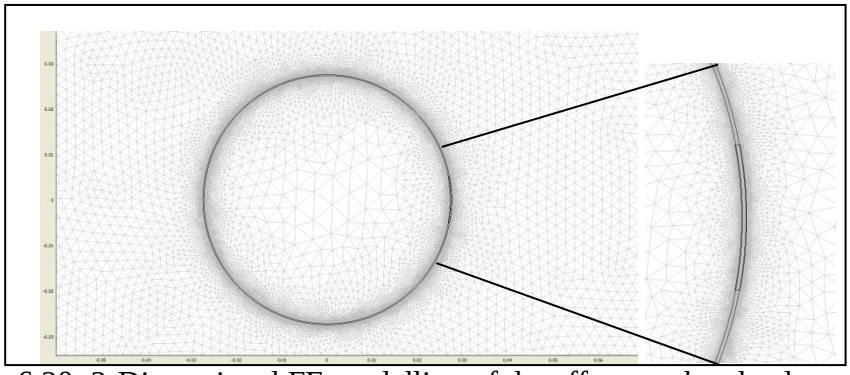

Figure 6.20: 2-Dimensional FE modelling of the effect on the glued overlapping section (section blown up for clarity).

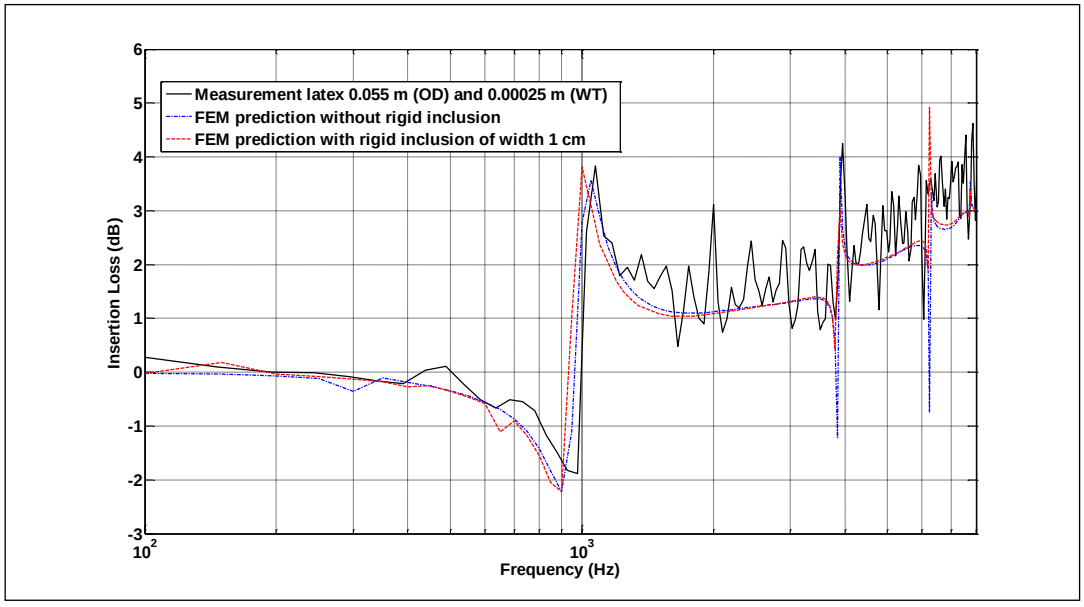

Figure 6.21: Measured and FEM-prediction IL spectra due to a single latex cylinder (with and without rigid inclusion) of outer diameter (OD) 0.055 m and wall thickness (WT) 0.00025 m

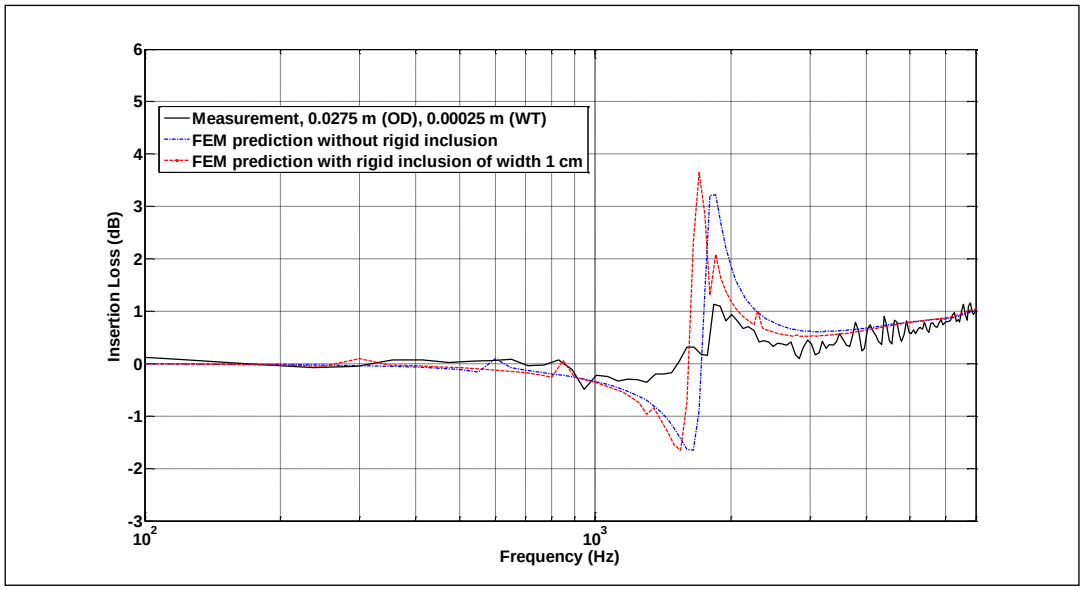

Figure 6.22: Measured and FEM-prediction IL spectra due to a single latex cylinder (with and without rigid inclusion) of outer diameter (OD) 0.0275 m and wall thickness (WT) 0.00025 m

In figure 6.21, measured and FEM-predicted IL spectra (with and without rigid inclusion) are due to a single latex cylinder (OD 0.055 m and WT 0.00025 m) are compared. Clearly, the effect of introducing a rigid inclusion is very small. The first peak which corresponds to the breathing mode is predicted to be shifted slightly (by 100 Hz) to a lower frequency if there is a 1 cm rigid inclusion. Figure 6.22 shows a similar comparison for a single scatterer with smaller OD 0.0275 and WT 0.00025 m. The FEM-predictions also agree well with the measured data except for over prediction of the IL level in the case of the smaller latex cylinder. Nevertheless, in the frequency regions where the breathing mode there is good agreement between data and predictions. This study supports the hypothesis that increasing the material stiffness leads to a lower breathing mode frequency (see section 6.7).

6.14) Effect of disc attachment on the latex scatterer

The industrially-manufactured latex cylinders used for some of the experiments were delivered in 0.7 m lengths due to the limitating size of the standard mould used during the manufacturing process. To lengthen the cylinder, a Perspex disc of slightly larger diameter was used to join the individual latex cylinders together (see figure 6.23). This improvised approach also served to restore and maintain their cylindrical shape as the latex cylinders were flattened when they are delivered. Nevertheless segments along the scatterers were observed to be more elliptical than cylindrical. The difference is more prominent at the “extreme flat region” which has the largest semi-major axis. Another anomalous region is the “inflated region”, about 0.05 m deviation from the joining disc, where the cylinder starts to deviate from the cylindrical shape maintained by the disc. The average dimensions taken from 5 cylinders for these two regions are shown in the insert in figure 6.23. Laboratory measurements have been carried out to check on the influence on the breathing mode of the introduction of rigid disc and the changes in shape along each latex scatterer. For convenience, measurements performed at the semi-major axis are denoted as “face” measurements and those made at “extreme flat and inflated” regions are denoted as ‘edge’ (see figure 6.23).

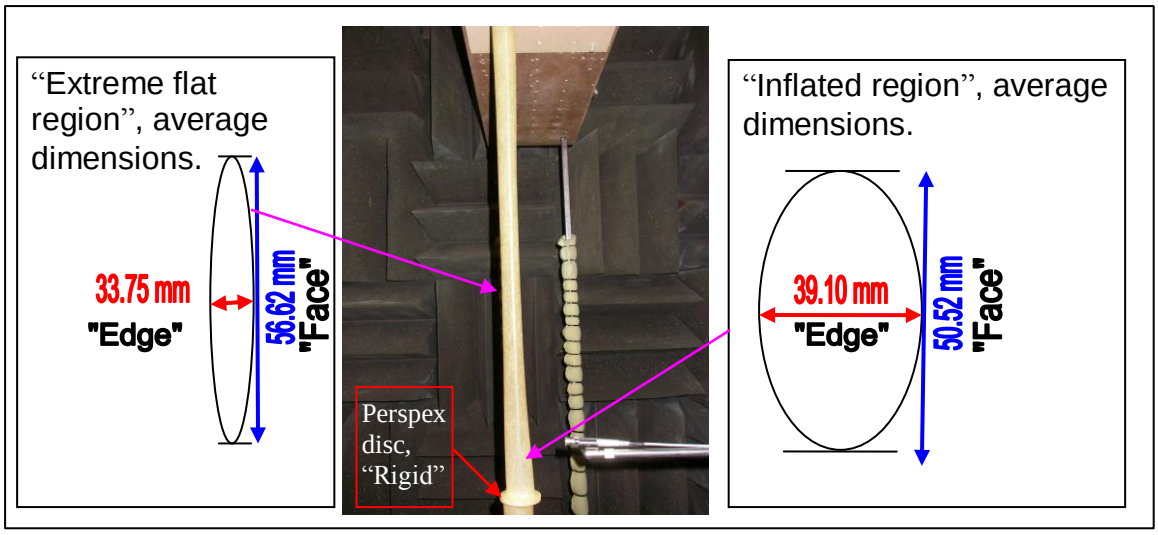

Figure 6.23: Industrially-manufactured latex cylinders joined by a Perspex disc ("Rigid") and mounted between supports in the anechoic chamber. The insert on the left shows the shape of an "Extreme flat region" with averaged dimensions and the insert on the right shows an "Inflated region" with averaged dimensions.

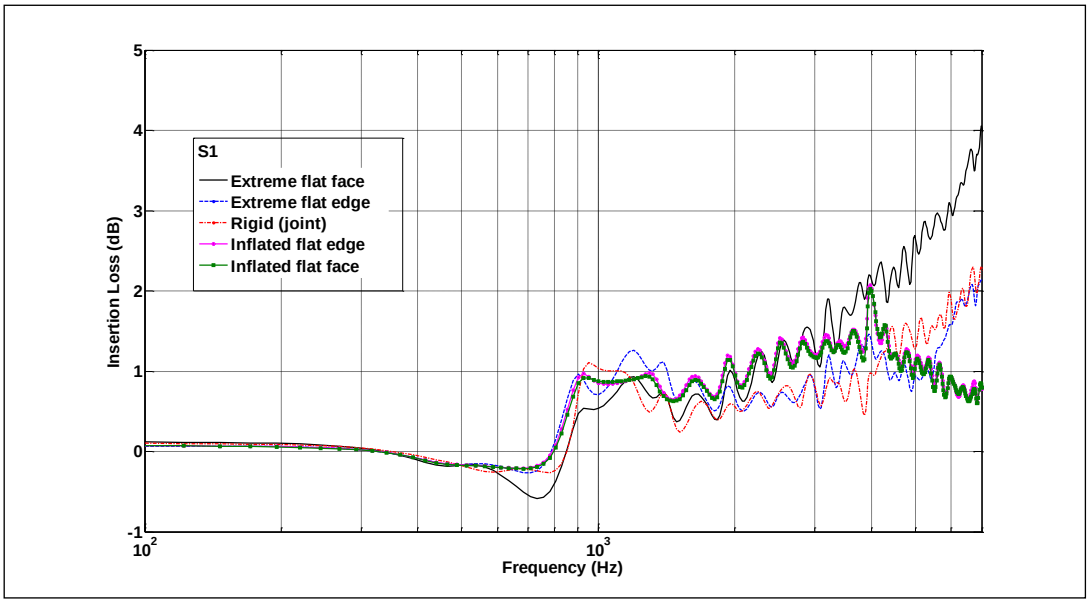

Figure 6.24: IL spectra of single industrial latex (Sample 1, S1) at all 5 positions (Extreme flat face/edge, rigid and inflated face/edge).

Figure 6.24 shows the IL spectra of a single industrially-manufactured latex cylinder at all 5 positions illustrated in figure 6.23. Clearly, the breathing mode resonance near 900 Hz is preserved in all the positions despite the non-uniformity of the scatterer. This indicates that the breathing mode resonance is little influenced by the method of joining the latex cylinders.

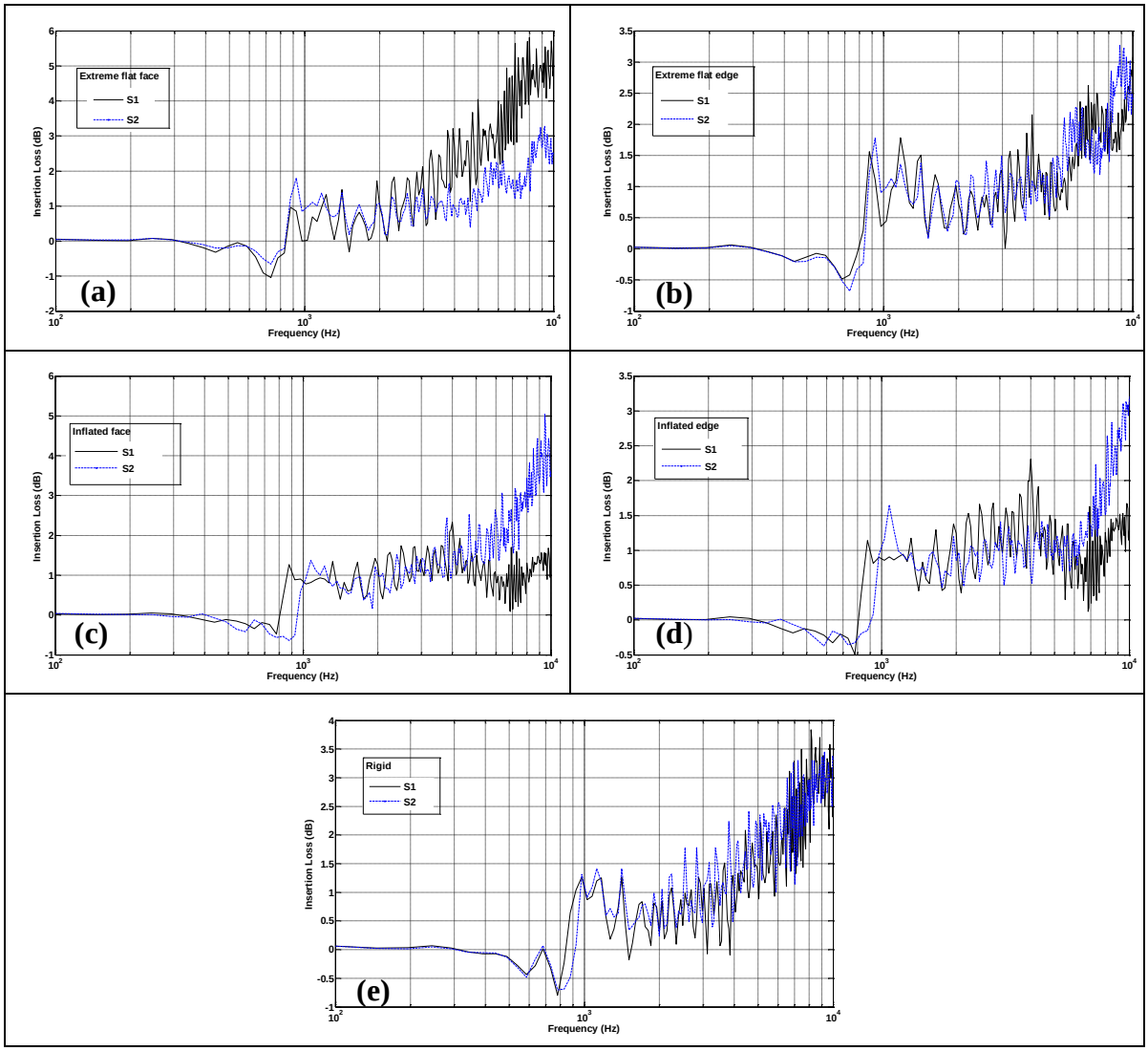

Figure 6.25: IL spectra of consistency test for 2-single industrial latex (Sample 1 (S1) and 2 (S2)) at all 5 positions (Extreme flat face (a) or edge (b), inflated face (c) or edge (d) and rigid (e)).

Laboratory measurements have been made on another single industrial latex cylinder constructed in a similar way using Perspex disc. Figure 6.25 shows the IL spectra comparing two single industrial latex cylinders at 5 different receiver locations opposite portions with (a) an extremely flat face (b), an extremely flat edge (c) an inflated face (d) an inflated edge and (e) rigid. The results show that the breathing mode resonance frequency (near 1 kHz) is fairly consistent between both cylinders. The deviation between the IL spectra at higher frequency could be due to the

precise location of receiver with respect to the cylinder. These single elastic cylinders results confirm the robustness of the breathing mode resonance.

6.15) Industrial latex array results

Based on the successful prototype test on the single latex cylinder, arrays of elastic cylinders have been constructed and their performance has been determined by laboratory measurements.

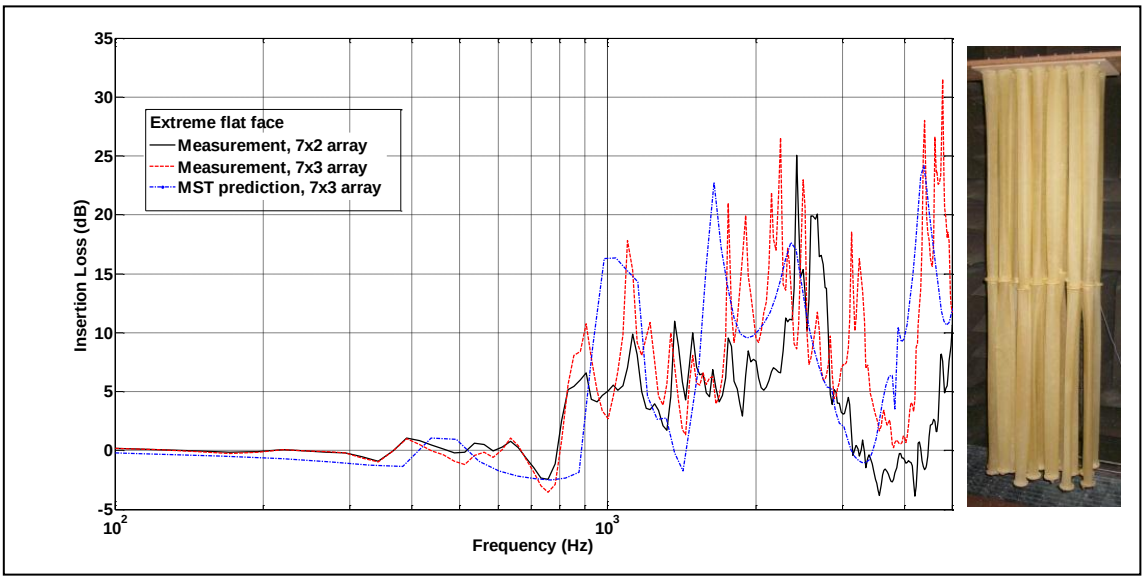

Figure 6.26: Measured IL spectra due to 7x2 and 7x3 arrays of industrial latex cylinders and an MST predicted IL spectrum for a 7x3 latex array. The insert on the right shows a photograph of the industrial latex array.

Figure 6.26 shows measured IL spectra due to 7x2 and 7x3 arrays of industrial latex cylinders at normal incidence. The receiver was located at 0.05 m from the centre of the nearest row of the array. The lattice constant for this set up is 0.069 m and the calculated Bragg band gap central frequency is 2.5 kHz (refer to PWE chapter equation 2.13). Indeed the peak due to the Bragg band gap is near 2.5 kHz in both measured IL spectra and this band gap is enhanced by the breathing mode resonance of the latex which is at 900 Hz.

The MST predicted IL spectrum for the 7x3 latex arrays also shows the 2 distinct band gap peaks and the other features in the predicted IL spectrum agrees with those in the measured spectrum. These results indicate that significant improvement in band gap widths can be achieved by adding a row to the array but one has to consider the larger array area and costs that would be incurred.

Chapter 7

Enhancing the performance of sonic crystal noise barriers by using Split Ring Resonator (SRR) and composite cylinders

7.1) Introduction

In the previous chapter, it was shown that the insertion loss spectra produced by periodic arrays of resonant scatterers using thin elastic shells benefit from both Bragg scattering and individual scatterer resonance. However, an array of elastic shells exposed to the environment would not be practical as an outdoor noise barrier. Moreover there are types of resonant elements other than thin elastic shells. So in this chapter, the possibilities for using alternative local resonance methods will be explored. One such possibility is the use of the Split Ring Resonator (SRR). The concept of SRR was initially introduced by Pendry *et al* in 1999 [112] in the context of the electromagnetism. There have been theoretical and experimental studies on SRR which introduce ranges of frequencies related to the resonant frequency in which waves cannot propagate through the system [113 and 114]. This potentially allows increasing insertion loss in the low-frequency regime if the resonant frequencies of the scatterer lie below the first stop band associated with the Bragg-scattering-type mechanism. In recent years the application of such scatterers in the design of negative index metamaterials has been studied intensively [115 and 116]. It has also been shown numerically that good sound focusing can be achieved by an array of SRRs arranged in a

lens-like configuration [117]. A particular type of resonator (known as a Helmholtz resonator) consists of a bottle almost entirely enclosing a volume of air, with a small opening, or neck, resulting in a coupling between the air in the neck and the external air in the room [118]. There are also similar air cavity-type resonators such as half- and quarter-wave tubes used commonly on air intake systems to attenuate noise at specific frequencies [119]. The dimensions of the resonator are small compared with the wavelength of sound at which it will resonate.

7.2) Working principles of a conventional Helmholtz resonator

Helmholtz resonators are often used as components in acoustic filters, the acoustic analog of electric wave filters. Helmholtz resonator consists of a rigid cavity with a protruding neck that connects to the cavity (see figure 7.1). The behaviour of a Helmholtz resonator is analogous to that of a vibration absorber in that the volume of air in the neck of the Helmholtz resonator behaves much like a vibration absorber mass and the volume of air acts like a compliance (reciprocal of stiffness). The excitation is provided by pressure fluctuation acting over the opening of the neck, resulting in oscillations of the volume of air in the neck. Damping is the result of radiation losses at the neck ends and viscous losses due to friction of the oscillating air in the neck. When air is forced into a cavity, the pressure inside increases. When the external force pushing the air into the cavity is removed, the higher-pressure air inside will flow out. The cavity will be left at a pressure slightly lower than the

outside, causing air to be drawn back in. This process repeats with the magnitude of the pressure changes decreasing with time.

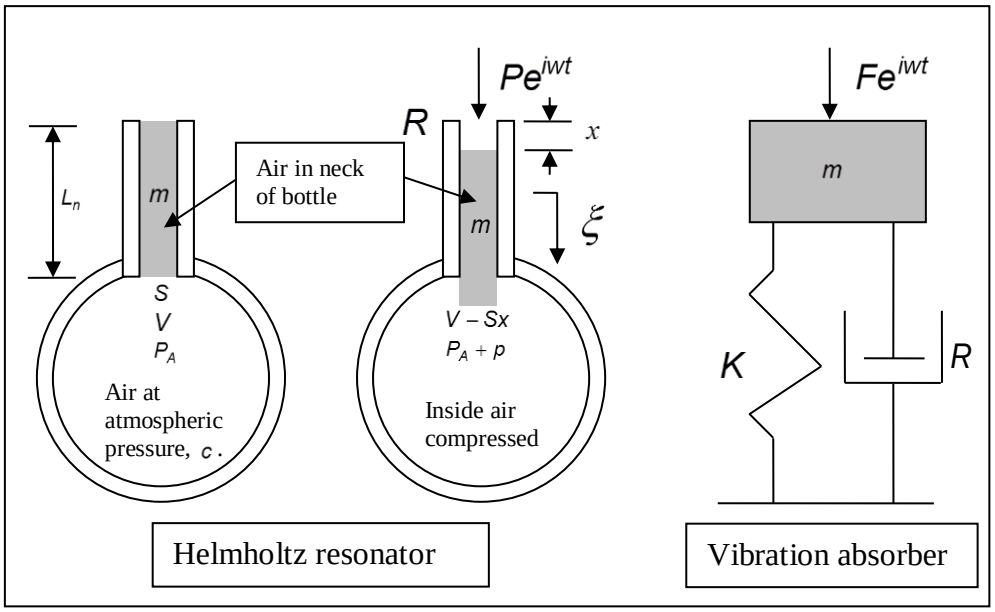

Figure 7.1: Illustration of Helmholtz resonator and vibration absorber.

It can be shown that the effective mass of a Helmholtz resonator is approximately,

$$m = \rho S L_n , \qquad \textbf{(7.1)}$$

where ρ is the density of the air, S is the cross section area of the neck and L_n is the effective neck length which includes a correction factor for mass-loading due to air entrainment near the neck extremities [120]. If this "plug" of air descends a small distance x into the bottle, it compresses the air in the container so that the air that previously occupied volume V now has $V - Sx$. Consequently the pressure of the air rises from atmospheric pressure p_A to a higher value $p_A + p$.

For such vibrations that give rise to sound, changes to the increasing pressure in respect of the decreasing volume are fast and temperature rises on compression, giving a large change in pressure. This is an adiabatic process and the resulting equation involves a constant γ, the ratio of specific heats, which is about 1.4 for air. The pressure change p produced by a small volume change ΔV can be expressed by,

$$\frac{p}{p_A} = -\gamma \frac{\Delta V}{V} = -\gamma \frac{Sx}{V}. \qquad \textbf{(7.2)}$$

The mass m is moved by the difference in pressure between the top and bottom of the neck, i.e. a net force pS, so acceleration a can be determine using Newton's law (second law of motion):

$$F = ma,$$
$$\text{or } \frac{d^2x}{dt^2} = \frac{F}{m}, \qquad \textbf{(7.3)}$$

substituting for F and m gives:

$$\frac{d^2x}{dt^2} = \frac{pS}{\rho S L_n} = -\gamma x \frac{Sp_A}{\rho V L_n}, \qquad \textbf{(7.4)}$$

so that the restoring force is proportional to the displacement. This is an equation for Simple Harmonic Motion (SHM) at a frequency which is $\frac{1}{2\pi}$ times the square root of the constant of proportionality i.e.,

$$f = \frac{1}{2\pi}\sqrt{\frac{\gamma S p_A}{\rho V L_n}}\,, \tag{7.5}$$

The speed c of sound in air is determined by the density, the pressure and ratio of specific heat so equation 7.5 can be written as,

$$f = \frac{c}{2\pi}\sqrt{\frac{S}{V L_n}}\,, \tag{7.6}$$

An example calculation of the pressure inside a 2D Helmholtz resonator at its resonant frequency has been performed by the Finite Element Method (FEM) using COMSOL® and is shown in figure 7.2. The parameters are L_n = 0.01 m, outer radius = 0.0275 m, inner radius = 0.0255 m and the opening = 0.004 m. The pressure map at 410 Hz indicates that the maximum values of the acoustic pressure occur inside the cavity. This result agrees with the calculated resonance frequency of 415 Hz using equation 7.6.

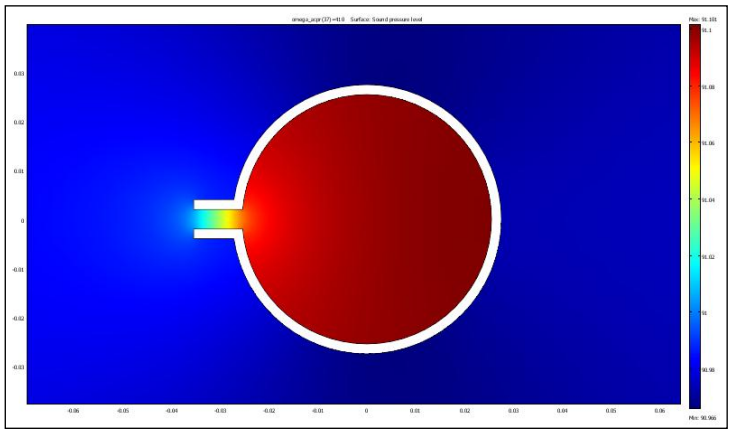

Figure 7.2: COMSOL® pressure plot at 410 Hz of a 2D Helmholtz resonator.

7.3) SRR array design

SRRs have been formed from Polyvinyl Chloride (PVC) cylinders by gouging out 0.004 m width slits along the majority of their lengths (Figure 7.3). However, the difference between the opening in a bottle and a slit on a pipe requires a special geometrical approximation [121]. This approximation takes account of both the length (i.e. the thickness of the walls) and the aperture of the neck of the resonator in order to consider the slit pipe as a Helmholtz resonator. Alternatively, the resonance frequency can be found by running a FEM simulation in COMSOL®. Arrays of such SRRs could then potentially be used to create band gaps in the range of frequencies below the bandgap associated with Bragg scattering. The dimensions of the various SRRs used in our laboratory and outdoor *in situ* experiments are listed in table 7.1. To enable a direct comparison between their performances, the dimension of laboratory scatterer type SRR1 is made similar to those of the non-resonating (rigid PVC) and resonating (elastic shell breathing mode) reference elements considered previously. However a larger size of scatterer (SRR2) is used for the outdoor measurements. The laboratory measurements and data analysis are performed as described for the rigid PVC and elastic shells discussed in chapters 2 and 6. Details of the measurement techniques can be found in chapter 5. For convenience, an illustration of the laboratory measurement arrangement for an SRR array is provided in figure 7.4.

Figure 7.3: Example slotted pipe SRR

Scatterer type	Diameter, d (m)	Wall thickness, (mm)	Slit width, α (mm)	Lattice constant, L (mm)	Array size
SRR1†	0.055	2	4	70, 80 and 135	7x3
SRR2*	0.110	3	12	160	54x3
† used in laboratory measurements. * used in outdoor measurements.					

Table 7.1: Specifications of array geometries

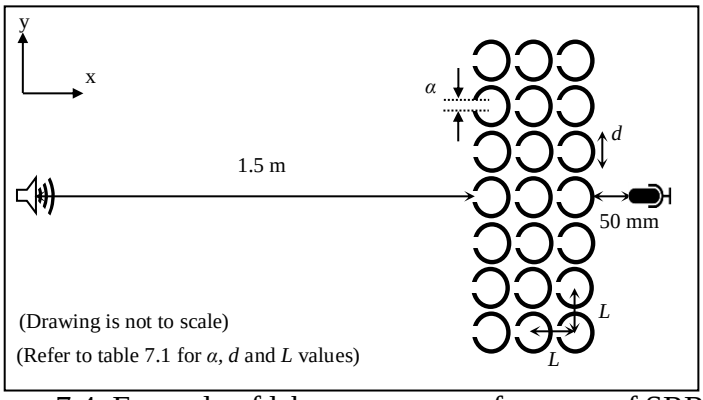

Figure 7.4: Example of laboratory set up for array of SRR.

7.4) Numerical model

Finite element based software COMSOL® Multiphysics (version 3.5a) has been used to simulate the scattering of acoustic waves in 2D first with a single slotted pipe SRR and then for 3 rows of 7 SRRs arranged in a square lattice in air. For the FEM modelling, the dimensions of the various SRR scatterers and the experimental setup used are described in table 7.1 and figure 7.4. The geometry of the SRR can be easily modified from the complete circular “acoustically hard” scatterer (chapter 4) by building the SRR domain using the standard 2D draw tool menu. Following the descriptions on chapter

4, the source is implemented with cylindrical waves and Perfectly Matched Layers (PML) is used for the domain boundaries. To obtain the level of accuracy, triangular element meshing is done with the number of elements per wavelength chosen to be at least 6.

7.5) SRR results

Insertion Loss (IL) spectra have been calculated using chapter 3 equation 3.37 to determine the performance of the SRR scatterer. It should be noted that the slits are all facing the source at the Ox plane as illustrated in figure 7.4. The FEM results are then compared with data.

7.5.1) Single SRR

For single SRR, the result is compared with non-resonating reference (i.e. cylinder made from PVC without any slit) of the same geometry. For convenience, the non-resonating references for type SRR1 and SRR2 will be referred to as NRR1 and NRR2 respectively.

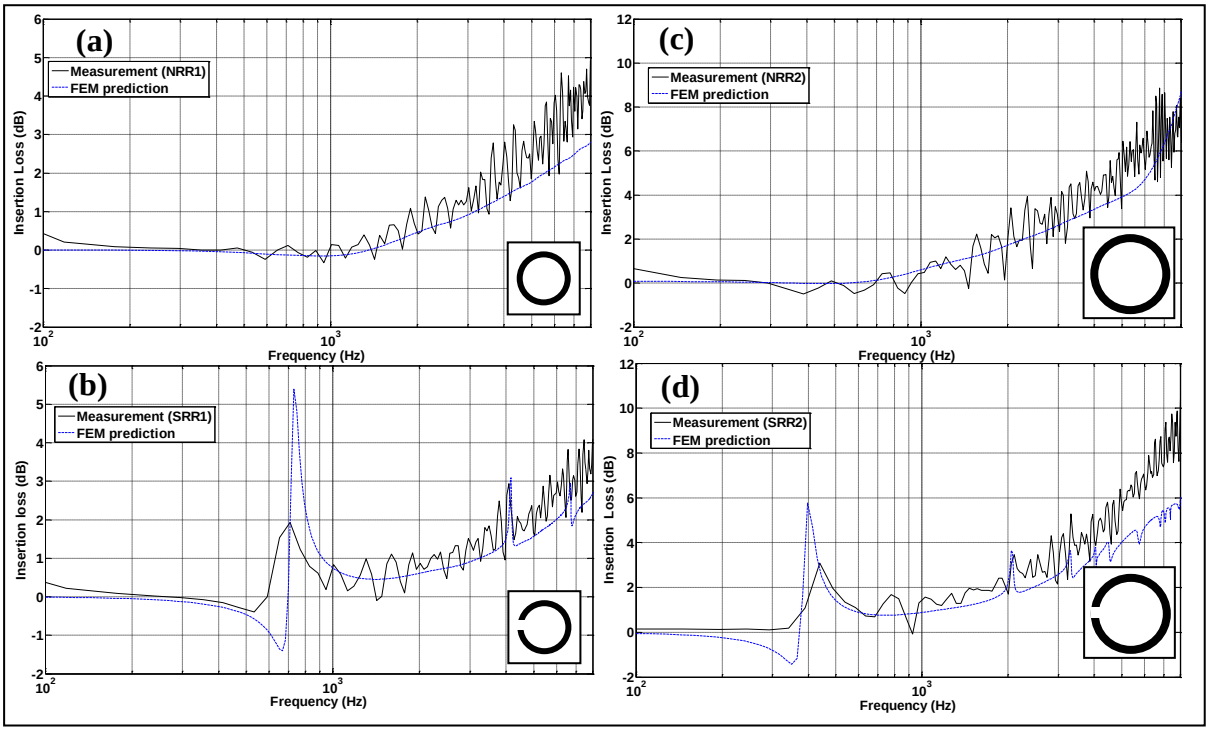

Figure 7.5: Measurements and FEM predictions (of IL spectra for the single cylinders of type (a) NRR1, (b) SRR1, (c) NRR2 and (d) SRR2 (see table 7.1)

In figure 7.5, IL spectra resulting from measurements on single cylinders of types NRR1, SRR1, NRR2 and SRR2 are plotted against FEM predictions. The IL spectra for single SRR scatterers have low frequency peaks near 700 Hz for SRR1 and 450 Hz for SRR2 (see figures 7.5(b) and 7.5(d) respectively). These can be assumed to be the result of resonances since they are not present in the IL spectra for identical PVC cylinders (i.e. with the same diameter and wall thickness) without slits (see figures 7.5(a) and 7.5(c)). Notably, the measured resonance peak amplitudes are smaller than predicted for both types of SRR scatterers which could be the result of damping that is not taken into account in the FEM model. Narrow band gaps are predicted at higher frequencies for both SRR1 and SRR2. However these higher order band gaps are predicted to have small amplitudes and are not distinguishable in the measured spectra.

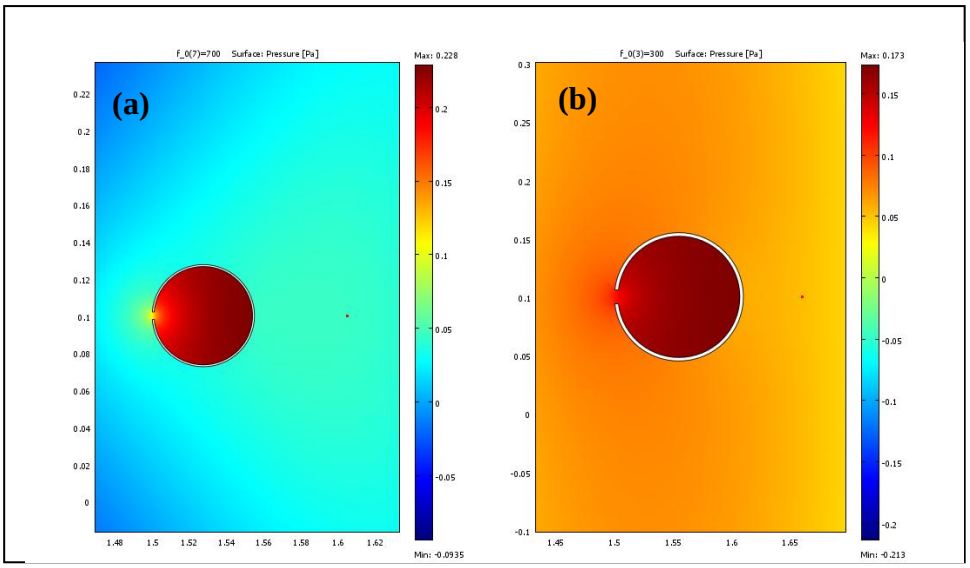

Figure 7.6: Pressure maps predicted using COMSOL® for incident cylindrical waves on (a) a single scatterer SRR1 at 700 Hz and (b) a single scatterer SRR2 at 300 Hz.

Figure 7.6(a) shows an FEM-predicted pressure map at 700 Hz for a cylindrical wave incident on a single scatterer SRR1. The maximum values of the acoustic pressure are inside the cavity. Similar effects are observed during the scattering of a 300 Hz wave by slit cylinder SRR2. These predictions correspond to the low frequency IL peaks shown in figure 7.5(b) and 7.5(d) for SRR scatterers SRR1 and SRR2 respectively.

7.5.2) Single SRR – influence of slit orientation

Intuitively, the configuration will work best for the SRR when the slit opens towards the source since this will trap the majority of the incoming waves. This hypothesis has been tested empirically by measuring the Insertion Loss (IL) of the single SRR in laboratory while rotating the slit to different angles (see figure 7.7). For this experiment, SRR1 is used (refer to table 7.1).

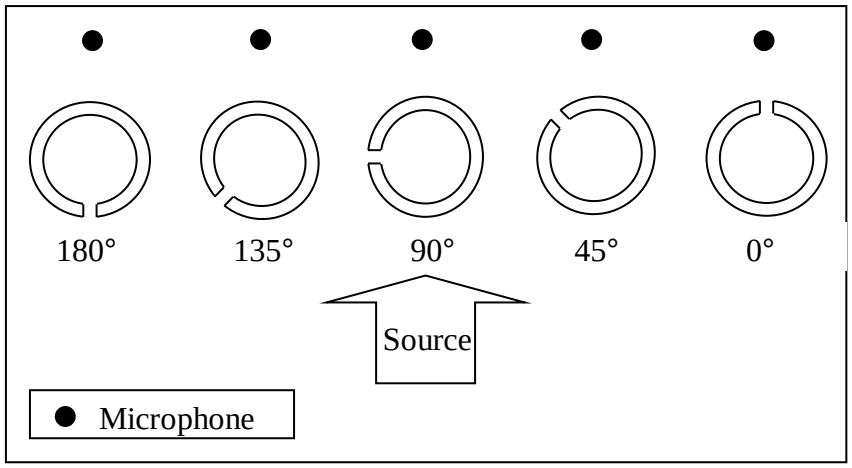

Figure 7.7: Single SRR orientation.

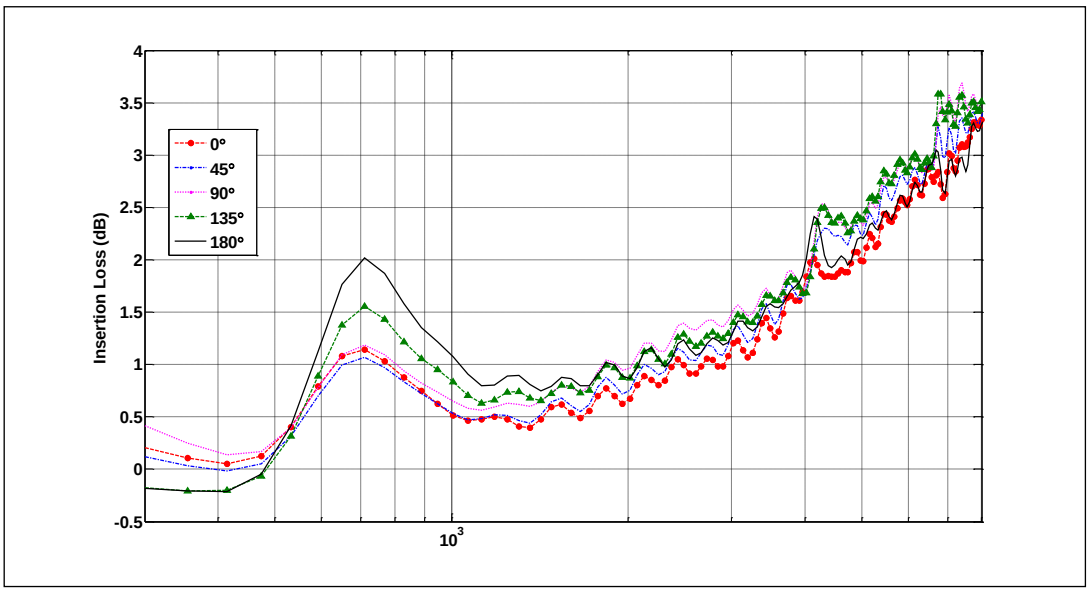

Figure 7.8: Measured Insertion Loss spectra of the radiation pattern of single SRR (refer to figure 7.7 for the definition of the orientated angle).

Figure 7.8 shows the IL spectra measured with different orientations of the slit in a single SRR. As expected, the resonance amplitude is at least twice as much for the slit facing the source (i.e. at 180°) than any other angles. This will lay the foundation of future sonic crystal designs using SRR.

7.5.3) The influence of the size of slit opening in a single SRR

The effects of the width of the slit opening have been studied using FEM for scatterer SRR1.

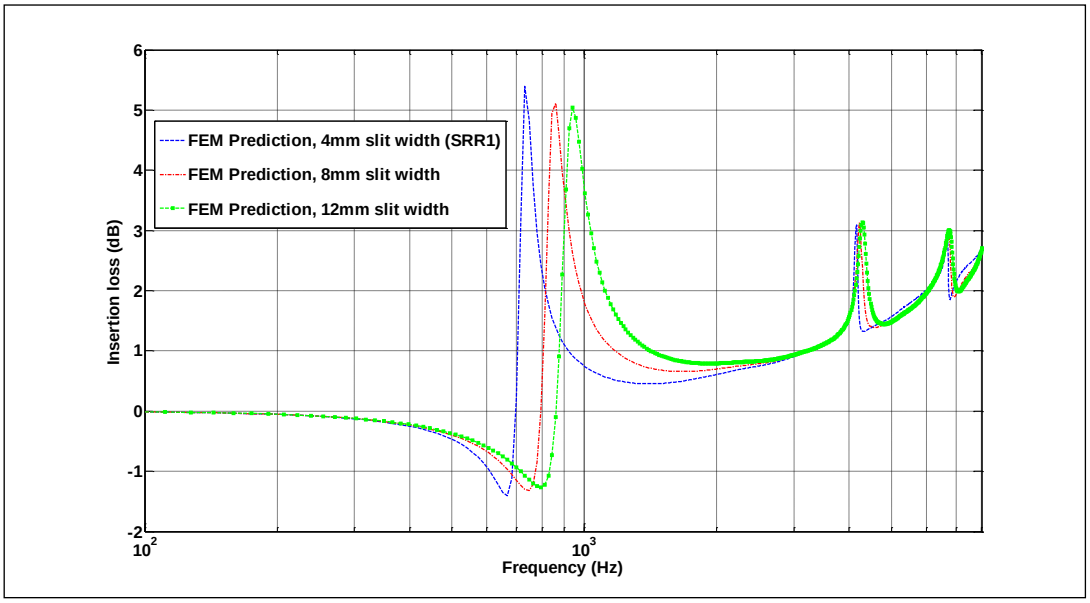

Figure 7.9: FEM predictions of IL spectra for the single SRR1 with increasing slit width.

FEM predicted IL spectra for a single SRR1 with slit widths of 4, 8 and 12 mm are shown in figure 7.9. The 750 Hz cavity resonance for the original SRR1 is shifted to 850 and 950 Hz for slit widths of 8 and 12 mm respectively. This suggests that increasing the slit width will shift the cavity resonance to higher frequencies.

7.5.4) Arrays of SRRs

The FEM model described previously (See chapter 4) has been adapted to predict the acoustical performances of finite arrays of SRRs. 7x3 square lattice arrays of SRR1 scatterers with three different lattice constants of 135, 80 and 70 mm have been modelled and the resulting predictions of IL

spectra are compared with data in figures 7.10. The details of the outdoor experiment are reported in Section 5.4.

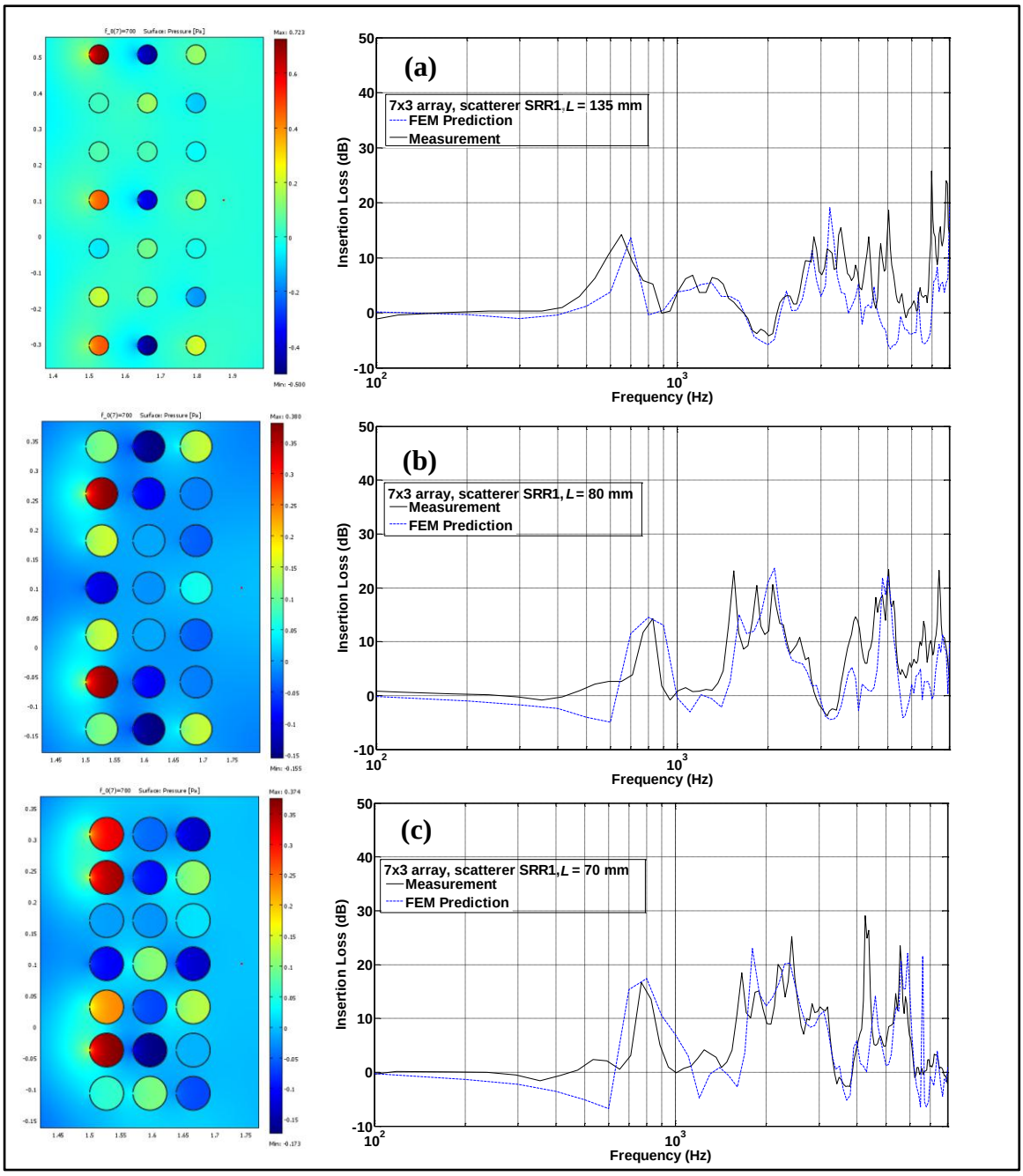

Figure 7.10: Predicted and measured Insertion Loss spectra due to square arrays of SRR1 (refer to table 7.1) with lattice constants of (a) 135, (b) 80 and (c) 70 mm. Also shown in the left hand panels are pressure maps at the first Bragg diffraction frequency for the corresponding array geometry.

The IL spectra shown in figure 7.10 for arrays of split ring resonators reveal considerable enhancement between 700 Hz and 1 kHz corresponding to the resonance frequency observed with a single SRR1 (refer to figure 7.6(b)). These additional peaks are not observed for reference arrays of pipes of the same size but no slits (FEM chapter, figure 4.5). The band gaps due to the periodicity of the arrays are preserved in these IL spectra for SRR1 arrays. A possible cause of discrepancies between predictions and measurements is the non-continuous slit construction. The pressure maps suggest that the maximum values of the acoustic pressure are localised in the cavities of some of the pipes with lengthwise slits. This is consistent with resonance of the slit cylinders.

7.5.5) Outdoor measurements (SRR array)

The encouraging laboratory results observed for SRR encouraged making larger scale outdoor trials at the OU test barrier site. The outdoor measurements used 3 rows of 54 by 3 m long SRR2 scatterers (refer to table 7.1). The SRR2 scatterers were arranged in square lattice arrays with a lattice constant of 160 mm. Detailed descriptions of the outdoor measurements are covered in chapter 5 but for the reader's convenience, the geometry used for the outdoor experiments is briefly discussed here. The plan view of the array is shown in figure 7.11(a). The source and receiver are placed 5 m apart from the array with the source positioned at the asphalt ground and the receiver positioned at the grass area to simulate a realistic road traffic environment. To test the angle dependency of the SRR barrier performance, the source was

displaced laterally and vertically. (i.e. angles subtended from Ox plane in figure 7.11(a)) and from the Oz plane in figure 7.11(b)).

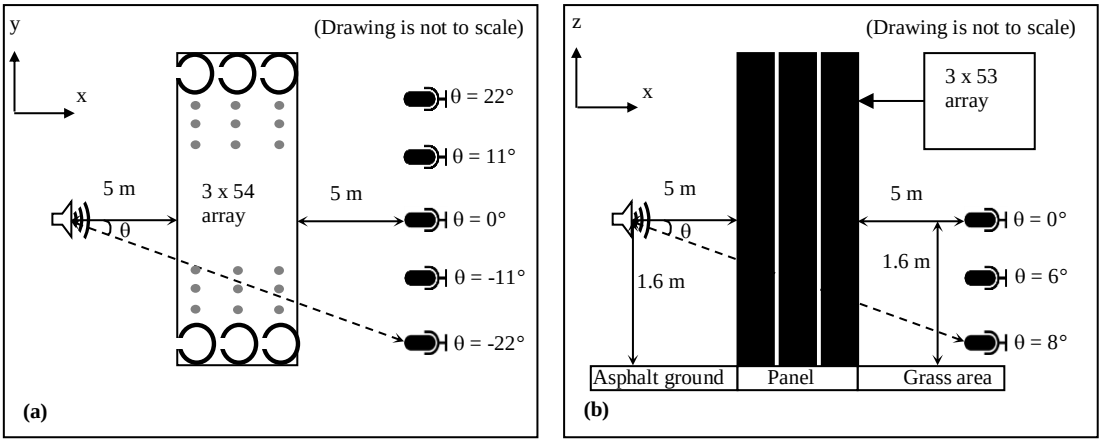

Figure 7.11: Example outdoor measurement arrangement (a) lateral displacements of the microphone along the length of barrier. (b) Vertical displacement of the microphone along the height of barrier.

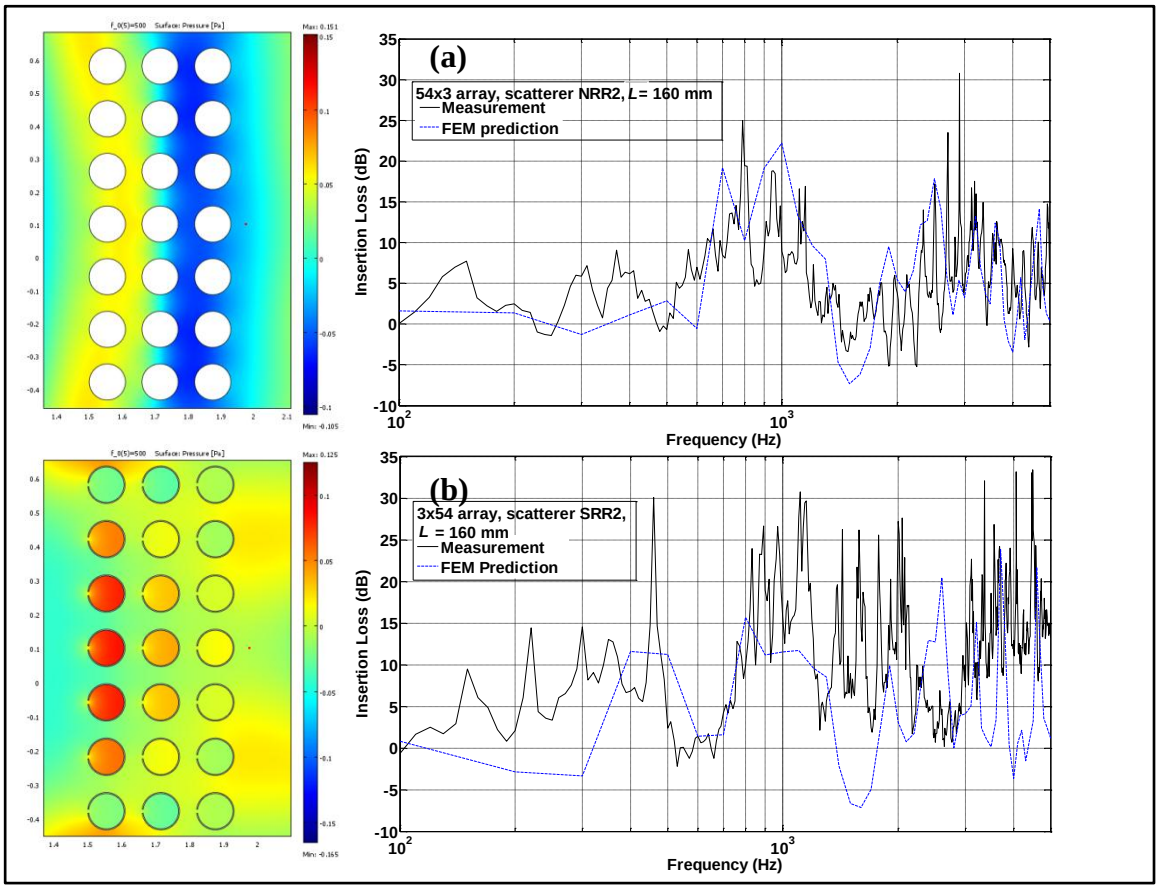

Figure 7.12: Predicted and measured Insertion Loss spectra at outdoor for square arrays of reference no slit cylinders (NRR2) and SRR scatterers (SRR2) with lattice constants, L, of 160 mm (refer to table 7.1). (a) 54x3 square lattice array of scatterer NRR2. (b) 54x3 square array of scatterer SRR2. Corresponding pressure maps at 500 Hz are shown in the left-hand panels.

The IL spectra measured outdoors are compared with FEM predictions in figure 7.12(a). Both data and FEM predictions show a Bragg band gap centred around 1 kHz and higher order modes. In this case it has been found possible to obtain a close approximation of the IL spectra using a reduced size model in COMSOL®. This is necessary to limit the computational demands in making predictions for the exact outdoor geometry (array size as well as distances for source and receiver). The IL peaks below the Bragg band gap could be due to scattering from ground or other objects near the vicinity of the less controlled environment or due to finite array effects. In

addition to the first Bragg band gap around 1 kHz, a strong insertion peak occurs at around 450 Hz corresponding to the cavity resonance for the SRR2 scatterer (see figure 7.5(d)). This effect is predicted also. The measured data also show higher order modes in comparison with arrays of cylinders with no slits for the same geometry (figure 7.12(a)). We also note the anomalous noise created by such a barrier with the presence of high downwind (source to receiver) speeds.

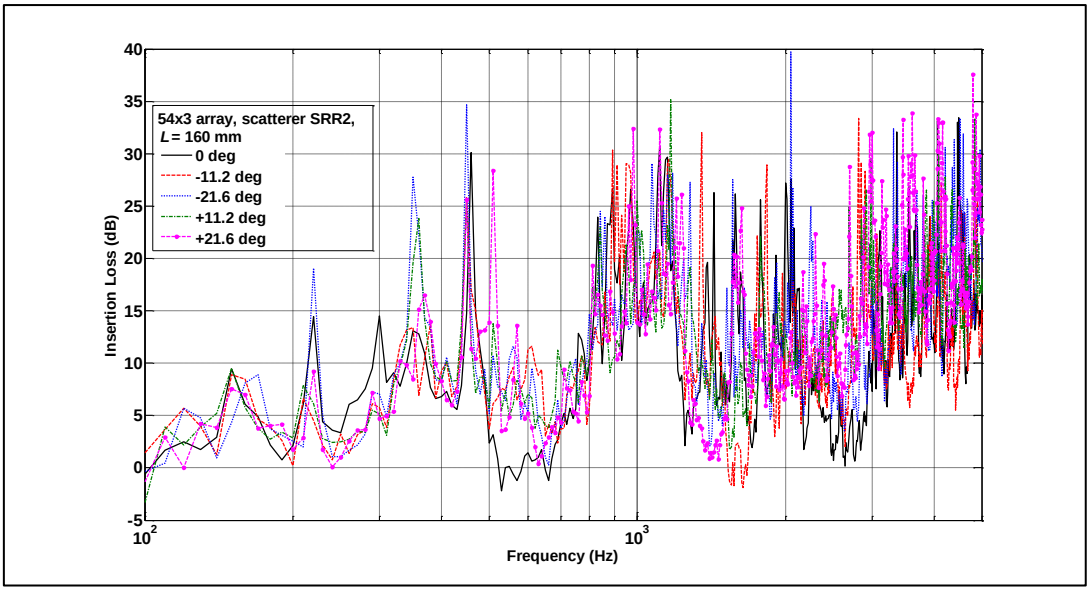

Figure 7.13: Measured Insertion Loss spectra of various lateral angles at outdoor for square lattice arrays of SRR2 (see table 7.1) with lattice constant of 0.16 m.

Figure 7.13 shows the IL spectra measured for the 54x3 array of SRR2 (refer to table 7.1) when the microphone position is laterally displaced up to ±22 degree from normal incidence (see figure 7.11(a)). The constancy of the low frequency peaks near 450 Hz offers experimental support for the hypothesis that the IL peaks corresponding to resonances of the SRRs are relatively independent of the source-receiver angle. Further displacement of

the microphone was not possible due to the presence of the neighbouring conventional fence-type barrier panels.

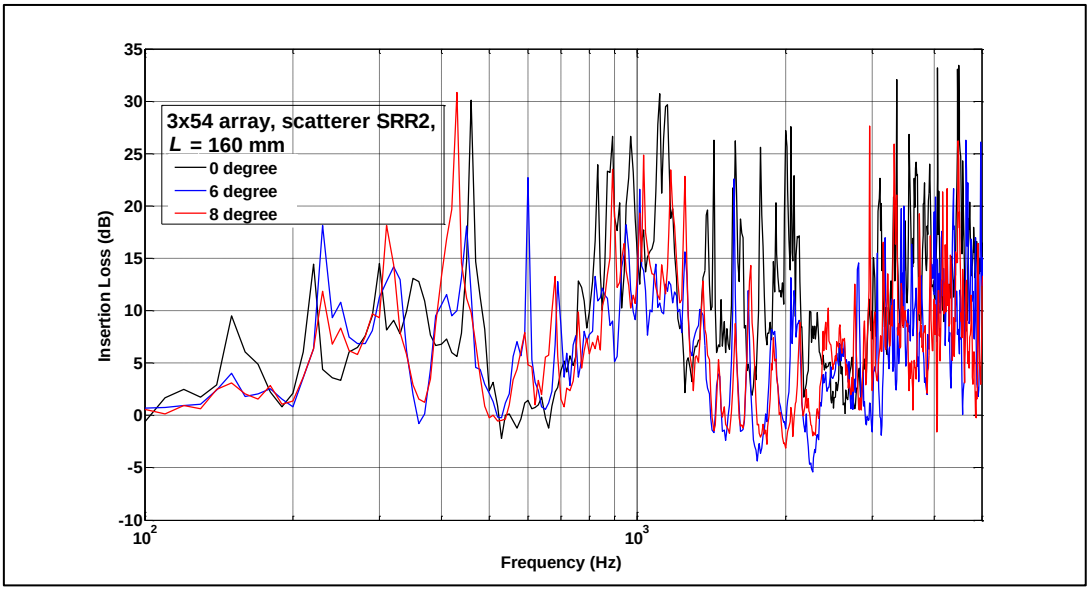

Figure 7.14: Measured Insertion Loss spectra due to outdoor square arrays of split ring resonators, SRR2 (see table 7.1) with lattice constant of 0.16 m at various inclinations of the source-receiver axis.

Figure 7.14 shows the IL spectra measured for the 54x3 array of SRR2 (see table 7.1) when the microphone position is vertically displaced up to 8 degrees from normal incidence (see figure 7.11(b)). Again the low frequency peaks near 450 Hz corresponding to resonances of the SRR are relatively independent of the source-receiver angle. The bang gap occurring around 1 kHz is due to the Bragg type scattering mechanism and higher order modes are also observed.

7.6) Coupled resonating elements

Arrays of composite scatterers, such as concentric split ring resonators [117 and 122] are shown to support band gaps generated by the multiple resonances of each scatterer in the array. Since an array of SRR and thin

walled elastic shell in air have been shown to possess strong resonance in the low-frequency range, improvement of the sonic crystal design could be achieved by combining both types of resonator. These composite scatterers, referred to as composites serve a double purpose. First, they support multiple resonances including Helmholtz and annular cavity resonances and also the breathing mode resonance of the elastic shell. Secondly, since an array of elastic shells exposed to the environment would not be practical for an outdoor noise barrier, protecting the shells using concentric outer PVC cylinders containing slits offers a simple solution. Recent experimental studies by Cui *et al* suggest the possibility of using hollow tubes with multiple narrow slits [123], such that all the slits occupy the quadrants facing the source, to create a broader band gap. In contrast with the slit locations used by Cui *et al*, multiple symmetrical slits (referred to as N-slit cylinders) have been used in our experiment. To solve the scattering problem for N-slit cylinders we use boundary conditions dependent on polar angle [124]. In the present model the finite thickness of the wall of the N-slit cylinder is taken into consideration. This avoids the use of adjustable parameters introduced for numerical stability [124 and 125] and provides a more accurate description of the real structure used in the experiments. The solution inside slits is replaced by jump conditions [126] that describe the slit interface as a moving piston. It should be noted that use of jump conditions to replace the slits make it possible to accurately predict the total wave field in the low- and mid-frequency range. The resulting approximations are of particular interest for studying the low-frequency resonant behaviour of a single composite arrangement and a finite periodic array of them.

7.6.1) Semi-analytical formulation of single composite scatterer

The description of the theory follows from the development work carried out by our collaborators [128]. Consider the two-dimensional problem of acoustic wave scattering by a single N-slit acoustically rigid cylindrical shell of thickness h and external radius r_o. The sound is generated by the cylindrical source placed at the origin of the coordinate system which is defined by either the Cartesian (x, y) or polar (r, θ) coordinates. The widths of consecutive slits in the O_{xy} plane are denoted by d_n, $n = 1,..., N$ and they are infinitely long in the direction of the cylinder main axis O_z. The external length of the rigid arc is referred to as D_m (see figure 7.15(a)). It is also assumed that the thickness of the rigid shell is much smaller than its radius so that the following geometric simplifications can be applied:

(i) Internal and external arc lengths of the rigid strip have the same length.

(ii) Internal and external arcs subtend the same angle.

(iii) The angle ϕ_n subtended by the arc of n-th slit and its width d_n are related by $d_n = \phi_n r_o, n = 1,..., N$.

(iv) The angle ψ_m subtended by the arc between slit $(n-1)$ and slit n and its width D_m are related by $D_m = \psi_m r_o, m = 1,..., N$.

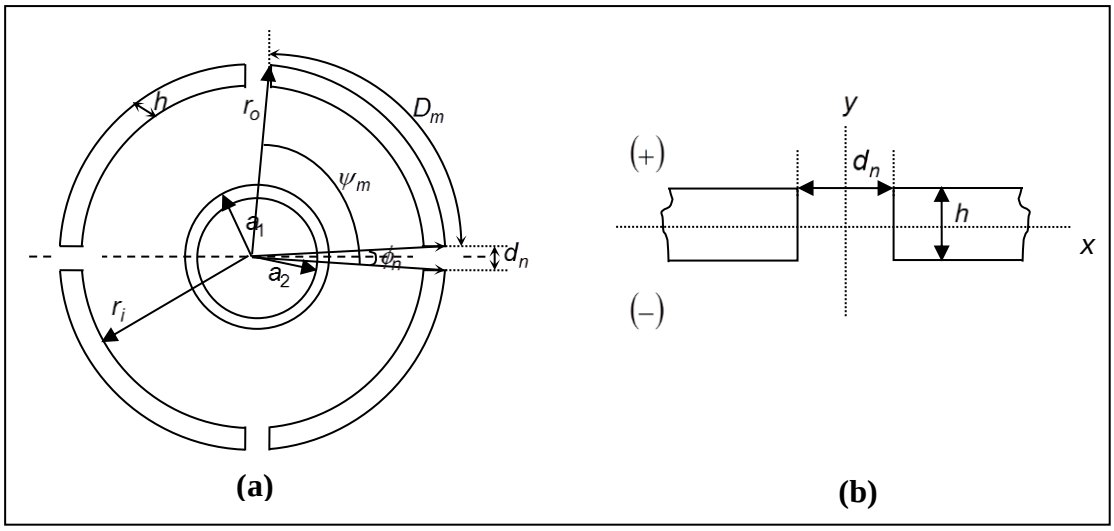

Figure 7.15: (a) Cross section of composite element consisting of a concentric arrangement of an outer 4-slit rigid cylinder and an inner elastic cylindrical shell. (b) Geometry of the slit.

Without loss of generality, it is assumed that radius of the vector passing through the middle of the first slit makes an angle of either zero or π with the O_z axis. The acoustic environments outside and inside the N-slit cylinder and within the slits are assumed to be identical and are described by density ρ and sound speed c.

The equation for cylindrically-spreading acoustic waves in a lossless fluid medium previously shown in chapter 4, equation 4.1 is repeated here for convenience. The displacement potential $p(\mathbf{r})$ in the acoustic medium satisfies the two-dimensional Helmholtz equation,

$$\nabla^2 p + k_\alpha^2 p = 0, \qquad \textbf{(7.7)}$$

where $\nabla^2 = \frac{\partial^2}{\partial x_1^2} + \frac{\partial^2}{\partial x_2^2}$ is the Laplacian, $k_\alpha = \frac{2\pi f}{c_\alpha}$ is the wave number in air defined as the ratio between angular frequency ω and sound speed of the

outer acoustic environment c_α, is a given wave vector. Subscript α relates the properties to one of the acoustic media (i.e., it is “o”, “i” and “s” to denote outside the configuration, inside it and within the slits respectively).

The outer solution $p_o(\mathrm{r})$ also satisfies Sommerfeld’s radiation condition,

$$\frac{\partial p_o}{\partial r} - ikp_o = o\left(r^{-\frac{1}{2}}\right), \text{ as } r \to \infty, \qquad \textbf{(7.8)}$$

where $r = \sqrt{x^2 + y^2}$.

To treat the boundary conditions imposed on the surface of the N-slit cylinder we first solve an auxiliary problem for the slits. The geometry of this problem is illustrated in figure 7.15(b). Waves propagating inside the slit are described by the plane wave solution in the form,

$$p_s = C_1 e^{iky} + C_2 e^{-iky}, \qquad \textbf{(7.9)}$$

where C_1 and C_2 are unknown coefficients. It is assumed that contribution of the x-dependent components to p_s is negligible when slits are small compared with the wavelength ($kd_n < 1$ and $kh < 1$).

Equation 7.9 is subject to the continuity conditions imposed on the slit faces $y = \pm\frac{h}{2}$ which are

$$p_\alpha = p_s, \qquad \textbf{(7.10)}$$

$$q_\alpha = \frac{\partial p_s}{\partial y}, \tag{7.11}$$

where $q_\alpha = \frac{\partial p_\alpha}{\partial_n}$ is the normal derivative on the slit faces and index α = i or o.

Using solution 7.8 and its unknown coefficient, equation can be transformed to the jump condition [126]

$$p_i = p_o - hq_o, \tag{7.12}$$

$$q_i = k^2 h p_o + q_o. \tag{7.13}$$

This relates the wave field inside the N-slit cylinder to that of the outer region at the slit interface.

The solution of equation 7.7 is subject to the jump conditions (equation 7.12 and 7.13) as well as to the Neumann conditions imposed on the rigid surface of the N-slit cylinder. The former and the latter can be combined into the set of two boundary conditions [124] that are

$$\frac{\partial p_i}{\partial r} = \frac{\partial p_o}{\partial r} + f(\theta) k^2 h p_o, \tag{7.14}$$

$$\frac{\partial p_o}{\partial r} - \frac{f(\theta)}{h} + (p_o - p_i) = 0, \tag{7.15}$$

where the stepwise function $f(\theta)$ of the polar angle θ introduces the distribution of slits along the N-slit cylinder surface over the interval $0 \in [0,2\pi]$ so that

$$f(\theta)=\begin{cases}1 & \textbf{if } \theta \in \left[-\frac{\phi_1}{2},\frac{\phi_1}{2}\right] \cup \cdots \cup \left[2\pi-\frac{\phi_1}{2}-\phi_N-\psi_N, 2\pi-\frac{\phi_1}{2}-\psi_N\right] \\ 0 & \textbf{otherwise}\end{cases}, \quad \textbf{(7.16)}$$

For the non-zero value of this function equations 7.14 and 7.15 are transformed to the jump conditions 7.12 and 7.13 whereas the Neumann conditions can be obtained from equation 7.14 and 7.15 by setting $f(\theta)$ to zero.

The periodic angle distribution of N slits can be introduced through the alternative form of $f(\theta)$,

$$\begin{aligned} f(\theta)=\sum_{n=2}^{N}\left\{H\left(\theta-\frac{2\pi(n-1)}{N}+\frac{\phi_n}{2}\right)-H\left(\theta-\frac{2\pi(n-1)}{N}-\frac{\phi_n}{2}\right)\right\}+, \\ \sum_{j=0}^{1}\left\{H\left(\theta-2\pi\ j+\frac{\phi_1}{2}\right)-H\left(\theta-2\pi\ j-\frac{\phi_1}{2}\right)\right\} \end{aligned} \quad \textbf{(7.17)}$$

where $H(\theta)$ is the Heaviside function.

The total wave field outside the slit cylinder is given by

$$p_o = H_0^{(1)}(kr)+\sum_{n=-\infty}^{+\infty} A_n H_n^{(1)}(k\hat{r})e^{in\bar{\theta}}, \quad \textbf{(7.18)}$$

where $\hat{r}(r,\theta)$ and $\hat{\theta}(r,\theta)$ are the polar coordinates of receiver with origin placed at the centre of the scatterer and A_n are unknown coefficients. The solution inside the slit cylinder is given by

$$p_i = \sum_{n=-\infty}^{+\infty}\left[B_n J_n(k\hat{r}) + C_n Y_n(k\hat{r})\right]e^{in\hat{\theta}}, \qquad \textbf{(7.19)}$$

where coefficients B_n and C_n have to be found. The coefficient C_n can be derived in terms of B_n or set to zero according to the type of the core so that:

$$C_n = B_n C_n,\ n \in \mathrm{Z}, \qquad \textbf{(7.20)}$$

where

$$C_n = 0, \text{ N-slit cylinder alone,} \qquad \textbf{(7.21)}$$

$$C_n = \frac{J_n^{'}(ka_1)}{Y_n^{'}(ka_1)}, \text{ rigid core,} \qquad \textbf{(7.22)}$$

$$\begin{aligned} C_n = &-\left[\left(J_n^{'}kR\right)^2\right]\left[(1-k_sR)^2+n^2\right] \\ &\times\left[J_n^{'}(kR)Y_n^{'}(kR)\left[(1-k_sR)^2+n^2\right]+\left[n^2-(k_sR)^2\right]\times\rho\left(\rho_s\pi Rh\right)^{-1}\right], \end{aligned} \quad \text{Elastic shell core} \qquad \textbf{(7.23)}$$

where primes $\left(^{'}\right)$ denote the derivative with respect to polar coordinate $\hat{r}$. In equation 7.23, the elastic shell is described by wave number $k_s = \frac{\omega}{c_s}$, density ρ_s, dilatational wave speed c_s, radius of the elastic shell mid-surface $R = \frac{a_1 + a_2}{2}$ and its half thickness $h_s = \frac{a_1 - a_2}{2}$. The dilatational wave speed c_s for a thin elastic plate is given by

$$c_s = \sqrt{\frac{E}{\rho_s\left(1-\nu^2\right)}}, \qquad \textbf{(7.24)}$$

with Young's modulus E and Poison's ratio ν. We consider the thin viscoelastic shells made of latex discussed in chapter 6. For the numerical predictions the size of each elastic shell is always defined by the outer radius a_1 = 0.0215m and thickness $2h_s$ = 0.00025 m.

To find the unknown coefficients A_n we apply Graf's addition theorem (see Appendix B) to the outer solution (equation 7.18). This enables us to express (r,θ) in terms of $(\hat{r},\hat{\theta})$. Then, substituting (equation 7.18) and (7.19) into the boundary conditions (equations 7.14 and 7.15) and taking the inner product we arrive at infinite algebraic system of equations in A_n, $n \in Z$, variables as follows:

$$\sum_{n=-\infty}^{\infty} A_n \left\{ \delta_{m,n} 2\pi h H_n^{(1)'}(kr_o) - F_{n-m}\left[H_n^{(1)}(kr_o) - H_n^{(1)'}(kr_o)\mathrm{I}_n\right] + \frac{k^2 h}{2\pi} H_n^{(1)}(kr_o) \sum_{j=-\infty}^{\infty} F_{j-m} F_{n-j} \mathrm{I}_j \right.$$

$$= \sum_{n=-\infty}^{\infty} H_n^{(1)}(kQ) e^{-in(\pi+\alpha)} \left\{ -\delta_{m,n} 2\pi h J_n'(kr_o) + F_{n-m} \right\} \left[J_n(kr_o) - J_n'(kr_o)\mathrm{I}_n\right] \qquad \textbf{(7.25)}$$

$$\left. - \frac{k^2 h}{2\pi} J_n(kr_o) \sum_{j=-\infty}^{\infty} F_{j-m} F_{n-j} \mathrm{I}_j \right\} \qquad , \; m \in Z,$$

where $\delta_{m,n}$ is Kronecker delta, vector $Q = Q(\cos\alpha, \sin\alpha)$ is the radius vector to the centre of the slit cylinder,

$$\mathbf{I}_n = \frac{J_n(kr_i) + C_n Y_n(kr_i)}{J_n^{'}(kr_i) + C_n Y_n^{'}(kr_i)}, \qquad \textbf{(7.26)}$$

and F_n is the Fourier transform of function $f(\theta)$ given by

$$F_n = \begin{cases} \sum_{\iota=1}^{N} \theta_\iota & \textbf{for } n = 0 \\ \frac{2}{n} \sum_{\iota=0}^{N-1} \sin\left(\frac{n\phi_l}{2}\right) e^{-2in\pi\iota/N} & \textbf{for } n \neq 0 \end{cases}, \qquad \textbf{(7.27)}$$

Note that factor C_n and the geometrical parameters of the slits only appear in I_n and F_n, respectively. This makes the form of system (equation 7.25) invariant with respect to scatterer core type and the arrangement and size of the slits.

Taking $\phi_\iota = 0,\ \iota \in Z$, the solutions of system (equation 7.25) is reduced to the case of scattering by rigid cylinder that is

$$A_m = \frac{-J_m^{'}(kr_o)}{H_m^{(1)'}(kr_o)} H_m^{(1)}(kQ) e^{-im(\pi+\alpha)},\ m \in Z, \qquad \textbf{(7.28)}$$

To find the numerical solution the infinite system (7.25) has to be truncated at some number $m, n, j = -M, \ldots, M$. In general, the convergence of the numerical solution is dependent on the radius r_o of the N-slit cylinder, number of slits and their angles ϕ_ι (i.e. their length) as well as on the frequency. Reducing the angle ϕ_n of the slit results in faster convergence so that numerical solution approaches the value defined in (equation 7.28).

7.6.2) FEM modelling of single composite scatterer

Alternatively, the transmission problem for a 2 dimensional single composite scatterer can be solved using FEM (COMSOL® Multiphysics). The dimensions of the various scatterer can be found in table 7.2. The acoustic structural interaction model is exactly similar to that for the single latex cylinder described in chapter 6.11 except for the addition of PVC outer cylinder with 4 symmetrical slits. Hence, it is necessary to modify the boundary conditions in chapter 6 (table 6.3) to include the PVC cylinder (see table 7.3). The modified model is then solved in a similar way to that used for the single latex cylinder.

Scatterer type	PVC Outer Diameter, OD (m)	PVC wall thickness, (mm)	Slit width, α (mm) (x 4)	Latex Outer Diameter, OD (m)	Latex wall thickness, (mm)
SRR3†	0.055	2	4	0.043	0.25
SRR4*	0.110	3	12	0.043	0.5

† used in laboratory measurements.
* used in outdoor measurements.

Table 7.2: Specifications of composite scatterer geometries.

Domain	Air outside latex cylinder	Elastic cylinder	Air inside latex cylinder
Model suffix	Acpr (Acoustic)	smps (Structural Mech.)	acpr2 (Acoustic)
Inner wall of latex	Continuity	Load (N/m^2) -p2*nx_smps (x-direction) -p2*ny_smps (y-direction)	Normal acceleration (m/s^2) u3_tt_smps*nx_smps+ v3_tt_smps*ny_smps
Outer wall of latex	Normal acceleration (m/s^2) u3_tt_smps*nx_smps+ v3_tt_smps*ny_smps	Load (N/m^2) -(p+p_i_acpr)*nx_smps (x-direction) -(p+p_i_acpr)*ny_smps (y-direction)	Continuity
Additional boundary conditions for outer shell PVC with 4 symmetrical slits			
Domain	Air outside PVC cylinder	PVC cylinder	Air inside PVC cylinder
Model suffix	Acpr (Acoustic)	smps (Structural Mech.)	acpr2 (Acoustic)
Inner wall of PVC	Sound hard boundary	Load (N/m^2)=0 (inactive domain)	Sound hard boundary
Outer wall of PVC	Sound hard boundary	Load (N/m^2)=0 (inactive domain)	Sound hard boundary
Slit region	Sound hard boundary	Load (N/m^2)=0 (inactive domain)	Sound hard boundary

Table 7.3: Summary of boundary conditions used in the acoustic structural interaction model.

7.6.3) Results for single composite scatterer

The semi-analytical MST and FEM models enable us to compute the insertion loss spectra for composite scatterers and the results are compared with data from measurements (see chapter 5 for detailed descriptions). First, the acoustical performance of a single PVC with 4-symmetrical slits is considered. The geometry of the study of 4-slits PVC will use the component specification of SRR3. A simple modification of the FEM model discussed in section 7.4, to include the additional 3 slits can be achieved in a straightforward manner. The FEM predictions are compared with data from laboratory experiments.

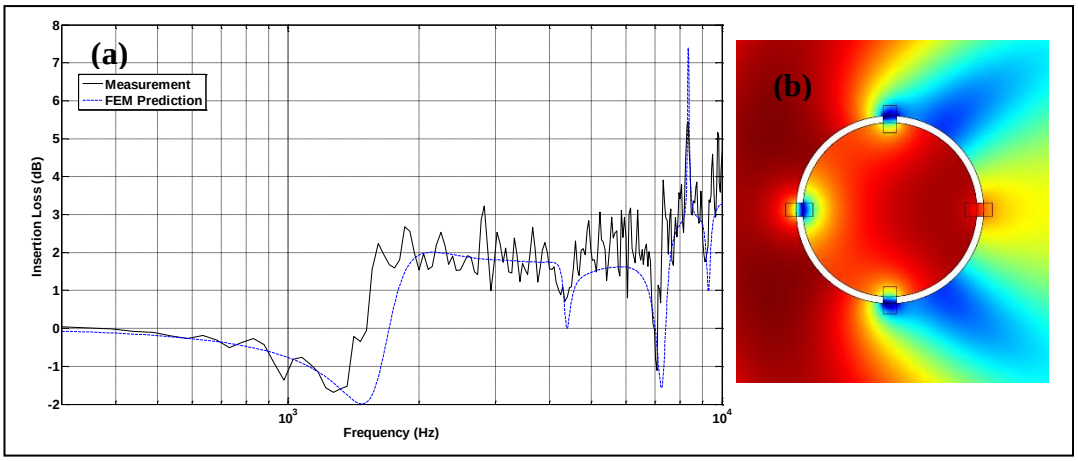

Figure 7.16: (a) Measured and FEM predicted IL spectra due to a single PVC cylinder with 4 symmetrical slits (component of SRR3, see table 7.2). (b) FEM (COMSOL®) predictions of pressure maps at 2 kHz for a similar scatterer showing the interior and exterior environments.

In figure 7.16, the IL spectrum predicted by FEM agrees with the measurement data for the PVC cylinder with 4 symmetrical slits. The same size of scatterer but with only one slit was found to have a resonance at 700 Hz (figure 7.5(b)). So increasing the number of slits results in a significant shift of this Helmholtz type resonance towards higher frequencies, in this case to near 2 kHz.

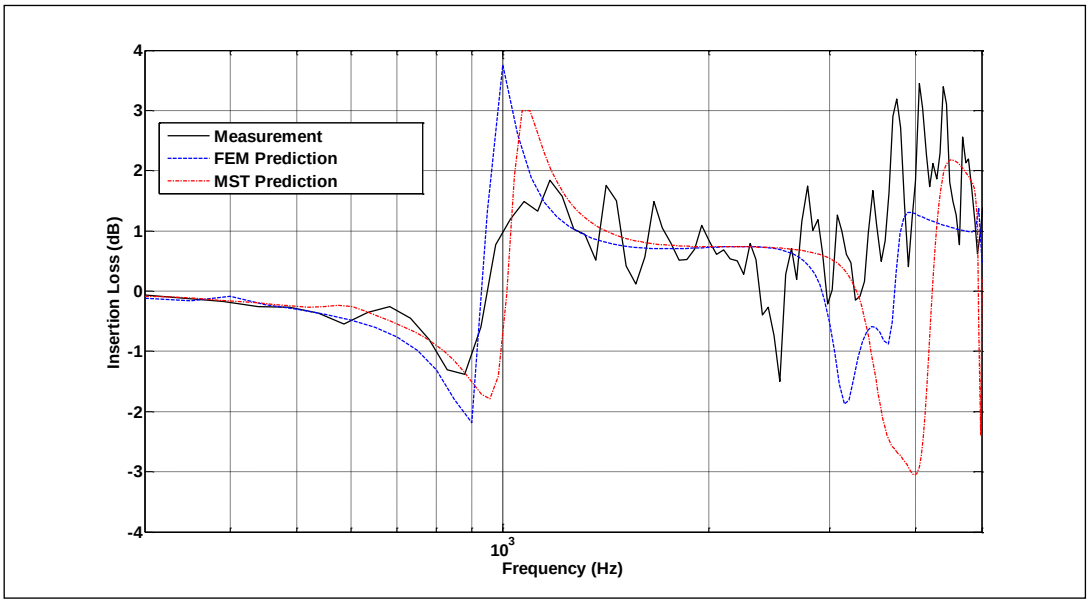

Figure 7.17: Measured and predicted (MST and FEM) IL spectra for a single composite scatterer, SRR3 (refer to table 7.2)

According to figure 7.17, the IL spectra (measured and predicted by MST and FEM) shows a strong resonance at around 1 to 2 kHz for composite scatterer SRR3 (refer to table 7.2). Higher order resonances at higher frequencies are also observed. For all measurements and predictions, the receiver is positioned 0.05 m away from the scatterer. Contrary to the predictions obtained by our collaborators from Salford [128], our MST predictions disagree with measurements after 2.5 kHz. This could be the result of a lower truncation number M in our computations which were limited by our computational resource to 6 rather than 35 which was used in the paper.

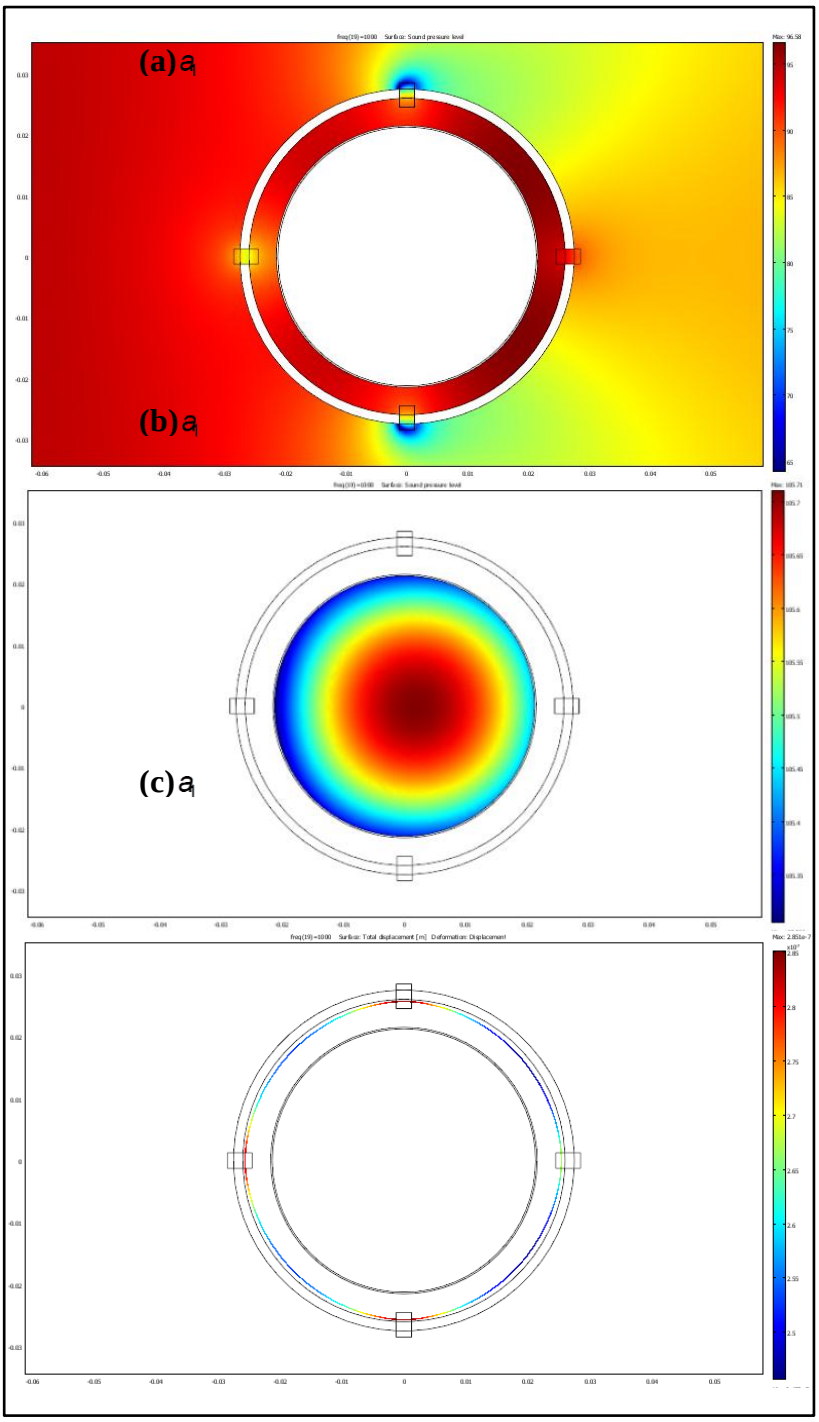

Figure 7.18: FEM (COMSOL®) predicted pressure maps at 1 kHz for SRR3 showing the exterior and annular cavity environments (a), interior environment of the latex cavity (b) and static deformation plot on the "Breathing mode" shape of elastic element in air.

In figure 7.18, FEM predicted pressure maps at 1 kHz for SRR3 (refer to table 7.2) are shown. According to these pressure maps, higher energies are observed to be trapped inside annular cavity (see a) and interior of the

elastic shell (see b). Also at this frequency, the “Breathing mode” (mode 0) of the elastic shell is also observed (see (c)).

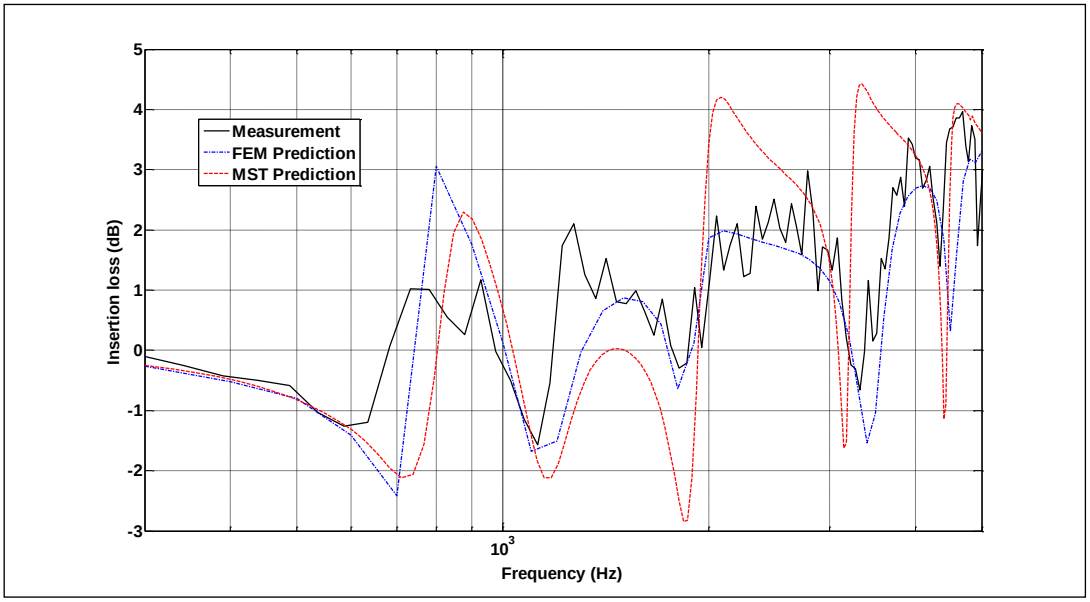

Figure 7.19: Measured and predicted (MST and FEM) IL spectra for a single composite scatterer, SRR4 (refer to table 7.2)

In figure 7.19, the IL spectrum predicted by FEM agrees with both MST predictions and our laboratory measurement data for the single composite scatterer SRR4 (refer to table 7.2). Although the same truncation number (6) is used in the MST computation as for SRR3, doubling the size of the scatterer could result in better accuracy for the range of frequencies shown.

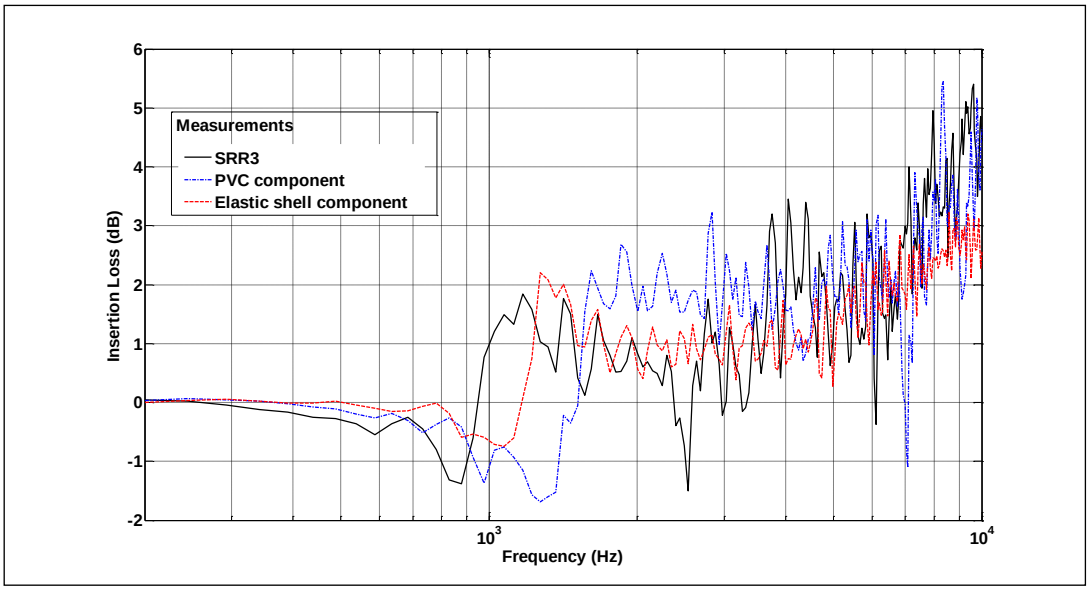

Figure 7.20: Measured IL spectra for a single composite scatterer, SRR3 and it's own component (refer to table 7.2).

The measured IL spectrum for the latex cylinder in Fig. 7.20 shows the breathing mode resonance near 1.5 kHz. The resonance for the 4 slits PVC cylinder is near 1.8 kHz. When combined to form a concentric composite cylinder, the resulting IL spectrum shows a modified resonance at about 1 kHz. This indicates that the coupling between two resonators leads to the shift of the shell's resonance to a lower frequency. This is confirmed also by the FEM static deformation plot in figure 7.18(c).

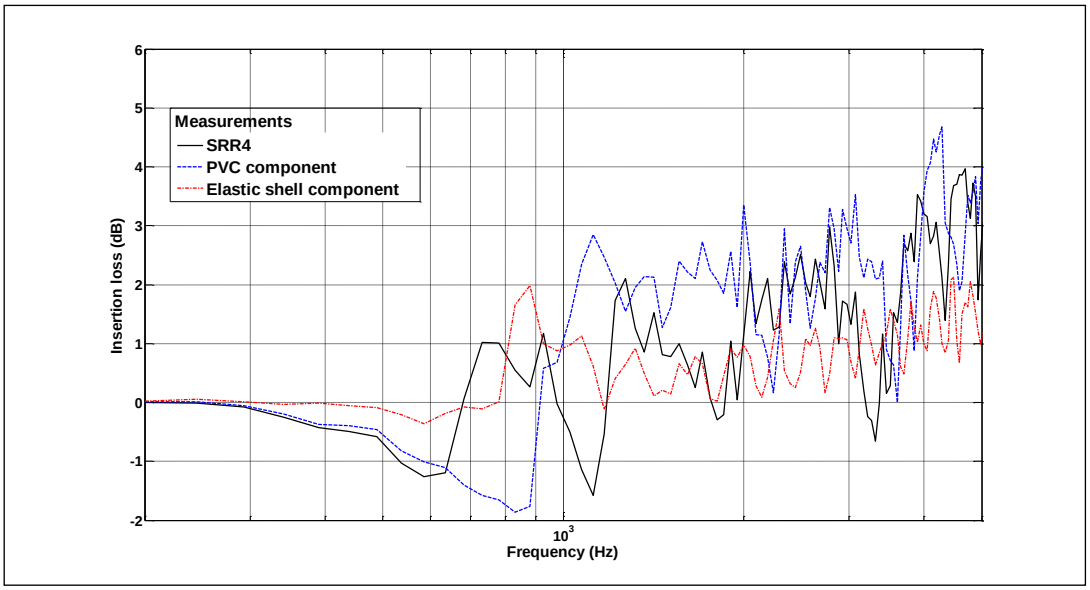

Figure 7.21: Measured (in laboratory) IL spectra for a single composite cylinder (SRR4) and its components (i.e. single 4 slit PVC and latex, see table 7.2).

The corresponding IL spectrum in figure 7.21 shows that the breathing mode resonance for a single latex cylinder of the type used in the outdoor measurements is near 900 Hz. That measured for a single 4 slits PVC cylinder is near 1.2 kHz. When the cylinders are combined to form a concentric composite cylinder, the resulting IL spectrum shows two peaks with reduced magnitude near 750 Hz and 900 Hz and negative IL (dips) before and after the resonance. These phenomena are similarly observed in the results for the smaller geometry scatterer (see figure 7.20).

7.6.4) Semi-analytical formulation of an array of composite cylinders

Following the work of our collaborators [128], this section has been adapted to finite arrays of scatterers. We first formulate the method of multiple scattering that is described by the superposition of scattered wave fields of each element of the array [129] and boundary conditions (equations 7.14 and 7.15) imposed on the surface of all scatterers in the array. As a result the solution p_o of the Helmholtz equation (equation 7.18) in the acoustic environment outside scatterers takes the following form

$$p_o(r,\theta) = H_0^{(1)}(kr) + \sum_{m=1}^{N} \sum_{n=-\infty}^{+\infty} A_n^m H_n^{(1)}(k\hat{r}_m) e^{in\hat{\theta}_m} , \qquad \textbf{(7.29)}$$

where N is the number of scatterers in the array, variables $\hat{r}_m(r,\theta)$, $\hat{\theta}_m(r,\theta)$ are the polar coordinates with origin in the centre of scatterer of index m and A_n^m are unknown coefficients. The form of the solution inside of the m-th slit cylinder is the same as in the case of single scatterer problem that is equation 7.19.

Using Graf's addition theorem (see Appendix B) we can rewrite solution (equation 7.29) in terms of polar coordinates $(\hat{r}_m, \hat{\theta}_m)$ of m-th scatterer that gives

$$p_o(\hat{r},\hat{\theta}) = \sum_{n=-\infty}^{+\infty} J_n H_n^{(1)}(k\hat{r}_m)(kQ_m) e^{-in(\pi+\alpha_m)} +, H_0^{(1)}(kr) + A_n^m H_n^{(1)}(k\hat{r}_m) +$$
$$\sum_{p=1,\, p\neq m}^{N} \sum_{q=-\infty}^{+\infty} A_q^p J_n(k\hat{r}_m) H_{q-n}^{(1)}(kQ_{mp}) e^{i(q-n)(\alpha_{mp}+\pi)} e^{in\hat{\theta}m} \qquad \textbf{(7.30)}$$

,

$$m = 1,\ldots,N$$

where vector $Q_m = Q_m(\cos\alpha_m, \sin\alpha_m)$ is the radius vector to the centre of m-th scatterer, vector $Q_{mp} = Q_{mp}(\cos\alpha_{mp}, \sin\alpha_{mp})$ defines the position of p-th scatterer with respect to m-th scatterer and $Q_{mp} > \hat{r}_m$ that is the requirement of the addition theorem. The expansion (equation 7.30), along with the inner solution (equation 7.19), is subject to the boundary conditions (equations 7.14 and 7.15). This results in an infinite algebraic system of equations in A_n^m, $m = 1,\ldots,N$, $n \in Z$, variables given by

$$\begin{aligned}
&\sum_{n=-\infty}^{\infty} A_n^p \left\{ \delta_{m,n} 2\pi h H_n^{(1)'}(kr_{o,p}) - F_{n-m}^p \left[H_n^{(1)}(kr_{o,p}) - H_n^{(1)'}(kr_{o,p}) I_n^p \right] \right. \\
&\left. + \frac{k^2 h}{2\pi} H_n^{(1)}(kr_{o,p}) \sum_{j=-\infty}^{\infty} F_{j-m}^p F_{n-j}^p I_j^p \right\} + \\
&\sum_{s=1,\, s\neq p}^{N} \sum_{n=-\infty}^{\infty} \sum_{\nu=-\infty}^{\infty} A_n^s H_{n-\nu}^{(1)}(kQ_{ps}) e^{-i(n-\nu)(\pi+\alpha_{ps})} \times \\
&\left\{ \delta_{m,\nu} 2\pi h J_n'(kr_{o,p}) - (F_{\nu-m}^p) \left[J_n(kr_{o,p}) - J_n'(kr_{o,p}) I_n^p \right] + \right. \\
&\left. \frac{k^2 h}{2\pi} J_\nu(kr_{o,p}) \sum_{j=-\infty}^{\infty} F_{j-m}^p F_{\nu-j}^p I_j^p \right\} = \\
&\sum_{n=-\infty}^{\infty} H_n^{(1)}(kQ_p) e^{-in(\pi+\alpha_p)} \left\{ -\delta_{m,n} 2\pi h J_n'(kr_{o,p}) + \right. \\
&F_{n-m} \left[J_n(kr_{o,p}) - J_n'(kr_{o,p}) I_n^p \right] - \\
&\left. \frac{k^2 h}{2\pi} J_n(kr_{o,p}) \sum_{j=-\infty}^{\infty} F_{j-m}^p F_{n-j}^p I_j^p \right\}, m \in Z,\, p = 1,\ldots,N,
\end{aligned} \qquad \textbf{(7.31)}$$

where factors I_m^p and F_m^p are given by equations 7.26 and 7.27 respectively. The superscript p relates these factors to p-th scatterer. To find the unknown

coefficients we again use truncated system of $N(2M+1)$ algebraic equations. Note that for the slit angles $N(2M+1)$, equation 7.31 is transformed to the well-known algebraic system describing multiple scattering problem for an array of rigid cylinders [129].

7.6.5) Results for array of composite scatterers

Solving the algebraic equation (equation 7.31) enables us to compute the total wave field (equation 7.29) which can yield the insertion loss. Again the results for an array of PVC cylinders with 4 symmetrical slits will be shown before the composite scatterers. This simply expands the FEM model developed in figure 7.16 and the result is validated with laboratory experiments. FEM modelling could not be performed for an array of composite cylinders due to the high computational resources required and therefore only predictions of the MST theory described above have been compared with experimental data.

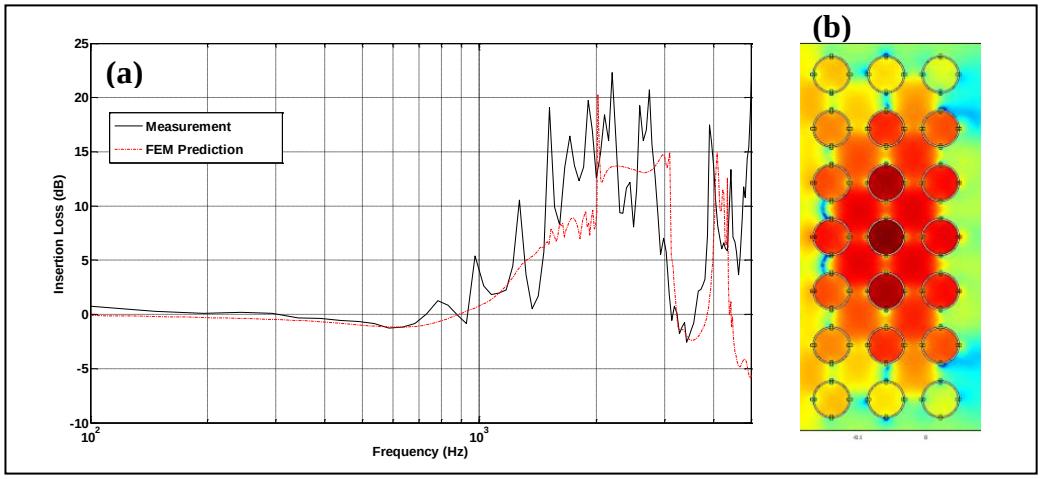

Figure 7.22: (a) Measured and FEM predicted IL spectra for 7x3 PVC array of lattice constant 0.08 m (PVC with 4 symmetrical slits, component of SRR3, see table 7.2). (b) FEM (COMSOL®) predicted pressure maps at 2 kHz for a similar scatterer array showing the interior and exterior environments.

Figure 7.22 shows the results of laboratory measurements and FEM predictions of IL spectra for a 7x3 4-slits PVC array arranged in square lattice with lattice constant 0.08 m. The cylinder is the PVC (4 slits) component of SRR3 defined in table 7.2. The band gap effect related to the cavity resonance (see figure 7.16) and associated with a high insertion loss peak is predicted and observed between 1 - 3 kHz. The difference in measured and predicted amplitudes of the band gap could be due to the fact that the slits on the PVC cylinders are narrower at their mid points due to the change in their structural integrity caused by the slits.

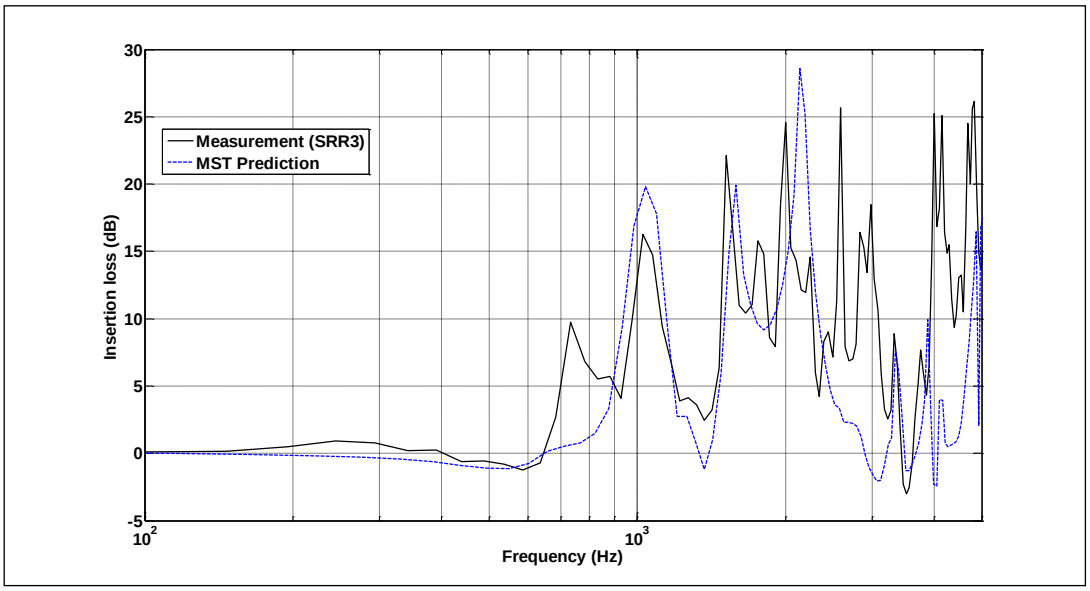

Figure 7.23: Measured and MST predicted IL spectra for 7x3 array of composite scatterers SRR3 (see table 7.2) arranged in square lattice of lattice constant 0.08 m.

Figure 7.23 compares the measured and MST predicted IL spectra due to 7x3 arrays of composite scatterers of type SRR3. This shows the best agreement between predictions and data. However the predictions use 0.3 mm instead of 0.25 mm for the thickness of the latex shell. This suggests that the thickness of the latex may not be precisely 0.25 mm as stated by the manufacturer. Further analysis on the latex thickness variation has been

performed in table 7.4 which justify the thickness parameter used in the prediction. The MST predictions agree fairly well with measurements except at high frequencies. The coupled resonances of the composite cylinders generate several band gaps that result in high insertion loss peaks. One of these peaks is observed around 1 kHz and is related to the shifted breathing mode resonance of latex elastic shell. The insertion loss peak associated with the shifted Helmholtz resonance in the slit cylinder is observed around 2.6 kHz and it follows the first Bragg band gap peak observed and expected around 2 kHz for the given lattice constant.

Position number	Measured thickness (mm)
1	0.32
2	0.28
3	0.31
4	0.33
5	0.29
6	0.3
7	0.34
8	0.29
9	0.31
10	0.28
Average thickness: 0.305 mm Standard deviation: 0.02 mm	

Table 7.4: Measured thickness on latex strip with average and standard deviation values.

Measurement has been carried out to determine the average thickness of the latex shell using a micrometer. To be statistically sufficient, this is done with thickness measurement on 10 different positions on a strip of latex (see table 7.4). According to the results, this yields an average thickness of 0.3 mm and a standard deviation of 0.02 mm. In view of this, all MST predictions involving latex of 0.25 mm (as stated by the manufacturer) reported in this Thesis are calculated using the average thickness of 0.3 mm.

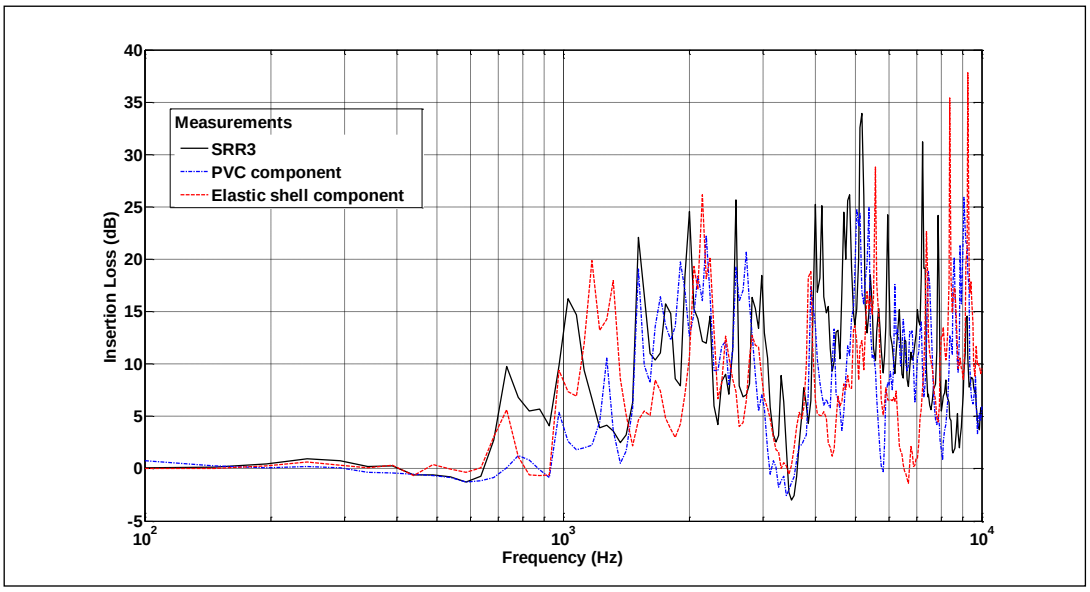

Figure 7.24: Measured IL spectra due to 7x3 arrays of composite scatterer, SRR3 and the two components separately (refer to table 7.2).

The results in figure 7.24 for 7x3 arrays of composite cylinders, show that the measured Bragg band gap near 2 kHz matches with the calculated first Bragg centre frequency for a lattice constant of 80 mm. An additional peak is observed near 1 kHz which corresponds to the modified latex breathing mode resonance (See figure 7.20). The enhanced peak near 750 Hz may be associated with the finite height of the array since it also appears with reduced magnitude in the IL for the PVC pipe array. Similar measurements for an array of SRR4 composites were not possible due to the restricted size of the anechoic chamber. However such measurements have been made outdoors.

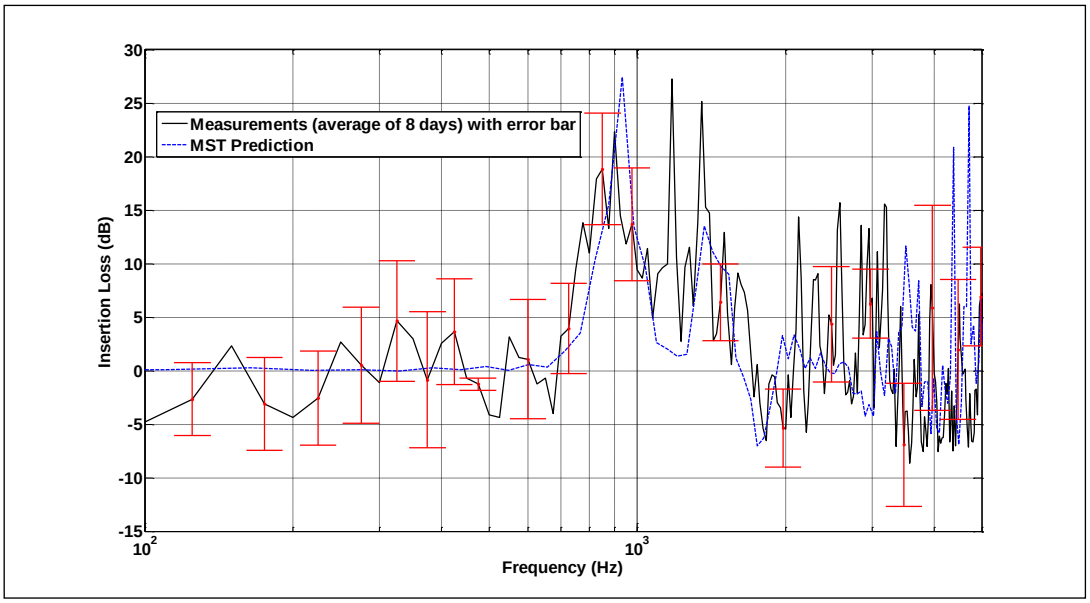

Figure 7.25: Average of 8-day measurements (outdoor) and MST IL spectra for 54x3 arrays of composite scatterers SRR4 (see table 7.2) arranged in square lattice of lattice constant 0.16 m. Error bars are plotted for the measured spectrum.

Eight day averages of measured IL spectra due to 54x3 arrays of composite scatterer SRR4 (arranged in square lattice of lattice constant 0.16m) at an outdoor test site on the Open University Milton Keynes campus have been obtained and are shown together with corresponding MST predictions in figure 7.25. The error bars represent the spread of data at each frequency. The setup shown in figure 7.11(a) has been used with the receiver positioned at $\theta = 0°$. The dimensions of the inner latex tube are the largest permitted by the manufacturer's capabilities. Both data and predictions show a strong insertion loss peak at 1 kHz which corresponds to both the breathing mode of the inner elastic shell and the Bragg band gap. The proximity in frequency of these effects is not ideal for a noise barrier design. For such an uncontrolled outdoor environment subject to variation of ambient noise and meteorological conditions, the prediction agrees fairly well with measurement up to about 2 kHz. We also note that there are negative insertion losses at various frequencies.

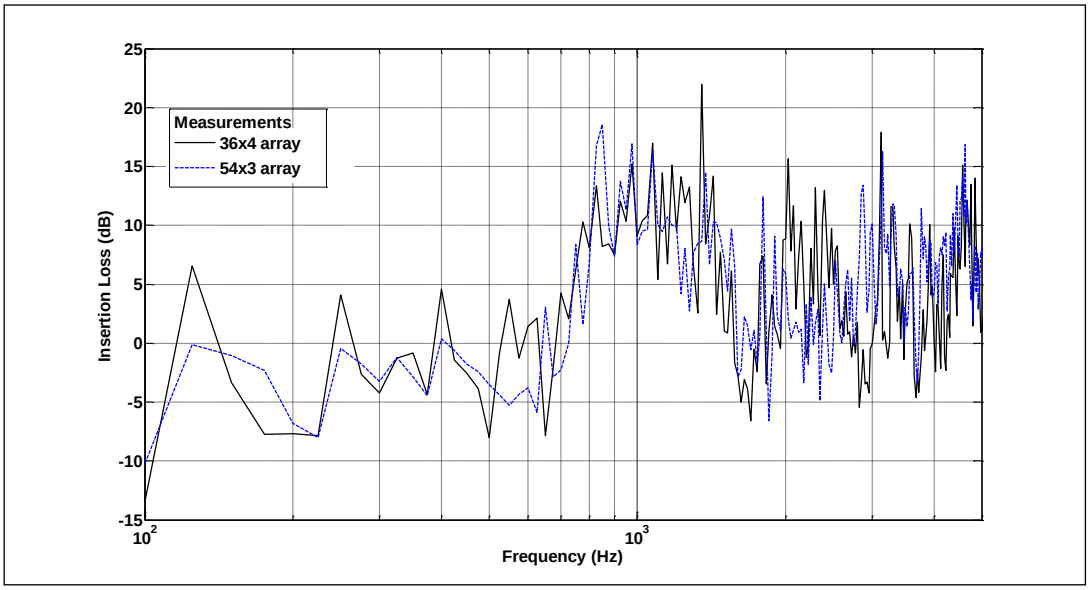

Figure 7.26: Measured IL spectral of 36x4 and 54x3 arrays of concentric cylinders (averaged of all 8 measurements).

Figure 7.26 compares measured IL spectra for 36x4 and 54x3 arrays of concentric cylinders obtained on two different days (averaged of 8 measurements). Both days had similar meteorological conditions; upwind with average wind speed of 0.7 m/s and 0.9 m/s for the 36x4 and 54x3 concentric array measurements respectively (see Appendix E(I and ii)). The IL shows more or less similar performance around the band gap at 1 kHz despite adding an additional row.

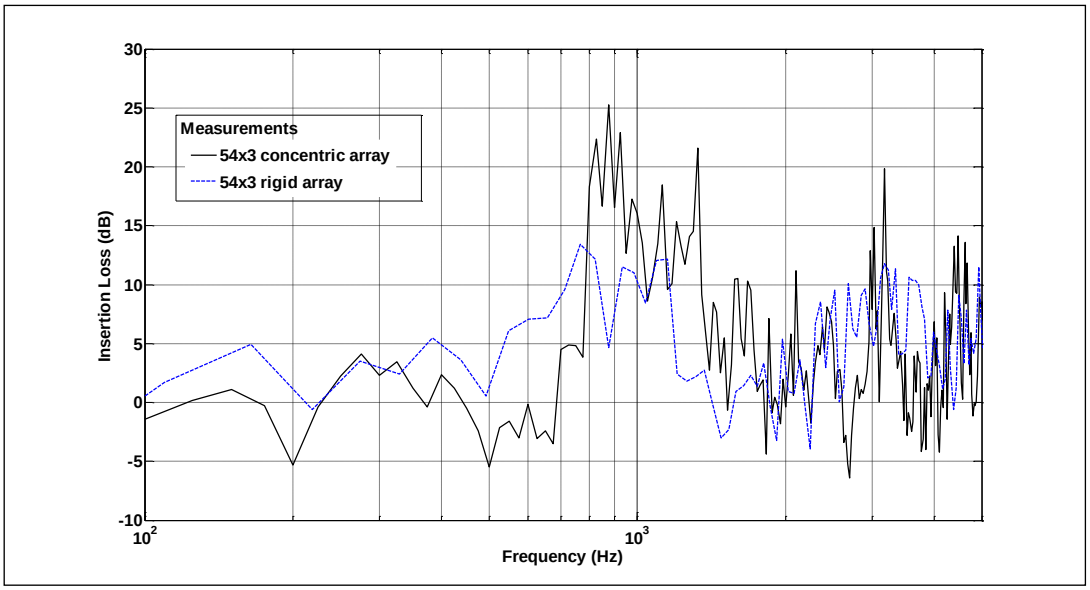

Figure 7.27: Measured IL spectral of 54x3 arrays of concentric cylinders (average of 8 measurements) and rigid no slit cylinders (average of 3 measurements).

Figure 7.27 compares the measured IL spectra for 54x3 arrays of concentric cylinders and rigid no slit cylinders. Although for the concentric cylinders configuration there is some improvement in the frequency range near 1.2 – 2 kHz, there is a worse performance between 500 Hz and 800 Hz. Thus, some modifications are necessary to improve the performance of barriers based on arrays of the composite cylinders. The proposed modifications to the current design for the concentric scattereres are elaborated in suggestion 5 of section 9.3 (see Chapter 9).

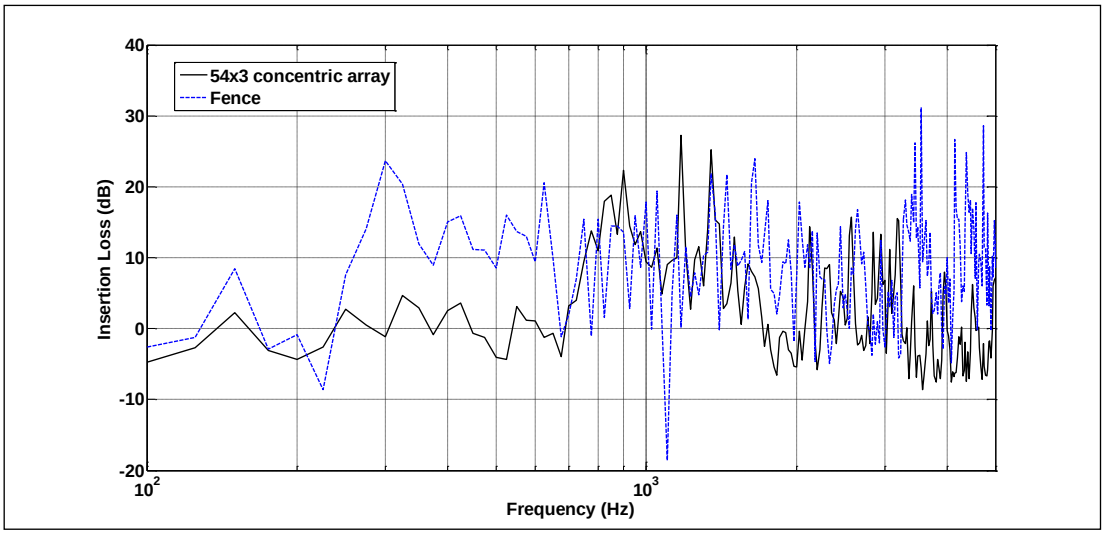

Figure 7.28: Measured IL spectral of 54x3 arrays of concentric cylinders (averaged of 8 measurements) and fence (average of 8 measurements).

Figure 7.28 compares the measured IL spectra for 54x3 arrays of concentric cylinders and a typical fence at normal incidence. It can be observed that generally the performance of a typical fence is superior to sonic crystal except for the distinctive improvement at 1.2 kHz. The IL dip for the fence at this frequency could be attributed by factor such as holes along the uneven ground where the fence is placed.

7.7) Influence of adjustable parameters on the acoustical performance of composite scatterer arrays outdoors

The elastic shell outer diameter, elastic shell thickness and the slit widths in the PVC cylinders can be varied to improve the performance of composite cylinder arrays as outdoor noise barriers. MST predictions have been used to investigate the effects of varying these parameters and therefore the possibilities for better designs.

7.7.1) The predicted influence of the elastic shell outer diameter

The influence of the outer diameter of the inner elastic shell has been studied using MST computations. The composite cylinder arrays considered for this study are 54x3 arrays of SRR4 scatterers arranged in a square lattice with a lattice constant of 0.16 m. The shell outer diameter has been increased up to 83 mm in increments of 10 mm. The latex material properties used for the predictions have been assumed to be density = 1100 kg/m^3, longitudinal velocity = 954 m/s, Transverse velocity = 23 m/s, Poisson ratio = 0.4997 as in chapter 6. Source and receiver have been considered to be 5 m away from front and back faces of the array with the source to receiver line of sight centred at the gap between the 2 central scatterers (see figure 7.11). Frequency steps of around 50 Hz have been used in all predictions.

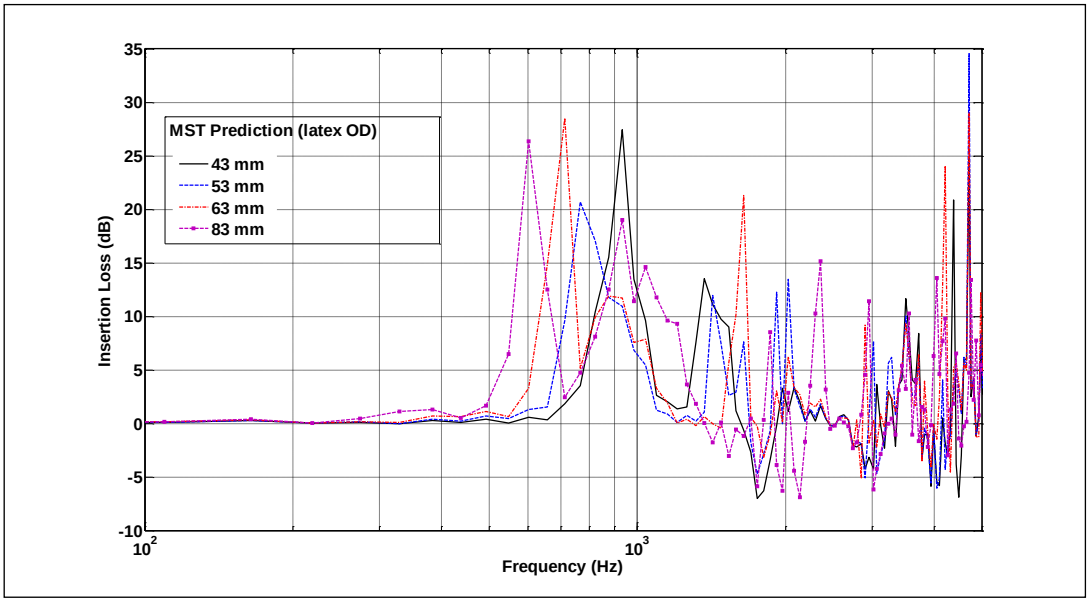

Figure 7.29: IL spectra for the MST predicted effect on changing latex outer diameter for 54x3 square lattice array of SRR4 scatterer with lattice constant of 0.16 m.

Figure 7.29 shows that the first IL peak is predicted to be moved to lower frequencies as the latex tube diameter is increases and leads to increasing separation of the modified latex resonance from the 1 kHz Bragg band gap. Also there is a relationship between the predicted amplitude of the modified latex resonance and that of the IL peak associated with the Bragg band gap as they are separated. As the predicted IL peak amplitude corresponding to the modified latex resonance increases there is a decrease in the predicted Bragg band gap amplitude and vice-versa. However again enhancement of sound (i.e. negative IL) is predicted at high frequencies.

7.7.2) The predicted influence of elastic shell wall thickness

Another parameter that has been investigated is the wall thickness of the inner elastic shell. Following the predictions in figure 7.29 which show that an elastic shell outer diameter of 83 mm will result in a separate low frequency band gap. The wall thickness for such scatterer has been varied from 0.5 to 2 mm.

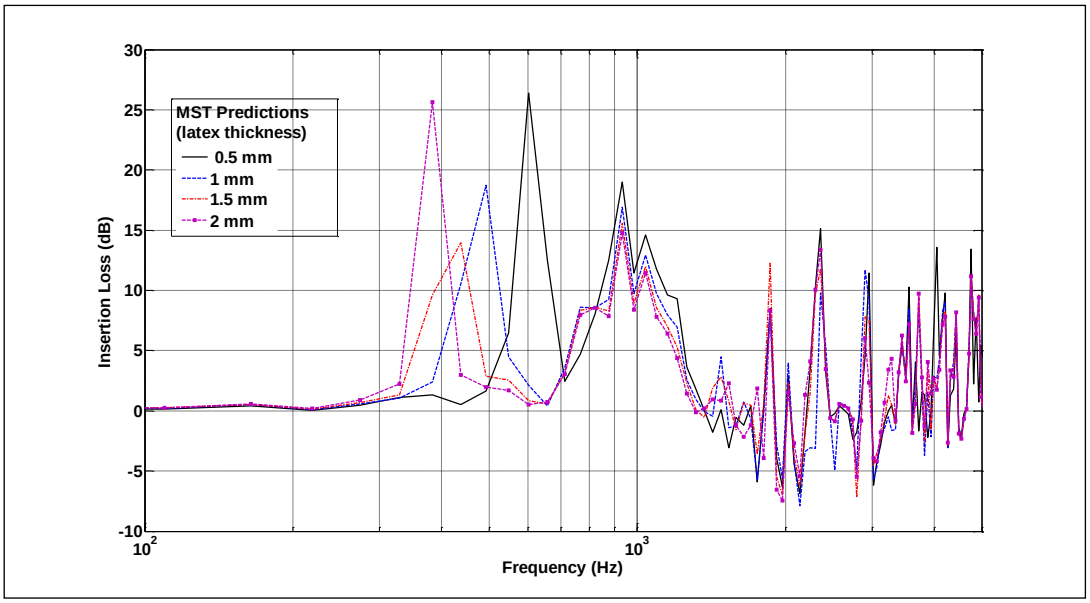

Figure 7.30: IL spectra for the MST predicted effect on changing latex wall thickness for 54x3 square lattice array of SRR4 scatterer with lattice constant of 0.16 m.

The resulting predictions are shown in figure 7.30. The IL peak is shifted to lower frequency and decreased in amplitude (except for 2 mm thickness) as the latex wall thickness is increased. The Bragg band gap remains fairly constant at about 920 Hz. However again enhancement of sound is observed at high frequencies.

7.7.3) Predicted influence of the slit widths in the outer PVC cylinder

The effects of varying the slit widths in the outer 4-slits PVC cylinder have been predicted. The assumed slit width has been varied from 3 to 12 mm.

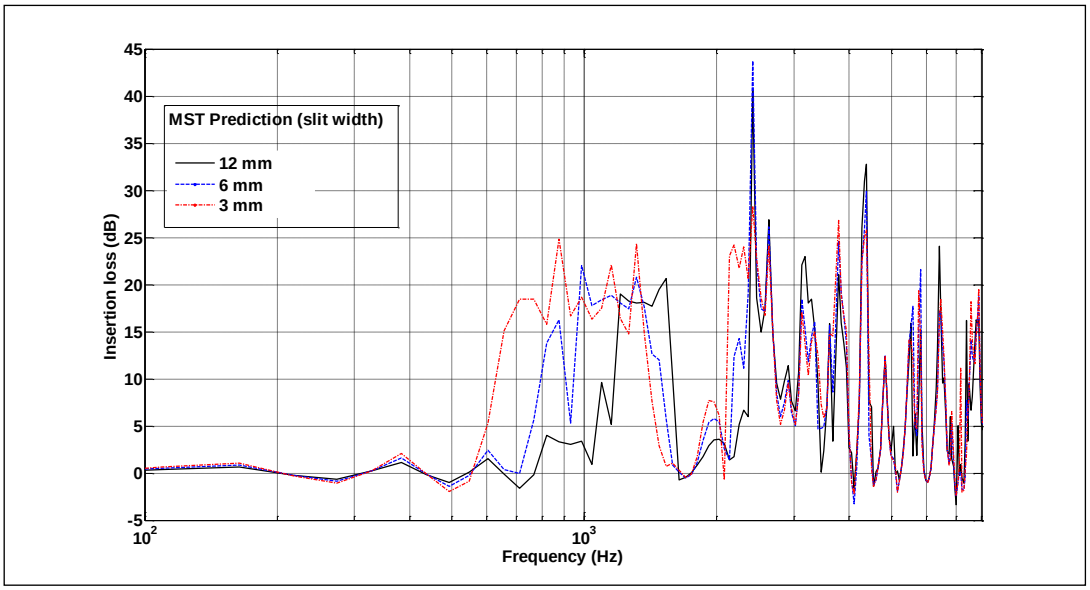

Figure 7.31: MST predicted IL spectra for 54x3 square lattice array with lattice constant of 0.16 m as the slit widths in the outer PVC cylinders are varied from 3 to 12 mm.

The resulting IL spectra predictions are shown in Figure 7.31 for 54x3 4-slits PVC arrays with lattice constant 0.16 m and different slit widths. The IL peak associated with the Bragg band gap slowly broadens near 1 kHz as the slits width decreases. This may explain the modification of the 1st Bragg band gap in data for our current outdoor setup (see figure 7.25). The predicted effects of varying the parameters of the composite elements can lead to better array design for outdoor noise reduction. This will be pursued in chapter 9.

Chapter 8

Performance of sonic crystal noise barriers above a ground surface

8.1) Introduction

Outdoor sound propagation is subject to a combination of influences along the propagation path including geometrical spreading, atmospheric absorption and extra attenuation (i.e. barrier and ground effect) [131]. Geometrical spreading of the wave fronts leads to a declining source pressure at a rate that depends on the type of source (point source or line source). Atmospheric absorption is the results of shear velocity, heat conduction and molecular relaxation losses. Natural or artificial obstacles impede the sound propagation. The wind profile can also have pronounced effect. For example a down wind condition (wind blowing towards the receiver from the source) will refract sound waves downwards, resulting in increased noise levels behind the barrier. At distances less than 100 m, meteorological effects play a minor role and the acoustical properties of the ground – typically given by the surface impedance are most important [132].

Regular arrays of cylindrical scatterers embedded in a medium with different physical properties are known to produce acoustic band gaps, also called stop bands, which prevent sound transmission at selective frequencies. If the scatterers are solid and the host medium is air then these are called Sonic Crystals (SC). At these frequencies, the amplitudes of the transmitted

waves decrease as they pass through the crystal. Conversely there are pass bands within which the amplitudes of transmitted waves are relatively high. Pass bands and band gaps are a consequence of multiple scattering of waves in a periodic structure and also due to the effect of local resonance mechanism in certain type of scatterer as discussed in chapters 6 and 7. Given an interest in the potential use of sonic crystals as environmental noise barriers, recent research into sonic crystal barriers for highway noise has focused on methods to achieve a broader band gap and promising results have been obtained using locally-resonant cylinders such as thin-walled elastic shells [101], slit cylinders (Helmholtz resonance) [117] or a combination of both as shown in chapter 7. However, much of the literature on sonic crystals considers their acoustical performance in the absence of a ground plane. Clearly this will be unrealistic if SCs are to be used as noise barriers since a ground will always be present. On the other hand, the problem of sound scattering by a single cylinder over a plane boundary has been investigated [132 and 133] and the sound diffraction effect of a Quadratic Residual Diffuser (QRD) profile, a type of Edge-Modified Barrier (see chapter 9.2), for a single noise barrier has been studied using a 2 dimensional Boundary Element Method [145]. The prime objective of this chapter is to study the total effect of SC and a reflecting ground. First there is an overview on acoustical characterisation of the ground which requires a method to determine the ground impedance. Laboratory and outdoor *in-situ* measurements of various types of plane surfaces are performed and data is fitted with a ground impedance model. Subsequently, a semi-analytical approach for predicting the transmission properties of sonic crystals in 2-

Dimensional (2D) has been developed for circular scatterers and it is based on the superposition of the solution for a single scatterer. Although the most interesting situation is likely to involve periodic vertical finite cylinder arrays, this would inevitably require solution of a 3-Dimensional problem where high computation resource is necessary. Hence the more feasible 2D problem is considered involving a periodic array of cylinders (rigid or elastic) with their axes parallel to the ground. The semi-analytical method is used to analyse the performance of rigid or elastic cylindrical scatterers suspended with their axes parallel to a rigid ground. In this chapter, square lattice arrays of 7x3 scatterers are considered. The predicted performance of the sonic crystal arrays in the presence of rigid ground is compared with that of the same arrays in the free field. Insertion Loss (IL) data from laboratory experiments are compared with predictions. Laboratory studies have been performed for rigid or elastic arrays over a finite impedance ground. Some preliminary laboratory measurements on vertical cylinder arrays on hard ground are also described.

8.2) Ground impedance models for propagation modelling

The prime objective of this chapter is to study the total effect of sonic crystals over a reflecting plane but first an understanding of acoustic characterisation of the ground is necessary. In many predictions schemes [135] ground surfaces are considered as either ‘acoustically hard’, which means they are perfectly reflecting, or ‘acoustically soft’, which implies that they are perfectly absorbing. According to ISO 9613-2, any ground surface of

low porosity maybe considered acoustically hard and any vegetation-covered ground is to be considered acoustically soft. Although this might be an adequate representation in some circumstances, it is an over simplification of a considerable range of properties and resulting effects. Even different versions of the category of ground known as 'grassland' can result in a significant variation in ground effect [136]. Characterizing the sound field above a surface can be done through measuring the sound pressure (easiest parameter than can be measured for sound field) at one or more locations. A convenient indicator of the acoustical characteristics of the ground can be determined from the spectrum of the ratio of the direct source to receiver total sound level without $\left(p_{Free\_field}\right)$ and with $\left(p_{Total\_field}\right)$ a ground surface (equation 8.1), keeping the distance between source to receiver and the source strength constant. This is called the Excess Attenuation (EA) due to the ground surface and it depends on the source-ground-receiver geometry and the ground properties. If expressed in decibels, a positive value will imply that the sound pressure is lower than the sound pressure in free field. We note that this formula is only true as long as the ground is considered as locally reacting, that is the surface impedance is independent of the angle of incident sound [136].

$$EA = 20\log\left|\frac{p_{Total\_field}}{p_{Free\_field}}\right|. \qquad \textbf{(8.1)}$$

Frequently ground properties are represented by a semi-empirical single parameter model developed by Delany and Bazley [137] in 1970. They published empirical relationships for determining the propagation constant, k_c,

and relative characteristic impedance, Z_c (equation 8.2 and 8.3). The variables in these relationships were frequency and flow resistivity, σ, of the material where the flow resistivity represents the ratio of the applied pressure gradient to the induced volume flow rate per unit thickness of material due to the porosity. This single parameter model has been widely used in deducing the acoustical properties of several types of porous materials [137].

$$k_c = \left(\frac{\omega}{c_0}\right)\left[1 + 0.0978X^{-0.700} + i0.189X^{-0.595}\right]. \quad \textbf{(8.2)}$$

$$Z_c = 1 + 0.0571X^{-0.754} + i0.087X^{-0.732}, \quad \textbf{(8.3)}$$

where $X = \sqrt{\frac{\rho_0 f}{\sigma}}$, ρ_0, is the density of air, σ, is an effective flow resistivity and f the frequency.

These equations are based on best fits to a large number of impedance tube measurements on fibrous materials having porosities close to 1. It is semi-empirical since X is related to the dimensionless ratio of the pore dimension to the thickness of the viscous boundary layer and this ratio is crucial in the acoustical characteristic of rigid-porous material. Nevertheless, the model has been used with tolerable success to characterize outdoor surface impedance. Other impedance models are available such as variable porosity, Hamet, and Wilson relaxation models which require more parameters (i.e. porosity rate of change with depth, porosity, tortuosity, structure factor viscous and thermal relaxation times etc…) [139].

8.3) Ground impedance measurement

8.3.1) Single microphone method

A straight forward method uses a point source of broadband sound located above the surface and a receiver point also located above the surface as shown in figure 8.1(a). This allows the total field pressure $\left(p_{Total\_\,field}\right)$ to be measured. The free field spectrum level is obtained either by removing the ground plane or by raising the source and receiver sufficiently far above the surface that ground effect may be ignored. The latter method proved to be more prone to error due to the required precision for the source-receiver distance (see equation 8.1). Thus in our laboratory measurement, a flat table elevated to a height of about 1 m from the floor of the anechoic chamber (figure 5.16) is used as the ground plane support so that to establish the free field spectrum, both the ground plane and the supporting table were removed without altering the positions of the source and receiver.

8.3.2) Transfer function method

The above measuring technique serves well for deducing the excess attenuation when conditions allow an accurate free field spectrum level to be measured. However, this technique is difficult to use in outdoor *in-situ* measurements where the ground to be measured is fixed. It is more convenient to use the difference in spectra between two separate receiver locations. The locations maybe separated horizontally or vertically. This

transfer function method (sometime known as the template method) is standardised in ANSI S1.18 [140]. It allows for a very convenient determination of the surface impedance with only basic knowledge of acoustical measurements and without complicated mathematical routines. A typical measurement setup for the transfer function method is shown in figure 8.1(b). The sound pressure emitting from the loudspeaker is measured simultaneously with two microphones at different locations. If rotational symmetry is assumed the transfer function between the two locations will characterize the sound field which depends on the surface impedance and geometry. The user has to measure the Level Difference (LD) using only magnitude between the two microphone locations and swop around both microphones to cancel out any errors introduced by the measuring system. The level difference spectrum is then calculated as the difference between the excess attenuation spectra at the two receivers. Since this method eliminates the need of reference measurement, temporal changes in the propagation conditions have relatively little influence.

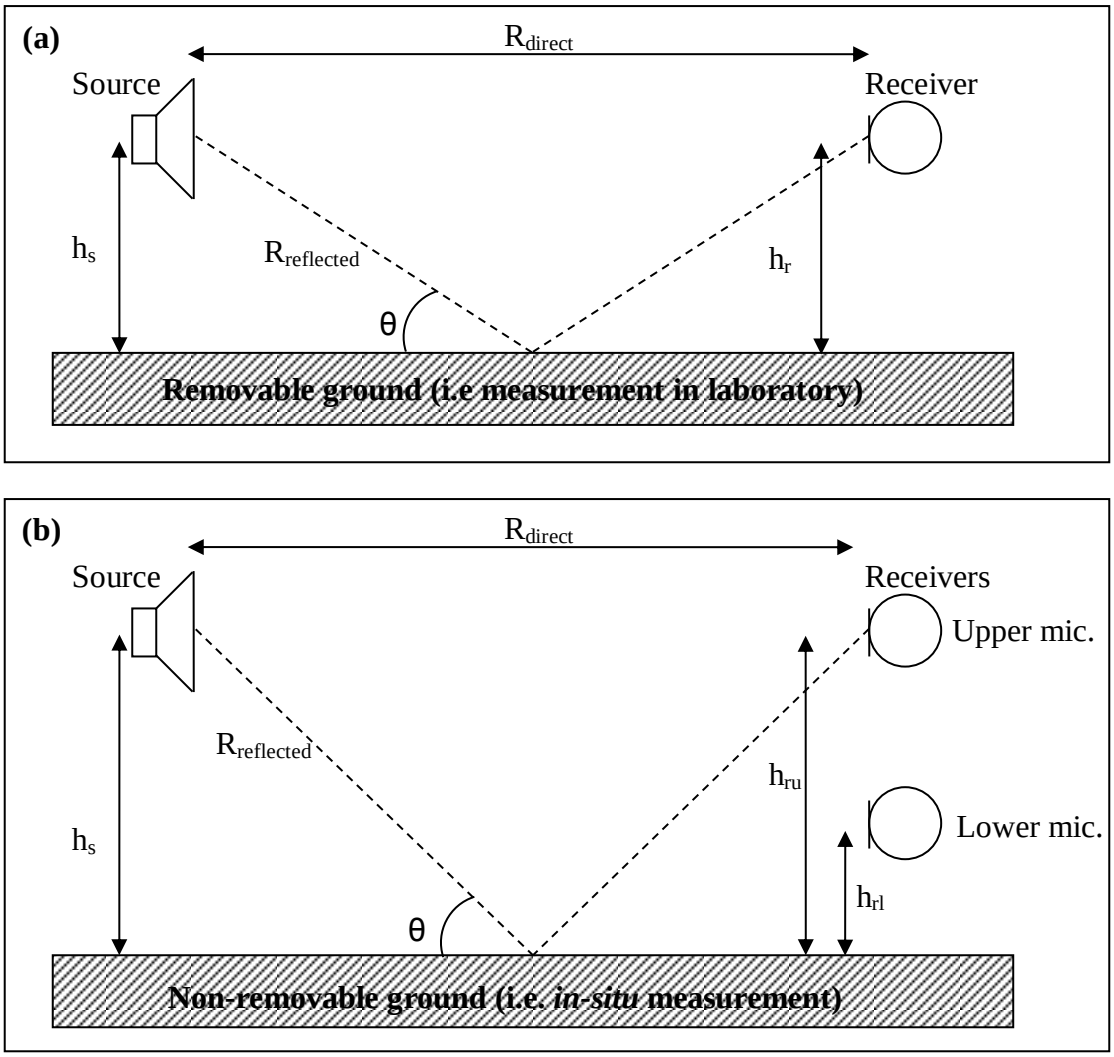

Figure 8.1: Measurement configuration to determine the surface impedance. (a) Single microphone method (laboratory) and (b) Transfer function method (outdoor in situ).

Two Medium Density Fibre (MDF) boards and a glass plate have been used to provide 'acoustically hard' ground surfaces in the laboratory. A layer of polyurethane form layer has been used as 'acoustically soft' ground. The surfaces and their dimensions are listed in table 8.1. Various ranges (source to receiver distance) and heights of source and receiver have been used according to the different types of surface materials (see table 8.2). During measurements, care was taken to ensure that the ground planes were horizontal by testing with a tubular sprit level gauge (see figure 8.2).

Ground (Material measured in laboratory)	Length (m)	Width (m)	Thickness (m)
MDF 1	2	1.3	0.006
MDF 2	1.2	0.94	0.018
Glass	1.2	1.2	0.005
Polyurethane form	2	1.2	0.03

Table 8.1: Ground materials and dimensions.

Ground (Material)	Range (m)	Source height (m)	Receiver height (m)
MDF 1	1	0.10	0.10
	1	0.20	0.20
	1	0.30	0.30
MDF 2	0.8 and 1.2	0.23	0.11
	0.8 and 1.2	0.23	0.23
	0.8 and 1.2	0.23	0.35
Glass	1	0.10	0.10
	1	0.15	0.15
	1	0.20	0.20
Polyurethane foam	0.8 and 1.2	0.23	0.11
	0.8 and 1.2	0.23	0.23
	0.8 and 1.2	0.23	0.35

Table 8.2: Dimensions for the range and heights of source and receiver for each Excess Attenuation (EA) measurement in laboratory.

Figure 8.2: Levelling test for MDF board using tubular spirit level gauge.

8.4) Excess Attenuation (EA) and Level Difference (LD) results

8.4.1) EA spectra over MDF 1 board

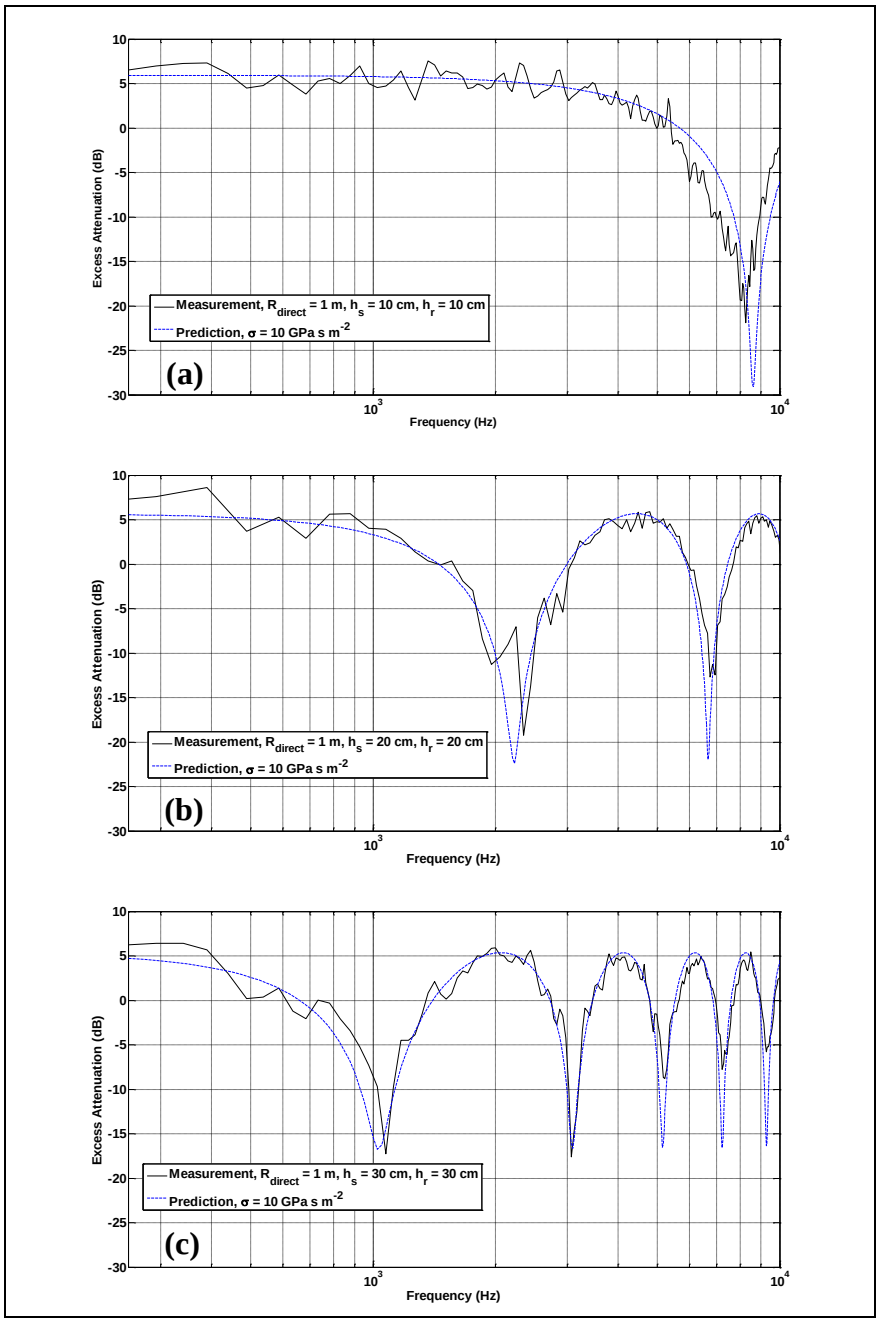

Figure 8.3 – Measured and predicted EA spectra for ground (MDF 1) at source and receiver heights at (a) 0.10 m (b) 0.20 m and (c) 0.30 m (see Tables 8.1 and 8.2)

Figure 8.3 shows the excess attenuation spectra obtained over the surface of MDF 1 with various source and receiver heights (see tables 8.1 and

8.2). For source and receiver heights of 0.10 m, the minima for the ground effect are at 8.2 kHz (figure 8.3(a)). Higher order dips are observed for source and receiver heights of 0.20 and 0.30 m (figures 8.3(b) and 8.3(c)) when the source and receiver are elevated. The excess attenuation predicted using the Delany and Bazley one parameter model with an effective flow resistivity of 10 GPa s m^{-2} gives reasonable agreement with the data in the frequency range of interest except in respect of dip amplitudes (figure 8.3(c)). Such ground is considered as locally reacting, that is the surface impedance is independent of the angle of incident sound [138]. The formula used in the EA prediction is only valid when this condition is met for the ground.

8.4.2) EA spectra over MDF 2 board

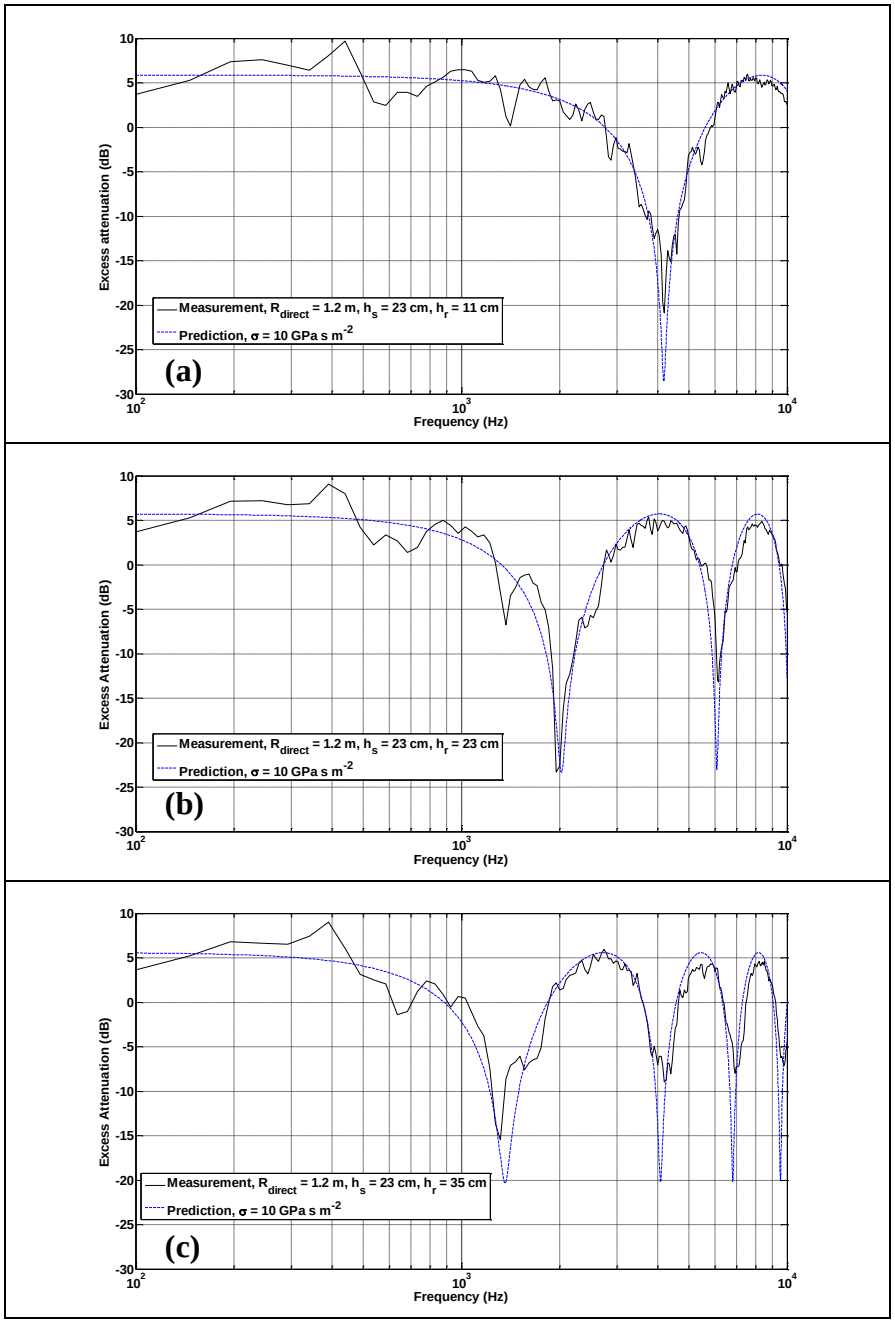

Figure 8.4 – Measured and predicted EA spectra over MDF 2 ground with source height fixed at 0.23 m and receiver heights of (a) 0.11 m (b) 0.23 m and (c) 0.35 m (see tables 8.1 and 8.2)

Figure 8.4 shows the excess attenuation spectra obtained over the MDF 2 board (see table 8.1) using a fixed source height of 0.23 m and three receiver heights (see table 8.2). Despite the difference in dimensions of MDF

2 from MDF 1, the ground effect minima agree reasonably well with predictions using the one parameter model for ground impedance with an effective flow resistivity of 10 GPa s m^{-2}. The enhancements around 400 Hz could be due to the effect of diffraction by the edges of the board as the dimensions of the MDF2 board are smaller.

8.4.3) EA spectra over glass board

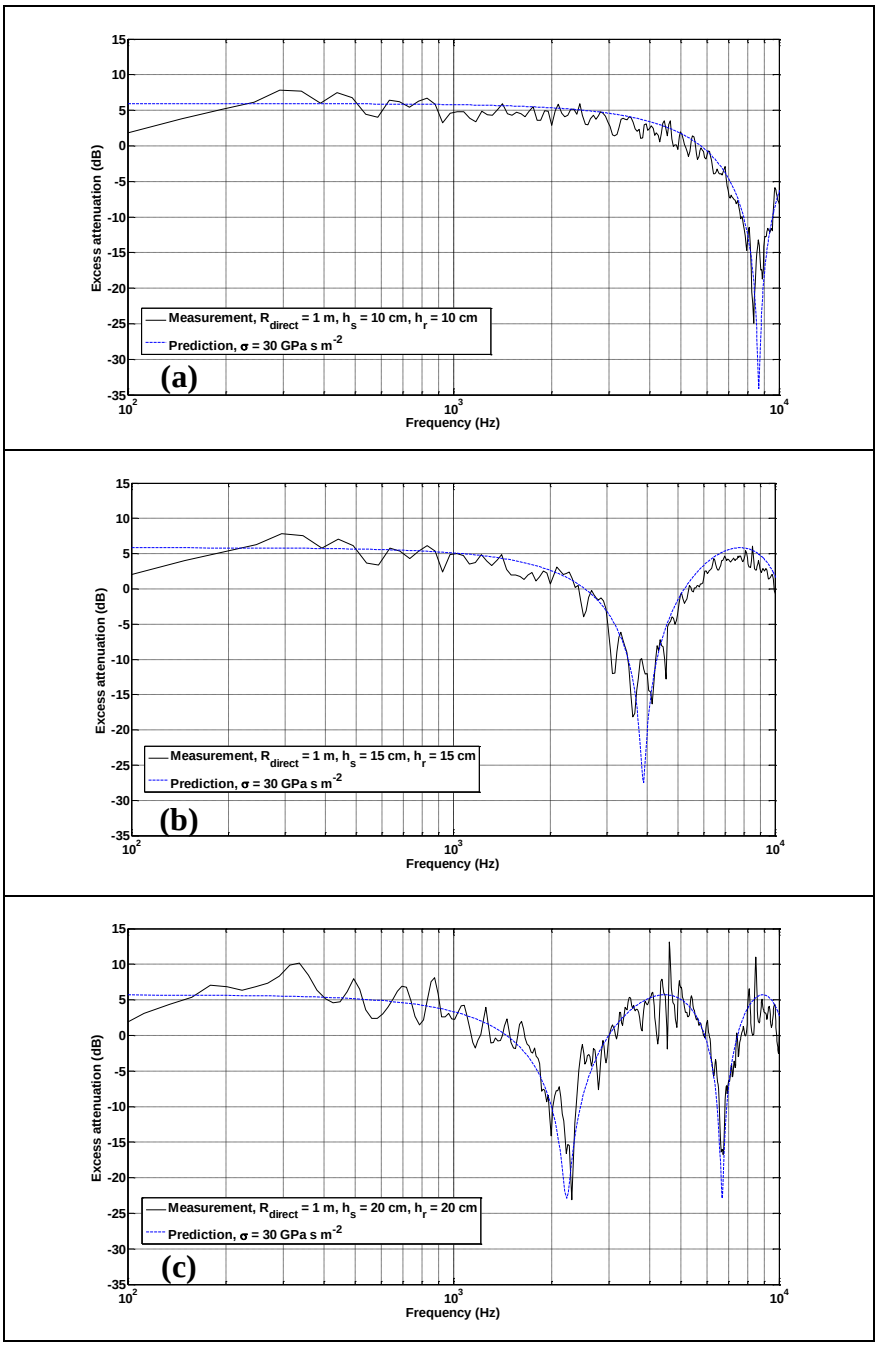

Figure 8.5 – Measured and predicted EA spectra over ground (glass) with source and receiver heights at (a) 0.10 m (b) 0.15 m and (c) 0.20 m respectively (see tables 8.1 and 8.2).

Figure 8.5 shows the excess attenuation spectra obtained over the glass plate (see table 8.1). The source and receiver heights were 0.10, 0.15

and 0.20 m show in figure (a), (b) and (c) respectively. The measured ground effect minima agree with predictions using the one parameter model for ground surface impedance with an effective flow resistivity of 30 GPa s m^{-2}. This higher fitted flow resistivity value suggests that the glass plate is acoustically harder than either MDF board.

8.4.4) EA spectra over polyurethane foam layer

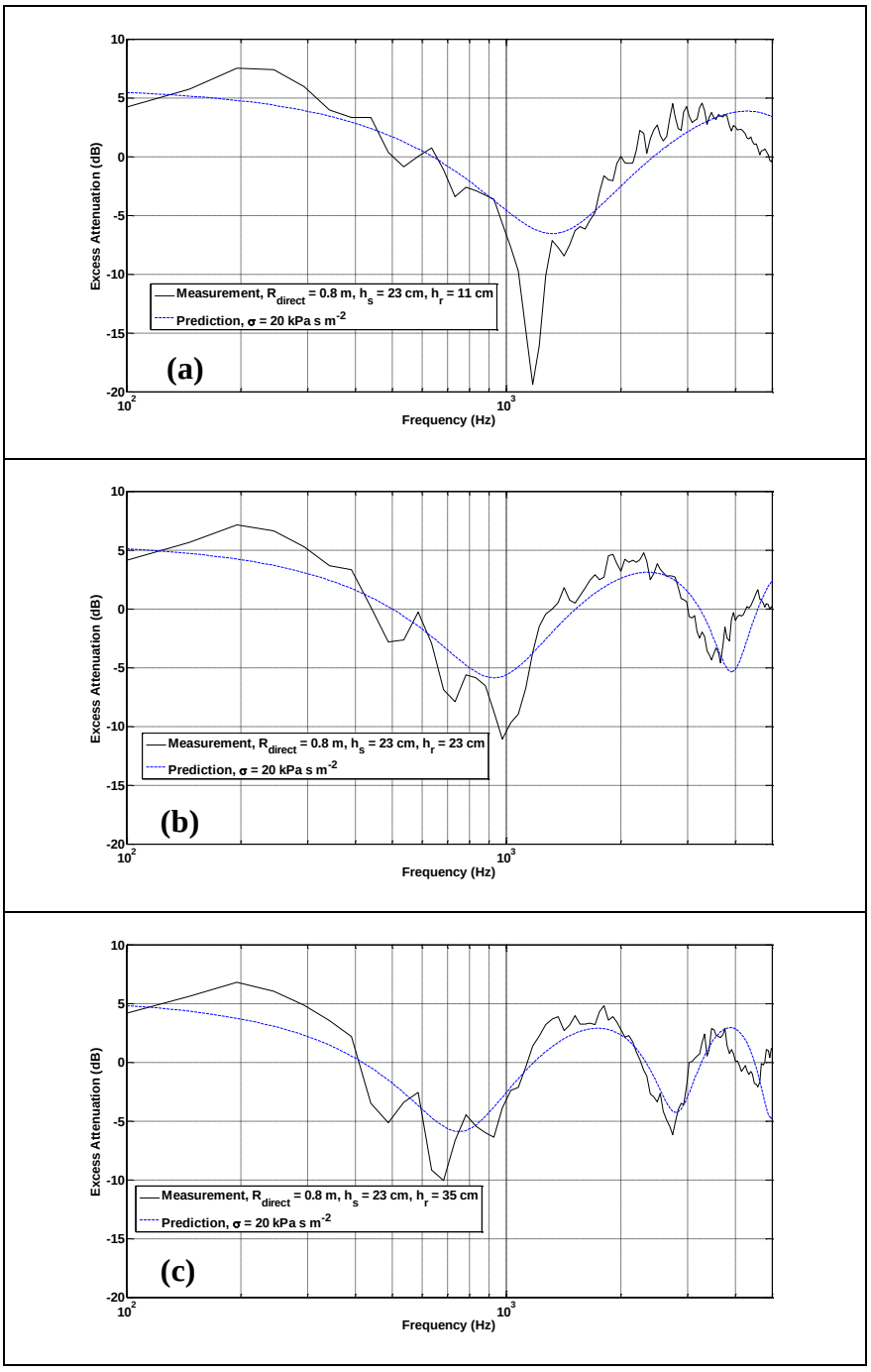

Figure 8.6 – Measured and predicted EA spectra over ground (polyurethane foam) with source height fixed at 0.23 m and receiver heights of (a) 0.11 m (b) 0.23 m and (c) 0.35 m (see tables 8.1 and 8.2)

Figure 8.6 shows the excess attenuation spectra obtained over the polyurethane foam layer (see table 8.1). The source height is fixed at 0.23 m

and receiver heights were 0.11, 0.23 and 0.35 m in figure (a), (b) and (c) respectively (see table 8.2). The predicted ground effect minima using the one parameter model for ground surface impedance with an effective flow resistivity of 20 kPa s m^{-2} are in reasonable agreement with the data in the frequency range of interest except in respect of dip amplitudes.

8.4.5) Level Difference (LD) spectra over MDF 2

The transfer function method described in section 8.3.2 was tested first in the laboratory on the MDF 2 board. Since such method requires simultaneous measurement of 2 microphones, the data acquisition system is different from that used for excess attenuation measurement i.e. the one channel MLSSA system. A similar omnidirectional source was used for both experiments but a sweep-sine signal was used for the LD measurement instead of MLS pulses. Detailed descriptions of both measuring systems are provided in chapter 5.

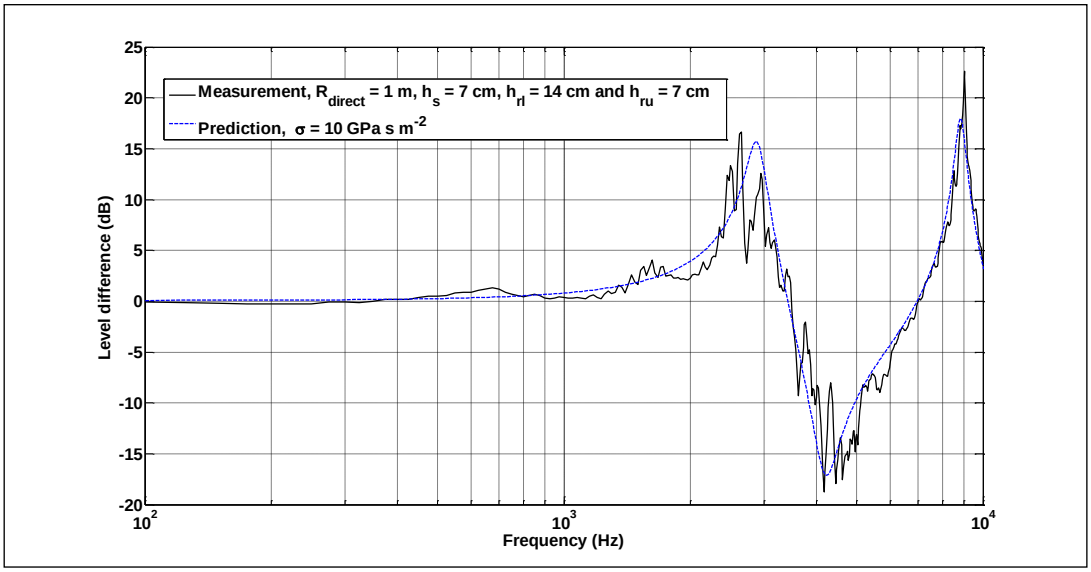

Figure 8.7 – Measured and predicted LD spectra over MDF 2 with source height fixed at 0.07 m and receiver heights of 0.07 m and 0.14 m (see tables 8.1 and 8.2)

Figure 8.7 shows predicted and measured level difference spectra obtained over the MDF 2 board (see table 8.1) using a source height of 0.07 m and receiver heights of 0.07 and 0.14 m (see table 8.2). The measured ground effects agree reasonably well with predictions using the one parameter model for ground impedance with an effective flow resistivity of 10 GPa s m^{-2} as was the case for the data obtained with the one microphone method (see figure 8.4). This confirms the reliability of the transfer function method for ground impedance characterisation.

8.4.6) LD spectra over asphalt (Outdoor *in situ* measurement)

Given the consistency of the flow resistivity deduced for MDF 2 board by both methods in the laboratory (section 8.3.1 and 8.3.2); the transfer function method has been adopted for measurement of outdoor ground properties *in situ*. Geometry B suggested by ANSI S1.18 has been considered for the outdoor measurement (see table 8.3).

Geometry	Source height (h_s)	Distance source-receiver (R_{direct})	Height of lower microphone (h_{rl})	Height of upper microphone (h_{ru})
A	0.325	1.75	0.23	0.46
B	**0.2**	**1**	**0.05**	**0.20**
C	0.4	1	0.05	0.40

Table 8.3: Source-receiver geometries for the transfer function method specified by ANSI S1.18 (data in meters).

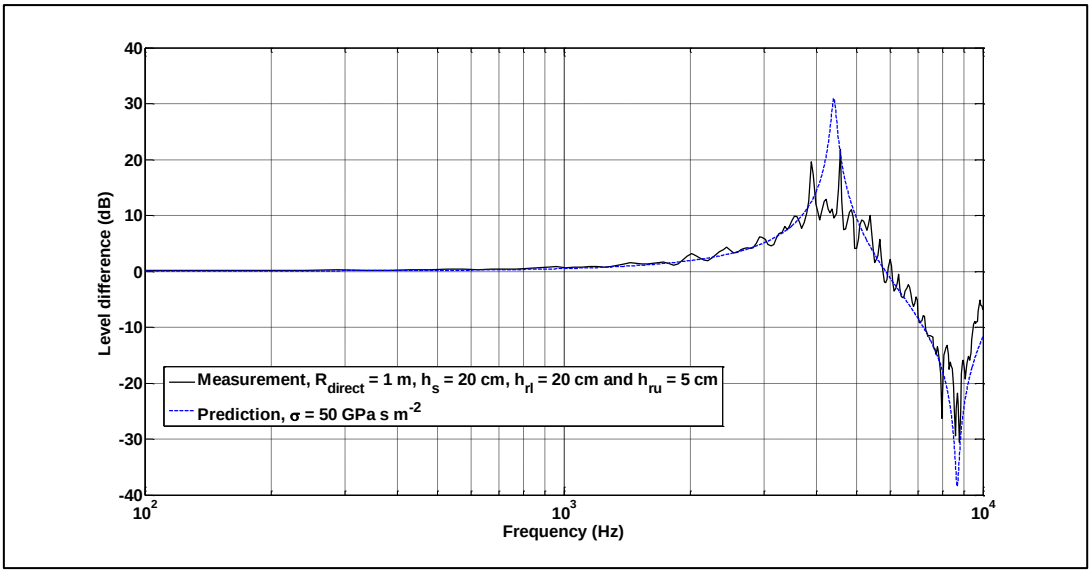

Figure 8.8 – Measured and predicted LD spectra over asphalt surface with measurement geometry 2 (table 8.3).

Figure 8.8 shows the level difference spectra obtained over the asphalt surface at the vicinity of the outdoor barrier test site. The measurement follows the geometry (B) suggested by ANSI (see table 8.3) with a source height of 0.2 m and receiver heights of 0.05 and 0.2 m. The measured ground effects agree reasonably well with predictions using the one parameter model for ground impedance with an effective flow resistivity of 50 GPa s m^{-2}, except for the maxima and minima where the amplitudes are over predicted. This suggests that asphalt ground is acoustically harder than glass plate and MDF board.

8.4.7) LD spectra over grass covered ground *in situ*

The ground impedance for grass covered ground has been deduced following the same procedure as for asphalt (section 8.4.6).

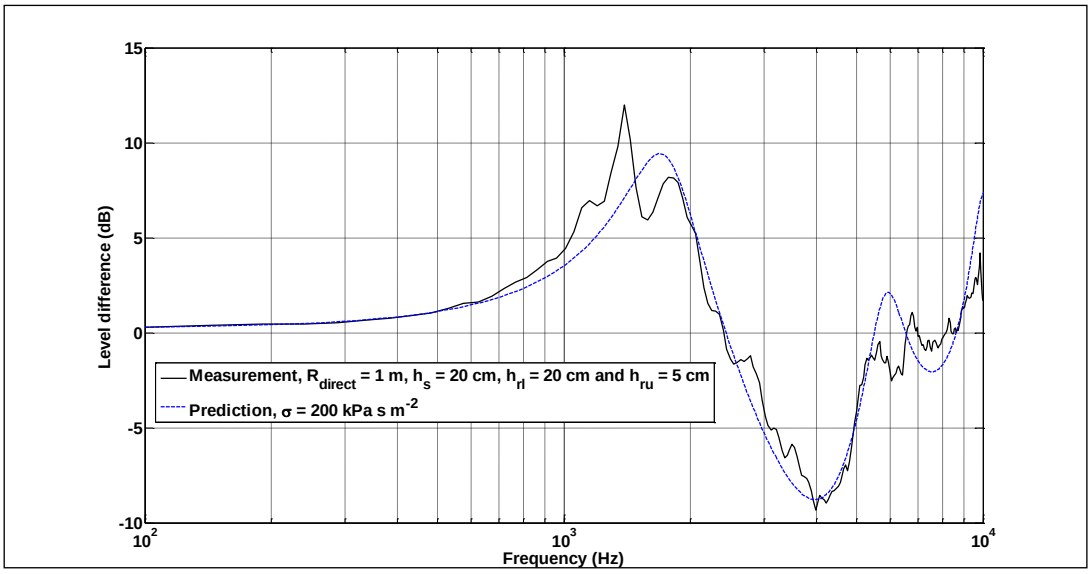

Figure 8.9 – Measured and predicted LD spectra over grass surface with measurement geometry B (table 8.3).

Figure 8.9 shows the level difference spectra obtained over the grass surface at the vicinity of the outdoor barrier test site. Predictions (using the Delany and Bazley model give a better fit with the grass ground than obtained with asphalt. The effective flow resistivity is predicted to be 200 kPa s m^{-2} which is in good agreement with typical flow resistivity values (150 – 300 kPa s m^{-2}) for outdoor grass surfaces [136].

8.5) Analytical formulation for array of sonic crystals with their axes parallel to a rigid ground

Following the development work by our collaborators [147], assuming the ground to be considered 'acoustically hard', then the multiple scattering method (see chapter 3) can be modified using the method of images to construct the reflected acoustic field [141]. This semi-analytical method is used to analyse the performance of arrays of rigid or elastic cylindrical scatterers suspended with their axes parallel to a rigid ground. In this section,

square lattice arrays of 7x3 scatterers are considered. The predicted performance of the sonic crystals in the presence of rigid ground is compared with that of the crystals placed in the free field. Insertion Loss (IL) spectra measured in an anechoic chamber are compared with predictions.

8.5.1) Rigid scatterers

We consider an array of M circular scatterers placed in a (positive) half-space characterised by the sound speed in air c = 344 m/s and density $\rho = 1.2$ kg/m^3. The source is assumed to be a point source. Figure 8.10 illustrates the geometry of the array and its image. The position of each scatterer C_m, $m = 1 \ldots M$, is given by the vector R_m. The position of the scatterer C_m is defined by the radius vector $R_m^{'}$. The scatterers are considered to be arranged in a square lattice which is defined by the lattice constant L. However the method described subsequently can be applied to any other lattice configuration.

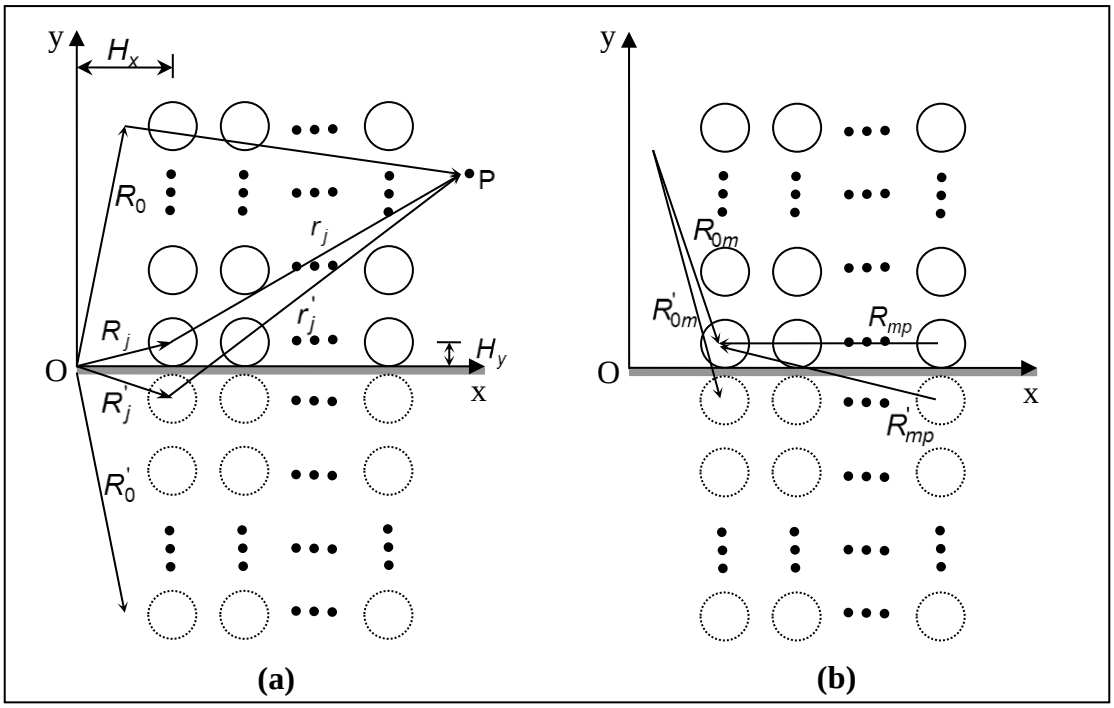

Figure 8.10: Square lattice array above a perfectly reflecting plane. (a) Set of vectors used in equation (8.6). (b) Set of vectors employed in equation (8.14).

The equation for cylindrically-spreading acoustic waves in a lossless fluid medium previously shown in chapter 4, equation 4.1 is repeated here for convenience. This equation satisfies the two-dimensional Helmholtz equation in the half-space that is written in polar coordinates (r,θ) as,

$$\nabla^2 p(\mathbf{r}) + k^2 p(\mathbf{r}) = 0, \qquad \textbf{(8.3)}$$

where $\nabla^2 = \frac{\partial^2}{\partial x_1^2} + \frac{\partial^2}{\partial x_2^2}$ is the Laplacian, $k = \frac{2\pi f}{c}$ is the wave number in air defined as the ratio between angular frequency ω and sound speed in air, c. $\mathbf{r} = r(\cos\theta, \sin\theta)$ is the radius vector and p is acoustic displacement potential.

The solution $p(\mathbf{r})$ also satisfies Sommerfeld's radiation condition,

$$\frac{\partial p}{\partial r} - ikp = o\left(r^{-\frac{1}{2}} \right), \text{ as } r \to \infty . \tag{8.4}$$

We imposed Neumann condition on the boundary of acoustic half-space (i.e. rigid ground) and on the surface of the scatterers (this condition has to be replaced by continuity conditions if scatterer is an elastic shell described in chapter 6) that is

$$\frac{\partial p}{\partial n} = 0 . \tag{8.5}$$

Following the multiple scattering described in chapter 3 and the method of images [141] the general solution of the formulated problem can be written as [142]

$$p(\mathbf{r}) = p_0(\mathbf{r}) + p_s(\mathbf{r}). \tag{8.6}$$

whereby contributions from the point source and its image are collected in p_0 which can be expressed by

$$p_0(\mathbf{r}) = p_{0,d}(\mathbf{r}) + p_{0,r}(\mathbf{r}), \tag{8.7}$$

$$p_{0,d}(\mathbf{r}) = H_0^{(1)}(kr_0), \tag{8.8}$$

$$p_{0,r}(\mathbf{r}) = H_0^{(1)}(kr_0'), \tag{8.9}$$

whereas the scattered field components are described by

$$p_0(\mathbf{r}) = p_{s,d}(\mathbf{r}) + p_{s,r}(\mathbf{r}), \tag{8.10}$$

$$p_{s,d}(\mathbf{r}) = \sum_{m=1}^{M} \sum_{n=-\infty}^{+\infty} A_n^m Z_n^m H_n^{(1)}(kr_m) e^{in\theta_m}, \quad \textbf{(8.11)}$$

$$p_{s,r}(\mathbf{r}) = \sum_{m=1}^{M} \sum_{n=-\infty}^{+\infty} A_n^m Z_n^m H_n^{(1)}(kr_m') e^{-in\theta_m'}. \quad \textbf{(8.12)}$$

The vector $\mathbf{r}_0 = r_0(\cos\theta_0, \sin\theta_0)$ connects the point source and the receiver point (i.e. point P in figure 8.11(a)). The vector $\mathbf{r}_m = r_m(\cos\theta_m, \sin\theta_m)$ connects the centre of scatterer C_m and the receiver. The prime $(')$ is used to indicate the geometrical parameters for the image source and the image scatterers placed in the negative half-space. A_n^m, $n \in \mathbf{Z}$, $m = 1 \ldots M$, are unknown coefficients. The solution for the unbounded acoustic space can be retrieved from equation 8.6 by putting to zero in equations (8.7) and (8.10) all terms related to the constructed images that are $p_{0,r}$ and $p_{s,r}$ respectively. One can also deduce from equation (8.6) and vector definitions in figure 8.10(a) that for the source and receiver both on the ground, the acoustic pressure in a half-space is double the pressure in the unbounded acoustic space.

The factors Z_n^m describe the type of conditions imposed on the surface of the scatterers and in case of rigid cylinders they can be expressed as

$$Z_n^m = \frac{\partial_r J_n(ka_m)}{\partial_r H_n^{(1)}(ka_m)}, \quad \textbf{(8.13)}$$

where a_m is the radius of scatter C_m and ∂_r is the derivative with respect to polar coordinate r.

Applying the addition theorem (see Appendix B), to the solution (equation 8.6) and substituting it to the boundary condition (equation 8.5), the algebraic system of equations can be derived to find the unknown coefficients A_n^m. This system is given by

$$A_n^m + \sum_{q=-\infty}^{\infty} \sum_{p=1,\, p\neq m}^{M} \left\{ A_q^p Z_q^p H_{q-n}^{(1)}\left(kR_{mp}\right) e^{i(q-n)(\pi+\alpha_{mp})} + \sum_{p=1}^{M} A_q^p Z_q^p H_{q+n}^{(1)}\left(kR'_{mp}\right) e^{-i(q+n)\alpha'_{mp}+iq\pi} \right\} = \tag{8.14}$$

$$-H_n^{(1)}\left(kR_{0p}\right) e^{-in(\pi+\alpha_{0m})} - H_n^{(1)}\left(kR'_{0m}\right) e^{-in\left(\pi+\alpha'_{0m}\right)}, n \in Z, m = 1 \ldots M ,$$

where vector $\mathbf{R}_{0m} = R_{0m}\left(\cos\alpha_{0m}, \sin\alpha_{0m}\right)$ defines the position of scatterer C_m with respect to point source and vector $\mathbf{R}_{mp} = R_{mp}\left(\cos\alpha_{mp}, \sin\alpha_{mp}\right)$ defines the position of scatterer C_p with respect to scatterer C_m. Again the system of equations 8.14 can be transformed to that for the case of unbounded acoustic space by eliminating all terms dependent on the geometrical parameters of image source and scatterers (see equation 3.36). To solve numerically for the infinite system of equations 8.14 is truncated to the finite number of M(2N+1) equations. If N is equal to 6, the numerical solution is accurate up to four significant figures [49]. It is also noted that for the considered configurations and frequency range the computation time required to solve system (equation 8.11) on an IntelCore 2 Duo PC with 2 GB of RAM is between 60 and 180 s.

Also note that throughout this chapter the insertion loss (equation 3.37) is calculated. In free field the cylinders locations in the lower half of the 7x3 array are defined by the coordinates identical to those of the image cylinders in the half-space problem.

8.5.2) Elastic shell scatterers

The multiple scattering analysis can be extended to predict the insertion loss spectrum due to an array of elastic shells with their axes parallel to a rigid ground. The identical elastic shells are characterised by their density (ρ_s), Young's modulus (E), Poisson's ratio (ν), shear velocity (c_2), half-thickness (h) and the mid-surface radius $(S = a_m - h)$. For certain ranges of value of these parameters, the first elastic shell resonance associated with the breathing mode can be observed below the first Bragg band gap associated with the lattice constant of the array in the unbounded acoustic space (see chapter 6). This results in additional positive insertion loss peaks.

The asymptotic theory of thin elastic shells [107] has been used to derive the factors

$$Z_n^m = \frac{\partial_r J_n(kS)}{\partial_r H_n^{(1)}(kS) + iU_n}, \qquad \textbf{(8.15)}$$

where

$$U_n = \frac{\varepsilon}{\kappa} \frac{n^2 - k_3^2 S^2}{\pi S h \left(1 + n^2 - k_3^2 S^2\right) \partial_r J_n(kS)}. \qquad \textbf{(8.16)}$$

$\varepsilon = \dfrac{\rho c}{\rho_s c_2}$ is the relative impedance, $\kappa = \dfrac{c}{c_2}$ and $\kappa_3 = \omega \sqrt{\dfrac{\rho(1-\nu^2)}{E}}$. If the relative impedance ε tends to zero, then U_n becomes negligible and the form of Z_n^m in (equation 8.15) reduces to that in (equation 8.13).

8.5.3) Laboratory measurements

Measurements of the insertion loss spectra due to arrays of regularly spaced parallel rigid cylinders and elastic shells without and with ground planes have been carried out in an anechoic chamber. The rigid cylinders consisted of 2 m long PVC pipes with outer diameter of 0.055 m. 2 m long elastic shells were made from 0.25 mm thick sheets of latex by overlapping the edges and gluing them together. The sound source was a Bruel & Kjaer (B&K) point source loudspeaker controlled by a Maximum-Length Sequence System Analyzer (MLSSA) system enabling determination of impulse responses in the presence of noise. A B&K ½ inch microphone was used as the receiver. Figure 8.12 (a), (b) and (c) shows example measurement arrangements. Supports for the 2 m long cylinders were provided by holed MDF boards at the top and base of each array. To maintain their shape and vertical orientation, the latex cylinders were slightly inflated above atmospheric pressure through a common pipe connecting to a small pump.

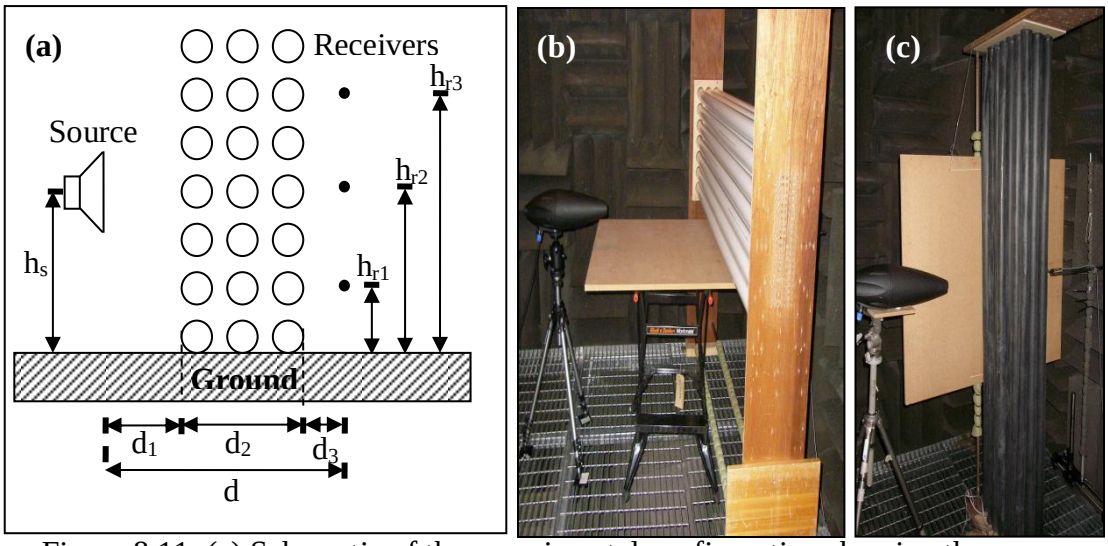

Figure 8.11: (a) Schematic of the experimental configuration showing the source location, the sonic crystal array and three receiver locations. (b) Photograph of experimental arrangement with rigid cylinder above rigid (MDF 2 board) ground. (c) Photograph of experimental arrangement with latex shell array near to rigid (MDF 1 board) ground (see table 8.1).

An MDF board large enough to avoid the diffraction at the edges was used as a rigid surface. The rigid cylinders could be arranged horizontally above a horizontal MDF board (figure 8.11 (b)). However since the latex cylinders had to be arranged vertically to preserve their shape, the MDF board was also supported vertically (figure 8.11 (c)). In both cases the cylinder axes were parallel to the board. For simplicity all distances to the MDF board in both setups are referred to as heights. As shown in figure 8.11(a), the loud speaker point source was positioned d_1 = 0.75 m from the array of rigid cylinders and d_1 = 0.35 m from the array of latex shells at the height of the horizontal mid-plane of the array (h_s = 0.23 m above the ground). The height of the receiver microphone was h_{r1} = 0.11 m, h_{r2} = 0.23 m and h_{r3} = 0.35 m and it was placed in a vertical plane d_3 = 0.25 m from the back of the array. The receiver heights were chosen to be below, at and above, the horizontal mid-plane of the array. In all cases, the distance between the microphone and

the cylinder array has been considered the same. The difference between the sound levels recorded in the x direction (0°) at the same point behind the array and without the ground was measured.

8.5.4) Comparisons of data and predictions for rigid cylinders array with their axes parallel to a rigid ground.

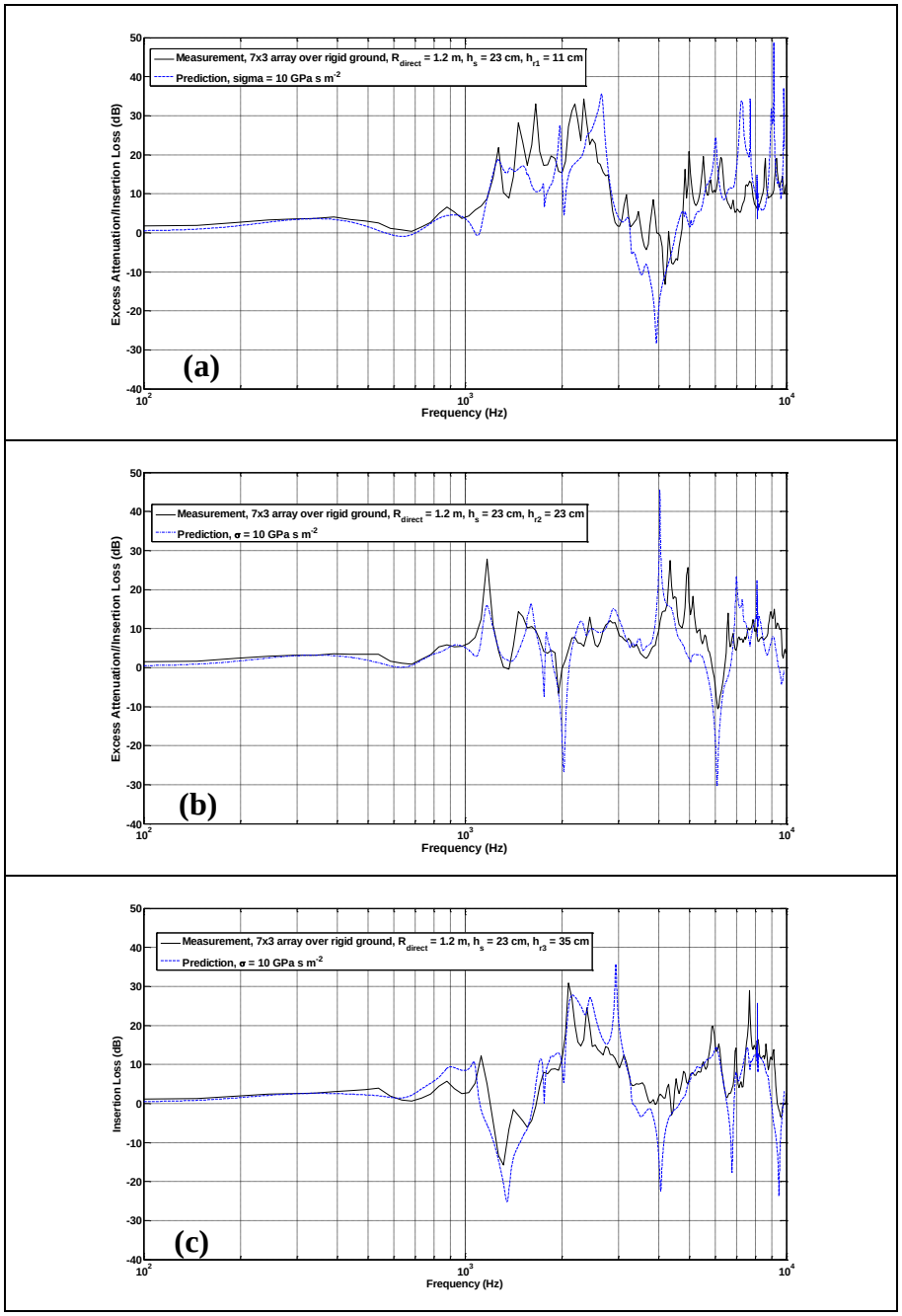

Figure 8.12 – Measured (solid line) and predicted (broken line) IL spectra due to a square lattice array of 7x3 rigid cylinders of diameter 0.055 m over acoustically-rigid ground with source coordinates (0, 0.23) m and receiver coordinates (a) (1.20, 0.11) m, (b) (1.20, 0.23) m and (c) (1.20, 0.35) m.

Figure 8.12 compares measured and predicted insertion loss spectra for a 7x3 rigid cylinder array over rigid ground for three receiver heights. The predictions assume the source-array-receiver geometries used in the experiments described in section 8.5.3. Up to 1.5 kHz the predictions and data are in close agreement. Above 1.5 kHz there are some discrepancies which may be due to unwanted reflections and departures from the assumed ideal geometry. Both data and predictions in figures 8.12(a) and 8.12(b) show IL maxima near 2.5 kHz which are associated with the Bragg band gaps expected in the unbounded domain. Both data and predictions for the elevated receiver height (0.23 m and 0.35 m) show the adverse influence of the rigid ground effect on the IL spectra near 2 kHz and 1.25 kHz. This point will be further elaborated in figure 8.13 with the IL spectra plotted against the excess attenuation spectra. Indeed in figure 8.12(b), for the receiver at 0.235 m height, it is clear that the destructive interference in the ground effect near 2.5 kHz is rather dominant.

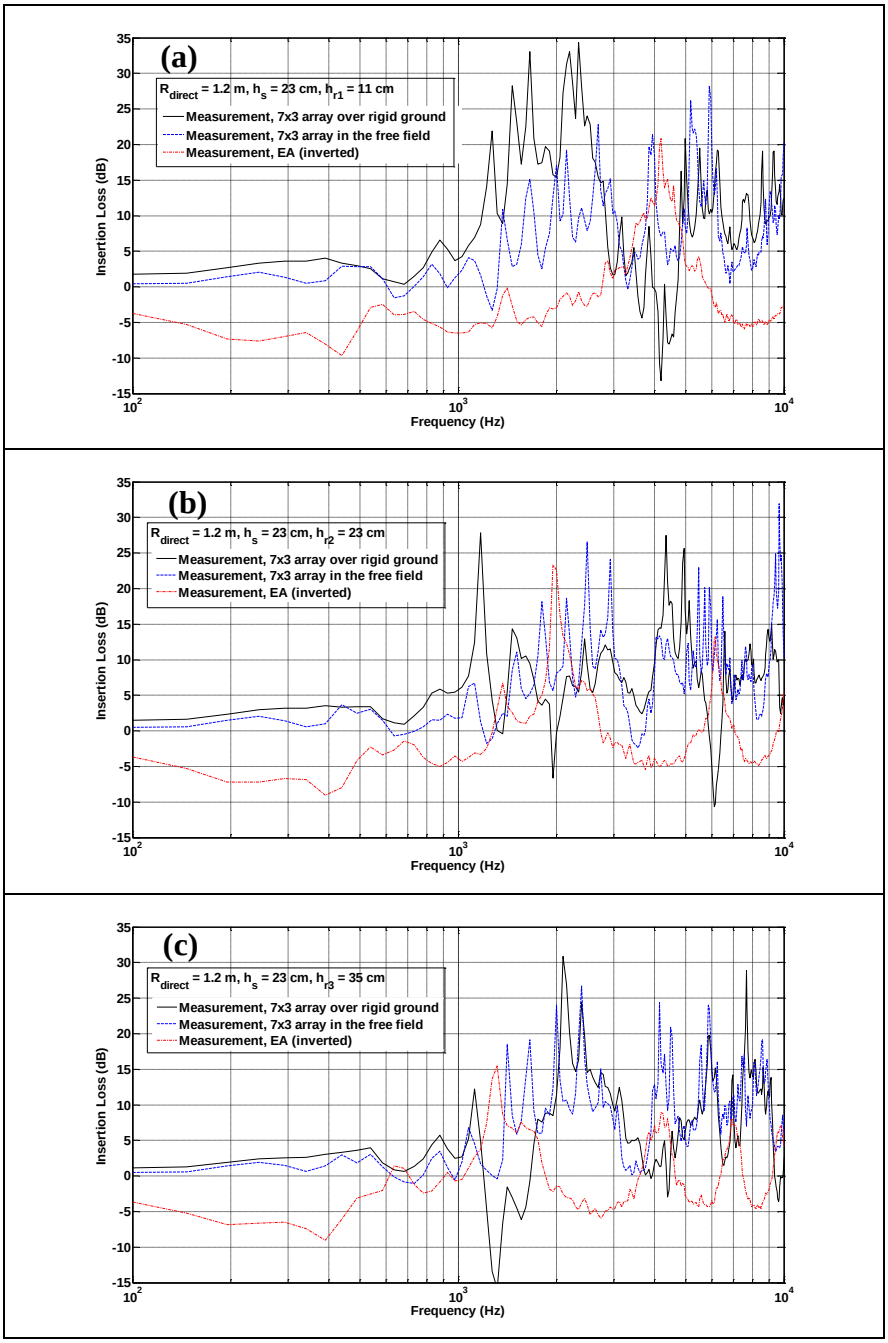

Figure 8.13 – Measured insertion loss spectra due to a 7x3 rigid cylinders array over acoustically rigid ground (solid line) compares with identical array measured in free field (broken line) as well as measured inverted excess attenuation (dash dot line) The source is at coordinates (0.0.235) m and the receiver coordinates are (a) (1.20, 0.11) m, and (c) (1.20, 0.35) m.

Figure 8.13 compares the measured IL spectra for a horizontal PVC pipe array with and without a rigid (MDF 2) ground at source height of 0.23 m and three receiver heights of 0.11, 0.23 and 0.35 m as shown in (a), (b) and (c) respectively. The measured excess attenuation spectrum due to rigid (MDF 2) ground for a similar source-receiver geometry to that used for the IL measurements is superimposed into the IL plot but inverted (see figure 8.4). The Bragg band gap in this particular arrangement (lattice constant of 0.69 m) is near 2.5 kHz. The array band gaps are impaired, resulting in negative insertion loss, where they coincide with the minima in the ground.

8.5.5) Comparisons of data and predictions for elastic shells array with their axes parallel to a rigid ground.

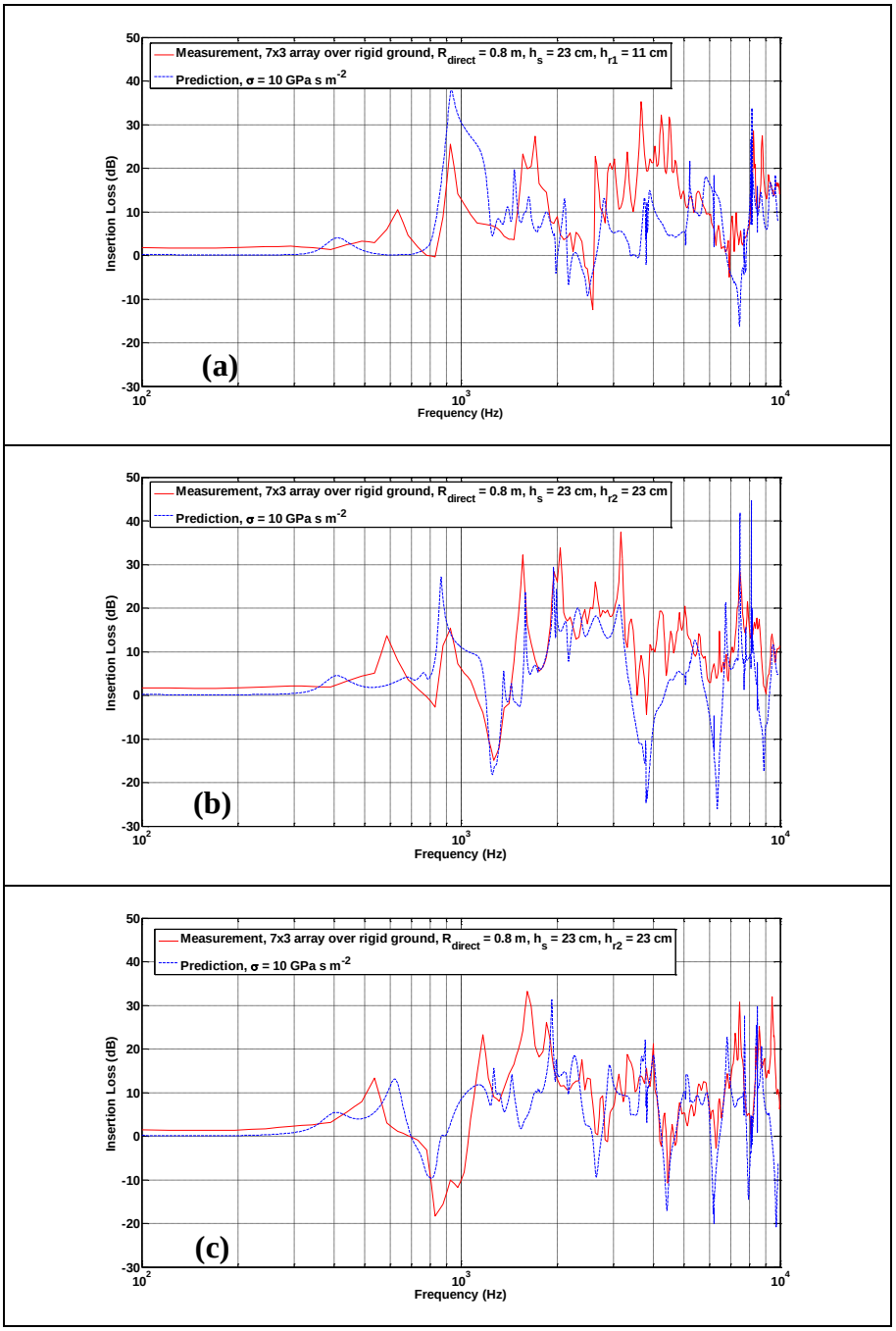

Figure 8.14 – Measured (solid line) and predicted (broken line) IL spectra due to a square lattice array of 7x3 latex shell cylinders of diameter 0.055 m over acoustically-rigid ground with source coordinates (0, 0.23) m and receiver coordinates (a) (0.8, 0.11) m, and (c) (0.8, 0.35) m.

.

The measured and predicted performance of 7x3 array of latex shells over the rigid ground shown in figure 8.14 are similar to that described in section 8.5.2. In particular, figure 8.14(c) shows that when the first ground effect dip is in the vicinity of the breathing mode resonance of the shell (near 900 Hz) the corresponding positive IL peak is no longer present. Again, this point will be further elaborated in figure 8.15 with the excess attenuation spectra plotted against the insertion loss spectra.

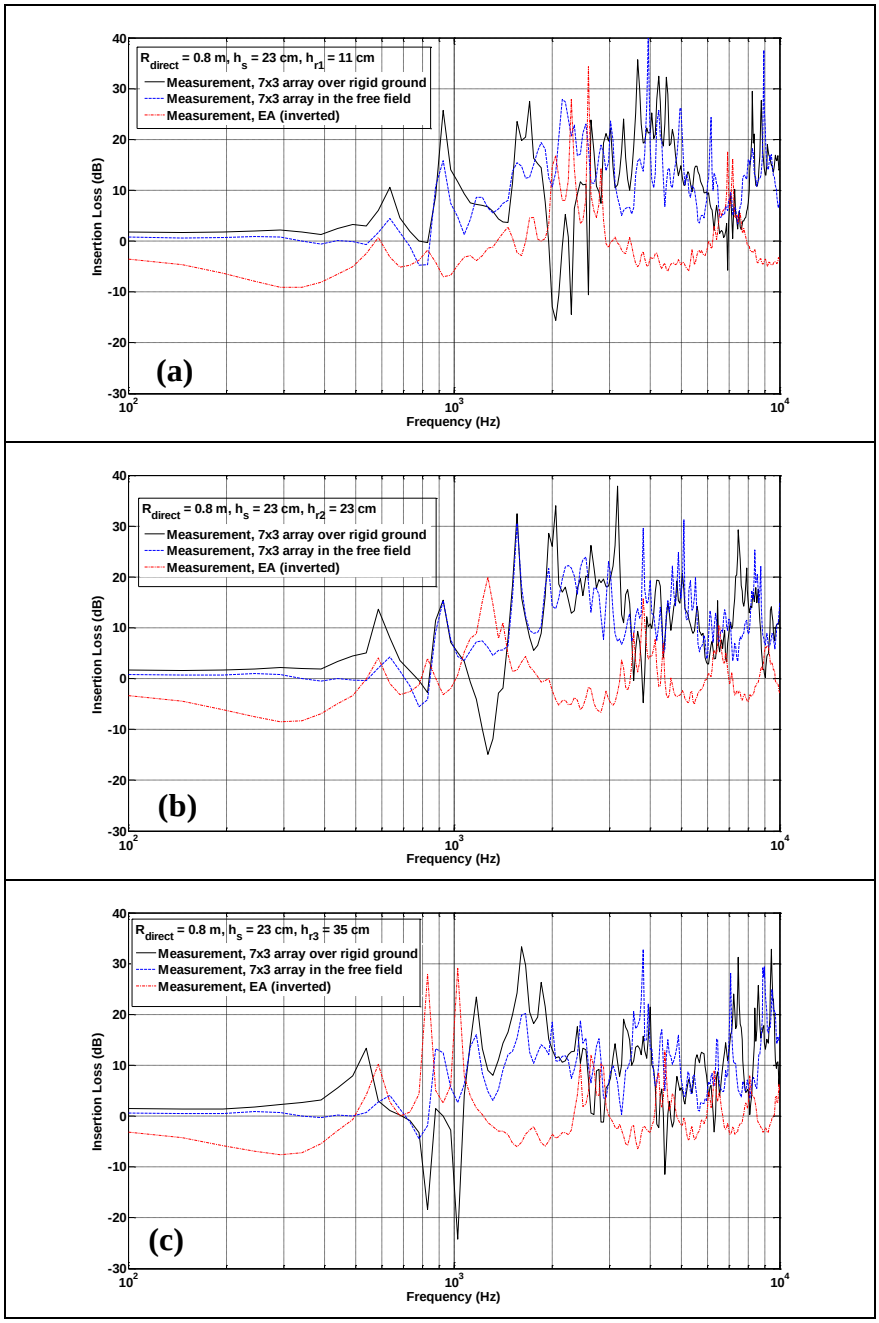

Figure 8.15 – Measured insertion loss spectra due to a 7x3 latex shell cylinders array over acoustically rigid ground (solid line) compares with identical array measured in free field (broken line) as well as measured inverted excess attenuation (dash dot line) The source is at coordinates (0.0.235) m and the receiver coordinates are (a) (1.20, 0.11) m, and (c) (1.20, 0.35) m.

Figure 8.15 compares the measured IL spectra (see equation 1.9) for a horizontal elastic shell cylinders array with and without a rigid (MDF 2) ground at source height of 0.23 m and three receiver heights of 0.11, 0.23 and 0.35 m as shown in (a), (b) and (c) respectively. The measured excess attenuation

spectrum due to rigid ground for a similar source-receiver geometry to that used for the IL measurements is superimposed into the IL plot but inverted. The Bragg band gap in this particular arrangement (lattice constant of 0.069 m) is near 2.5 kHz. The array band gaps are impaired, resulting in negative insertion loss, where they coincide with the minima in the ground.

8.6) Laboratories studies on rigid and elastic cylinder arrays with their axes parallel to a finite impedance ground.

8.6.1) IL spectra for horizontal rigid cylinders array over a finite impedance ground.

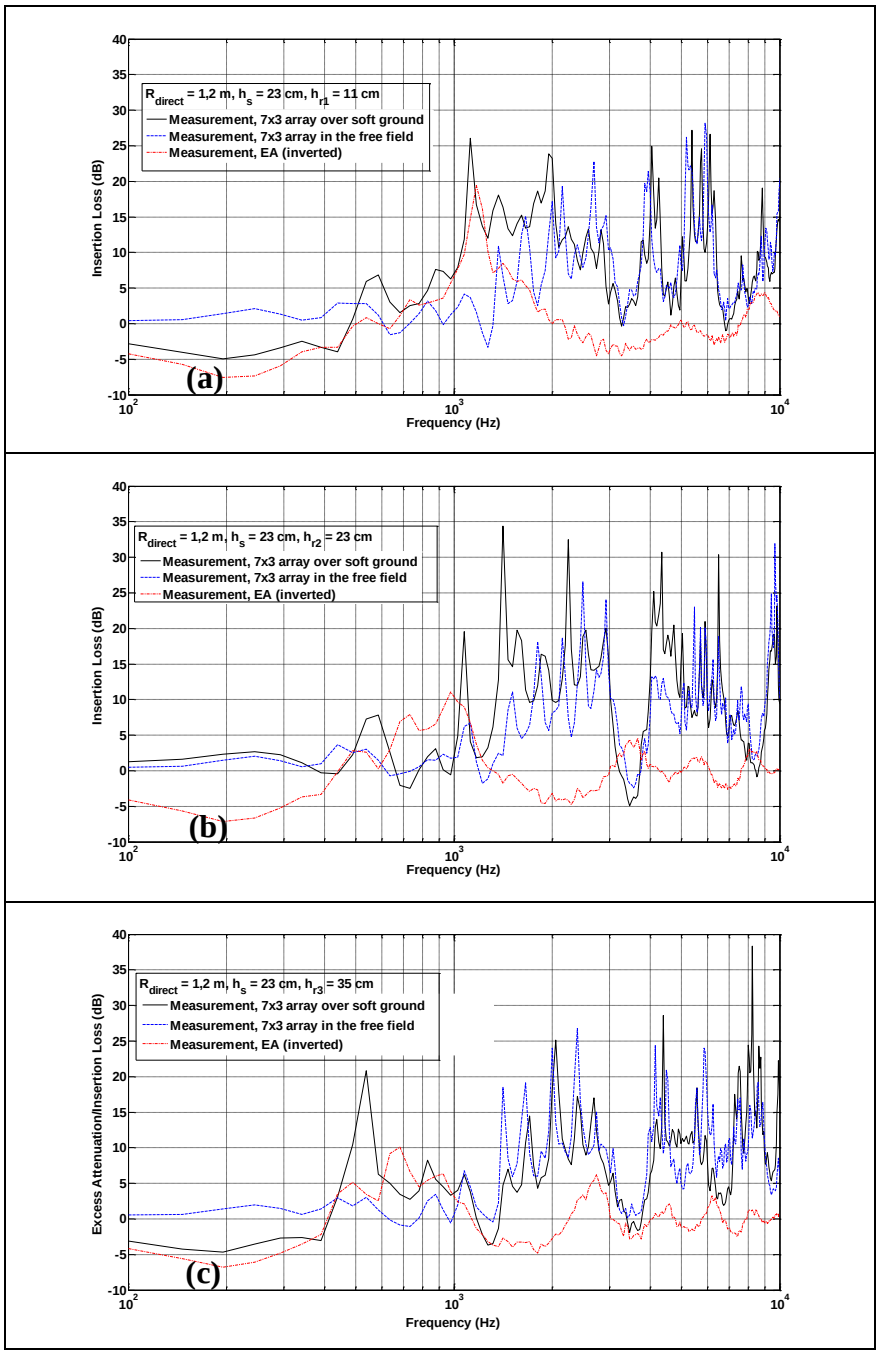

Figure 8.16: Measured insertion loss spectra due to a 7x3 rigid cylinders array over finite impedance (Polyurethane foam) ground (solid line) comparing with identical array measured in free field (broken line) as well as measured inverted excess attenuation spectra of the ground (dash dot line) taken at same source-receiver distances. The source is at coordinates (0.0.235) m and the receiver coordinates are (a) (1.20, 0.11) m, and (c) (1.20, 0.35) m.

Figure 8.16 compares the measured insertion loss spectra due to 7x3 rigid cylinder arrays over finite impedance ground (Polyurethane foam) for three receiver heights using the source location described in section 8.5.3. The measure IL spectra due to identical arrays without the presence of the ground and excess attenuation (inverted) due to the Polyurethane foam layer with the same source-receiver geometry are superimposed to the plots. Compared to the results for the rigid ground plotted in figure 8.13, the minima associated with the finite impedance ground effect seem to enhance the IL peaks and also we note that the ground effects are also shifted towards lower frequency. This effect could be exploitable in the design of SC-based noise barriers.

8.6.2) IL spectra for horizontal elastic shell cylinders array over a finite impedance ground.

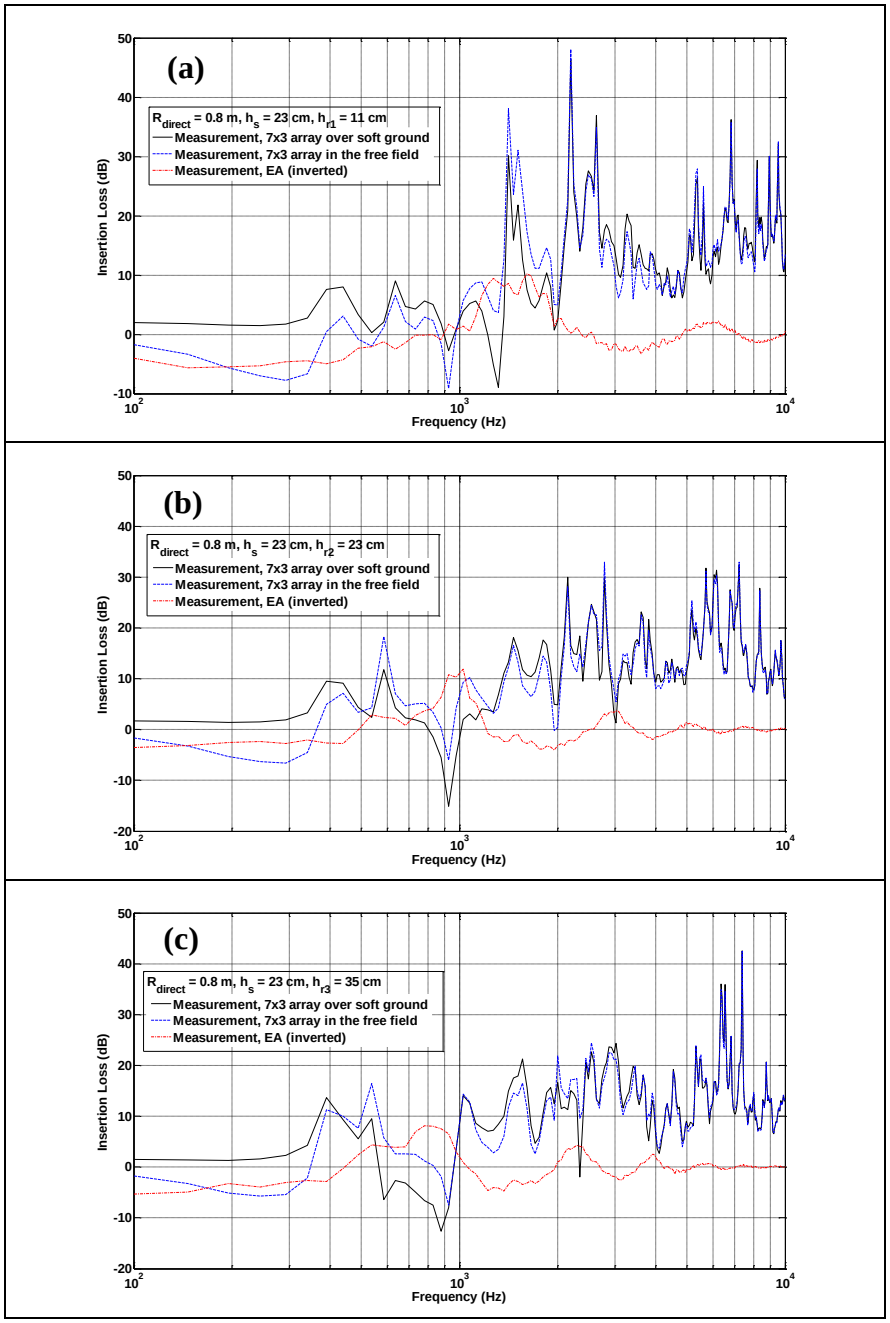

Figure 8.17 – Measured insertion loss spectra due to a 7x3 latex shell cylinders array over finite impedance (Polyurethane foam) ground (solid line) compared with that due to an identical array measured in free field (broken line) as well as measured inverted excess attenuation spectra due to the ground alone (dash dot line) The source is at coordinates (0.0.235) m and the receiver coordinates are (a) (1.20, 0.11) m, (b) (1.20, 0.23) m and (c) (1.20, 0.35) m.

Figure 8.17 compares the measured insertion loss spectra due to 7x3 latex cylinder arrays over finite impedance ground (Polyurethane foam) for three receiver heights using the source location described in section (a), (b) and (c) respectively. The measure IL spectra for identical arrays without the presence of the ground and excess attenuation spectra (inverted) of the Polyurethane foam with the same source-receiver geometry are superimposed on the plots. According to figure 8.17, the ground effects are contrary to what has been observed for the PVC cylinders array over the finite impedance ground (see figure 8.16). Again, the band gaps are impaired, resulting in negative insertion loss, where they coincide with the first minima in the ground. Subsequent dips are too small in amplitude and have negligible effects as seen for higher frequencies.

8.6.3) Laboratories studies on a vertical axis cylinder array over a horizontal acoustically rigid ground (MDF 1)

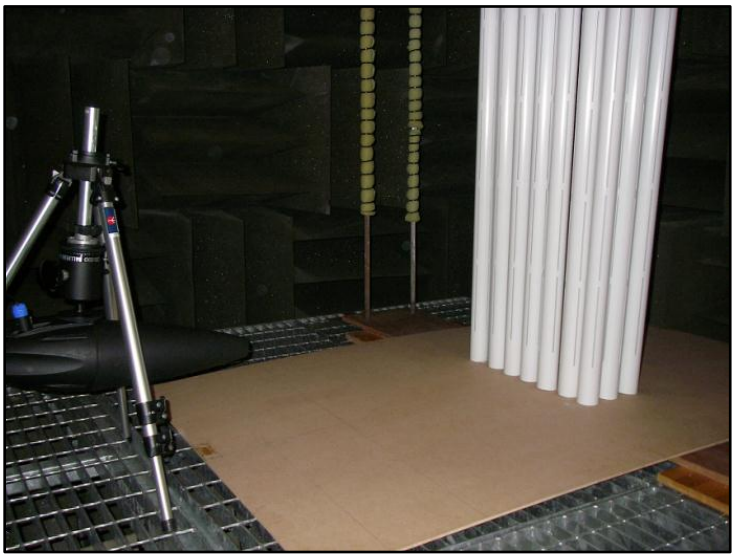

Figure 8.18: 7x3 PVC cylinders in vertical array orientation above a MDF ground (MDF 1).

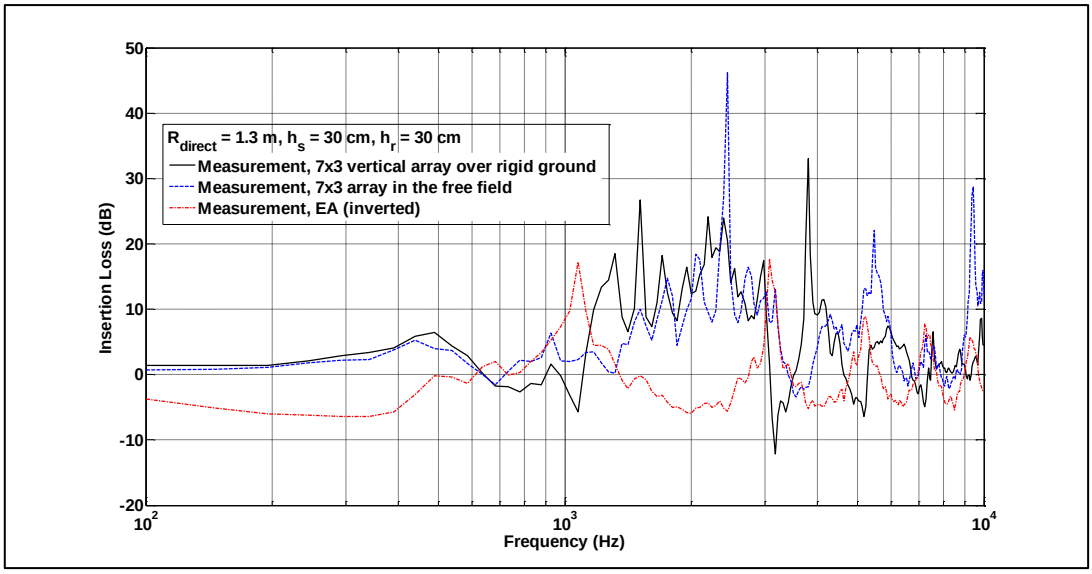

Figure 8.19: Measured insertion loss spectra of vertical array with source and receiver at 0.3m height with (solid line) and without (broken line) the MDF 1 ground plane. Measured inverted excess attenuation (inverted) spectra of the ground (dash dot line).

Figure 8.19 compares IL spectra due a vertical axis array without and with the MDF 1 surface and source and receiver at 0.3 m height. Without the ground surface, there is a band gap centred at about 2.5 kHz, due to multiple scattering by the (acoustically hard) cylinders. This corresponds with the first Bragg diffraction frequency (see equation 2.14). However, in the presence of the reflecting surface, the first and higher order band gaps are impaired when they coincide with minima in the EA spectra. On the other hand, for this geometry, the first ground attenuation maximum due to the MDF 1 board is shifted in frequency by the presence of the vertical array.

8.7) Laboratories studies on vertical axis array over acoustically rigid ground (glass plate)

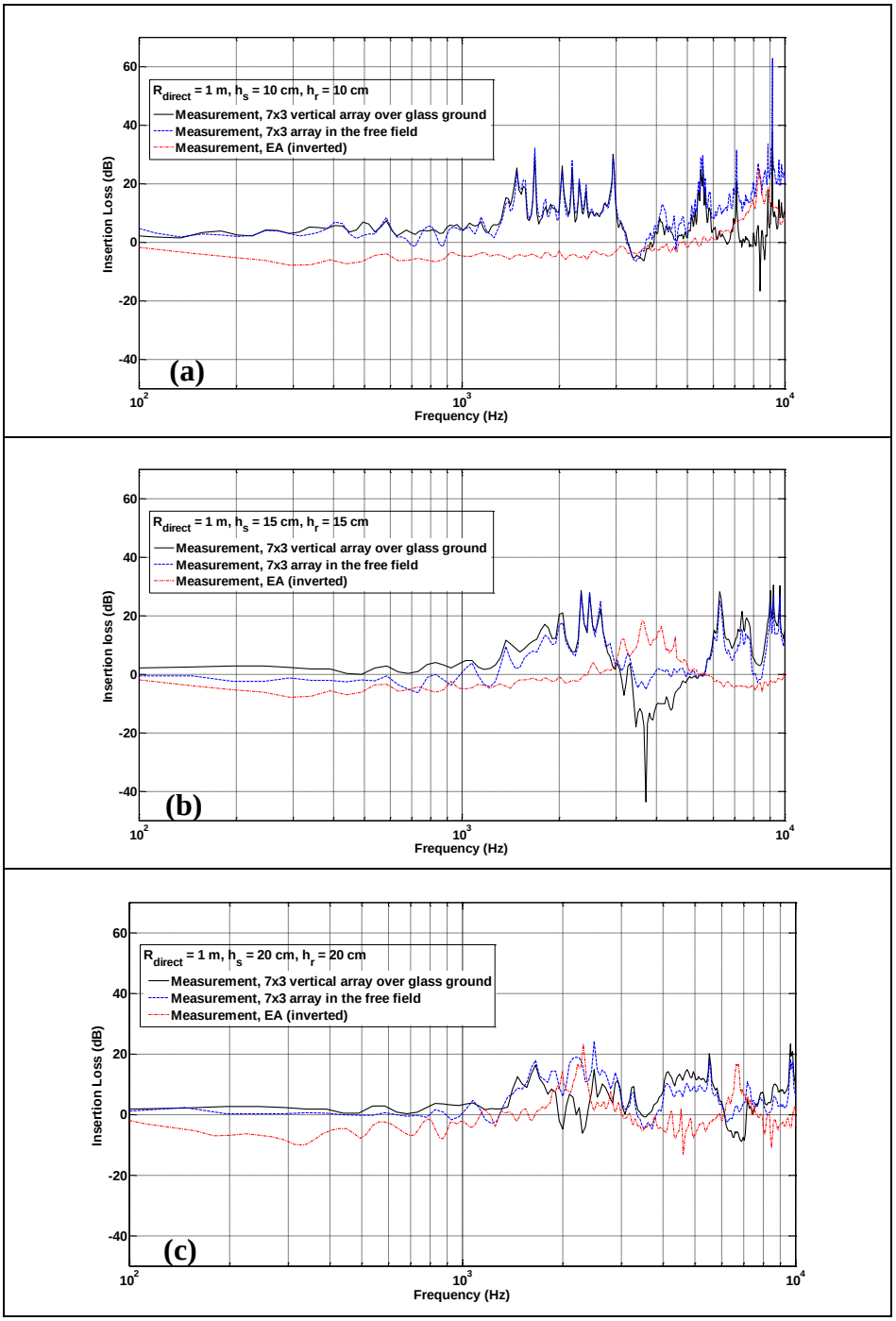

Figure 8.20 – Measured insertion loss spectra of sonic crystal in vertical orientation with (solid line) and without (broken line) a ground plane (glass plate). The source and receiver heights are at (a) 0.1, (b) 0.15 and (c) 0.2 m respectively. Measured excess attenuation (inverted) spectra of the ground is also shown (dash dot line).

Figure 8.20 compares the measured insertion loss spectra for 7x3 rigid cylinder arrays over acoustically solid ground (glass plate) for three receiver heights using the source and receiver location described in table 8.2. The destruction of the band gap at around 2.3 kHz due to its coincidence with a ground effect minimum for this geometry can be observed again (see figure 8.20 (c)).

Chapter 9

Summary and concluding remarks

9.1) Summary of contents

Chapter 1 provided an introduction to acoustic wave theories and derivations of some formulations for both fluid and elastic waves. Only linear wave phenomena were considered. The issue of road traffic noise impact was outlined together with the mitigation method using a conventional noise barrier. A review of past work on the use of sonic crystals as noise barrier was performed along with describing the underlying basis of crystallography.

Chapter 2 reviewed the Plane Wave Expansion (PWE) Method as a semi-analytical technique for analysing the performance of a sonic crystal, employing aspects of the wave and crystallography theories discussed in Chapter 1. The PWE technique describes the acoustic wave transmission inside an infinite two-dimensional periodic composite (solid-fluid) structure. PWE allows the computation of eigenfrequencies (using MATLAB®) in the first irreducible Brillouin zone specified by the three principal symmetry directions (Γ, X and M) of a square lattice crystal. The dispersion relationship was represented using a band structure diagram (figure 2.2). It was demonstrated that a periodic square array of rigid cylinders in air can give rise to complete and partial stopbands in which sound cannot propagate through at all or only at certain angles respectively. It was seen also that by tuning the lattice constant, the Bragg band gap frequency could be shifted to a region of

interest. A simple formula given in equation 2.13 was found to be able to predict the centre frequency of the Bragg band gap for a specific square lattice array. This formula must be modified if the configuration of the array is changed to another Bravais lattice (i.e. hexagonal, see equation 4.8). The comparison between the theoretical results (presented as band structure) and the laboratory results (finite size and presented as Insertion Loss (IL)) for a similar periodic structure yielded favourable agreement in determining the Bragg band gap. An investigation of the effect of varying the size of the scatterer (which inherently varies the filling fraction) was performed using the PWE method. It was predicted that, for a higher filling fraction, ff, enlargement of Bragg band gaps and the enhancement of the IL performance of the SC in the ΓX direction could be achieved. The last section of this chapter, enabled us to infer that it is, in fact, the density contrast that strongly influences the occurrence of the band gaps. The ability to determine the band structure through PWE could be a cost effective way for making the proper design choice for a sonic crystal noise barrier.

Chapter 3 studied another theoretical method to determine the acoustic transmission loss for a two dimensional (2D) periodic array of identical rigid circular cylinders based on Multiple Scattering Theory (MST). This method demonstrated how a general 2D acoustic wave diffraction problem concerning a structure consisting of a number of separate circular scatterers can be solved exactly in terms of the diffraction characteristics of each individual scatterer. The basis of this theory uses the multipole methods to combine separated solutions of the Helmholtz equation using an addition theorem (See

Appendix B) for expanding multipoles centred at one origin in terms of similar multipoles centred on a different origin. Two essential wavefunctions to describe the scattering of waves by circular scatterers were involved. The first used a Hankel function to express the incident wave which satisfies Sommerfeld radiation condition and the second employed a Bessel function of the first kind to express an outgoing wave radiating from each cylinder. Contrary to the PWE method described in Chapter 2 which is restricted to infinite arrays, MST calculates the total wave field (pressure) for a finite size array at any point exterior to the cylinders. This method thereby offers a means of direct comparison with laboratory results. The incident wave can be modelled using a plane or cylindrical waves where the latter can take account of the near field effects (i.e. when source is placed close to the array). The MST method has proved to be powerful, and self-consistent with the ability to solve in principle all multiple-body (i.e. the configuration of the scatterers can be periodic or random) diffraction problems of which the solutions for an individual scatterer are already known. This method was used to calculate the insertion loss for a 7x3 square lattice arrays consisting of rigid circular scatterers. The perfectly-reflecting Neumann boundary condition was used to define the acoustically-hard boundary to model the rigid surface of the scatterers. Insertion losses for three different configurations were computed and the results were compared with laboratory data. The MST predicted results (both plane and cylindrical incident waves) were found to agree well with the laboratory data and these results complimented the hypothesis that the Bragg band gap could be tuned to the desired frequency by varying the lattice constant of the rigid scatterers. The data indicated minor peaks at

frequencies below the first Bragg band gap is observed for the case of lattice constant equal to 0.069 and 0.08 m that could be the effect of finite width or height of the sonic crystal array. This extra low frequency band gap could be exploited in SC noise barrier design. The accuracy of the MST has been investigated and for a 7x3 square lattice array of rigid circular scatterers with radius of 0.0275 m and lattice constant of 0.135 m, truncation numbers $M \geq 4$ and $M \geq 3$ respectively are necessary to obtain reliable results for plane and cylindrical incident waves. The main drawback of this iterative technique is that the time for computation rapidly increases as the number of scatterers increases.

Chapter 4 concerned FEM modelling of the acoustic transmission through 2D sonic crystal using the commercial software COMSOL® Multiphysics (version 3.5a). FEM provides a good technique to solve scattering problem of acoustic waves which involve complicated geometries and when several physical problems are coupled (see chapter 6). Both plane and cylindrical incident waves were simulated and the Insertion Loss (IL) calculated for each incident wave was compared with data for an equivalent SC configuration taken in the laboratory. The FEM predicted results were found to agree well with the laboratory data in term of predicting the bandgaps (see figure 4.5). The computation time for FEM is much longer than that for MST for the same SC configuration. Nevertheless, the computation time has been found to be reasonable period even for the case with the largest number of elements (mesh density). Comparisons with theoretical and experimental results have shown that increasing the number of elements in the FEM model

leads to better convergence results for higher frequencies. Three different shapes scatterer (triangle, square and elliptical) with similar cross section area as the circular scatterer (arranged in square lattice) were considered. Their performances were compared with that of the circular shape scatterers and, according to the FEM results, the triangular shape scatterer with arrangement 3 (see figure 4.8) offers a better IL performance than the other shapes. Comparisons made for hexagonal and square lattice arrangement for circular scatterers, have shown that the square lattice is more suitable as for road traffic noise barrier design. An efficient FEM for calculating the acoustical properties of 2D sonic crystals was solved by the use of Perfectly-Matched Layer (PML). Preliminary work using FEM on transient analysis was performed also for SC with vacancies which potentially could be used to guide the incoming waves.

Chapter 5 detailed the measurement arrangements, data acquisition systems and signal processing. A robust indoor measuring system has been set up to measure the insertion loss of the sonic crystal in the anechoic chamber using the one channel Maximum-Length Sequence System Analyzer (MLSSA). Studies on the effect of transducer size and post processing of the measured signal (i.e. different window sizes and functions) were reported. To perform accurate measurements, the acoustical environment in the chamber was improved. The method of construction of scatterer (i.e. elastic scatterer and Split Ring Resonator) and the supporting structure in the chamber were also described. The chapter continued to describe the outdoor measurement taken at the Open University barrier test site. For these outdoor

measurements, a multiple channels data acquisition system was used instead of MLSSA. Two contributing factors for this change are; the question of the reliability using MLSSA at outdoor conditions and second, the means of obtaining multiple data simultaneously (following ANSI S12.8 standards) for both the microphones and sonic anemometer. Pertaining to the reliability of the source, a modified white noise (termed as Traffic Noise signal in this Thesis) was used instead of an MLS signal. A Graphical User Interface (GUI) was developed using MATLAB® for enabling the user to control the data acquisition system. The control is through clicking of buttons on the display screen and the associate time or frequency domain signal spectrum taken during the measurement will then be plotted on the display. Saving the data is subsequently done with a click on the save button to allow post-processing of data. The outdoor barriers IL performance testing takes account of various degrading effects such as the estimated background noise (measured separately) and the difference in microphones responses based on a calibration process. Microphone distance corrections were also necessary for barrier measurements. A wind vector diagram was plotted for every measurement based on the outputs from the sonic anemometer and has enabled analysis of the meteorological effects on SC performance. In this chapter, an alternative swept sine source was also considered. The outdoor measuring system (except that the source is replaced with a natural made sound) was used to perform measurements on a SC arranged in quasi-ordered lattice arrangement near a weir at Worcester (‘Organ of Corti’ project). The measured IL was compared with MST predictions and an

investigation of the influence of the quasi periodicity in the array was carried out.

SCs composed of elastic shells have been considered in chapter 6. Additional low-frequency bandgaps are predicted in an infinite periodic structure formed by the thin elastic shells made of suitable non-vulcanised rubber (latex). The additional bandgap due to the breathing mode resonance of the shell is predicted to be the widest among those generated by the shell resonances. Proof of concept for the breathing mode was performed using modal analysis with FEM. A semi-analytical method (based on MST) was found to offer a fast and reliable approach to solving the problem of scattering by an array of cylindrical elastic shells. It provided a tool for choosing the material as well as radius and thickness of the shell so that the first resonance frequencies could be positioned below the first Bragg bandgap of the array. The computational time required by using the MST is less than one tenth of that needed for traditional numerical methods such as FEM for modelling a transmission problem for a single elastic shell. The predicted performance of single and arrays of elastic shells in the low-frequency range was verified by laboratory experiments. The combination of the resonance and classical band gaps (first Bragg diffraction frequency) could be used to yield designs of barriers suitable for traffic noise. Laboratory experiments using periodic arrays of elastic thin-walled and hollow rigid split cylinders demonstrated relatively angle-independent insertion loss at frequencies below the first classical band

gap. Attempts at an alternative design using polyethylene scatterers (See Appendix C) were unsuccessful.

Use of an alternative local resonance scatterer termed Split Ring Resonator (SRR) which is made from single slit cylindrical cylinder was explored in chapter 7. Initial activities confirmed a result already known from the literature that arrays of single slit cylindrical 'Helmholtz' resonators produce an additional angle-independent band gap at frequencies below the first Bragg band gap. The re-visiting of this work also served to provide a better understanding of the possible influences (i.e. slit width, area of cavity and slit orientation) on the performance of the SRR which were studied both numerically and experimentally in laboratory. Outdoor measurements were performed on the full scale SC barriers made with SRR and their performance was compared with that of a non-resonating SC barrier. The additional and fairly angle independent bandgap corresponding to the cavity resonance of such SRR array provides another means of enhancing the barrier performance. Subsequent sections of Chapter 7 tackled the question of practicality of using latex cylinders (studied in chapter 6) in outdoor environments since without some form of protection, arrays of latex cylinders would be impractical in outdoor environments. Therefore the acoustical effects of providing suitable protection were investigated. It was found theoretically and experimentally that increasing the number of slits in an empty pipe causes an increase in the frequency of the Helmholtz-type resonance. A low-frequency approximation which models the slit cylinder by an equivalent fluid

layer predicted that the frequency increase is proportional to the square root of the number of slits and this was confirmed experimentally. Subsequent work investigated novel configurations of concentric cylinders (having the elastic shells arrange inside the rigid 4-slit pipes) and suggested that it is possible both to protect the elastic cylinders and, effectively, to broaden the band gaps. The IL of a 7x3 array of 55 mm outer diameter PVC cylinders with 4 mm wide slits and an inner latex cylinder with 43 mm outer diameter and 0.25 mm thick walls was measured and demonstrated the efficacy of this arrangement. The concentric arrangements resulted in resonances associated with both circular and annular cavities. With an inner elastic shell, an additional breathing mode resonance of the shell is preserved but modified by the presence of the outer 4-slit pipe. This is due to the coupling between the components of the concentric arrangement results in shifts in the resonant frequencies corresponding to each element of the composite configuration. This is similar to the effect that is observed in mass-spring systems with multiple degrees of freedom. A theoretical formulation used boundary conditions dependent on polar angle to represent arbitrary positioned slits. For simplicity, in the studied geometries the slits are positioned symmetrically. Jump boundary conditions imposed on the slit interface were used to represent the solution inside the slits. The method can be applied to various types of 2D resonators with concentric multiple layered/ solid cylinder inner. A low-frequency approximation for the acoustical properties of the concentric arrangement with an elastic shell inner correctly predicted the observed frequency shift in the breathing mode resonance. When used in periodic arrays the concentric arrangements with inner elastic shells and outer 4-slit

cylinders resulted in additional sound attenuation in the low-frequency range below the first Bragg band gap while still preserving the Bragg band gaps. This concentric arrangement is more practical than the use of unprotected elastic shells, hence is a potentially useful basis for a sonic crystal barrier design. Full scale field trials of such a sonic crystal barrier (using 3 rows each containing 54 110 mm outer diameter slit PVC cylinders and commercially-produced latex cylinders) and comparisons of its performance with that of a conventional noise fence were performed on a test site that has been constructed on the OU campus. The parameters used for the outdoor concentric cylinder array did not result in as good an acoustical performance as might be possible (see figure 7.28). An alternative manufacturer would be required to make latex cylinders with the desired dimensions. Nevertheless, the numerical modelling results (see figure 9.1) indicated that the outdoor array performance would be improved significantly with the use of narrower slits and larger latex cylinders.

The influence of the presence of a reflecting or absorbing ground on sonic crystal band gaps produced by the effect of multiple scattering from acoustically-hard and -soft cylinders was studied in Chapter 8. Two ground impedance measurement methods (i.e. single microphone and transfer function method) were used to yield the Excess Attenuation (EA) spectra for different experimental conditions (i.e. in the laboratory and outdoor *in-situ*). In the laboratory, acoustical properties of 2 Medium Density Fibreboard (MDF) of different dimensions, a glass plate and a polyurethane foam were measured, Those of asphalt and grass covered ground were measured *in-situ*. Fits to

these spectra using a one parameter empirical impedance model confirm that the ground planes used were either acoustically-hard (MDF and glass) or – soft (polyurethane foam and grass covered ground). A semi-analytical method has been derived for predicting multiple scattering effects of a finite arrays of cylinders with axes parallel to either rigid or impedance ground. Results of the semi-analytical method have been compared with laboratory data. 7x3 square lattice arrays consisting of both rigid and elastic scatterers have been placed with their axes parallel to the grounds and the insertion losses at various source and receiver heights have been measured. Laboratory experiments have shown also that it is possible to augment the barrier effect of a sonic crystal array by means of the ground effect i.e. the interference between sound travelling directly from source to receiver and that reflected from the ground beneath the barrier. The data show that sonic crystal band gaps are much reduced when their frequency coincides with excess attenuation minima associated with the acoustically 'hard' ground. Depending on the source-array-receiver geometry the presence of a rigid ground can result in destruction of the positive IL peak associated with the first Bragg band gap if the first destructive interference minimum in the ground effect is coincident. However, introduction of the impedance ground results in the shift of ground effect minima to lower frequencies so that the Bragg band gap is maintained. This work revealed that it should be possible for ground effect and SC stop and pass bands to be used synergistically. Preliminary studies of a vertical axis SC arrays over an acoustically 'hard' ground were found to show the same phenomena as observed with the horizontal axis SC.

9.2) Concluding remarks

In this work, an alternative road traffic noise barrier using an array of periodically arranged vertical cylinders known as a Sonic Crystal (SC) is investigated. Such SCs exhibit a selective sound attenuation in particular frequency bands, called band gaps related to the spacing and size of the cylinders. This Thesis considers the propagation of acoustic waves through SCs and explores means of enhancing the stop bands notably in the low frequency regime. Theoretical studies using Plane Wave Expansion (PWE), Multiple Scattering Theory (MST) and Finite Element Method (FEM) have enabled study of the performance of SC barriers. In addition to multiple scattering that can lead to band gaps, strategies for improving the band gaps by employing the intrinsic acoustic properties of the scatterer are considered: for example (i) making each cylinder in the form of a Split Ring Resonator (SRR) and (ii) substituting the acoustically rigid scatterer with thin elastic shell. Such designs are shown to increase Insertion loss (IL) in the low-frequency range if the tube cavity (similar to Helmholtz) resonances in SRR or the breathing mode resonance observed in elastic shells occur at frequencies below the Bragg resonance stop band. With the better knowledge of the factors affecting the frequency response for both the SRR and thin elastic shells, a novel design of composite scatterer uses these 2 types of scatterers arranged in a concentric configuration with multiple symmetrical slits on the outer rigid shell. An array of such composite scatterers forms a system of coupled resonators and gives rise to multiple low-frequency resonances. Measurements have been made in an anechoic chamber and also on a full-scale prototype of an outdoor SC noise barrier taking account of

meteorological conditions (i.e. wind profiles and temperature gradients). Theoretical and experimental results confirmed the existence of the Bragg band gaps for SC barriers and the significant improvements when locally resonant scatterers are used. Such resonant arrays are found to give rise to relatively angle-independent stop bands in a useful range of frequencies. Good agreement between computational modelling and experimental work is obtained. Further studies of the acoustical performances of regular arrays of cylindrical elements, with their axes aligned and parallel to either an acoustically “hard” or “soft” ground plane, have been made using predictions and laboratory experiments. Some data have also been obtained also for scatterers with their axes perpendicular to the ground plane.

The most important contributions in this Thesis are:

- novel designs of SC noise barriers based on multiple resonances to enhance the noise shielding performance at frequencies below the first Bragg band gap.
- pioneering investigations of the influence of ground effects on SC noise barriers.

9.3) Suggestions for future studies

Possible areas of research and further research along the lines of the present investigation pursued here are recommended as follows.

1) The formulation developed for interaction of acoustic waves and SC structure in the present study are for a either a plane or a fixed single point source. According to Section 5.6.4, multiple point sources could potentially improve the prediction results. Extensions of the prediction methods to allow for multiple fixed or transient sources should be explored.

2) In the present study, the predictions are modelled in a 2D system where the scatterers are infinitely long in the z-axis. It would be interesting to know how the diffraction at the ends of the finite cylinders influences the scattering. An extended study could look into the combination of an SC barrier with an Edge-Modified Barrier (EMB) which has been widely researched recently [143 and 144] to increase the noise shielding efficiency.

3) Although the breathing mode resonance from the elastic scatterers (which are protected from the rigid cylinder) work in principle they are still subject to harsh outdoor environments including (UV, temperature, humidity etc…). Degradation of material is inevitable under these circumstances and so properties of the elastic shell may change. Therefore some form of climatic cycling tests on the elastic scatterers

will be necessary to address this non-acoustic engineering practicality. More outdoor data taken with the monitored meteorological conditions will also aid in such studies.

4) The SC barrier studied is suitable only for straight road. It would be interesting to study the performance along bends which will cause the SC barrier periodicity to vary due to the curvature.

5) The parameter values chosen for the full scale prototype are far from the optimum values as a consequence of unavailability of the numerical modelling routines (now developed) at the time of their design. According to subsequent MST predictions (see figure 9.1), the slits in the outer cylinders (grouted by hand in the prototype) are too wide and the 0.043 m diameter of the latex cylinders, although the largest that could be obtained at the time of the prototype construction, is too small. These problems should be overcome by using larger latex cylinders (0.08 m diameter of the same thickness) with a different method of support and by precision manufacture of narrower slits (0.004 m) in the outer cylinders. This would potentially offer a significantly better performance than the current configuration.

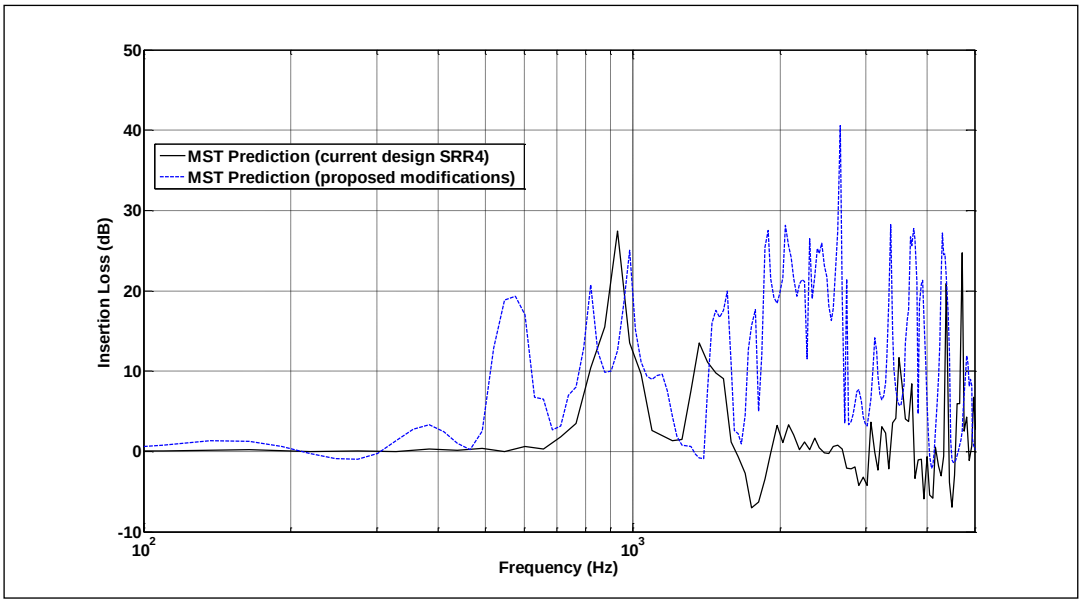

Figure 9.1: Proposed modification for current composite design.

6) One other way of improving the current concentric SC design might be to alter the shape of the outer rigid scatterer from circular to triangular and to use an arrangement similar to that in figure 4.8(e).

Appendix A

MATLAB® Coding for Plane Wave Expansion (PWE) method

Plane Wave Expansion MATLAB® script modified from codes obtained from Daniel Peter Elford PhD thesis [43].

```
tic;
num_Eigenvals = 10;
nmax = 10;
n1=(-nmax:nmax);
n2=(-floor((2*nmax+1)^2/2):floor((2*nmax+1)^2/2));

lat_a=0.135;
ro=0.0275;
f=pi*ro^2/lat_a^2;
pa=1380;
pb=1.2;

delp=(pb/pa-1)/(f*pb/pa+1-f);

va=2400;
vb=344;
pcla=(va^2)*pa;
pclb=(vb^2)*pb;
delt=(pclb/pcla-1)/(f*pclb/pcla+1-f);

nx_arr=repmat(n1,1,2*nmax+1);
ny_arr=round(n2/(2*nmax+1));

[nx,nxp]=meshgrid(nx_arr, nx_arr);
[ny,nyp]=meshgrid(ny_arr, ny_arr);

fill =ones(1,length(nx_arr));
fillt =diag(fill);
G_Gp=sqrt(4*pi*f*((nx-nxp).^2+(ny-nyp).^2))+fillt;
fG_Gp=2*f*besselj(1,G_Gp)./G_Gp;

mode=1;

if mode==1
   for kyind=1:3
      onoff=1;


      for kx=.05:.05:.5 XXIX

         if kyind == 1
         kxt=kx;
         kx=.55-kx;
         ky=kx;
```

```
            elseif kyind==2
            kxt=kx;
            ky=0;
            elseif kyind==3
            kxt=kx;
            ky=.5;
            end

mag_k_p_g=((kx+nx).^2+(ky+ny).^2);
k_p_g_dot_kp_p_g=(kx+nx).*(kx+nxp)+(ky+ny).*(ky+nyp);
kro_del_ggp=(nxp==nx)&(nyp==ny);

M=mag_k_p_g.*kro_del_ggp+delp.*fG_Gp.*k_p_g_dot_kp_p_g.*(1-kro_del_ggp);
N=kro_del_ggp+fG_Gp.*delt.*(1-kro_del_ggp);

A=N^-1*M;
[a,b]=eig(A);
g=find(b~=0);
eigs=(sort(b(g)));
eigs(1:num_Eigenvals);
k=repmat(kxt,1,num_Eigenvals);
min(b(g));

if onoff == 1
    omega=[((340)/lat_a)*real(sqrt(eigs(1:num_Eigenvals)))'];
    karr=[k];
if kyind == 1
    omegafull=[((340)/lat_a)*real(sqrt(eigs(1:num_Eigenvals)))'];
    karrfull=[k];
end
onoff = 0;
else
  omega=[omega,((340)/lat_a)*real(sqrt(eigs(1:num_Eigenvals)))'];
    karr=[karr,k];
  omegafull=cat(1,omegafull,((340)/lat_a)*real(sqrt(eigs(1:num_Eigenvals)))');
    karrfull=cat(1,karrfull,k);
end

        end
     if kyind==1
        myfig = figure;
        ymax=10000;
        subplot(1,3,1)
        b1=plot(karr,omega,'*');
        ax1=gca;
        po=get(gca, 'position');
        set(gca, 'YLim', [0,ymax]);
        set(gca, 'XLim', [0,.5]);
        set(gca, 'nextplot', 'add');
        left_side=po(1);
        set(gca, 'xtick', []);
        width=po(3);
        right_side=left_side+width;
        set(gca, 'xticklabel', {});
        ylabel('Frequency (kHz)')
     elseif kyind==2
        subplot(1,3,2)
        b2=plot(karr,omega,'*');
        po=get(gca, 'position');
        po(1)=right_side;
```

```
        ax2=gca;
        set(gca, 'nextplot', 'add');
        set(gca, 'YLim', [0,ymax]);
        set(gca, 'XLim', [0,.5]);
        set(gca, 'ytick', []);
        left_side=po(1);
        width=po(3);
        right_side=left_side+width;
        set(gca, 'xticklabel', {});

    elseif kyind==3
        subplot(1,3,3)
     b3=plot(karr,omega,'*');
     po=get(gca, 'position');
     po(1)=right_side;
        ax3=gca;
       set(gca, 'nextplot', 'add');
        set(gca, 'ytick', []);
         set(gca, 'YLim', [0,ymax]);
        set(gca, 'XLim', [0,.5]);
         left_side=po(1);
        width=po(3);
right_side=left_side+width;
set(gca, 'xticklabel', {});

text(-1,-.05*ymax,'M');
text(-.5,-.05*ymax,'\Gamma');
text(0,-.05*ymax,'X');
text(.5,-.05*ymax,'M');
text(-.3,-.1*ymax,'Reduced Wave Vector', 'HorizontalAlignment','Center');
text(-.3,1.075*ymax,['Disperaion Relation for Square Lattice of PVC Cylinder in
Air'],'HorizontalAlignment', 'Center');
text(-.3,1.025*ymax,['f=',num2str(f),'
a=',num2str(lat_a),'mr_{o}=',num2str(ro)],'HorizontalAlignment', 'Center');
        end
    end
end
    to
```

Appendix B

Graf's Addition Theorem

Addition theorems can be considered to be one of the most important concepts for the multiple scattering theories. Generally speaking, they are used to transform one expansion about some point in space into a similar expansion about a different point. Since our multiple scattering model is two-dimensional therefore the discussion here will be based on two-dimensional addition theorems for cylindrical coordinates.

For clarity, the Graf's additional theorem will be explained based on our Multiple Scattering Theory model (Chapter 3). We consider two points of origins at the *j*-th and *q*-th scatterers. Let $\vec{r_k}$ be the position vector of a receiver point with respect to k, where $k = j, q$. The position vector $\overrightarrow{R_{jq}}$ of *j*-th scatterer with respect to *q*-th scatterer so that $\vec{r_j} = \vec{r_q} + \overrightarrow{R_{jq}}$. Let $\vec{r_j} = \left(r_j \cos\theta_j, r_j \sin\theta_j\right)$ and $\overrightarrow{R_{jq}} = \left(R_{jq}\cos\left(2\pi - \alpha_j\right), R_{jq}\sin\left(2\pi - \alpha_j\right)\right)$. See figure B1 for the description of the geometry.

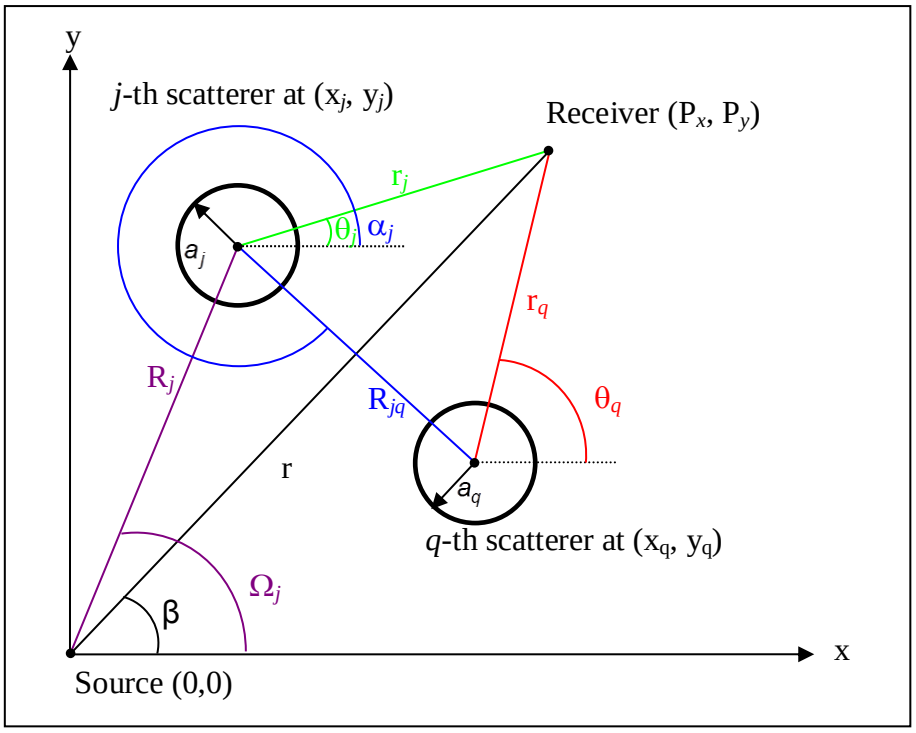

Figure B1: Geometry descriptions for two-dimensional addition theorems

Graf's Addition Theorems for $J_m(kr)e^{im\theta}$

For $m = 0, \pm 1, \pm 2, \ldots,$ we have

$$J_m(kr_j)e^{im\theta_j} = \sum_{n=-\infty}^{n=+\infty} J_n(kR_{jq})e^{in(2\pi-\alpha_j)} J_{m-n}(kr_q)e^{i(m-n)\theta_q} \quad \text{a}_1, \qquad \textbf{(B1.1)}$$

$$= \sum_{n=-\infty}^{n=+\infty} J_{m-n}(kR_{jq})e^{i(m-n)(2\pi-\alpha_j)} J_n(kr_q)e^{in\theta_q}$$

Where J_n is the n-th order Bessel function.

Graf's Addition Theorems for $H_m^{(1)}(kr)e^{im\theta}$

For $m = 0, \pm 1, \pm 2, \ldots,$ we have

$$H_m^{(1)}\left(kr_j\right)e^{im\theta_j} = \sum_{n=-\infty}^{n=+\infty} H_{m-n}^{(1)}\left(kR_{jq}\right)e^{i(m-n)(2\pi-\alpha_j)} J_n\left(kr_q\right)e^{in\theta_q} \quad a_1, \qquad \textbf{(B1.2)}$$

For $r_q < R_{jq}$, and

$$H_m^{(1)}\left(kr_j\right)e^{im\theta_j} = \sum_{n=-\infty}^{n=+\infty} J_{m-n}\left(kR_{jq}\right)e^{i(m-n)(2\pi-\alpha_j)} H_n^{(1)}\left(kr_q\right)e^{in\theta_q} \quad a_1, \qquad \textbf{(B1.3)}$$

For $r_q > r_{jq}$.

Where $H_n^{(1)}$ is the n-th order Hankel function of the first kind.

Appendix C

i) Experimental study of the use of Polyethylene scatterers in a sonic crystal noise barrier.

Initial experiments on sonic crystals containing locally resonant characteristics used Polyethylene tubing made from commercially available Lay Flat Tubing (LFT). Perspex end caps with attaching bolts (for mounting purpose) were fitted to the LFT as shown in figure C1. A small hole is made through one end of the end cap and a small pipe is glued to the opening. Hoses are then attached to all the cylinders in order to inflate then with air using a small pump. Measurements of single and 7x3 square lattice array of lattice constant 0.15 m are performed.

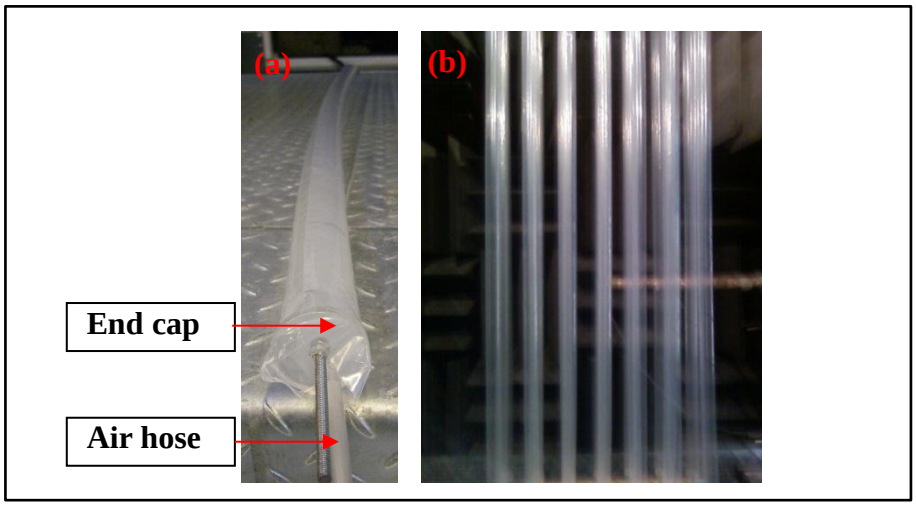

Figure C1: (a) Single LFT and (b) 7x3 square lattice array of LFT with lattice constant 0.15 m.

Results:

Figure C2 shows the IL spectra for 2 single-LFT of similar diameter 0.055 m but different wall thicknesses of 0.0001 and 0.00018 m. Clearly, very little breathing mode resonance is seen for either of the Polyethylene scatterers.

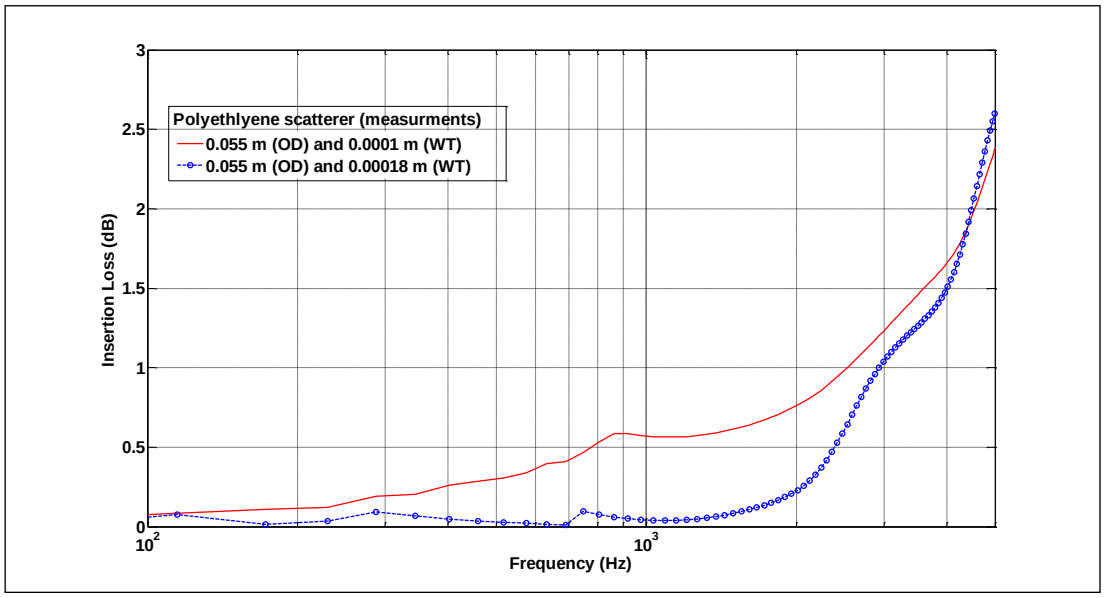

Figure C2: IL spectra for single LFT cylinders of diameter 0.055 m and wall thicknesses (WT) of 0.0001 m and 0.00018 m.

The negligible contribution of breathing mode resonance is further confirmed by experiments on a 7x3 square lattice array of LFT with diameter 0.55 m, WT 0.0001 m and lattice constant 0.15 m (see figure C3). Only the classical band gap (Bragg) at 1.1 kHz is observed in the plot and we conclude there is no advantage in using LFT as the scatterer.

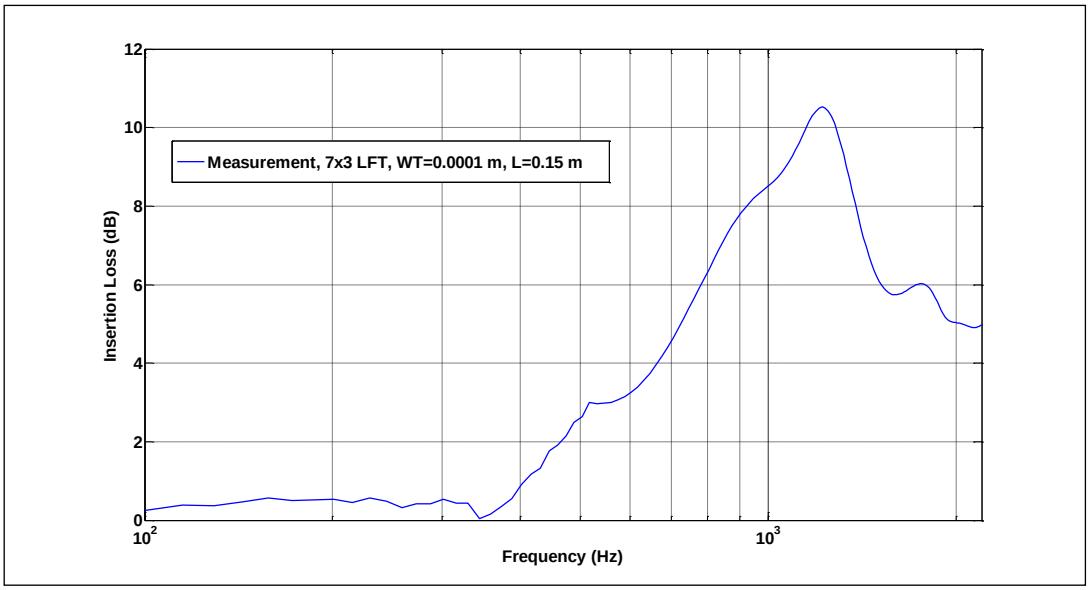

Figure C3: IL spectra for 7x3 square lattice array of LFT with diameter 0.055 m, wall thickness (WT) of 0.0001 m and lattice constant (L) of 0.15 m.

ii) Experimental study on the use on periodic stiffening along the scatterer length.

The possibility of enhancing resonance-related band gaps due to elastic thin-walled cylinders by periodic stiffening along their lengths has been investigated experimentally. Such structures were achieved by overlapping and gluing together multiple vertical sections using “gaffer” tape. The width of the tape sections is 0.05 m and they are periodically spaced at 0.05 m throughout the length of the elastic cylinder as shown in figure C4. The IL spectrum for a single elastic cylinder with periodic stiffening has been measured in the laboratory.

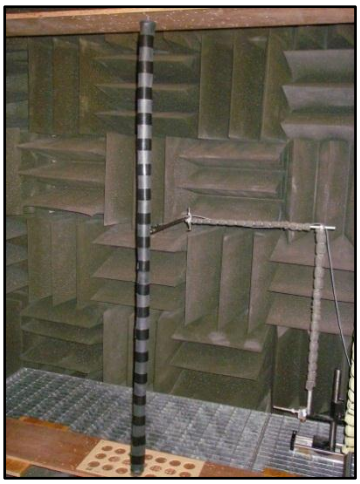

Figure C4: Single elastic cylinder with periodic stiffening mounted inside the anechoic chamber.

The measured IL spectra of single elastic cylinder with periodic stiffening is plotted against an identical elastic cylinder without any stiffening. Clearly, the breathing mode resonance is reduced by periodic stiffening. There is around 2.5 dB drop in amplitude at the resonance frequency. The resonance frequency also reduced from around 1.2 kHz to 800 Hz by the increased stiffness. This laboratory test indicates that such a design is not useful for the noise barrier problem.

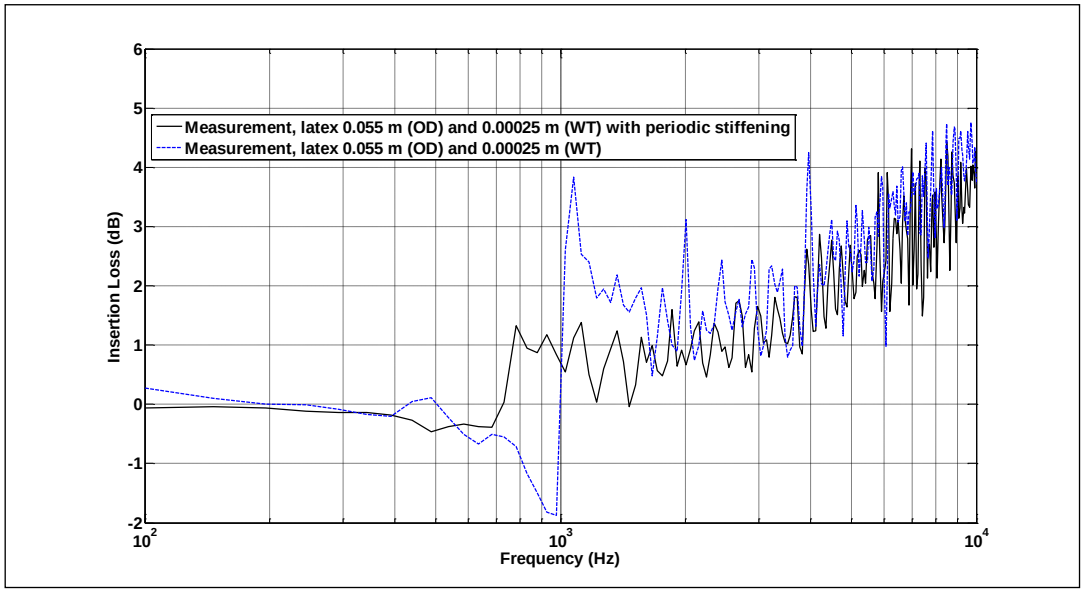

Figure C5: IL spectra of single elastic cylinder with (solid line) and without (broken line) periodic stiffening.

Appendix D

Tensile test

A Tensile test was performed to determine the elastic properties of the cylinders made from latex and polyethylene. Specifically the Young's Modulus which is defined as the ratio of the uniaxial stress over the uniaxial strain in the range of stress in which Hooke's Law holds has been obtained. For most materials, during the initial portion of the test, the relationship between the applied force and the elongation (change in length) is linear (see figure D1). The region is known as the elastic region since here the material would return to its original shape if the load is removed. Beyond this elastic limit, the material starts to deform plastically and therefore the region is call the plastic region in which the load increases to a maximum, equivalent to maximum stress value known as ultimate stress (UTS). Subjecting to further applied force will lead to a decrease of load with increasing elongation and eventually reached the material breaking point.

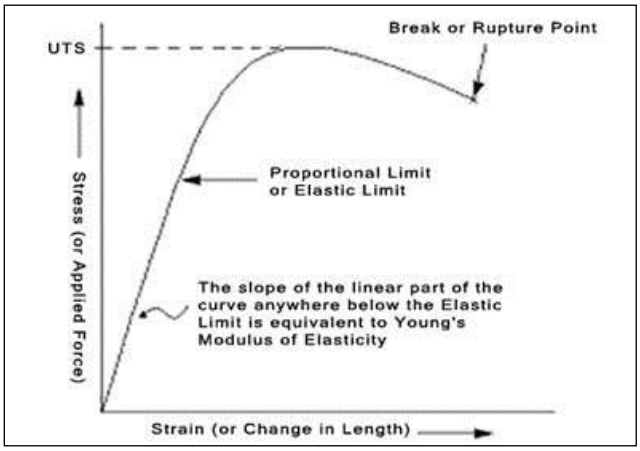

Figure D1: Tensile test: stress-strain curve of typical material.

A rectangular strip of non-vulcanized latex or polyethylene strip was cut to dimension of length and width of 0.06 m and 0.025 m respectively and mounted on an MTS universal test system. The tensile test involved applying a continually increasing tensile force at one end of the specimen. The other end of the specimen was fixed to ensure that the sample is slowly pulled apart by the tension. Simultaneous measurements were made of the applied loads and the corresponding deformation (elongation) using the MTS Test Star II data acquisition software. The inverse problem (relaxation) was performed for the industrial rubber as well.

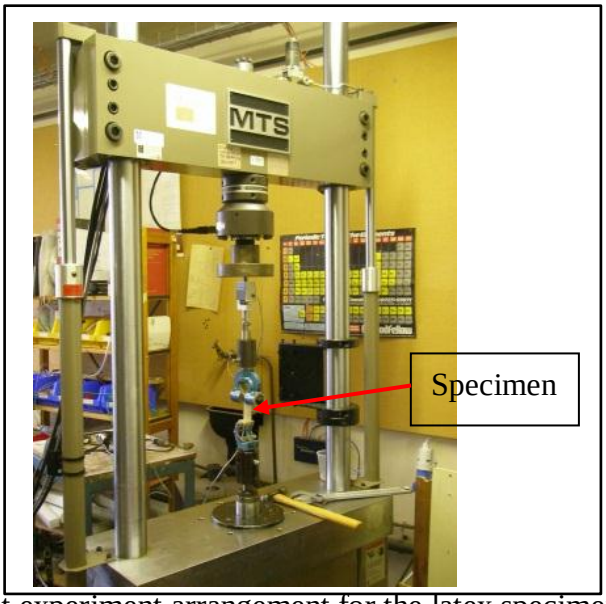

Figure D2: Tensile test experiment arrangement for the latex specimen using MTS Universal Testing System.

Figure D3 presents the stress-strain curve obtained for the industrial rubber (latex) specimen. This stress-strain curve characterizes the behaviour of the latex specimen with wall thickness of 0.5 mm. The dotted line shows either the data for either tension or relaxation and the best fit is obtained by a linear regression method. As we can see the curve contains a straight line where the load is proportional to the displacement. The gradient of the line

gives the Young Modulus which is 0.89 and 0.81 MPa for tension and relaxation respectively. The slight deviations of the data between tension and relaxation could be attributed by factors such as axial tilt due to insecure mounting, precision of the stepper motor during the testing or the sensitivity issue caused by the load.

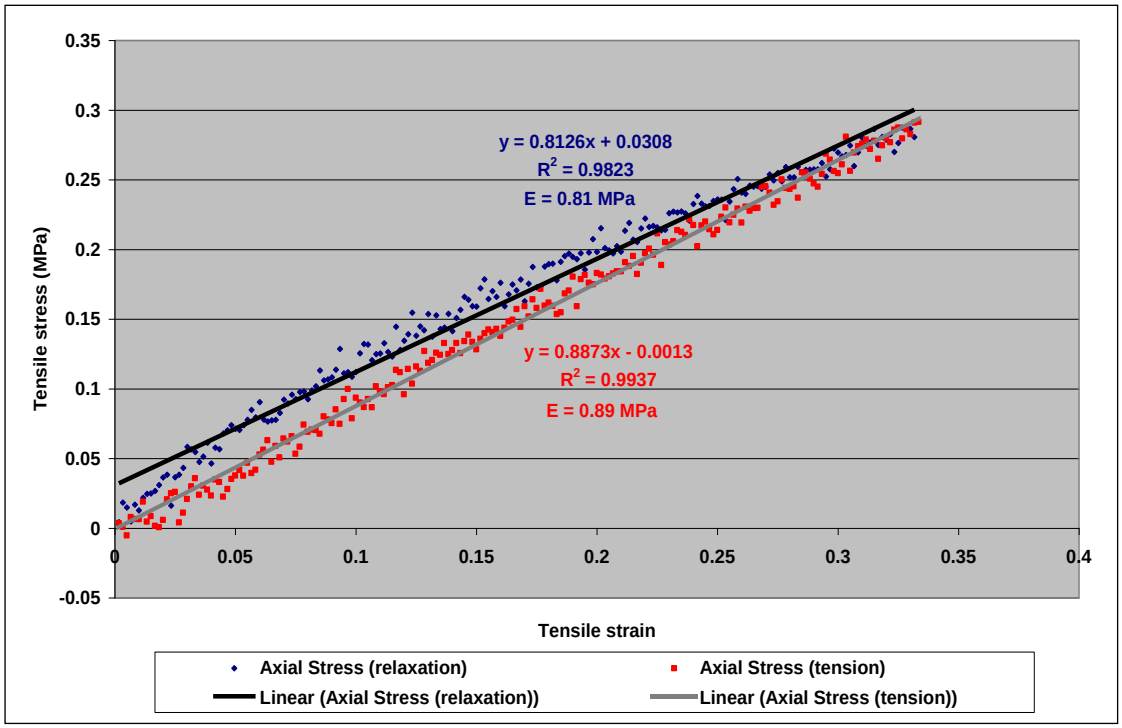

Figure D3: Results of tests to obtain the Young's Modulus of industrial rubber Sample size: length 60 mm, width 25 mm and thickness 0.50 mm.

Figure D4 presents the stress-strain curve obtained for the Polyethylene specimen. The Polyethylene specimen measured has a wall thickness of 0.15 mm. The dotted line shows the data for tension and the best fit is again obtained by a linear regression method. As we can see the data can be fitted by a straight line where the load is proportional to the displacement. The gradient of the line gives the Young Modulus which is 178 MPa for tension. This result suggests that the specimen is a low density

Polyethylene where, according to a reference from public source, the Young's Modulus is around 200 MPa. This test supports the observed lack of breathing mode resonance in a scatterer manufactured from such material since it does not satisfy the stiffness condition.

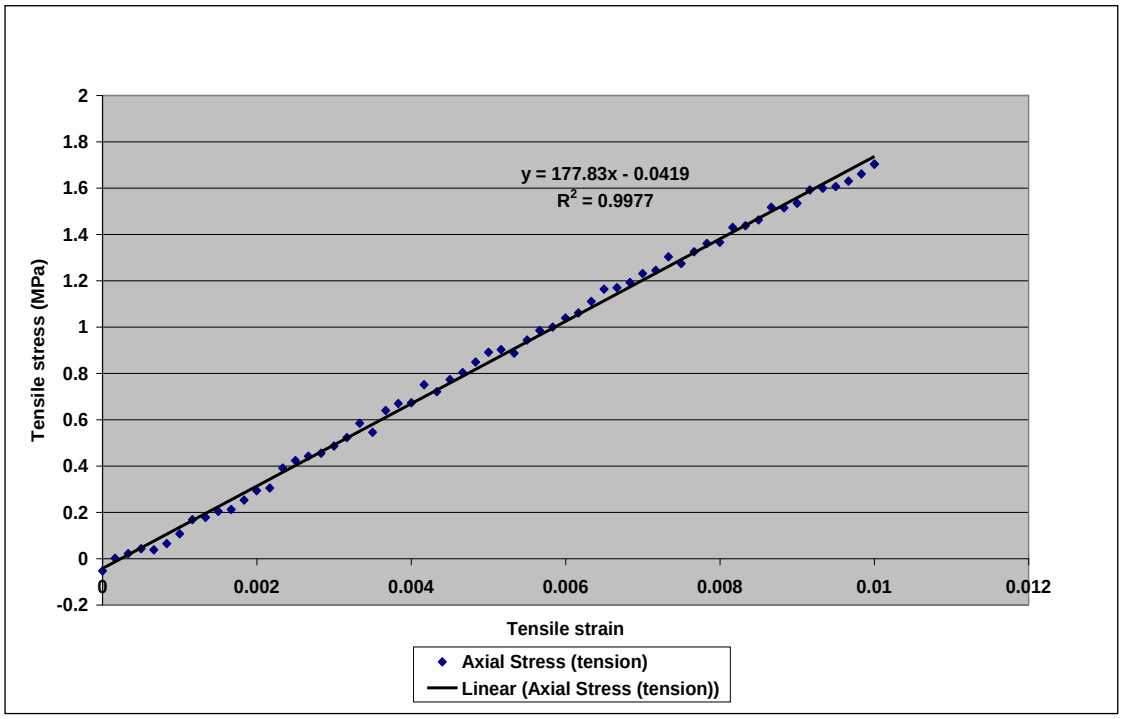

Figure D4: Young's Modulus of Polyethylene tubing. Sample size: length 60 mm, width 25 mm and thickness 0.1 mm.

Appendix E(i): Meteorological conditions - Compass plot for outdoor measurement on **12/5/11**

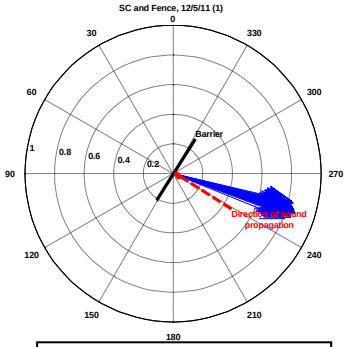

Measurement 1
Wind Speed = 0.8 m/s
Up wind
Temp = 16.6°C
SOS = 341.2m/s

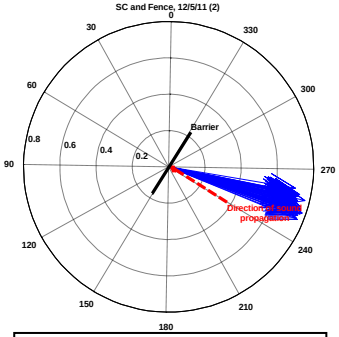

Measurement 2
Wind Speed = 0.8 m/s
Up wind
Temp = 16.6°C
SOS = 341.1m/s

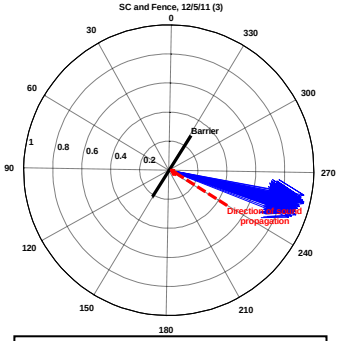

Measurement 3
Wind Speed = 0.9 m/s
Up wind
Temp = 17.2°C
SOS = 341.5m/s

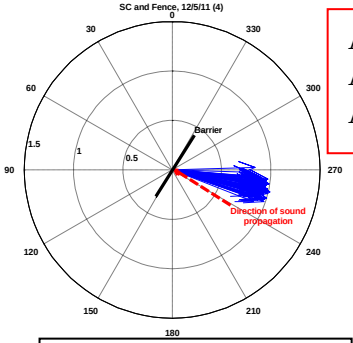

Measurement 4
Wind Speed = 1 m/s
Up wind
Temp = 17.1°C
SOS = 341.4m/s

Average wind speed = 0.9m/s
Average temp = 17.1°C
Average SOS = 341.4m/s

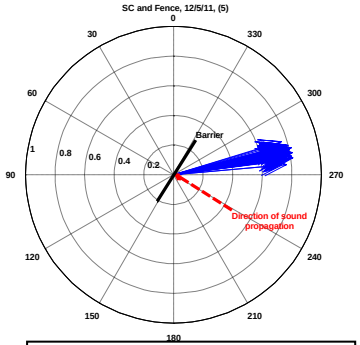

Measurement 5
Wind Speed = 0.8 m/s
Up wind
Temp = 17.1°C
SOS = 341.4m/s

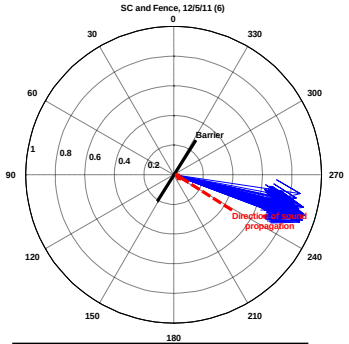

Measurement 6
Wind Speed = 0.9m/s
Up wind
Temp = 17.3°C
SOS = 341.5m/s

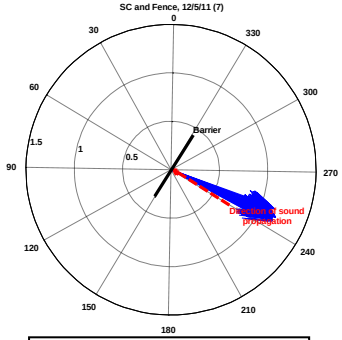

Measurement 7
Wind Speed = 1.2m/s
Up wind
Temp = 17.2°C
SOS = 341.5m/s

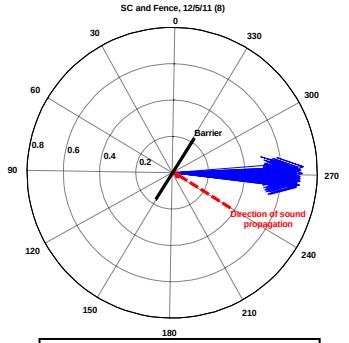

Measurement 8
Wind Speed = 0.7m/s
Up wind
Temp = 17.7°C
SOS = 341.8m/s

*Speed of sound (SOS)

Appendix E(ii): Meteorological conditions - Compass plot for outdoor measurement on **27/5/11**

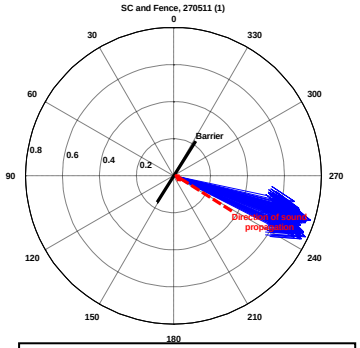

Measurement 1
Wind speed = 0.8 m/s
Up wind
Temp = 15.1°C
SOS = 340.3m/s

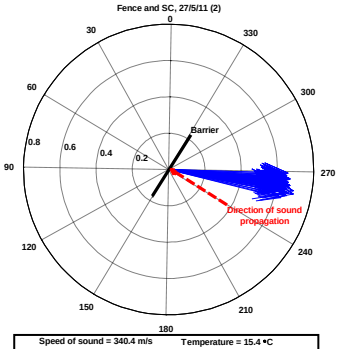

Measurement 2
Wind speed = 0.7 m/s
Up wind
Temp = 15.4°C
SOS = 340.4m/s

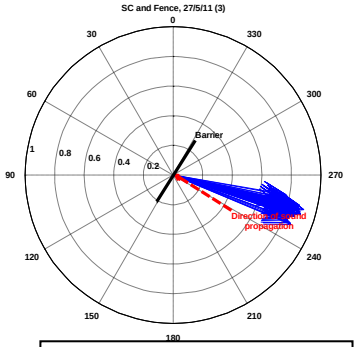

Measurement 3
Wind speed = 0.9 m/s
Up wind
Temp = 15.4°C
SOS = 340.5m/s

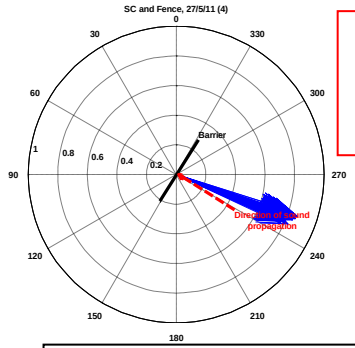

Measurement 4
Wind speed = 0.9 m/s
Up wind
Temp = 15.5°C
SOS = 340.5m/s

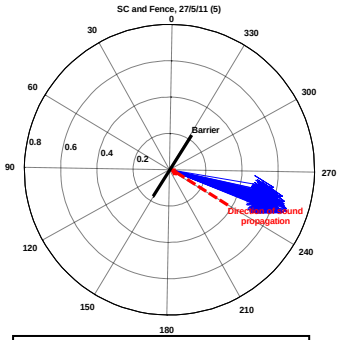

Measurement 5
Wind speed = 0.7 m/s
Up wind
Temp = 15.7°C
SOS = 340.6m/s

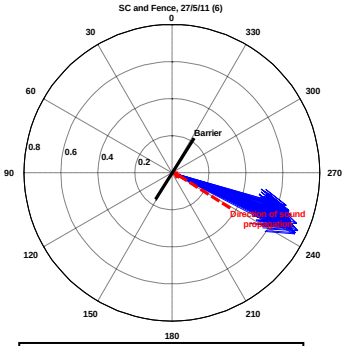

Measurement 6
Wind speed = 0.7 m/s
Up wind
Temp = 15.6°C
SOS = 340.5m/s

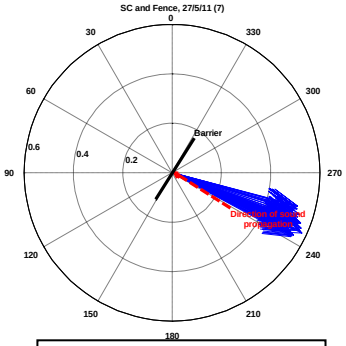

Measurement 7
Wind speed = 0.5 m/s
Up wind
Temp = 15.8°C
SOS = 340.7m/s

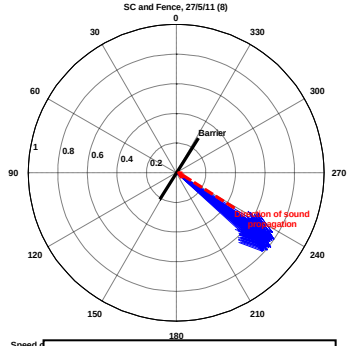

Measurement 8
Wind speed = 0.5 m/s
Up wind
Temp = 15.9°C
SOS = 340.7m/s

Average wind speed = 0.7m/s
Average temp = 15.6°C
Average SOS = 340.5m/s

*Speed of sound (SOS)

References

[1] M. Ewing, “Elastic waves in layered media”, McGraw Hill (1957).

[2] P.M. Moses and K.U. Ingard, “Theoretical acoustic”, McGraw Hill (1968).

[3] D.T. Blackstock, “Fundamentals of physical acoustics”, Wiley-Interscience publication (2000).

[4] Y. de Kluizenaar, S.A. Janssen, F.J. van Lenthe, H.M.E. Miedema and J.P. Mackenbach, “Long-term road traffic noise exposure is associated with an increase in morning tiredness”. J. Acoust. Soc. Am., **126** (2), pp. 626-633 (2009).

[5] W.F. Babisch, B. Beule, M. Schust, N. Kersten and H. Ising, “Traffic noise and risk of myocardial infraction”. EPIDEMIOLOGY, **16** (1), pp. 33-40 (2005).

[6] W.F. Babisch “Road traffic noise and cardiovascular risk”, Noise & Health, **10**, pp. 27-33 (2008).

[7] B.J. Smith, R.J. Peter and S. Owen, “Acoustics and noise control”, Longman (1985).

[8] European Parliament and of the council, Directive relating to the assessment and management of environmental noise (2002/49/EC) (2002).

[9] L. Sutherland and G.A. Daigle, “Atmospheric sound propagation. Encyclopaedia of Acoustics”, Ed. M. J. Crocker, Ch. 32, Wiley, New York (1997).

[10] British Standards Institution, Normalised traffic noise spectrum, (BS EN 1793-3) (1998).

[11] L. Brillouin, “Wave propagation in periodic structures”, Dover Publications Inc (1946).

[12] E. Yablonovitch, “Inhibitated spontaneous emission in solid state physics and electronics”. Physical Review letters, **58**, 2059 (1987)

[13] H. Altug and J. Vuckovic, “Experimental demonstration of the slow group velocity of light in two-dimensional coupled photonic crystal microcavity arrays”. Applied Physics Letters, **86** (11), 111102 (2005).

[14] X. Hu and C. T. Chan, “Photonic crystals with silver nanowires as a near-infrared superlens”. Applied Physics Letters, **85** (9), 1520 (2004).

[15] O. Painter, R. K. Lee, A. Scherer, A. Yariv, J. D. O'Brien, P. D. Dapkus and Kim, “Two-Dimensional Photonic Band-Gap Defect Mode Laser”. Amer. Assoc Advancement Science, **285** (5421), 1919-1821 (1999).

[16] A. Mekis, J.C. Chen, I. Kurland, S. Fan, P.R. Villeneuve and L.D. Joannopoulos, “High transmission through sharp bends in photonic crystal waveguides”. Physical Review letters. **77**, 3787–90 (1996).

[17] D. Schurig, J.J. Mock, B.J. Justice, S.A. Cummer, J.B. Pendry, A.F. Starr, D.R. Smith, “Metamaterial Electromagnetic Cloak at Microwave Frequencies”. Amer. Assoc Advancement Science, **314** (5801), 977-980 (2006).

[18] A. Chutinan, S. John, and O. Toader. “Diffractionless flow of light in all-optical microchips”. Physical Review letters, **90**:123901, (2003).

[19] J.L. Volakis and K. Sertel, “Narrowband and Wideband Metamaterial Antennas Based on Degenerate Band Edge and Magnetic Photonic Crystals”. Proceedings of the IEEE, **99** (10), 1732-1745 (2011).

[20] R. Martínez-Sala, J. Sáncho, J.V. Sánchez, V. Gómez, J. Llinares and F. Meseguer, “Sound attenuation by sculpture”. Nature (London). **378**, 241 (1995).

[21] J. V. Sanchez-Perez, C. Rubio, R. Martinez-Sala, R. Sanchez-Grandia and V. Gomez, “Acoustic barriers based on periodic arrays of scatterers”. Applied Physics Letters, **81**, 5240 (2002).

[22] V. Romero-Garcia, L.M. Garcia-Raffi and J.V. Sanchez-Perez, “Evanescent waves and deaf bands in sonic crystals”. Amer. Inst. Physics Advances, **1** (4), 041601 (2011).

[23] A. Gupta, C.H. Chew and K.M. Lim, “Effect of periodic structure on sound propagation”. 4th International Conference on experimental mechanics, 7522 - 75223D (2010).

[24] R. Martinez-Sala, C. Rubio C, L.M. Garcia-Raffi, “Control of noise by trees arranged like sonic crystals”. Journal of Sound and Vibration, **291**, 100-106 (2006).

[25] J. Sánchez-Dehesa, V.M. Garcia-Chocano, D. Torrent, F. Cervera and S. Cabrera, “Noise control by sonic crystal barriers made of recycled material”. J. Acoust. Soc. Am., **129** (3), 1173-1183 (2011).

[26] D.P. Elford, L. Chalmers, F.V. Kusmartsev and G.M. Swallowe, “Matryoshka locally resonant sonic crystal”. J. Acoust. Soc. Am., **130** (5), 2746-2755 (2011).

[27] C. Kittel, “Introduction to solid state physic”, John Wiley & Sons Inc, 8 editions (2005).

[28] R.H.III. Olssen and I. EL-Kady, “Microfabricated Phononic Crystal devices and applications”. Meas. Sci. Technol., **20** 012002 (2009).

[29] T. Miyashita, “Sonic crystals and sonic wave-guides”. Meas. Sci. Technol., **16**, 47-63 (2005).

[30] M. Plihal and A.A. Maradudin, “Photonic band structure of two-dimensional systems: The triangular lattice”. Physical Review B, **44**, 8565-8571 (1991).

[31] P.R. Villeneuve and M. Piché, “Photonic band gaps in two-dimensional square and hexagonal lattices”. Physical Review B, **46**, 4969-4972 (1992).

[32] R.D. Meade, K.D. Brommer, A.M. Rappe, and J.D. Joannopoulos, “Existence of a photonic band gap in two dimensions”, Applied Physics Letters, **61**, 495-497 (1992).

[33] K.M. Ho, C.T. Chan, and C.M. Soukoulis, “Existence of a photonic gap in periodic dielectric structures”. Physical Review Letters, **65**, 3152-3155 (1990).

[34] Y.M. Soliman, M.F. Su, Z.C. Leseman, C.M. Reinke, I. El-kady and R.H.III Olsson, “Phononic crystals operating in the gigahertz range with extremely wide band gaps”. Applied Physics Letters, **97**, 193502 (2010).

[35] J.V. Sánchez-Pérez, D. Caballero, R. Martínez-Sala, J. Sánchez-Dehesa, F. Meseguer, J. Llinares and F. Gálvez, “Sound Attenuation by a Two-Dimensional Array of Rigid Cylinders”. Physical Review Letters, **80**, 5325 (1998).

[36] M.S. Kushwaha and B. Djafari-Rouhani, “Complete acoustic stop bands for cubic arrays of spherical liquid balloons”. Applied Physics, **80**, 3191-3195 (1996).

[37] Y. Chen and Z. Ye, “Theoretical analysis of acoustic bands in two-dimensional periodic arrays”. Physical Review E, **64**, 036616 (2001).

[38] J.O. Vasseur, P.A. Deymier, B. Djafari-Rouhani, Y. Pennec, A-C. Hladky-Hennion, “Absolute forbidden bands and waveguiding in two-dimensional phononic crystal plates”. Physical Review B, **77**, 085415 (2008).

[39] M.S. Kushwaha, P. Halevi , G. Martínez, L. Dobrzynski and B. Djafari-Rouhani, “Theory of acoustic band structure of periodic elastic composites”. Physical Review B, **49**, 2313-2322 (1994).

[40] M. Wilm, S. Ballandras, V. Laude and T. Pastureaud, “A full 3D plane-wave-expansion model for 1-3 piezoelectric composite structures”. J. Acoust. Soc. Am., **112**, 943-952 (2002).

[41] Y. Cao, Z. Hou and Y. Liu, “Convergence problem of plane-wave expansion method for phononic crystals”. Physics Letter A, **327**, 247-253 (2004).

[42] www.engineeringtoolbox.com/wood-density-d_40.html, last accessed on 15/2/11.

[43] D. P. Elford, “Band gap formation in acoustically resonant phononic crystals”, PhD thesis (2010).

[44] M.I. Mishchenko, D.W. Mackowski and L.D. Travis, “Scattering of light by bispheres with touching and separated components”. Applied Optics, **34**, 21, 4589 (1995).

[45] F. Zaviska, “Uber die beugung elektromagnetischer wellen an parallelen, unendlich langen kreisylindern”. Ann. Phys., **40**, 1023 (1913).

[46] D.W. Mackowski and M.I. Mishchenko, “Direct simulation of multiple scattering by discrete random media illuminated by Gaussian beams”. Physical Review A, **83**, 013804 (2011).

[47] V. Twersky, “Multiple scattering of radiation by an arbitrary configuration of parallel cylinders”. J. Acoust. Soc. Am., **24**, 1, 42-46 (1952).

[48] L.L. Araujo, G.F. Foran and M.C. Ridgway, “Multiple scattering effects on the EXAFS of Ge nanocrystal”. Journal of Physics: Condense Matter, **20**, 165210 (2008).

[49] C.M. Linton and D.V. Evans, “The interaction of waves with arrays of vertical circular cylinders”. J. Fluid Mech., **215**, pp549-569 (1990).

[50] S. Boscolo and M. Midrio, “Three-Dimensional Multiple-Scattering Technique for the Analysis of Photonic-Crystal Slabs”. J. of Lightwave Technology, **22** (12), 2778-2786 (2004).

[51] J.M. Elson, “Infrared light scattering from surfaces covered with multiple dielectric overlayers”. Applied Optics **16** (11), 2872–2881 (1977).

[52] A. Aubry, A. Derode, “Multiple scattering of ultrasound in weakly inhomogeneous media: Application to human soft tissues”. J. Acoust. Soc. Am., **129** (1), 225-233 (2011).

[53] P.A. Martin, “MULTIPLE SCATTERING – Interaction of Time-Harmonic Waves with N Obstacles”, Cambridge University Press (2006).

[54] L. Rayleigh, “On the influence of obstacles arranged in rectangular order upon the properties of a medium”. Phil. Mag., Series 5, 34, 481-502 (1892).

[55] A.K. Mal and S.K. Bose, “Dynamic elastic moduli of a suspension of imperfectly bonded spheres”. Proceeding of the Cambridge Philosophical Society, **76**, 587-600 (1974).

[56] P.C. Waterman, “Symmetry unitarity and geometry in electromagnetic scattering”. Physical Review D, **3**, 825-839 (1971).

[57] V. Twersky, Multiple scattering of radiation by an arbitrary configuration of parallel cylinders”, J. Acoust. Soc. Am., **24**, 42-46, (1952).

[58] I.S. Gradshteyn and I.M. Ryzhik, “Table of integrals, series and products”, 6 editions, 8.51-8.52, MO 27, 926 (2000).

[59] O. Umnova, K. Attenborough and C.M. Linton, “Effects of porous covering on sound attenuation by periodic arrays of cylinders”. J. Acoust. Soc. Am., **119**, 278-284 (2006).

[60] R.D. Cook, D.S. Malkus, M.E. Plesha and R.J. Witt, “Concepts and applications of finite element analysis”. John Wiley & Sons, 4 editions, Chapter 1, pp 10 (2002).

[61] G.M.L. Gladwell, “A finite element method for acoustics”. Proceedings of the 5th International Congress on Acoustics, Leigh, Belgium (1965).

[62] B.R. Mace, D. Duhamel and M.J. Brennan, “Finite element prediction of wave motion in structural waveguides”. J. Acoust. Soc. Am., **117**(5), 2835-2843 (2005).

[63] M. Hofer, N. Finger and G. Kovacs, “Finite-element simulation of wave propagation in periodic piezoelectric SAW structures”, IEEE Transcactions on ultrasonics ferroelectrics and frequency control, **53** (6), 1192-1201 (2006).

[64] T. Delort, “Finite-element method for gratings”. J. Opt. Soc. Am., A, **10**, 12, 2592-2601 (1993).

[65] X. Wei, A.J. Wachters and H.P. Urbach, “Finite-element model for three-dimensional optical scattering problems”, J. Opt. Soc. Am., A, **24**, 3, 866-881 (2007).

[66] C. Lally, F. Dolan and P.J. Prendergast, “Cardiovascular stent design and vessel stresses: a finite element analysis”. Journal of Biomechanics, **38** (8), 1574-1581 (2005).

[67] P. Majumdar, R. Jayaramachandran and S. Ganesan, “Finite element analysis of temperature rise in metal cutting process”. Applied thermal engineering, **25** (4), 591-601 (2005).

[68] E. Ferrie, J.Y. Buffiere and W. Ludwig, “Fatigue crack propagation: In situ visualisation using X-ray microtomography and 3D simulation using the extended finite element method”. ACTA Materialia, **54** (4), 1111-1122 (2006).

[69] O. Ozgun and M. Kuzuoglu, “Non-Maxwellian locally-conformal PML absorbers for finite element mesh truncation”. IEEE Transactions on Antennas and propagation, **55**(3), 931-937 (2007).

[70] J. Mackerle, “Some remarks on progress with finite elements”. Computers & structures, **55** (6), 1101-1106 (1995).

[71] O.A. Kaya, A. Cicek and B. Ulug, “Forcusing with two-dimensional angular-symmetric circular acoustic lenses”. Acoustical Physics, **57** (3), 292-300 (2011).

[72] M. Hirsekorn and P.P. Delsanto, “Design and optimization of locally resonating sonic crystals”, 2003 IEEE Ultrasonics Symposium Proceedings, **1**, 1491-1494 (2003).

[73] S. Guenneau and A.B. Movchan. “Analysis of elastic band structures for oblique incidence”. Archieve for Rational Mechanics and Analysisl, **171**, 129-150 (2004).

[74] COMSOL® Multiphysics Modelling Guide, version 3.5a, chapter 3, 26 (2008).

[75] M.S. Mohamed, O. Laghrouche and A. El-kacimi, “Some numerical aspects of the PUFEM for efficient solution of 2D Helmholtz problem”. Computers & Structures, **88** (23), 1484-1491 (2010).

[76] L. Wu and L. Chen, “The dispersion characteristics of sonic crystals consisting of elliptic cylinders”. Journal of Physical D: Applied Physic, **40**, 7579-7583 (2007).

[77] M. Zampolli, A. Tesei, F.B. Jensen, N. Malm, J.B. Blottman, “A computationally efficient finite element model with perfectly matched layers applied to scattering from acially symmetric objects”. J. Acoust. Soc. Am., **122**, 1472-1485 (2007).

[78] http://www.liminal.org.uk/organ-of-corti/, last accessed on 25/7/11.

[79] T. Miyashita, W. Sato and Y. Nakaso, “Experimental studies on two-dimensional defect-mode waveguides in a sonic/phononic crystal”, Japanese Journal of Applied Physic Part 1-Regular papers brief communications & review papers, **46** (7B), 4684-4687 (2007).

[80] Y. Pennec, B. Djafari-Rouhani, H. Larabi, J. Vasseur, A.C. Hladky-Hennion, “Phononic crystals and manipulation of sound”, Physica status solidi C – current topics in solid state physics, **6** (9), 2080-2085 (2009).

[81] V. Romero-Garcia, J.V. Sanchez-Perez, L.M. Garcia-Raffi, J.M. Herrero, S. Garcia-Nieto, X. Blasco, “Hole distribution in phononic crystals: Design and optimization”. J. Acoust. Soc. Am., **125** (6), 3774-3783 (2009).

[82] T. Miyashita, “Acoustic defect-mode waveguides fabricated in sonic crystal: Numerical analyses by elastic finite-difference time-domain method”, Japanese Journal of Applied Physic Part 1 - Regular papers brief communications & review papers, **45** (5B), 4440-4447 (2006).

[83] J.D. Turner and A.J. Pretlove, “Acoustic for engineers”, Macmillan (1991).

[84] M.R. Schroeder, “Integrated-impulse method for measuring sound decay without using impulses”. **66**, no. 2, pp. 497–500 (1979).

[85] M. Vorländer and M. Kob, “Practical aspects of MLS measurements in building acoustics”. APPLIED ACOUSTICS, **52** (3-4), 239-258 (1997).

[86] K Heutschi and A. Rosenheck, “Outdoor sound propagation measurements using an MLS technique”. Applied Acoustics, **51** (1), 13-32 (1997).

[87] D.G. Ciric and M.A. Milosevic, “Transient noise influence in MLS measurement of room impulse response”. ACTA Acustica United with Acustica, **91** (1), 110-120 (2005).

[88] D.D. Rife, “Maximum-Length-Sequence-Analyzer (Reference Manual)”, DRA Laboratories, Ver. 10WI, Rev. 8 (1987).

[89] BS EN 1793-6, “Road traffic noise reducing devices. Test method for determining the acoustic performance. Part 6. Intrinsic characteristics. In situ values of airborne sound insulation under direct sound field conditions” (2010).

[90] F.J. Harris, “On the use of windows for Harmonic Analysis with the Discrete Fourier Transform”. Proceeding of the IEEE, 66, 1 (1987).

[91] ANSI S12.8 - 1998, “Methods for Determination of Insertion Loss of Outdoor Noise Barriers” (2008).

[92] A. Farina, “Simultaneous measurement of impulse response and distortion with a Swept-sine technique”. 108th Audio Engineering Society Convention, 5093 (D-4) (2000).

[93] T. Legouis and J. Nicolas, “Phase gradient method of measuring the acoustic impedance of materials”, J. Acoust. Soc. Am., **81** (1), 33-50 (1987).

[94] S. Guy-Bart and E. Jean-Jacques, A. Dominique, Comparison of different impulse response measurement techniques”, Journal of Audio Engineering Society, **50** (4), 249-262 (2002).

[95] K. Suzuki, “X-ray studies on precipitation of metastable centers in mixed crystals nacl-cdcl2”, J.Phys. Soc. Jpn., **16**:67 (1961).

[96] D. Caballero, J. Sánchez-Dehesa, R. Martínez-Sala, C. Rubio, J.V. Sánchez-Pérez, L. Sanchis, and F. Meseguer. “Suzuki phase in two-dimensional sonic crystals”. Physical Review B, **64**:064303 (2001).

[97] F.G. Wu, Z.L. Hou, Z.Y. Liu, and Y.Y. Liu. “Point defect states in two-dimensional phononic crystals”. Physics Letter A, **292**:198 (2001).

[98] M. Sigalas, “Eastic wave band gaps and defect states in two-dimensional composites”. J. Acoust. Soc. Am., **101**, 1257 (1997).

[99] R. Sainidou, B. Djafari-Rouhani, Y. Pennec and J.O. Vasseur, “Locally resonant phononic crystals made of hollow spheres or cylinders”. J. Acoust. Soc. Am., **119**, 278-284 (2006).

[100] M. Hirsekorn, P.P. Delsanto, N.K. Batra and P. Matic, “Modelling and simulation of acoustic wave propagation in locally resonant sonic materials”. Ultrasonics, **42**, 231-235 (2004).

[101] M.S. Kushwaha and P. Halevi, “Stop bands for cubic arrays of spherical balloons”. J. Acoust. Soc. Am., **101**, 619-622 (1997).

[102] E. Fuster-Garcia, V. Romero-Garcia, J. V. Sánchez-Pérez, and L. M. Garcia-Raffi, “Targeted band gap creation using mixed sonic crystal arrays including resonators and rigid scatterers,” Applied Physics Letter **90**, 244104 (2007).

[103] F. Wang, C.K. Mechefske, “Modal Analysis and testing of a thin-walled gradient coil cylinder model”. Concepts in Magnetic resonance part B – Magnetic resonance engineering, **27B**, 34-50 (2005).

[104] A. Krynkin and O. Umnova, “Characteristics of wave propagation through doubly-periodic array of elastic shells”. paper presented at EuroNoise (2009).

[105] N.A. Nicorovici, R.C. Mcphedran, “Photonic band gaps for arrays of perfectly conducting cylinders”. Physical Review E, **52**, 1135-1145 (1995).

[106] G.C. Gaunaurd, “Sonar cross section of a coated hollow cylinder in water”. J. Acoust. Soc. Am., **61**, 360–368 (1977).

[107] J.D. Kaplunov, L. Yu. Kossovich and E.V. Nolde, “Dynamic of thin walled elastic bodies”. Academic Press London, 110 (1998).

[108] B. Merheb, P.A. Deymier, M. Jain, M. Aloshyna-Lesuffleur, S. Mohanty, A. Barker and R.W. Greger, “Elastic and viscoelastic effects in rubber-air acoustics band gap structure: A theoretical and experimental study”. J. Applied Physics, **104**, 064913 (2008).

[109] http://www.makeitfrom.com/data/?material=Natural_Rubber, last accessed on 11 Aug 2011.

[110] http://www.engineeringtoolbox.com/density-solids-d_1265.html, last accessed on 11 Aug 2011.

[111] A. Krynkin, O. Umnova, A.Y.B. Chong, S. Taherzadeh and K. Attenborough, “Predictions and measurements of sound transmission through a periodic array of elastic shells in air”. J. Acoust. Soc. Am., **128**, 3496-3506 (2010).

[112] J.B. Pendry, A.J. Holden, W.J. Stewart, and I. Youngs, “Magnetism from conductors, and enhanced non-linear phenomena.” IEEE Trans. Microw. Theory Tech., **47**, 2975 (1999).

[113] A.B. Movchan and S. Guenneau, “Split-ring resonators and localized modes”. Physical Review B, **70**, 125116 (2004).

[114] L.Y. Wu, L.W. Chen, M.L. Wu, “The nondiffractive wave propagation in the sonic crystal consisting of rectangular rods with a slit”, Journal of physics – Condensed Matter, **20**, 295229 (2008).

[115] R. Marques, F. Mesa, J, Martel and F Medina, “Comparitive analysis of edge- and broadside- coupled split ring resonators for metamaterial design, theory and experiments”. IEEE Transactions on Antennas and Propagation, **51**, 2572 (2003).

[116] K. Aydin and E. Ozbay, “Capacitor-loaded split ring resonators as tunable metamaterial components”. Journal of Applied Physics, **101**, 024911 (2007).

[117] X. Hu and C.T. Chan, “Two-dimensional sonic crystals with Helmholtz resonators”. Physical Review E, **71**, 055601 (2005).

[118] W. Elmore and M. Heald, “Physics of Waves”, New York: McGraw-Hill, p. 148 (1969).

[119] C.H. Sohn and J.H. Park, “A comparative study on acoustic damping induced by half-wave, quarter-wave and Helmholtz resonators”. Aerospace Science and Technology, **15**, 606 (2011).

[120] L. Kinsler, A. Frey, A. Coppens and J. Sanders, “Fundamentals of Acoustic”. John Wiley and Sons, New York, third edition (1982).

[121] F.P. Mechel, “Formulas of acoustics”, Springer Verlag, New York Inc (2008).

[122] S.G.L. Smith and A.M.J. Davis, "The split ring resonator". Proceedings of the Royal Society A, **466**, 3117-3134 (2010).

[123] Z.Y. Cui, T.N. Chen and Y.P. Su, “Experimental and calculated research on a large band gap constituting of tubes with periodic narrow slits”. Applied Acoustics **70**, 1087 (2009).

[124] F. Montiel and M. Neviere, “Perfectly conducting gratings: a new approach using infinitely thin strips”. Optics Communications, **144**, 82 (1997).

[125] B. Guizal and D Felbacq, “Numerical computation of the scattering matrix of an electromagnetic resonator”. Physical Review E, **66**, 026602 (2002).

[126] A.D. Rawlins, “Approximate boundary conditions for diffraction by thin transmissive media”. ZAMM - Journal of Applied Mathematics and Mechanics **87**, 711 (2007).

[127] M. Abramowitz and I.A. Stegun, “Handbook of Mathematical Functions, National Bureau of Standards, New York: Dover, 363 (1972).

[128] A. Krynkin, O. Umnova, A.Y.B. Chong, S. Taherzadeh and K. Attenborough, “Scattering by coupled resonating elements in air”. Journal of Physics D: Applied Physics, **44**, 125501 (2011).

[129] A. Kyrnkin, O. Umnova, J.V. Sanchez-Perez, A.Y.B. Chong, S. Taherzadeh, K. Attenborough, “Acoustic insertion loss due to two dimensional periodic arrays of circular cylinders parallel to a nearby surface”, J. Acoust. Soc. Am., **130**, (6) (2011).

[130] R. H. Olsson III , I. EI-Kady, M. F. Su, M. R. Tuck, F. B. McCormick and J. G. Fleming, “Research on micro-size acoustic bandgap structure”, SANDIA Report, SAND2010-0044, page 15 (2010).

[131] R. Kruse, “In-situ measurement of ground impedances”, PhD Thesis, (2008).

[132] W. K. Lui and K.M. Li, “The scattering of sound by a long cylinder above an impedance boundary”. J. Acoust. Soc. Am., **127** (2), 664-674 (2010).

[133] J. C. Bertrand and J. W. Young, “Multiple scattering between a cylinder and a plane”. J. Acoust. Soc. Am., **60** (6), 1265-1269 (1976).

[134] G. Watts, “Harmonise prediction model for road traffic noise”, Transport Research Laboratory report, PPP034 (2005).

[135] D. van Maercke and J. Defrance, “Development of an analytical model for outdoor sound propagation within the Harmonoise project”, ACTA Acustica United with Acustica, **93**, 201 (2007).

[136] K. Attenborough, K.M. Li, K. Horoshenkov, “Predicting Outdoor Sound”, Taylor & Francis, (2007).

[137] M.E. Delany and E.N. Bazley, “Acoustic properties of fibrous absorbent materials”. Applied Acoustics, **3**, pp 105-116 (1970).

[138] K. Attenborough and I. Ver, “Noise and vibration control engineering”. Beranek and Ver ed, New York (USA), 3rd Edition (2008).

[139] K. Attenborough, I. Bashir and S. Taherzadeh, “Outdoor ground impedance models”. J. Acoust. Soc. Am., **129** (5) 2806 – 2819 (2011)).

[140] American National Standard method for determining the acoustic impedance of ground surfaces (2010).

[141] P. Boulanger, K. Attenborough, Q. Qin and C.M. Linton, “Reflection of sound from random distributions of semi-cylinders on a hard plane: models and data”. Journal of Physics D: Applied Physics, **38**, 3480-3490 (2005).

[142] A. Krynkin and O. Umnova, “On performance of sonic crystals in presence of ground plane”. Proceedings of Inter-noise, Lisbon (2010).

[143] D.C. Hothershall, D.H. Crombie, S.N. Chandler-Wilde, “The performance of T-profile and associated noise barriers,” Applied Acoustics, **32**, 269-287 (1991).

[144] G.R. Watts, “Acoustic performance of a multiple edge noise barrier profile at motorway sites.” Applied Acoustics, **47**, 47-66 (1996).

[145] M.R. Monazzam and Y.W. Lam, “Performance of Profiled Single Noise Barriers Covered with Quadratic Residue Diffusers”, Applied Acoustics **66**, pp.709-730 (2005)

[146] J. Berenger "A perfectly matched layer for the absorption of electromagnetic waves". Journal of Computational Physics **114** (2), 185–200 (1994).

[147] A. Kyrnkin, O. Umnova, J.V. Sanchez-Perez, A.Y.B. Chong, S. Taherzadeh, K. Attenborough, “Acoustic insertion loss due to two dimensional periodic arrays of circular cylinders parallel to a nearby surface”, J. Acoust. Soc. Am., **130**, (6) (2011).